Atom interferometry: from fundamental physics to precision inertial measurements

Remi Geiger

To cite this version:

Remi Geiger. Atom interferometry: from fundamental physics to precision inertial measurements. Atomic Physics [physics.atom-ph]. Sorbonne Université, 2019. tel-02267800

HAL Id: tel-02267800
https://theses.hal.science/tel-02267800v1

Submitted on 19 Aug 2019

Sorbonne Université

Habilitation à Diriger des Recherches

Atom interferometry: from fundamental physics to precision inertial measurements

Remi Geiger

SYRTE – Systèmes de Référence Temps-Espace

Observatoire de Paris – 61 avenue de l'Observatoire – 75014 Paris, France

Thèse soutenue le 28 juin 2019 devant le jury composé de :

Mark Kasevich	Stanford University
Guglielmo Tino	European laboratory for nonlinear spectroscopy, INFN, University of Florence
Jacques Vigué	Laboratoire Collisions Agrégats Réactivité, CNRS, Université de Toulouse
Saïda Guellati	Laboratoire Kastler-Brossel, CNRS, Sorbonne Université
Alain Aspect	Institut d'Optique, CNRS, Université Paris-Saclay
Luc Blanchet	Institut d'Astrophysique de Paris, CNRS, Sorbonne Université

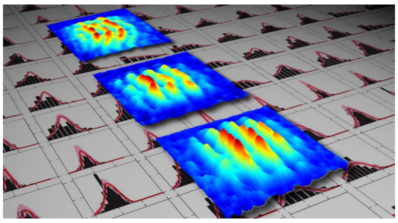

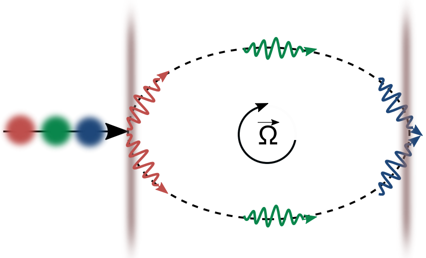

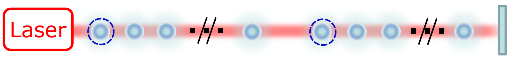

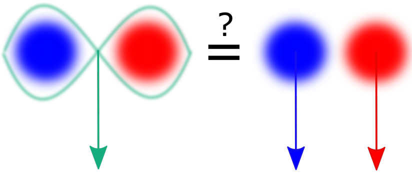

Remerciements – Acknowledgments

Je remercie les rapporteurs de cette thèse, Mark Kasevich, Guglielmo Tino et Jacques Vigué pour la lecture attentive de ce manuscrit et leurs remarques positives sur son contenu, ainsi que les autres membres du jury de ma soutenance, Saïda Guellati, Alain Aspect et Luc Blanchet pour leurs commentaires constructifs.

Noël Dimarcq et Arnaud Landragin, directeurs successifs du laboratoire SYRTE des six dernières années, m'ont accueilli chaleureusement et m'ont accordé leur confiance ; je les en remercie vivement. Merci également à Franck Pereira Dos Santos pour la direction de l'équipe interférométrie atomique et capteurs inertiels (IACI) qu'il assure avec efficacité et bienveillance depuis la nomination d'Arnaud en tant que directeur du laboratoire en 2014. Les interactions constructives et sympathiques avec les autres membres permanents de l'équipe IACI sont précieuses ; merci ainsi à Christian Bordé, Carlos Garrido-Alzar, Sébastien Merlet et Quentin Beaufils.

Le travail décrit dans ce manuscrit est le résultat d'un important travail d'équipe et le fruit de plusieurs collaborations sur la période 2011-2019, dont je souhaite remercier les principaux acteurs.

Les résultats de mes recherches de postdoctorat à Vienne n'auraient pas vu le jour sans le travail conséquent de David Adu-Smith qui m'a précédé sur le projet en menant la réalisation d'une grande partie du dispositif expérimental. Je le remercie pour la formation qu'il m'a procurée et pour m'avoir laissé la place alors que l'expérience commençait à porter ses fruits. Merci à Jörg Schmiedmayer pour son accueil dans son groupe, sa confiance et la grande liberté qu'il m'a laissée dans la conduite du projet. Je remercie très chaleureusement Tim Langen avec lequel j'ai travaillé main dans la main durant ces deux années: merci Tim pour ton amitié et tes efforts pour approfondir les points obscurs de l'expérience. Je remercie également Bernhard Rauer, Maximilian Kuhnert et Thomas Schweigler que j'ai eu beaucoup de plaisir à encadrer. Les interactions avec Jean-François Schaff ont été cruciales pour me permettre d'aborder la physique des condensats de Bose-Einstein, pour lesquelles je le remercie, ainsi que pour notre amitié qui s'est formée lors de notre séjour viennois.

Dès mon arrivée au SYRTE, j'ai eu la chance de travailler en toute liberté sur le projet de gyromètre-accéléromètre avant d'en assurer progressivement la conduite grâce à la confiance d'Arnaud Landragin que je remercie chaleureusement, tant pour nos échanges scientifiques et techniques que pour son soutien dans le développement de ma carrière. Je remercie également les six doctorants et trois postdoctorants avec lesquels j'ai travaillé avec plaisir depuis 2013 dans le cadre de ce projet : Matthieu Meunier, Indranil Dutta, Denis Savoie, Nicolas Mielec, Matteo Altorio, Romain Gautier, Bess Fang, Ranjita Sapam et Leonid Sidorenkov.

Le projet MIGA est mené en collaboration avec plusieurs laboratoires français. Je remercie ici tout particulièrement Benjamin Canuel du LP2N et Walid Chaibi du laboratoire ARTEMIS avec lesquels j'ai interagi le plus étroitement et avec plaisir durant les six dernières années, ainsi que Philippe Bouyer et Andrea Bertoldi du LP2N. Merci également à Louis Amand pour son important travail de conception et de réalisation du premier système MIGA réalisé au SYRTE, ainsi que pour nos interactions chaleureuses.

Les projets expérimentaux réalisés au SYRTE naissent et se développent grâce au support essentiel des services de mécanique, d'électronique et d'informatique dont je souhaite remercier tout particulièrement David Holleville, Bertrand Venon, David Horville, Michel Lours, José Pinto, Laurent Volodimer et Pascal Blondé. Merci également à Marine Pailler pour sa patience et son efficacité dans la gestion de mes contrats de recherche en tant qu'administratrice du laboratoire.

Le travail prospectif sur l'intrication et le principe d'équivalence décrit dans le dernier chapitre de ce manuscrit n'aurait pu voir le jour sans les idées novatrices et l'effort de collaboration de mon ancien collègue viennois Michael Trupke, ainsi que l'intérêt porté à ce projet par Peter Wolf au SYRTE, que je remercie vivement.

Enfin, une grande partie des résultats présentés ici ont été obtenus grâce au soutien financier de diverses agences et collectivités, que je remercie pour m'avoir accordé leur confiance dès le début de ma carrière au SYRTE.

I thank the reviewers of this thesis, Mark Kasevich, Guglielmo Tino and Jacques Vigué for the careful reading of this manuscript and their positive remarks on its content, as well as the other members of the jury of my defense, Saïda Guellati, Alain Aspect and Luc Blanchet for their constructive comments.

Noël Dimarcq and Arnaud Landragin, successive directors of the SYRTE laboratory for the last six years, have warmly welcomed me and put their trust in me; I thank them warmly. Thanks also to Franck Pereira Dos Santos for the direction of the Atomic Interferometry and Inertial Sensors Team (IACI) which he has been leading with efficiency and kindness since the appointment of Arnaud as director of the laboratory in 2014. The constructive and nice interactions with the other permanent members of the IACI team are valuable; thanks to Christian Bordé, Carlos Garrido-Alzar, Sébastien Merlet and Quentin Beaufils.

The work described in this manuscript is the result of an important team work and of several collaborations over the period 2011-2019, of which I wish to thank the main actors.

The results of my postdoctoral research in Vienna would not have been possible without the hard work of David Adu-Smith who preceded me on the project by leading the realization of a large part of the experimental device. I thank him for the training he gave me and for giving me the place as the experiment began to bear fruit. Thanks to Jörg Schmiedmayer for his welcome in his group, his confidence and the great freedom he left me in the conduct of the project. I warmly thank Tim Langen with whom I have worked hand in hand over the past two years: thank you Tim for your friendship and your efforts to understand the dark points of the experiment. I also thank Bernhard Rauer, Maximilian Kuhnert and Thomas Schweigler whom I had great pleasure in supervising. The interactions with Jean-François Schaff were crucial for me to address the physics of Bose-Einstein condensates, for which I thank him, as well as for our friendship that formed during our stay in Vienna.

As soon as I arrived at SYRTE, I had the chance to work freely on the gyroscope-accelerometer project before gradually taking the lead thanks to the trust of Arnaud Landragin, whom I thank warmly, both for our scientific and technical exchanges and for his support in the development of my career. I also thank the six doctoral students and three postdoctoral fellows with whom I have worked with pleasure since 2013 in the framework of this project: Matthieu Meunier, Indranil Dutta, Denis Savoie, Nicolas Mielec, Matteo Altorio, Romain Gautier, Bess Fang, Ranjita Sapam and Leonid Sidorenkov.

The MIGA project is conducted in collaboration with several French laboratories. I especially

thank Benjamin Canuel from LP2N and Walid Chaibi from the ARTEMIS laboratory with whom I have interacted most closely and with pleasure during the last six years, as well as Philippe Bouyer and Andrea Bertoldi from LP2N. Thank you also to Louis Amand for his important work on the design and the realization of the first MIGA system realized at SYRTE, as well as for our warm interactions.

The experimental projects carried out at SYRTE are born and developed thanks to the essential support of the mechanical, electronic and computer departments, of which I wish to particularly thank David Holleville, Bertrand Venon, David Horville, Michel Lours, José Pinto, Laurent Volodimer and Pascal Blondé. Thanks also to Marine Pailler for her patience and effectiveness in managing my research contracts as a laboratory administrator.

The prospective work on entanglement and the principle of equivalence described in the last chapter of this manuscript could not have been possible without the innovative ideas and collaborative effort of my former Viennese colleague Michael Trupke, as well as the interest in this project by Peter Wolf at SYRTE, whom I thank warmly.

Finally, a large part of the results presented here were obtained thanks to the financial support of various agencies and communities, which I thank for having given me their confidence from the beginning of my career at SYRTE.

Contents

Chapter 1

Introduction

Optical interferometry has led to some of the most important discoveries in physics, ranging from the Michelson-Morley experiment contradicting the aether theory in the late 19$^{\text{th}}$ century, to the recent detection of gravitational waves in 2015. Light interferometry is nowadays an established technique in several areas of science and technology. Interferometry with matter waves nearly dates back to the first ages of quantum mechanics as the concept of matter waves played a key role in the development of the quantum theory, following the theoretical work of de Broglie in 1924 and the ensuing experiments of Davisson, Germer and Thomson with electron beams. Since then, performing interference experiments with various types of matter-waves has driven the efforts of several communities working with electrons, neutrons, atoms, molecules, or anti-matter. The field of atom interferometry has developped rapidly with the advancement of atomic physics, which offers a high level of control and reliability to the experimental physicist. This degree of control has become even more impressive since the advent of laser cooling techniques in the 1980s, as they allow us to observe atomic waves for increased durations and in greater details compared to interferometry with atomic beams.

In the last 11 years (2008-2019), my research has focused on the development of atom interferometry as a probe of fundamental physics and as a way to perform precision measurements of gravitational and inertial effects. This manuscript summarizes my activity since the end of my PhD in 2011.

Chapter 2 describes my postdoctoral work in the *atomchip* group lead by Joerg Schmiedmayer at the Technical University of Vienna, from November 2011 to August 2013. There, I performed interference experiments with Bose-Einstein condensates produced on an atom chip in order to probe the non-equilibrium dynamics of one-dimensional, interacting, many-body quantum systems.

The rest of the manuscript presents my research conducted at the SYRTE laboratory of Paris Observatory since September 2013, which is mainly related to cold-atom inertial sensors. Before entering in the topic, I will introduce the international context on this active research field.

Context of the research on cold-atom inertial sensors

Since the pioneering experiments of 1991, the field of atom interferometry has progressed rapidly. Cold-atom inertial sensors based on atom interferometry have reached sensitivity and accuracy levels competing with or beating inertial sensors based on different technologies. Such sensors cover various applications ranging from geophysics and inertial sensing to metrology and tests of fundamental physics. Addressing these applications requires to constantly push further the performances of quantum sensors in terms of sensitivity, accuracy, dynamic range, compactness or robustness, and ease-of-use or cost. In France, the cold-atom inertial sensing activity was pioneered at the SYRTE laboratory in the late 1990s by André Clairon, Noël Dimarcq, Christian Bordé, and later by Arnaud Landragin and Franck Pereira Dos Santos, with a constant progress to establish it as a worldwide reference in the field.

As of 2019, more than 40 research groups worldwide are actively developing atom interferometers for different applications, and investigating techniques to improve the performances of cold-atom inertial sensors. Currently, the research focuses on three mains aspects:

1. pushing the performances of current sensors;
2. identifying new sensor architectures or generic techniques that can bring performance improvement;
3. using atom interferometers in fundamental and/or field applications.

The tables below (1.1,1.2,1.3) summarize the research interests of the main actors in the field.

Better performances not only means that the sensitivity of cold-atom inertial sensors should be improved, but also their stability, accuracy, dynamic range, compactness, transportability, ease-of-use and cost. While the first 20 years of research were essentially focused on sensitivity improvements and tests of fundamental physics in laboratory environments, more and more projects have started since 2010 to address field applications. This is particularly the case for inertial guidance, which requires at the same time high levels of stability, important dynamic ranges and sampling frequencies, compactness and robustness, where cold-atom sensors have failed so far to compete with other technologies (e.g. ring laser gyroscopes for navigation). The course for greater performance is, for example, at the core of the *Quantum Sensors and Metrology* pillar of the Quantum Technology Flagship initiated by the European Union. **Chapters 3 and 4** present my research in this context: the former introduces **new atom interferometry techniques** which are important for applications requiring **high sampling rates and high sensitivity**; the latter explores **new optical techniques** for shaping the lasers used in light-pulse atom interferometers.

Several proposals have addressed the potential of atom interferometry to **gravitational wave detection**, mainly to cover the sub-Hz frequency band. I will describe my activity in that context in **chapter 5**.

Regarding fundamental physics, atom interferometers have contributed in various ways. They have, for example, allowed to investigate peculiar effects of quantum mechanics [1] and its interplay with gravity [2], or to probe for possible new interactions beyond the standard model and general relativity [3]–[5]. Atom interferometers have also been used for recoil velocity measurements, yielding accurate measurements of the fine structure constant and therefore tests of quantum electrodynamics [6], [7]. On the metrology side, measurements of the Newtonian gravitational constant were achieved [8], [9], with a relative uncertainty as low as 150 parts per million. Several tests of the universality of free fall have also been performed by atom interferometry: they enable to probe the validity of this cornerstone of general relativity with microscopic proof masses described by quantum degrees of freedom, rather than with classical macroscopic proof masses [10]–[17]. Prospects for improved tests in space are also investigated [18]–[20]. In that context, I have proposed a way to **test the weak equivalence principle with a pair of entangled atoms of different species**, which I will shortly describe in **chapter 6**.

country	Institution	PI	topics/expertise	atom/techniques	link
France	SYRTE, Paris	Landragin, Pereira	gravimetry, gyroscope, gradiometer, trapped AI, GW detection	Rb, Cs	website
France	LKB, Paris	Guellati, Cladé	h/m, LMT, Bloch	Rb	website
France	ONERA, Palaiseau	Zahzam, Bidel	gravimetry, gradiometry, field applications	Rb	link
France	iXBlue/IOGS, Bordeaux	Barrett, Bouyer	inertial sensors	Rb	website
France	*muquans (company)*, Bordeaux	B. Desruelle (CEO)	gravimeter, gradiometer	Rb	website
France	*Thales Group (company)*, Palaiseau	–	accelerometer, atom chip	Rb	[21]
France	LP2N, Bordeaux	Bouyer, Canuel	EP, GW	Rb, Sr	website
France	LCAR, Toulouse Univ.	Vigué, Gauguet	test of atom neutrality, topological phases, atom chips	atomic beams, cold atoms	website
Germany	Hannover Univ.	Rasel	gravimeter, gradiometer, EP, GW, LMT	Rb, Yb, atom chips	website
Germany	Humboldt Univ.	Peters, Krutzik	gravimetry, EP	Rb	website
Greece	IESL-FORTH, Crete	von Klitzing	guided interferometry, BEC	Rb	website
Italy	LENS, Florence	Tino, Poli	gradiometry, trapped atom interferometry	Rb, Sr, Cd	website
Italy	*AtomSensors (company)*	–	gravimeter, gradiometer	Rb	website
UK	Univ. Birmingham	Bongs	towards field applications	Rb	website
UK	Imperial College London	Hinds	accelerometry, dark energy	Rb	website
UK	Univ. Nottingham	Fernholtz	guided interferometry	Rb	website
UK	*Teledyne e2v (company)*	–	gravimetry	Rb	website
UK	*M2 lasers (company)*	–	accelerometer	Rb	website

Table 1.1: Table summarizing the main actors in the field of cold-atom inertial sensors (Europe). WEP: Weak Equivalence Principle; GW: Gravitational Wave; LMT: Large Momentum Transfer techniques; BEC: interferometry with Bose Einstein Condensates; h/m: measurement of the recoil velocity.

country	Institution	PI	topics/expertise	atom/techniques	link
USA	Stanford	Kasevich, Hogan	EP, GW detection, LMT, BEC	Rb, Sr, 10-meter fountain	website
USA	Berkeley	Mueller	tests of fondamental physics, h/m, LMT	Cs	website
USA	JPL	Yu	applications in geodesy	Rb gradiometry	website
USA	Sandia National Lab.	Biederman	high sampling rates, multi-axis	vapor cell	website
USA	Cambridge	Stoner	LMT, BEC	–	[22]
USA	Univ. Washington	Gupta	LMT, BEC	–	website
USA	*AO Sense Inc.*	B. Young (CEO)	gravimetry, inertial sensors	–	website
USA	NIST	Kitching, Donley	miniature AI for inertial sensing	Rb	website
USA	Northwestern Univ.	Kovatchy	GW, LMT	–	website
USA	Goddard (NASA)	Saif	gradiometry	–	link
Mexico	Univ. San Lui Potosi	Gomez, Franco	gravimeter	Rb	website

Table 1.2: Table summarizing the main actors in the field of cold-atom inertial sensors (North America).

country	Institution	PI	topics/expertise	atom/techniques	link
Australia	ANU	J. Close, N. Robins	gravimeter, gradiometer	Rb	website
China	Wuhan Institute of Physics	M. Zhan	gravimeter, EP, GW	Rb, Sr, Cs, 10-meter fountain	website
China	Zhejiang Univ. of Technology	Q. Lin	gravimetry	Rb	[23]
China	HUST, Wuhan	Zhong-Kun Hu	gravimetry, EP	Rb	website
China	National Institute of Metrology, Beijing	Shao-Kai Wang	gravimetry	Rb	[24]
China	National Laboratory Shanghai	Shuai Chen	gravimetry	Rb	website
Korea	KRISS	Dai-Hyuk Yu	gravimeter	Rb	article
India	IISER Pune	Krishnakumar	AI with BEC	Rb	website
Israel	Weizman Institue	Davidson, Firstenberg	gravimeter, inertial navigation	Rb	website
Japan	Univ. Tokyo	Katori	optically guided interferometry	Sr	[25]
New Zealand	Univ. Otago	Andersen	gravimeter	Rb	website
Singapore	CQT	Dumcke	portable gravimeter	Rb	website
Singapore	NTU	S.-Y. Lan	hollow core fiber AI	Rb	website
Singapore	*Atomionics (company)*	–	inertial sensors	–	website

Table 1.3: Table summarizing the main actors in the field of cold-atom inertial sensors (Outside Europe and North America).

Chapter 2

Probing the dynamics of isolated quantum systems with matter-wave interferometry

The relaxation of isolated quantum many-body systems is an important open problem at the frontier between statistical and quantum physics. Studying relaxation processes in such systems remains a challenge despite considerable efforts. Experimentally, it requires the creation and manipulation of well-controlled and isolated quantum systems. In this context, ultracold neutral atoms provide unique opportunities to understand non-equilibrium phenomena because of the large set of available methods to isolate, manipulate and probe these systems [26].

During my postdoctoral experience at the *Atominstitut* of the Technical University of Vienna, I studied the relaxation dynamics of gases of ultra-cold ^{87}Rb confined in quasi-one-dimensional (quasi-1D) geometry by the trapping potential of an atom chip, via matter-wave interferometry. At a time where the research field was just starting, we performed pioneering experiments showing the importance of conserved quantities on the dynamics of the system.

2.1 Context

The context of our experiments is the understanding of the mechanism of thermalization in isolated (quantum) many-body systems, as detailed in a review paper from 2015, Ref. [27]. I summarize it here briefly for completeness. The general question under study is whether and how an isolated system can reach an apparent stationary (thermal equilibrium) state after having been artificially placed out of equilibrium, and if such a state can be described by the conventional ensembles of statistical mechanics. This problem is open and relevant to various areas of physics such as cosmology, high-energy physics or condensed matter physics. The *gedanken* experiment under study is the so-called quantum quench, which investigates the dynamical response of a system prepared in a state $|\psi_0\rangle$ of an Hamiltonian $\hat{H}$ subject to a sudden perturbation $\hat{H} \to \hat{H}'$. Can the expectation value of some observable after an evolution time t, $\langle\hat{\mathcal{O}}\rangle(t) = \langle\psi(t)|\hat{\mathcal{O}}|\psi(t)\rangle$, be described by the usual (e.g. canonical) statistical mechanics ensemble ? If yes, after which characteristic time-scale ? Thermalization towards such a state requires a complete loss of memory of the initial state $|\psi_0\rangle$. However, the unitary evolution of the isolated system prevents such a loss of memory, leading to a paradox that dates back to the 1930s.

The general key to resolving the paradox is the fact that the central role for observations is not played by the many-body wave function $|\psi(t)\rangle$, but instead by the outcomes of the measurement process. In a single run, a large quantum many-body system will evolve in a unitary way, but when observables are measured, their expectation values might become arbitrarily close to the prediction of a thermal state. A particular well-studied scenario to grasp this intuition more formally is the eigenstate thermalization hypothesis (ETH) [28]–[30], which conjectures that the initial state of a non-equilibrium evolution already has thermal properties on the level of individual many-body eigenstates. An intuitive picture for the ETH is that the isolated total system acts as an environment that thermalizes its few-body subsystems [31]. However, not all systems are expected to thermalize, the most notable exceptions being integrable and localized systems. If we assume that some isolated quantum systems can appear (for all practical purposes) thermalized, the next important question is how the thermalization proceeds. For example, there might be partial relaxation only, where instead of a complete loss of memory of the initial state, the system only partially forgets the initial conditions. Also, there might be different stages of relaxation connected to different time scales.

The experiments that we performed in Vienna aimed at contributing to understand this problem for a particular class of one-dimensional systems of bosons.

2.2 Principle of the experiments and methods

Quasi-1D Bose gas. Our experiments involved clouds of ultracold ^{87}Rb atoms in the so-called quasi-1D regime. This regime is characterized by a relation between 4 energy scales: $k_\mathrm{B}T, \mu, \hbar\omega_l < \hbar\omega_r$, with $k_\mathrm{B}T$ the thermal energy, μ the chemical potential characterizing the interaction energy, $\hbar\omega_l$ the energy associated with the longitudinal oscillation in the trap, and $\hbar\omega_r$ the energy associated with the radial trapping oscillations. In that regime, the physics occurs mainly through redistribution of energy among the longitudinal states of the trap. In our experiment, the typical parameters were $\omega_l/2\pi \simeq 11$ Hz, $\omega_r/2\pi \simeq 2.1$ kHz and $T \simeq 30 - 100$ nK (corresponding to frequencies from $0.6 - 2.0$ kHz). The number of atoms ranges from 4000 to 12000, which corresponds to $\mu \simeq h \times 1.1 - 2.5$ kHz for our trap geometry (linear densities $n_{1d} \sim 50\ \mu\mathrm{m}^{-1}$). The typical size of the cloud is 60 μm in the longitudinal direction and 0.3 μm in the radial direction (not resolved by the imaging systems). Figure 2.1 shows a picture of the atom chip setup used to create such quantum gases.

In the quasi-1D regime, the ultracold gas cannot be described by a single, homogeneous, macroscopic wavefunction as it is the case in a Bose-Einstein Condensate (BEC). On the contrary, the phase field exhibits fluctuations in the longitudinal direction, with a typical length scale $\lambda_T = 2\hbar^2 n_{1d}/mk_\mathrm{B}T \sim$ few μm. When the gas is released from its trap, the phase fluctuations translate into density fluctuation, which can be recorded by absorption imaging. Measuring the (spatial) spectrum of these fluctuations allows to extract the temperature of the system [32], [33]. The goal of our experiments is to study the dynamics of the longitudinal phase field, $\hat{\phi}(z)$, when the quasi-1D Bose gas is subject to sudden transformations, also referred to as quantum quenches in the literature.

Splitting the cloud. The atom chip system allows to radially split the cloud in two parts separated by a variable distance (in the range of few microns) and to raise a potential barrier between the two parts of the system, in a so-called double well system [34]. This feature can be used to prepare a system of two quasi-1D systems in the double well trap, or to prepare a system and then split it rapidly (compared to the time-scales associated with the longitudinal dynamics, ω_l^{-1}). Such a rapid splitting can be viewed as a beam splitter for the quasi-1D gas. The idea behind our experiments was to study the relaxation of the split system, investigate whether or not the split system relaxes to an equilibrium point, and if this equilibrium point has the same statistical properties as a system prepared in the double well trap. For a system initially prepared in the double-well trap at thermal equilibrium, the correlation length for the relative phase fluctuations between the clouds equals λ_T [35].

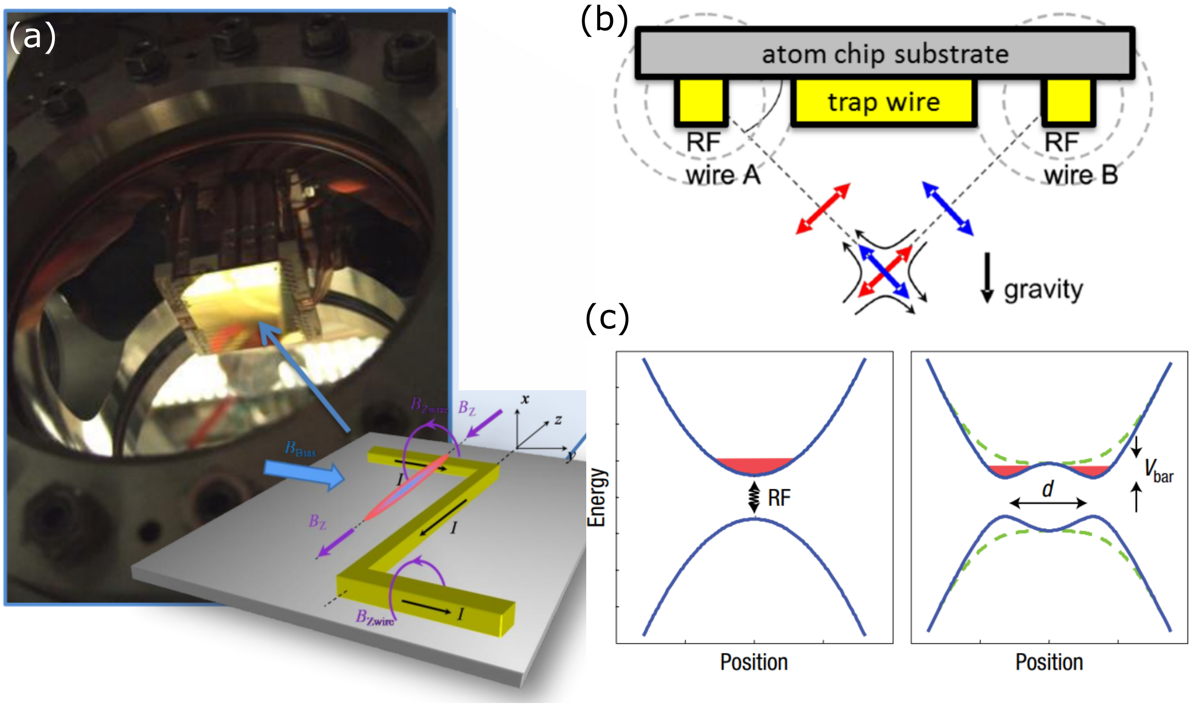

Figure 2.1: **Atom chip setup and double-well potential**. **(a)** View of the atom chip in the vacuum chamber. The cloud is magnetically trapped by a adding a bias field B_{bias} to the quadrupole potential created by sending DC current I in the chip wire. **(b)** Side view of the atom chip structure (not to scale). The central wire has a width of 100 μm and caries a constant current of typically 0.8 A. The two side wires (width of 30 μm) carry radio-frequency current ($\sim$ 20 mA) and couple different magnetic states, with a coupling constant that varies in space. The thickness of the gold layer is 2 μm. The atom cloud is trapped at a distance of typically 100 μm below the central wire. **(c)** (from [34]) The spatially dependent coupling allows to create a double-well potential with a (variable) separation $d \simeq 3$ μm and a (variable) barrier height $V_{\text{bar}} \simeq h \times 3$ kHz.

The principle of the relaxation dynamics experiments can be summarized as follows (see Figure 2.2):

1. preparation of a quasi-1D Bose gas of ^{87}Rb on an atom chip;
2. rapid splitting of the cloud in the transverse direction to initiate quantum dynamics;
3. evolution of the split system for a variable hold time;
4. release of the system and recombination of the two parts in time-of-flight to observe matter-wave interference;
5. repetition of the experiment in order to estimate the distribution/correlation functions of matter-wave interference (typically 200 repetitions per value of hold time).

2.3 Main results

I joined the experiment at a crucial point in November 2011. The team had just observed an interesting property of the relaxation of the system towards an apparent stationary state (on time-scales of tens of ms), which was far from the thermal equilibrium state, but could still be described by an effective thermal distribution. More precisely, the team showed that the relative phase correlations were much stronger than for a system of two quasi condensates prepared at

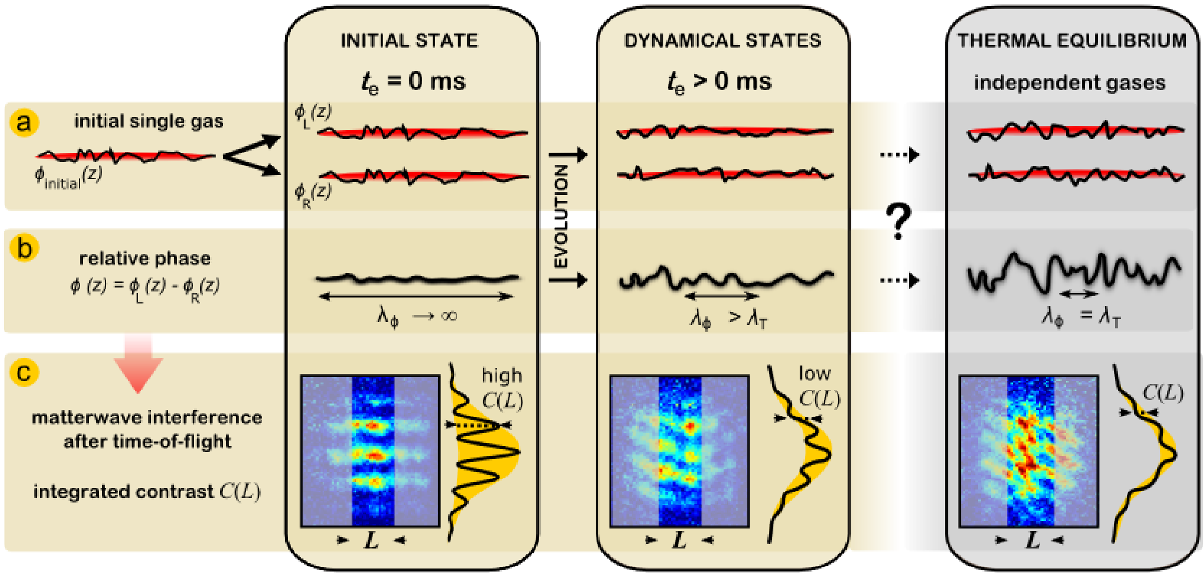

Figure 2.2: **Principle of the experiment probing relaxation dynamics by matter-wave interferometry** (from [36]). **(a,b)** A phase fluctuating 1D Bose gas is coherently split creating two gases with almost identical phase profiles $\phi_L(z)$ and $\phi_R(z)$ (represented by the black solid lines). The gases are then allowed to evolve in the double-well potential for some time t_e, which leads to the appearance of fluctuations in the local relative phase $\phi(z)$ and a decrease of the relative phase correlation length λ_ϕ. Our experiment aims at answering the questions whether and how this dynamical state reaches the thermal equilibrium state corresponding to two independently created quasi-condensates. In this thermal equilibrium state the phase difference between the gases fluctuates along its length and the correlation length λ_T is determined by the temperature and density of each cloud. (c) The phase difference $\phi(z)$ between the two 1D gases is probed through matter-wave interference in time-of-flight. The contrast $C(L)$ of the axially integrated interference pattern can then be used as a measure of the strength of the relative phase fluctuations.

the same temperature, T_{init}, than that of the system before splitting, and that the relative phase correlations could be well described by a thermal distribution associated to an effective temperature, T_{eff}, from five to ten times lower than T_{init} [37]. The corresponding relaxation process was entitled *prethermalization* as it was reminiscent of phenomena theoretically predicted for out-of-equilibrium systems in high energy physics (e.g. for the quark-gluon plasma produced in heavy ion collisions [38]). Although the experiments had been performed before my arrival, the team was in the process of understanding the underlying physics and subsequently had to argue with the reviewers of the article. One reason of the debate was the apparent contradiction of this result with previously published results from the Schmiedmayer group [39] that showed relaxation to thermal equilibrium in a similar experiment. The *Gring et al* paper (Ref. [37]) was finally published in September 2012.

In the first year, I participated to experiments aiming at confirming the results of Ref. [37], and extended the study to different regimes in order to understand in deeper details the prethermalization process. On the one hand, I took the lead of modeling the experiment, in order to understand the experimental limitations, in particular the impact of limited imaging resolution. On the other hand, building on the metrology expertise acquired during my PhD, I invested time in stabilizing the experiment by monitoring key environmental parameters (e.g. current in the coils), by improving the laser system to perform longer experimental runs (over up to three days consecutively), and by speeding up the experimental cycle (from 30 s to 10 s). Such technical improvements revealed critical for the subsequent experiments, since the core of our studies was the estimation of the correlation functions of the system, which required hundreds of experimental realizations. My first results, published in Ref. [40], clearly confirmed what was observed in [37] and were the starting point of the ensuing studies. After a theoretical description of the essential features of our system, I will describe below the two most important results which be obtained.

2.3.1 Theoretical background

I will present briefly the physics underlying our relaxation experiment; the theoretical details can be found in Ref. [41].

Hamiltonian. Each of the quasi-condensate can be described by its atomic field operator $\hat{\Psi}_j = \sqrt{\hat{n}_j(z)}\exp[i\hat{\theta}_j(z)]$, with $\hat{\theta}_j(z)$ and $\hat{n}_j(z)$ denoting the operators describing the phase and density of each quasi-condensate, respectively. Introducing the relative phase and relative density between the two gases through $\hat{\phi} = \hat{\theta}_1 - \hat{\theta}_2$ and $\hat{n} = (\hat{n}_1 - \hat{n}_2)/2$, and assuming a symmetric splitting (i.e. $N/2$ atoms in each condensate on average), it can be shown that the Hamiltonian of the interacting many-body system becomes quadratic in the relative density and relative phase operators:

$$\hat{H} = \frac{\hbar c}{2}\int dz\Big[\frac{K}{\pi}(\partial_z\hat{\phi})^2 + \frac{\pi}{K}\hat{n}^2\Big]. \tag{2.1}$$

Here $c = \sqrt{gn_0/m}$ is the speed of sound, m the mass of the ^{87}Rb atom $K = \frac{\hbar\pi}{2}\sqrt{\frac{n_0}{mg}}$ the Luttinger parameter, n_0 the 1D peak density, $g = 2\hbar\omega_r a$ the 1D interaction strength and $a \simeq 5$ nm the 3D scattering length. The Luttinger liquid model allows to describe the phononic (long wavelength) excitations of the system. This approximation is valid for the description of typical ultracold atom experiments, where optical methods with an imaging resolution corresponding to a few times the healing length are used to probe the excitations in the system.

Considering periodic boundary conditions for a gaz of side $\mathcal{L}$, the relative density and phase fields can be decomposed in a basis of plane waves as

$$\hat{n}(z,t) = \frac{1}{\sqrt{\mathcal{L}}}\sum_{k\neq 0}\hat{n}_k(t)e^{ikz} \quad , \ \hat{\phi}(z,t) = \frac{1}{\sqrt{\mathcal{L}}}\sum_{k\neq 0}\hat{\phi}_k(t)e^{ikz} \tag{2.2}$$

with the expansion coefficients given by:

$$\begin{aligned}\hat{n}_k(t) &= \sqrt{\frac{n_0 S_k}{2}}\Big(\hat{b}_k(t) + \hat{b}^\dagger_{-k}(t)\Big)\\ \hat{\phi}_k(t) &= \frac{1}{i\sqrt{2n_0S_k}}\Big(\hat{b}_k(t) - \hat{b}^\dagger_{-k}(t)\Big),\end{aligned} \tag{2.3}$$

where $S_k = \frac{\hbar|k|}{2mc} = \frac{|k|K}{\pi n_0}$. Here $\hat{b}^\dagger_k$ and $\hat{b}_k$ are the creation and annihilation operators for an elementary excitation with momentum $\hbar k$ in the relative degrees of freedom ($k = p\times 2\pi/\mathcal{L}$ with p integer different than 0). In this basis, the Hamiltonian of Eq. (2.1) takes the diagonal form

$$\hat{H} = \frac{\hbar c}{2}\sum_{k\neq 0}\Big[\frac{K}{\pi}k^2\hat{\phi}^\dagger_k\hat{\phi}_k + \frac{\pi}{K}\hat{n}^\dagger_k\hat{n}_k\Big] + \frac{\hbar\pi c}{2K}\hat{n}^\dagger_0 \tag{2.4}$$

with $\omega_k = c|k|$. It follows from the absence of coupling between the modes with different momentum k that *any momentum occupation numbers* $\langle\hat{b}^\dagger_k\hat{b}_k\rangle$ *that are initially imposed on the system will be conserved*, which reveals the integrability of the system.

Splitting process. When the splitting process is fast with respect to the interaction energy ($t_{\text{split}} \ll h/\mu = 2\pi\xi_h/c$), the local distribution of atoms in each small region of the quasi-condensate (of size $\sim \xi_h = \hbar/mc$) is binomial, with the respective minimum uncertainty relative-phase distribution. In that way, the coherent splitting copies the phase fluctuations of the initial quasi-condensate into both parts of the split system and the relative density fluctuations are given by the local shot noise. In terms of elementary excitations, this means :

$$\langle \hat{\phi}_k^\dagger \hat{\phi}_k \rangle|_{t=0} = \frac{1}{2n_0} \quad , \ \langle \hat{n}_k^\dagger \hat{n}_k \rangle|_{t=0} = \frac{n_0}{2} \tag{2.5}$$

In comparison, the thermal equilibrium state of two quasi-condensates at a temperature T would be characterized by [35]:

$$\langle \hat{\phi}_k^\dagger \hat{\phi}_k \rangle|_{\mathrm{therm}} = \frac{2}{\lambda_T k^2} \quad , \ \langle \hat{n}_k^\dagger \hat{n}_k \rangle|_{\mathrm{therm}} = \frac{k_{\mathrm{B}} T}{2g} \tag{2.6}$$

with $\lambda_T = \hbar^2 n_0 / m k_{\mathrm{B}} T$.

In terms of elementary excitations, it can be shown that the initial conditions of Eq. (2.5) lead to a thermal-like form of the occupation numbers that reads

$$\langle \hat{b}_k^\dagger \hat{b}_k \rangle = \frac{k_B T_{\mathrm{eff}}}{\hbar \omega_k}, \tag{2.7}$$

with the effective temperature given by $k_B T_{\mathrm{eff}} = n_0 g/2$. The fast splitting process thus equally distributes the energy $k_B T_{\mathrm{eff}}$ in the different k modes of the system.

Dynamics. Writting the equations of motion for the field operators yields the solutions [41]

$$\begin{aligned} \hat{\phi}_k(t) &= \frac{\pi}{kK} \sqrt{\frac{n_0}{2}} \sin \omega_k t \\ \hat{n}_k(t) &= \sqrt{\frac{n_0}{2}} \cos \omega_k t, \end{aligned} \tag{2.8}$$

which show the oscillation between the density and phase quadratures for the phononic excitations. *The energy, which was initially introduced in the system through the density quadrature (shot noise from the splitting process), will subsequently oscillate between the phase and density quadratures.*

2.3.2 Observation of the local emergence of thermal correlations (Refs. [42])

In our first work (Ref. [40]), we were probing the system on a global scale by measuring the interferometer integrated over a part of the cloud, which prevented us to access the local details of the relative phase correlation functions. Motivated by theoretical works on the velocity at which excitations spread during the relaxation of many-body quantum systems [43], [44], and by a recent observation of such effect from the Munich group on quenching the Bose-Hubbard model [45], we performed experiments to measure the evolution of the relative phase correlation function. This function is defined as $C(\bar{z}, t) = \exp\left(-\frac{1}{2}\langle \Delta\phi_{zz'}(t)^2 \rangle\right)$, where $\langle \Delta\phi_{zz'}(t)^2 \rangle \equiv \langle (\hat{\phi}(z,t) - \hat{\phi}(z',t))^2 \rangle$ denotes the phase variance between two points z and z' of the relative phase field, with $\bar{z} = z - z'$.

Observation. Our main experimental result is reported in Fig. 2.3. Directly after the splitting, the phase correlation function $C(\bar{z}, t)$ is close to unity for any distance $\bar{z}$, which is a manifestation of the long-range phase coherence produced by the splitting process. After a given evolution time t, the phase correlation function decays exponentially up to a characteristic distance $\bar{z}_c$ and stays nearly constant afterwards: $C(\bar{z} > \bar{z}_c, t) = C(\bar{z}_c, t)$. This means that beyond the distance $\bar{z}_c$ long-range phase coherence is retained across the system. With longer evolution time, the position of $\bar{z}_c$ shifts to larger distances and the value of $C(\bar{z} > \bar{z}_c, t)$ gradually decreases. The evolution continues until the system reaches a quasi-steady state, where the correlations decay exponentially throughout the entire system.

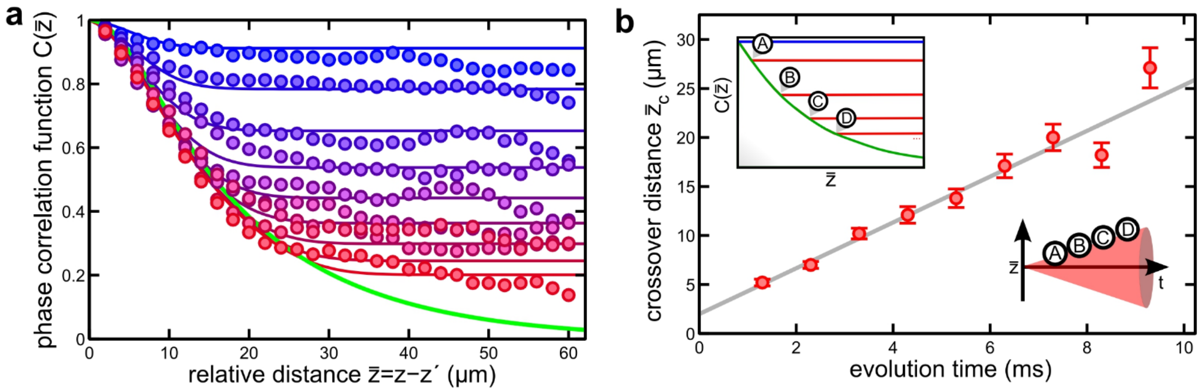

Figure 2.3: **Local emergence of thermal correlations in a light-cone-like evolution** (adapted from [42]). **(a)** Experimental phase correlation functions $C(\bar{z}, t)$ (filled circles) compared to theoretical calculations (solid lines). From top to bottom, the evolution time t increases from 1 ms to 9 ms in steps of 1 ms. The bottom (green) line is the theoretical correlation function of the prethermalized state. For each t, the constant values of $C(\bar{z}, t)$ at large $\bar{z}$ can be used to determine the crossover distance $\bar{z}_c(t)$ up to which the system forgets the initial long-range phase coherence. **(b)** Position of the crossover distance $\bar{z}_c$ as a function of evolution time t, revealing the light-cone-like decay of correlations. The solid line is a linear fit, the slope of which corresponds to twice the characteristic velocity of correlations. Insets: schematic visualization of the dynamics. The decay of correlations is characterized by a front moving with a finite velocity: for a given time t, $C(\bar{z}, t)$ is exponential (thermal) only up to the characteristic distance $\bar{z}_c(t)$ (points A-D). Beyond this horizon, long-range phase coherence is retained. Note that in the experimental data shown in (a), the sharp transitions (points A-D) are smeared out by the finite experimental imaging resolution.

From the experimental data, we extract the crossover points $\bar{z}_c$ through the level of long-range phase coherence. To this end, we consider for each t the region where the correlation function is constant, extrapolate the constant value to smaller $\bar{z}$ and determine the position $\bar{z}_c$ where it crosses the prethermalized correlation function. The result of this procedure is shown in Fig. 2.3(b). We observe a linear scaling of the position $\bar{z}_c = 2ct$, characterizing the local decay of correlations with time. This observation reveals that an arbitrary point in the gas loses its correlations with other points up to a certain separation $\bar{z}_c$, while long-range phase coherence persists outside this horizon. *The experimental data thus show that the prethermalized state locally emerges in a light-cone-like evolution*, where c plays the role of a characteristic velocity for the propagation of correlations in the quantum many-body system.

Interpretation. The result can be confronted to the theoretical model presented in the previous section: From Eqs. (2.2) and (2.8), the time evolution of the phase variance is given by

$$\langle \Delta\phi_{zz'}(t)^2 \rangle = \frac{\pi^2 n_0}{\mathcal{L} K^2} \sum_{k \neq 0} \frac{\sin(\omega_k t)^2}{k^2} \left(1 - \cos(k\bar{z})\right). \tag{2.9}$$

The sinusoidal term in the sum (2.9) represents the growth and subsequent oscillations in the amplitude of the phase fluctuations as they get converted from the initial density fluctuations. Mathematically, expression (2.9) is the Fourier decomposition of a trapezoid with a siding edge at $\bar{z}_c = 2ct$, so that the phase variance (and thus the phase correlation function) exhibits a two step feature. This two-step feature can physically be interpreted as follows: for a given time t, short wavelength modes will grow in amplitude and linearly increase the phase variance up to a distance $\bar{z}_c = 2ct$. Beyond that point the growth in amplitude of longer wavelength modes with $2\pi/k > \bar{z}_c$ exactly compensates the decrease in amplitude of the shorter wavelength modes with

$2\pi/k < \bar{z}_c$, leading to a constant phase variance. We observed this two-step property of the correlation function, with the sharp edge being smeared by the finite resolution of the imaging system. Moreover, we were able to extract the velocity characterizing the front of correlations, essentially determined by the sound velocity in the gas and the geometry of the longitudinal trapping potential (Fig. 3 of Ref. [42]).

2.3.3 Observation of a generalized Gibbs ensemble (Ref. [46])

Context. The level of details on the system brought by the study of the relative phase correlation functions pushed our team to acquire more and more data, in order to better understand the role of the conserved quantities on the dynamics (e.g. the mode occupation number $\langle \hat{b}_k^\dagger \hat{b}_k \rangle$ of Eq. (2.7)). In the first experiments aiming at measuring the two point phase correlation functions, we observed unexpectedly high level of correlation in $C(\bar{z}, t)$ at particular values of $\bar{z} = z - z'$. At that time, I thought that the reason for this excess of correlations could come from the trap which breaks the translational symmetry of the system. This pushed me to develop the model presented in Ref. [41], which was the key to explain the observations presented in the previous section. Moreover, my model showed that the excess of correlations could not be explained by the trap. We therefore had to look for another reason to explain the excess of correlation. Through an informal discussion with Isabelle Bouchoule (at Institut d'Optique in Palaiseau, France), we conjectured that the excess of correlations for particular evolution times and at particular values of $\bar{z}$ could originate from an asymmetric population of the odd and even k modes. In other words, the effective temperature defined in Eq. (2.7) would be different for odd and even k modes.

Experiment. To test this hypothesis of several temperatures, we studied the 2D correlation functions $C(z_1, z_2)$ without assuming translational symmetry of the system, for different splitting protocols. The experimental data are reported in Fig. 2.4, which compares the usual spliting protocol ((A)-used in the experiments of the previous section), and a different splitting protocol (B). The essential difference lies in the excess of correlation on the anti-diagonal of $C(z_1, z_2)$ for the (B) splitting. This excess of correlation remains over time evolution, in agreement with the theoretical modeling performed by collaborators from the University of Heidelberg (an extension of Ref. [41] to take into account an asymmetric initial mode distribution). The temperatures associated to the even and odd modes were fitted to the model and found to be respectively $T_{\text{eff}} + \Delta T$ and $T_{\text{eff}} - \Delta T$ with $k_{\text{B}} T_{\text{eff}} = (0.64 \pm 0.01) \times n_0 g/2$ and $\Delta T = (0.48 \pm 0.01) \times T_{\text{eff}}$.

The modification to the splitting protocol to reveal the excess of correlations on the antidiagonal of $C(z_1, z_2)$ was empiric (see Section 2 of the Supplementary Materials of Ref. [46]). In practise, the control parameter for the deformation of the trap and the properties of the final double-well potential is given by the amplitude of the radiofrequency currents which we injected in the side wires on the atomchip (see Fig. 2.1). Controlling this amplitude thus enables the realization of different splitting protocols. For the data presented in (A), we linearly increase the RF current to 8 mA over a time of 30 ms, which is followed by a faster increase to 25 mA in 12 ms. For the data presented in (B) of the main text, the RF current is increased linearly to the final 25 mA within a single 17 ms long ramp. A simple model of the double-well trap taking into account our trap geometry shows that, for both RF ramps, the decoupling of the two gases happens approximately 3 ms before the end of the RF ramp and within a period of less than 0.5 ms. After the splitting, the tunnel coupling between the two gases is negligible. In our interpretation, this modification to the splitting process changes the excitations of the common degrees of freedom before the two gases decouple from each other, with a residual impact on the relative degrees of freedom. This is only a naive conjecture since we did not dispose of a quantitative description of the splitting process for the many-body system (the complexity of theoretically describing the splitting process from the theoretical point of view is analyzed in section 4.5 of the Supplementary Materials of [46]). Empirically, we could nevertheless demonstrate control

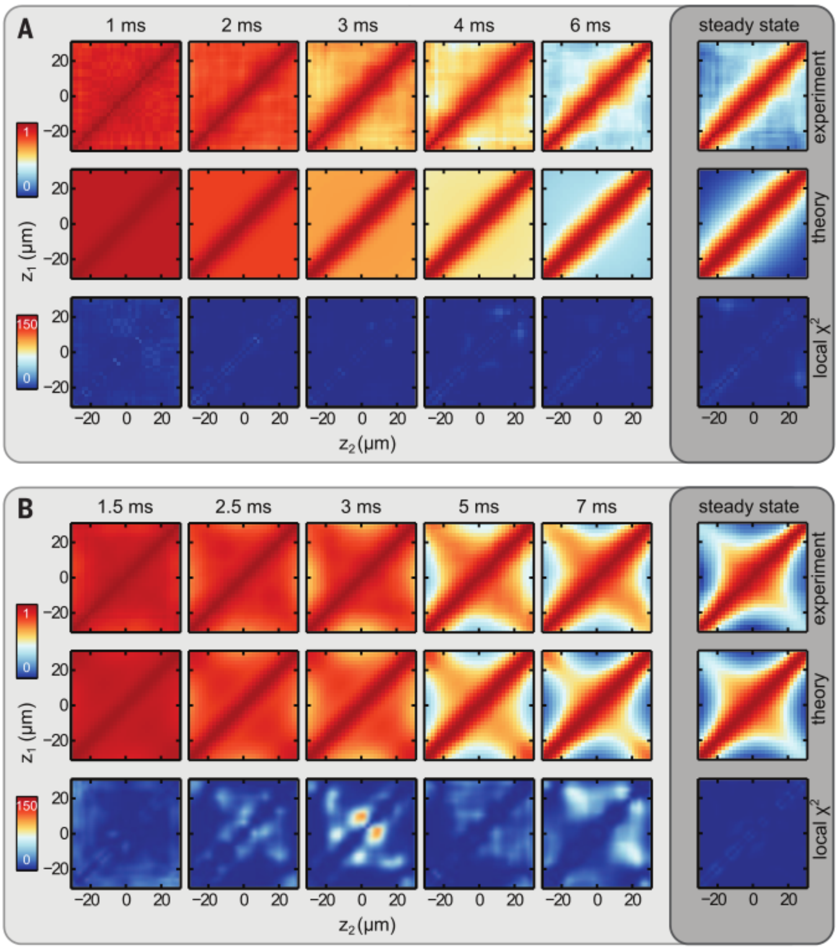

Figure 2.4: **Two-point phase correlation functions $C(z_1, z_2)$ for increasing evolution time.** (from [46]). Different initial states were prepared using two different splitting protocols. Both states show a characteristic maximum on the diagonal and a decay of correlations away from the diagonal. We used a χ^2 analysis to quantify the agreement of our theoretical model and the experiments. The steady state and the dynamics in (A) can be well described by a single temperature T_{eff}. The single-temperature model fails for the steady state and the dynamics in (B), which require more temperatures to explain additional correlations on the antidiagonal. The observation of different temperatures in the steady state constitutes our observation of a Generalized Gibbs Ensemble.

over the splitting process by varying the point in time where the change of slope of the current ramps occurs, in order to gradually modify the relative excitation of the even and odd modes. The detailed data are given in Fig. 6.3 of the PhD thesis of Tim Langen [47].

Implication. Our experiment revealed the key role of conserved quantities on the unitary evolution of a quantum many-body system, which puts constraints on the available phase space. Instead of relaxing to the usual (canonical) thermodynamical ensemble $\hat{\rho}_{\text{can}} = \frac{1}{Z}\exp(-\beta\hat{H})$ (with $\beta = 1/k_{\text{B}}T$), the density matrix of the relaxed system is described by a Generalized Gibbs Ensemble (GGE)

$$\hat{\rho} = \frac{1}{Z}\exp\left(-\sum_k \lambda_k \hat{I}_k\right) \tag{2.10}$$

where Z is the partition function, $\hat{I}_k = \hat{b}_k^\dagger \hat{b}_k$ are the (conserved) quasi-particle occupation numbers and λ_k are the Lagrange multipliers adjusted to yield the time invariant expectation values $\langle \hat{I}_k \rangle$. For bosonic excitations (phonons here), it can be shown that $\lambda_k = \ln(1 + I_k^{-1})$. Writting the multipliers in terms of the mode energies as $\lambda_k = \beta_k \hbar\omega_k$, the GGE defines different effective temperatures for every mode, $\beta_k = (k_B T_k)^{-1}$. The GGE reduces to a Gibbs ensemble if the λ_k are proportional to the energies as $\lambda_k = \beta_{\text{eff}} \hbar\omega_k$ with a single k-independent proportionality coefficient. In that case, we recover the prethermalized state of Fig. 2.4(A) associated with the initial condition of Eq. (2.7) for the mode occupation numbers, i.e. with a single coefficient β_{eff}. In the case of the (B) splitting, two distinct inverse temperatures $\beta^{\text{even}} = k_B(T_{\text{eff}} + \Delta T)^{-1}$ and $\beta^{\text{odd}} = k_B(T_{\text{eff}} - \Delta T)^{-1}$ are needed to describe the state of the system.

Deviations of steady states from the GGE description could be expected to manifest in higher-order correlation functions. To provide further evidence for our theoretical description and the presence of a GGE, we studied higher order correlation functions of the steady state, up to tenth order. Like the 2-point functions, the high order correlation functions were in good agreement with the theoretical model and clearly revealed the difference between the GGE and the usual Gibbs ensemble (see Fig. 4 of Ref. [46] for details).

Our experiment thus showed how the unitary evolution of a quantum many-body system connects to a steady state that can be described by a (generalized) classical statistical ensemble, a phenomenon which had only been observed in numerical simulations before our work.

2.4 Conclusion and perspectives

I focused in this chapter on two results associated to my work with the so-called "KRb" team of the atomchip group in Vienna. During my stay, we investigated several other aspects of our split quasi-condensate. In particular, I investigated the problem of observing revivals of coherence associated with the rephasing of the phononic modes, and I obtained solid preliminary data before leaving the team. I showed in Ref. [41], however, that a system with periodic boundary conditions would be more favorable for observing unambiguously the revivals, instead of a longitudinally trapped gas. The team, lead by Bernhard Rauer that I closely supervised during my stay in Vienna, later implemented a box-like potential with a blue detuned dipole trap and could clearly reveal the many-body revivals [48].

Moreover, I investigated the dynamics of two quasi-condensates in the presence of residual tunnel coupling J between the two halves. Such a system is interesting as the coupling introduces a non-linear term $J\cos(\hat{\phi}(z))$ in the Hamiltonian of Eq. (2.1) that maps the problem to the so-called Sine-Gordon Hamiltonian, which is relevant for diverse disciplines ranging from particle physics to condensed matter. I participated to the first experiments to characterize the tunnel coupling at thermal equilibrium and to study the effect of residual tunnel coupling after the splitting. Later, the team used the high-order correlation functions to characterize the many body state in thermal equilibrium with a PhD student (Thomas Schweigler) that I recruited in the team in January 2013 [49].

Finally, Bernhard Rauer and myself worked in close collaboration with the theoretician of the team, Igor Mazets, in order to understand the process of cooling of a Bose gas when entering more and more the 1D regime, where evaporative cooling is rendered ineffective by the absence of thermalizing collisions. We showed that the observed cooling could be modeled as a continuous density reduction extracting energy from the density quadrature of the free phononic excitations, which, together with the continuous dephasing described in this chapter, reduces the occupation number of each phonon mode and leads to a colder system. The study was published in 2016 in Ref. [50].

2.4.1 Students supervised during my postdoctoral stay in Vienna

- Maximilian Kuhnert, PhD student, from Nov. 2011 to Nov. 2012

- Tim Langen, PhD student, from Nov. 2011 to August. 2013
- Bernhard Rauer, Master student and then PhD student, from Nov. 2011 to August. 2013
- Thomas Schweigler, PhD student, from Jan. 2013 to August. 2013
- Antoine Ribuot, bachelor student from Institut d'Optique (Palaiseau, France), July-August 2012.

2.4.2 Publications linked with my postdoctoral experience in Vienna

1. *Prethermalization revealed by the relaxation dynamics of full distribution functions*
   David Adu Smith, Michael Gring, Tim Langen, Maximilian Kuhnert, Bernhard Rauer, Remi Geiger, Takuya Kitagawa, Igor Mazets, Eugene Demler, Jörg Schmiedmayer
   New Journal of Physics 15, 075011 (2013), Ref. [36]

2. *Multimode dynamics and emergence of a characteristic length-scale in a one-dimensional quantum system*
   Maximilian Kuhnert, Remi Geiger, Tim Langen, Michael Gring, Bernhard Rauer, Takuya Kitagawa, Eugene Demler, David Adu Smith, Jörg Schmiedmayer
   Phys. Rev. Lett.110, 090405 (2013), Ref. [40]

3. *Local emergence of thermal correlations in an isolated quantum many-body system*
   Tim Langen, Remi Geiger, Maximilian Kuhnert, Bernhard Rauer, Jörg Schmiedmayer
   Nature Physics 9, 640-643 (2013), Ref. [42]

4. *Prethermalization in one-dimensional Bose gases: description by a stochastic Ornstein-Uhlenbeck process*
   Tim Langen, Michael Gring, Maximilian Kuhnert, Bernhard Rauer, Remi Geiger, David Adu Smith, Igor E. Mazets, Jörg Schmiedmayer
   Eur. Phys. Jour. Special Topics 217, 43 (2013), Ref. [51]

5. *Local relaxation and light-cone-like propagation of correlations in a trapped one-dimensional bose gas*
   R. Geiger, T. Langen, I. Mazets, and J. Schmiedamyer
   New. Jour. of Physics 16, 053034 (2014), Ref. [41]

6. *Experimental Observation of a Generalized Gibbs Ensemble*
   Tim Langen, Sebastian Erne, Remi Geiger, Bernhard Rauer, Thomas Schweigler, Maximilian Kuhnert, Wolfgang Rohringer, Igor E. Mazets,Thomas Gasenzer, Jörg Schmiedmayer
   Science 348, 207 (2015), Ref. [46]

7. *Ultracold atoms out of equilibrium*
   T. Langen, R. Geiger and J. Schmiedamyer
   Annual Review of Condensed Matter Physics, Vol. 6 (2015), Ref. [27]

8. *Cooling of a One Dimensional Bose Gas*
   Bernhard Rauer, Pjotrs Grišins, Igor E. Mazets, Thomas Schweigler, Wolfgang Rohringer, Remi Geiger, Tim Langen, Jörg Schmiedmayer
   Phys. Rev. Lett. 116, 030402 (2016), Ref. [50]

Funding. My postdoc contract was funded by the Austrian Science Fund (FWF) under a Lise-Meitner grant for which I applied. The project was entitled *Dynamics of One-Dimensional Gases of Bosons and Fermions*, contract number M 1423-N27.

Teaching. During my stay in Vienna, I had the opportunity to give two lectures at the Master/doctoral level:

- Introductory Course on Ultra-cold Quantum Gases, Innsbruck, 9-12 July 2012: one lecture on atom interferometry and one lecture on atom chips;

- Course Atoms, Light, Matter waves, Atominstitut, TU Wien (Winter Semester 2012): one lecture on Laser Cooling and Trapping.

Chapter 3

Cold-atom gyroscope-accelerometer

In this chapter, I will present my research on the experimental development of a high-sensitivity cold-atom inertial sensor. This experiment was designed by Arnaud Landragin in 2008 and became operational as an inertial sensor with reduced sensitivity in 2013, shortly before my arrival at SYRTE. Since then, I have gradually taken the lead of the project and conducted the team to reach the design performances, and to demonstrate new generic atom interferometry techniques of interest to the community.

3.1 Principle of experiment and methods

3.1.1 Experimental setup

The basic technique at the heart of cold-atom inertial sensors is light-pulse atom interferometry [52], [53], in which two counter-propagating laser beams of angular frequencies ω_1 and ω_2 drive Raman transitions between the two hyperfine states of an alkaline atom. Cesium atoms are used in the case of the gyroscope-accelerometer setup, and the Raman lasers couple the clock states $|F=3, m_F=0\rangle$ and $|F=4, m_F=0\rangle$. During this two-photon process, the momentum of the light $\hbar\vec{k}_{\text{eff}} \equiv \hbar(\vec{k}_1 - \vec{k}_2)$ is transferred to the atom, resulting in a physical separation of the two states. The two photon recoil velocity is equal to $\hbar k_{\text{eff}}/M \simeq 7.0$ mm.s^{-1}, with M the mass of the Cesium atom.

Laser cooling. The Cesium atoms loaded from a 2D Magneto-Optical Trap (MOT) are trapped and laser-cooled in a 3D-MOT. We launch the atoms vertically at a variable velocity (up to 5.0 m.s^{-1}) using moving molasses with a (3D) cloud temperature of 1.2 μK. After the MOT and prior to the interrogation, the atoms are prepared in the $|F=4, m_F=0\rangle$ state using a selection scheme based on the Stern-Gerlach effect (magnetic deflection of the atoms in $m_F \neq 0$ states).

Raman beams. Light pulse interferometry is realized using two phase-locked Raman lasers which couple the Cesium clock states (hyperfine splitting of 9.192 GHz). The Raman lasers have a wavelength close to the D_2 line (wavelength $\lambda \simeq 852$ nm) and are detuned by 470 MHz from the excited state to reduce incoherent scattering. The Raman lasers are sent to the atoms through two optical windows separated by a variable distance, as shown in Fig. 3.1. In most of the experiments reported here, we used the maximum separation of 59 cm, which corresponds to a total interrogation time of 800 ms of the atoms in the interferometer. The Raman laser beams are gaussian with $1/e^2$ diameter equal to 40 mm and have a power of about 150 mW.

We use retro-reflected Raman beams, which forms two pairs of Raman beams that can induce two transitions: one in the $+\vec{k}_{\text{eff}}$ direction, and another in the $-\vec{k}_{\text{eff}}$ direction. Selectivity of the $\pm\vec{k}_{\mathrm{eff}}$ transitions is provided by tilting the Raman beams by an angle $\theta \simeq 3.80$ degrees with respect to the horizontal, in order to introduce a Doppler shift ($\pm k_{\mathrm{eff}} g T \sin\theta / 2\pi \simeq \pm 611$ kHz at the first and last $\pi/2$ pulses for $T = 400$ ms) which is much larger than the width of the Doppler distribution of the atom cloud (~ 40 kHz). To follow the resonance condition at each Raman pulse, we change the relative frequency between the two Raman lasers during the sequence with a Direct Digital Synthesizer (DDS).

Detection system. The interferometer output signal is determined by the probability of transition between the $F = 4$ and $F = 3$ states, which is read out via fluorescence detection of the two levels' populations after the atom interferometer light-pulse sequence. Specifically, the atoms pass on their way down through a set of three light sheets: the first light sheet of rectangular shape of 30 mm × 10 mm contains light tuned on the cycling transition $F = 4 \rightarrow F' = 5$ in order to detect the atoms in the $F = 4$ hyperfine state, N_4. The central light sheet of 30 mm × 2 mm contains repumping light to transfer the atoms from $F = 3$ to $F = 4$. The third light sheet (same size and the same frequency as the first one) detects all the atoms, N_{tot}. The light from the first and third light sheets is collected by an optical system with a collection efficiency of 2%. From these two observables, we determine the probability of transition, $P = N_4/N_{\mathrm{tot}}$. The detection system was improved during the PhD thesis of Denis Savoie [54] in order to reduce the crosstalks between the N_4 and N_{tot} channels and the level of scattered light. For 3×10^5 detected atoms (a typical number after a loading of the MOT during 55 ms), the signal to noise ratio of the detection is 300, about equally limited by the optical shot noise of the scattered light and the electronic (e.g. photodiode) noise.

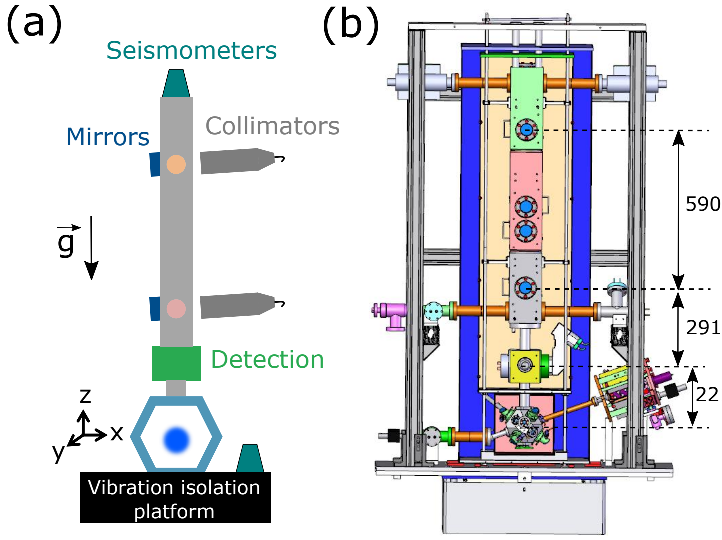

Figure 3.1: (a) Skematic view of the gyroscope-accelerometer experimental setup. The atoms are laser cooled (blue cloud) and launched vertically, interrogated by two Raman beams (brought from the gray collimators and retro-reflected on the blue mirrors), and detected on their way down (green box). The distance between the Raman beams is $\frac{3}{8} g T^2 \simeq 59$ cm for the maximally achievable interrogation time $2T = 0.8$ s. Seismometers are used to record the vibrations of the setup. (b) Mechanical drawing (dimensions in mm).

3.1.2 Sensitivity to inertial effects

The probability of transition is modulated according to $P = P_0 + A \sin\Phi$, where A is the visibility amplitude and Φ the interferometer phase. The interferometer can be operated in various configurations of light pulses in order to primarily sense either DC horizontal linear accelerations (in the direction of the Raman beams), or DC rotations of vector orthogonal to the plane of the interferometer area (along $\vec{e}_y$). I will focus below on the pure gyroscope configuration, for which we have performed most of the experiments, where a configuration of 4 light pulses is used to cancel the contribution of the DC acceleration to the interferometer phase. This interferometer configuration is sketched in the diagrams of Fig. 3.2.

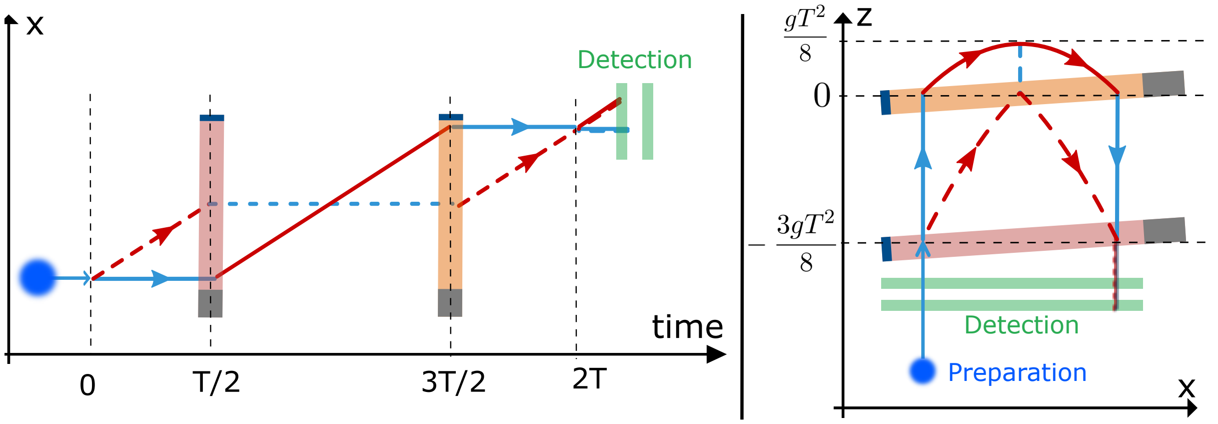

Figure 3.2: Left: Space-time diagram of the 4 pulse interferometer in the (t, x) plane. Right: Diagram of the interferometer in the (x, z) plane.

Sagnac effect

The Sagnac effect is the appearance of a phase shift in an interferometer where the two paths enclose a physical area $\vec{\mathcal{A}}$, while the entire setup rotates with a rate $\vec{\Omega}$. It is a special relativistic effect associated with the impossibility of a global synchronization of corotating observers. The effect is independent of the nature of the signal and in particular of its velocity of propagation. A detailed explanation of this effect and of the related historical developments can be found, for example, in the book of E. Gourgoulhon [55]. In the case of atom interferometers with a geometry analog to that of a Mach-Zehnder optical interferometer, the two waves are recombined after half a turn (instead of a full turn in typical optical interferometer experiments), and the Sagnac phase shift can be expressed as

$$\Delta\phi = \frac{2E}{\hbar c^2}\vec{\Omega}\cdot\vec{\mathcal{A}}, \tag{3.1}$$

where $E = Mc^2 \times [1-(v/c)^2]^{-1/2}$ is the total energy of the particle.

In the case of the symmetric 4 pulse interferometer sketched in Fig. 3.2, the Sagnac area $\vec{\mathcal{A}} = \mathcal{A}\vec{e}_y$ can be calculated as

$$\mathcal{A} = 2 \times \left(\left| \int_0^{T/2} z(t)\frac{\mathrm{d}x}{\mathrm{d}t}\mathrm{d}t \right| + \left| \int_{T/2}^{T} z(t)\frac{\mathrm{d}x}{\mathrm{d}t}\mathrm{d}t \right| \right) \tag{3.2}$$

where $(x(t), z(t))$ denotes the classical trajectory of the wave packets enclosing the area:

$$x(t) = \frac{\hbar k_{\text{eff}}}{M}(t-T) \quad , \quad z(t) = -\frac{3g}{8}T^2 + g\left(Tt - \frac{t^2}{2}\right). \tag{3.3}$$

The result reads

$$\mathcal{A} = 2 \times \frac{\hbar k_{\text{eff}}}{M} \times \left(\frac{1}{12}gT^3 + \frac{1}{24}gT^3\right) = \frac{1}{4}\frac{\hbar k_{\text{eff}}}{M}gT^3, \tag{3.4}$$

yielding the Sagnac phase shift (for $E \simeq Mc^2$)

$$\Delta\phi = \frac{1}{2}k_{\text{eff}}gT^3\vec{\Omega}\cdot\vec{e}_y. \tag{3.5}$$

For the interrogation time $2T = 800$ ms, the Sagnac area equals 11 cm^2 and the phase shift caused by the Earth rotation rate at the latitude of Paris ($\Omega = 52\ \mu\text{rad.s}^{-1}$) equals 239 rad.

Response of the interferometer to arbitrary rotations rates

I will calculate below the response of the 4 light pulse interferometer to time-dependent accelerations and rotations, extending the calculation presented in Ref. [56].

As an alternative to the Sagnac effect calculation, the interferometer phase shift can be calculated following the path integral approach [57]. As the Lagrangian of the problem is quadratic in position and momentum of the particle, the free propagation phase (corresponding to the difference of classical action along the paths) vanishes, such that remains only the contribution from the interaction of the atom with the laser field. The atom interferometer phase is thus given by

$$\Phi = \varphi(0) - 2\varphi\left(\frac{T}{2}\right) + 2\varphi\left(\frac{3T}{2}\right) - \varphi\left(2T\right) \tag{3.6}$$

where $\varphi(t) = \vec{k}_{\text{eff}} \cdot \vec{r}_{\text{cl}}(t)$ is the relative phase between the two counter-propagating Raman lasers (keeping here only the motional part) and $\vec{r}_{\text{cl}}(t)$ is the classical trajectory of the center of mass of the wavepacket.

In the case where the Raman lasers are rotating at a rate $\Omega(t)\vec{e}_y$ with respect to the direction of local gravity $\vec{g}$ (pointing towards the center of the Earth, in first approximation), the trajectory of the free falling wavepacket can be expressed in the rotating frame of the lasers as

$$\begin{aligned} X(t) &= x_{\text{cl}}(t)\cos\theta(t) + z_{\text{cl}}(t)\sin\theta(t) \\ Z(t) &= z_{\text{cl}}(t)\cos\theta(t) - x_{\text{cl}}(t)\sin\theta(t) \end{aligned}$$

with $\Omega(t) = \dot{\theta}(t)$. The relative Raman laser phase becomes $\varphi(t) = k_{\text{eff}}X(t)$ and reads

$$\varphi(t) = k_{\text{eff}}\left[\frac{\hbar k_{\text{eff}}}{2M}(t-T)\cos\theta(t) + g\left(Tt - \frac{t^2}{2} - \frac{3}{8}T^2\right)\sin\theta(t)\right]. \tag{3.7}$$

If we consider a rotation $\theta(t) = \theta_0\sin(\omega t)$ of small amplitude ($\theta_0 \ll 1$), then only the second term of Eq. (3.7) contributes to the interferometer phase shift and evaluating Eq. (3.6) yields, at first order in θ_0:

$$\Phi_\Omega = \frac{3\theta_0}{8}T^2 k_{\text{eff}} g \sin\left(2T\omega\right) \simeq \frac{3}{4}k_{\text{eff}} g T^3 \Omega_0. \tag{3.8}$$

The last approximation is performed for slow rotations $\omega T \ll 1$ and re-introducing $\Omega_0 = \omega\theta_0$. In the approximation of small rotations ($\theta_0 \ll 1$), this pure rotation phase shift can be interpreted as an integrated variation of the projection of the vertical component of the trajectory $z_{\text{cl}}(t)$ along the Raman beam direction. This expression Eq. (3.8) differs from that resulting from the evaluation of the Sagnac area (Eq. (3.5)). The reason is that we have only considered so far the pure rotation term and have neglected the variation of horizontal acceleration induced by the rotation of the Raman lasers under the presence of gravity. We evaluate this acceleration contribution using Eq. (3.6) with $\ddot{\varphi}(t) = k_{\text{eff}} g \sin\theta(t) \simeq k_{\text{eff}} g\theta(t)$. For slow rotations ($\omega T \ll 1$), the result is

$$\Phi_{\text{acc}} \simeq -\frac{1}{4}k_{\text{eff}} g T^3 \Omega_0, \tag{3.9}$$

resulting in a total phase shift

$$\Phi = \Phi_\Omega + \Phi_{\text{acc}} = \frac{1}{2}k_{\text{eff}} g T^3 \Omega_0, \tag{3.10}$$

in agreement with the Sagnac effect. The result of this calculation is also in agreement with that presented in Ref. [58] (section 4.3)[1].

Frequency-dependent scale factor. In the following sections, I will present the experimental work aimed at increasing the sampling rate of cold-atom inertial sensors in order to sample effects that are not necessarily slow compared to the interrogation time $2T$. In this context, I present here a calculation of the response of the interferometer to rotations of arbitrary frequency (still small, $\theta_0 \ll 1$) and take into account the sampling of the sensor. To this end, I consider that the measurements are performed sequentially at timings $t_m = mT_c$, where T_c is the cycle time and m an integer. Using Eq. (3.7), the result for the total phase shift $\Phi_\Omega + \Phi_{\text{acc}}$ reads:

$$\Phi(t_m) = \frac{4\theta_0 k_{\text{eff}} g}{\omega^2} \cos\left(\omega\left(T + t_m\right)\right) \sin\left(\frac{\omega T}{2}\right) \left[\cos\left(\frac{\omega T}{2}\right)\left(\frac{3}{8}T^2\omega^2 + 1\right) - 1\right]. \tag{3.11}$$

The response of the interferometer to rotation rates $\Omega(t) = \Omega_0 \cos(\omega t)$ (with $\Omega_0 = \omega\theta_0$) can be highlighted by rewriting this expression as

$$\Phi(t_m) = \mathcal{S}_\Omega(\omega)\Omega_0 \cos(\omega t_m + \omega T) \tag{3.12}$$

where $\mathcal{S}_\Omega(\omega)$ represents the frequency-dependent scaling factor of the gyroscope given by

$$\mathcal{S}_\Omega(\omega) = \frac{4k_{\text{eff}} g}{\omega^3} \sin\left(\frac{\omega T}{2}\right) \left[\cos\left(\frac{\omega T}{2}\right)\left(\frac{3}{8}T^2\omega^2 + 1\right) - 1\right]. \tag{3.13}$$

The scale factor to rotations is represented in Fig. 3.3. The sensor behaves approximately as a first order filter with a cutoff frequency around $1/2T$.

Impact of linear accelerations. The formalism of the sensitivity function [59] ca be used to assess the impact of acceleration noise on the rotation measurement. Specifically, we can estimate the contribution of each frequency band $[f_1 - f_2]$ to the variance of the interferometer phase noise as

$$\sigma_\Phi^2(f_1, f_2) = \int_{f_1}^{f_2} |H_a(2\pi f)|^2 S_a(2\pi f) df, \tag{3.14}$$

with $S_a(2\pi f)$ the power spectral density of acceleration noise and

$$|H_a(2\pi f)| = \frac{8k_{\text{eff}}}{\omega^2} \sin\left(\frac{\omega T}{2}\right) \sin^2\left(\frac{\omega T}{4}\right) \tag{3.15}$$

the transfer function of the 4 pulse interferometer to accelerations. This transfer function acts as a band-pass filter with a peak sensitivity centered close to $1/2T$ (Fig. 3.4).

Fig. 3.4 shows a typical spectrum of the linear acceleration noise recorded on the experiment standing on a passive isolation platform, $\sqrt{S_a(2\pi f)}$. This type of spectrum is obtained from the half-sum of the signals of the two seismometers represented in Fig. 3.1. The result of the numerical integration in Eq. (3.14) is given in Table 3.1. The main contribution to the interferometer phase noise is the frequency band centered around 0.5 Hz. The total rms phase noise is $\sigma_\Phi = 3.2$ rad and is about two orders of magnitude higher than the detection noise or the phase noise from the Raman lasers.

The domination of vibration noise over the other noise sources (in particular the quantum projection noise) is generic to cold-atom sensors featuring a large scale factor, as given in our case

---

[1] Note that when the calculation is performed by writing the equations of motion of the atom subject to gravity in the rotating (Earth) reference frame, the result obtained using Eq. (3.6) is directly $\frac{1}{2}k_{\text{eff}} g T^3 \Omega_{\text{Earth}}$, without the need to distinguish between the pure rotation and the pure acceleration effects. Such a calculation is therefore more rigorous but might limit interpretations. As written in Ref. [58] below Eq. (4.34), it is important to remember that the scale factor of the instrument to Earth rotation is $\frac{1}{2}k_{\text{eff}} g T^3$, while it is $\frac{3}{4}k_{\text{eff}} g T^3$ for platform rotations which are independent of Earth rotation, i.e. when the platform rotates with respect to $\vec{g}$.

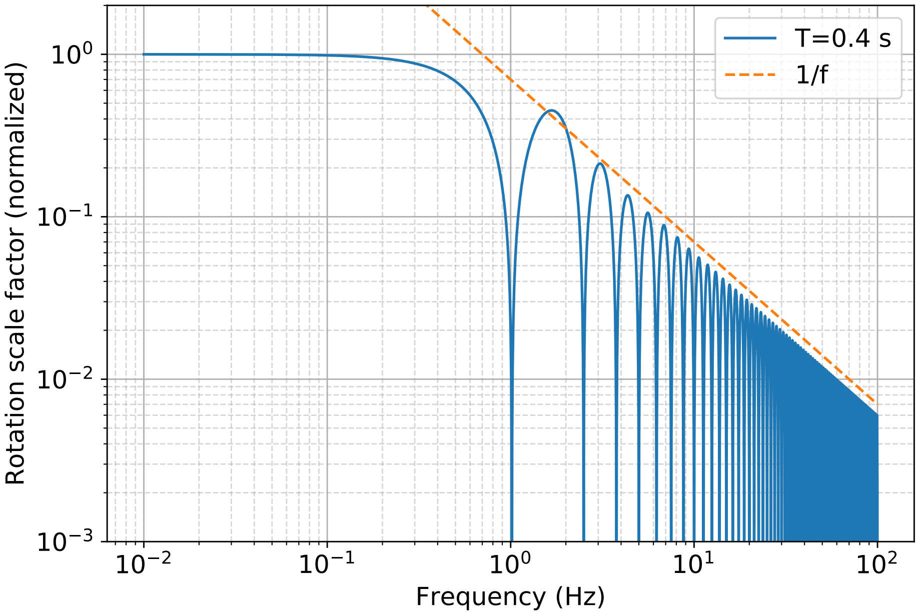

Figure 3.3: Dynamical scale factor of the gyroscope, $|\mathcal{S}_\Omega(\omega)|$, normalized to its value at zero frequency, $\mathcal{S}_\Omega(0) = k_{\text{eff}} g T^3/2$. The total interrogation time is $2T = 0.4$ s.

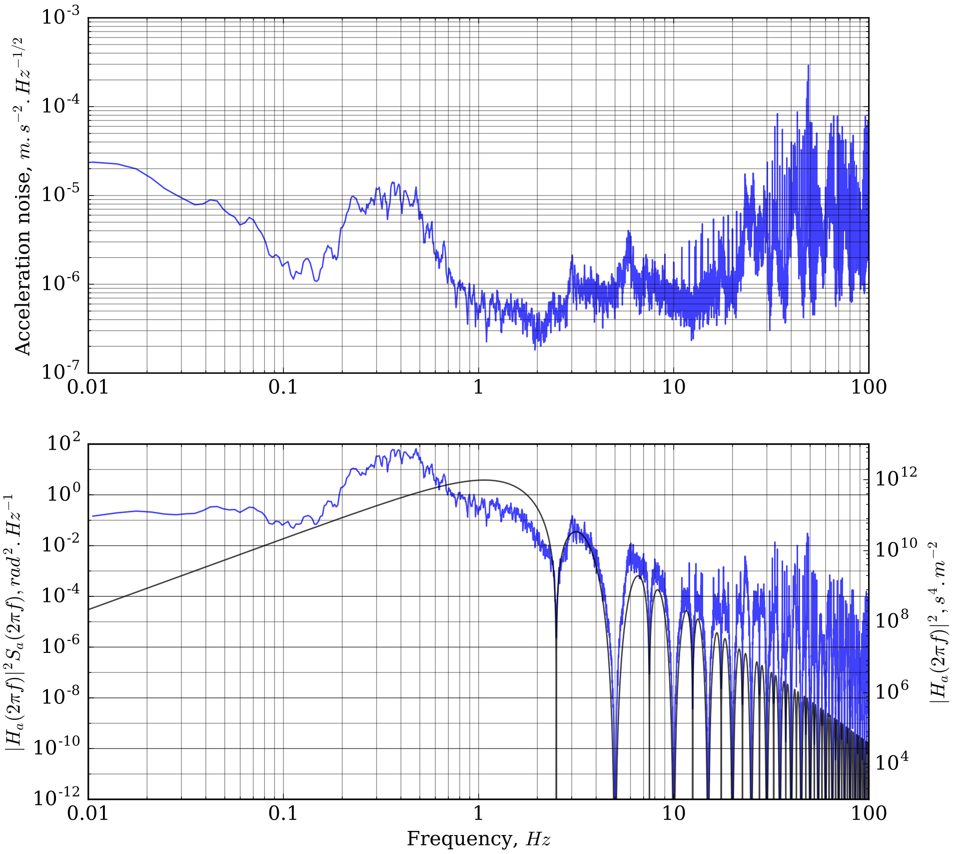

Figure 3.4: **Analysis of vibration noise.** Top: Amplitude spectral density of linear acceleration noise. Bottom: contribution to interferometer phase noise as from Eq. (3.14). The black line shows the acceleration transfer function of the interferometer, $|H_a(2\pi f)|^2$.

frequency band (Hz)	0.01-0.1	0.1-0.3	0.3-0.4	0.4-0.5	0.5-1	1-10	10-100	total
σ_Φ^2 (rad^2)	0.02	0.93	3.7	3.9	1.4	0.26	0.005	10.4

Table 3.1: Contribution of the linear acceleration noise to the interferometer phase noise by frequency band for an interrogation time $2T = 800$ ms. The total rms phase noise is $\sigma_\Phi = 3.2$ rad.

by the total interrogation time $2T = 0.8$ s. While differential sensors as used in gradiometers, tests of the universality of free fall or measurements of the recoil velocity can reject a large part of the inertial noise, instruments measuring inertial effects such as gravimeters, accelerometers or gyroscopes are largely concerned by this problem. Vibration noise represents a fundamental limitation since it arises from the equivalence principle, but his impact on a given sensor is technically determined by the ability of the interferometer to sample the inertial fluctuations at a high enough rate. The role of vibration noise aliasing is analogous to the Dick effect in atomic clocks, i.e. the limitation to the clock sensitivity owing to the sampling of the local (microwave or optical) oscillator noise and the dead times in the measurement. **Improving on the limitation associated with vibration noise was of major importance and has driven the efforts of our team in the last five years. The next section will present the main results obtained in that context.**

3.2 Main results

3.2.1 Continuous cold-atom inertial sensor

Most cold-atom interferometers such as clocks or inertial sensors are sequentially operated in a sequence of total duration T_c, and typically consisting of 3 main steps: *(i)* atom trapping, cooling, and preparation; *(ii)* interferometry sequence with microwave or light pulses (Ramsey-like interrogation); *(iii)* atomic state detection. While the signal of interest is probed during step *(ii)*, steps *(i)* and *(iii)* correspond to dead times and loss of information on the probed signal. Our goal is tom remove these dead times.

Step 1: Implementation in an atomic fountain.
As a first step towards continuous operation of an atom interferometer (i.e. operation without dead times), we proposed and demonstrated in 2014 a new method of interrogation of cold atom clouds in our atomic fountain [60]. The experiment was first performed in a clock-like geometry with two $\pi/2$ Raman pulses (using the bottom window shown in Fig. 3.1). Our so-called joint interrogation method was inspired from atom juggling methods originally introduced in the context of cold atom collisions in atomic fountain clocks [61] and only realized previously for concurrent measurements [62]–[64]. With an innovative and simple control sequence, we demonstrated the joint interrogation of up to 5 cold atom clouds simultaneously, resulting in a long Ramsey interrogation time (800 ms), high sampling rate (up to 5 Hz) and leading to a faster reduction of the Dick effect.

The principle of the joint operation is simple (see Fig. 3.5(a)): it consists in preparing a cloud of cold atoms (indexed i) while a previously launched cloud (indexed $i-1$) is being interrogated in the interferometer region. The cloud i is launched before the cloud $i-1$ is detected, such that the cloud entering the interferometer (i) and that exiting the interferometer ($i-1$) share a common $\pi/2$ pulse. In such a joint mode, the interrogation time equals the cycle time.

Selection of the atoms prior to the interferometer. One critical aspect of the *mise en pratique* of the joint operation is the preparation of the quantum state of the atoms before they enter the interferometer. Specifically, atom interferometers are almost exclusively operated with atoms in the $m_F = 0$ Zeeman sublevel in order to minimize the sensitivity to external magnetic fields. This is typically performed by a selection step involving a microwave radiation followed by a blow-away resonant laser beam. The microwave radiation used during the selection for cloud i shall not be resonant with a transition in the atom interrogated in the interferometer $(i-1)$. In Ref. [60], the selection was performed on the $|F=4, m_F=+1\rangle \rightarrow |F=3, m_F=0\rangle$ transition which was separated from the clock transition using a bias field of 18 mG. However the ensuing blow-away beam induced scattered light on the cloud $i-1$, causing light shifts and a reduction of the interferometer contrast. In the subsequent works, we improved the selection method: we adopted a selection based on the Stern-Gerlach effect, by applying a pulsed gradient of magnetic fields to the atoms right after their launch, in order to send the $m_F \neq 0$ atoms towards the walls of the vacuum chamber. While no radiation is emitted, this method has the drawbacks to introduce vibrations on the experimental setup (Laplace force acting on the coils) and thermal dissipation (20 Amperes are pulsed for 10 ms in the coils).

Efficient averaging of the local oscillator noise. In Ref. [60], we showed how such a zero-dead time operation yields an efficient averaging of the local oscillator noise (Fig. 3.5(b)), and analyzed the corresponding limitations in details. I just recall here the most important aspect of such efficient averaging, also demonstrated in [65]: in a Ramsey sequence, the phase of the 2-pulse atom interferometer is determined by the Raman laser phase difference imprinted on the atomic wave-function at the light pulses; at time t_i it reads $\Delta\Phi_i = \phi(T+t_i) - \phi(t_i)$, where $\phi(t)$ is the Raman laser relative phase. In the case of a white relative phase noise and after N cycles, the variance $\langle \Delta\Phi_N^2 \rangle$ of the accumulated atomic phase is inversely proportional to N. In the time domain, this means that the phase Allan deviation scales as $1/\sqrt{\tau}$ (τ is the integration time), which is the well-known result for successive uncorrelated measurements. With the cycle time T_c equal to the Ramsey time T, the second laser pulse $\phi(T+t_i)$ of cloud i is the same as the first pulse $\phi(t_{i+1})$ of cloud $i+1$: $\phi(T+t_i) = \phi(t_{i+1})$. As a result, the consecutive phase terms in the accumulated atomic phase cancel each other, so that the variance of the accumulated phase $\langle \Delta\Phi_N^2 \rangle$ scales as $1/N^2$ (Allan deviation of phase $\sim 1/\tau$). In other words the joint operation rejects the aliasing of the local oscillator noise (here the Raman laser relative phase noise) encountered when performing independent measurements of the phase with dead times. The rejection applies as long as the local oscillator noise spectrum has a bandwidth lower than the pulse Rabi frequency Ω_R, which we quantitatively anayzed in Ref. [60].

Two final important aspects of the joint method are the loss of contrast and the light shifts induced by the light scattered from the atoms in the MOT and the detection region towards the atoms in the interferometer. From the normal mode operation (no joint) to the joint interrogation, the contrast of the interferometer was reduced by 35%.

Step 2: Joint interrogation in inertial sensor configuration.

Following this first study, we implemented the joint method in an inertially sensitive configuration, specifically the 4 light-pulse interferometer presented in section 3.1. The results are presented in a paper published in 2016, Ref. [66]. In that work, the selection of the $m_F = 0$ state was performed by the Stern-Gerlach selection and the total interrogation time in the fountain was $2T = 800$ ms. With such a large interrogation time, the influence of vibration noise is critical, as it corresponds to several radians of interferometer phase noise (see Table3.1 above). Therefore, a careful management of the vibration noise was mandatory for recovering interference fringes. To this aim, we followed the well-established technique from our group of correlating the signal of the atom interferometer with that of auxiliary vibration sensors [67]. At that time, we used two broadband accelerometers (model Titan from Nanometrics) covering the DC to few 100 Hz band.

Correlation between the atom interferometer and auxiliary inertial sensors. The principle of the correlation technique consists in estimating at each cycle the phase seen by the interferometer from the measurement of auxiliary instruments featuring a much larger bandwidth

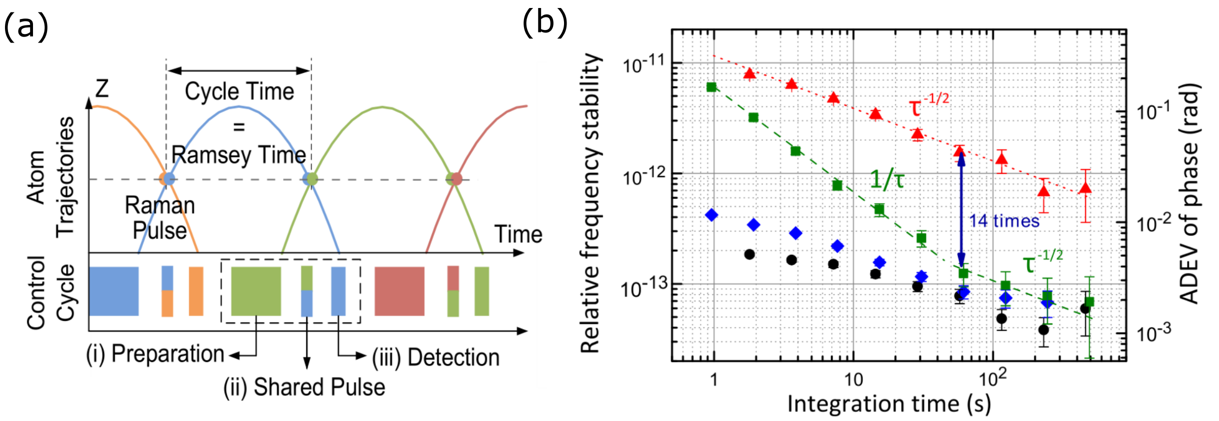

Figure 3.5: Adapted from [60]. (a) Illustration of the principle of the joint interrogation in an atomic fountain. (b) Allan deviations (ADEV) of the fountain relative frequency stability in normal and joint modes, for a Ramsey time $T = 480$ ms. Stability without adding noise for the normal (black circle) and joint (blue rhombus) operations. ADEV for the normal mode (red triangle) and the joint mode (green square) when adding white noise over a bandwidth of 400 Hz. The $1/\tau$ (dashed) and $\tau^{-1/2}$ (dotted) lines are guide to the eyes.

than the atom interferometer, i.e. capable of resolving small accelerations (in the range of 10^{-6} m.s^{-2}) of frequencies in the range $\sim [0.1/T, 10/T]$ where the interferometer is mostly sensitive. The atom interferometer phase is computed in real time at each cycle $t_m = mT_c$ (or in post-processing) by

$$\Phi_{\text{vib}}(t_m) = \int_{t_m}^{t_m+2T} g_a(t)a(t)dt = \int_{t_m}^{t_m+2T} g_v(t)v(t)dt, \tag{3.16}$$

where $g_a(t)$ and $g_v(t)$ are the interferometer sensitivity function to acceleration and velocity, respectively [59]. The sensitivity function is readily obtained from Eq. (3.6) giving the phase of the 4 light-pulse sequence, leading to

$$\Phi_{\text{vib}}(t_m) = k_{\text{eff}} \left(\int_{t_m}^{t_m+2T} v(t)dt - 2\int_{t_m+T/2}^{t_m+3T/2} v(t)dt \right), \tag{3.17}$$

where we expressed the output of the inertial sensor as a velocity signal $v(t)$.

Contrarily to previous experiments (e.g. cold-atom gravimeters) where a single retro-reflecting mirror defines the inertial reference whose vibrations must be recorded, two mirrors (distant by 59 cm) impact the measurement in our case. The vibration phase is thus given by Eq. (3.17) with the velocity in the first (second) integral corresponding to that of the bottom (top) mirror. However, due to the large magnetic fields generated by the accelerometers (several Gauss in contact), the experiment was not designed to accommodate the sensors just behind the mirrors. Instead, the sensors were placed on the structure of the gyroscope, at distances of about 50 to 70 cm from the mirrors located inside the two layer magnetic shield. This degrades the fidelity with which the accelerometers measure the vibrations of the two mirrors due to the imperfect rigidity of the frame of the experimental setup. After optimization, we found that the best correlations were obtained when using the half sum of the accelerometer signals to estimate Φ_{vib}. An example of correlation is shown in Fig. 3.6, where a signal-to-noise ratio of 5 is reached, corresponding to a 5-fold rejection of the vibration noise.

Parasitic interferometers. As mentioned in a 2011 paper from M. Kasevich' group [68], care has to be taken to parasitic interferometers which form because of the imperfect state transfer at the π pulses (see Fig. 3.7). These parasitic loops (dashed lines) have a different phase shift

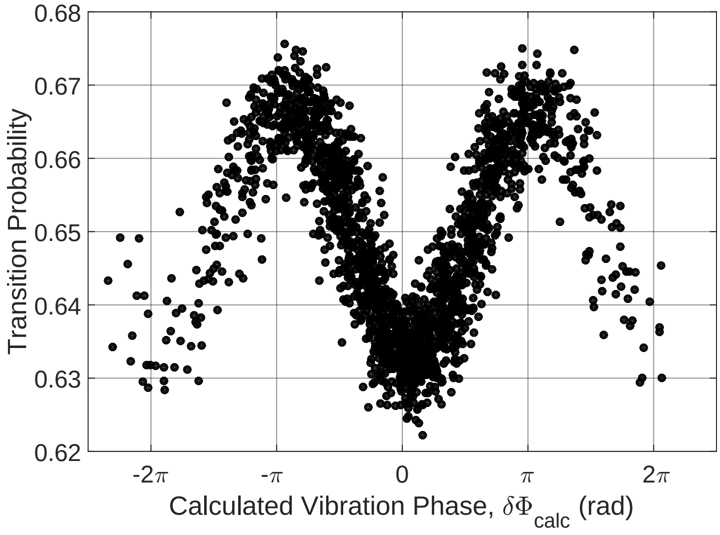

Figure 3.6: Correlation between the atom interferometer signal and the vibration phase calculated from the signal of auxiliary accelerometers. The interrogation time is $2T = 800$ ms. From [66].

than the central 4 pulse interferometer, which translates into probability noise owing to the randomness of the associated phase shift (originating from the vibration noise). This problem can be avoided by introducing a temporal asymmetry, ΔT, in the light pulse sequence, such that the parasitic paths do not recombine at the last $\pi/2$ pulse within the wavepacket coherence length. For our laser-cooled atom source with a temperature of 1.2 μK (coherence length of 30 nm), we observe in practise that a temporal assymetry $\Delta T = 40$ μs is required to restore the interferometer fringes. This assymetry introduces a large sensitivity to DC accelerations through $\Phi_{\mathrm{DC}} = 2k_{\mathrm{eff}}T\Delta T g \sin\theta \simeq 290$ rad, where $\theta = 3.80°$ is the angle between the Raman lasers and the direction of gravity. This shift is nevertheless well compensated by the chirp α applied to the Raman lasers frequency difference to follow the two-photon resonance condition throughout the light pulse sequence, resulting in a phase shift $\Phi_{\mathrm{DC}} = 2T\Delta T(k_{\mathrm{eff}}g\sin\theta - \alpha)$. Practically, we adjust α to compensate the DC acceleration at the level of 10 mrad. The DC acceleration phase shift can be further rejected by alternating sequences with opposite signs of the asymmetry ΔT.

Limitations of the experiment in Ref. [66].

1. The rotation rate sensitivity reported in Ref. [66] was 100 nrad.s^{-1}.Hz$^{-1/2}$, limited by the detection noise and the low contrast (4%) of the interferometer. The rotation rate stability averaged well as $\tau^{-1/2}$ during 10^4 s, to reach the level of 1 nrad.s^{-1}. The detection noise being white, correlations could not appear between successive measurements in joint mode, preventing from observing a scaling of the rotation rate stability faster than $\tau^{-1/2}$, as we observed in the case of the clock-like sequence. Later (during the PhD thesis of Denis Savoie) we reduced the level of scattered light in the detection and consequently the detection noise level by a factor of 4 [54]. Moreover, optimization of the Raman laser power increased our contrast by a factor of more than 2. These improvements resulted in a detection noise almost 10 times lower, negligible compared to the level of uncompensated vibration noise associated with the imperfect correlation with the accelerometers.

2. Moreover, in the work of Ref. [66], the interferometer was operated beyond his linear range, with a significant portion of the data on the bottom and top of the fringes, which

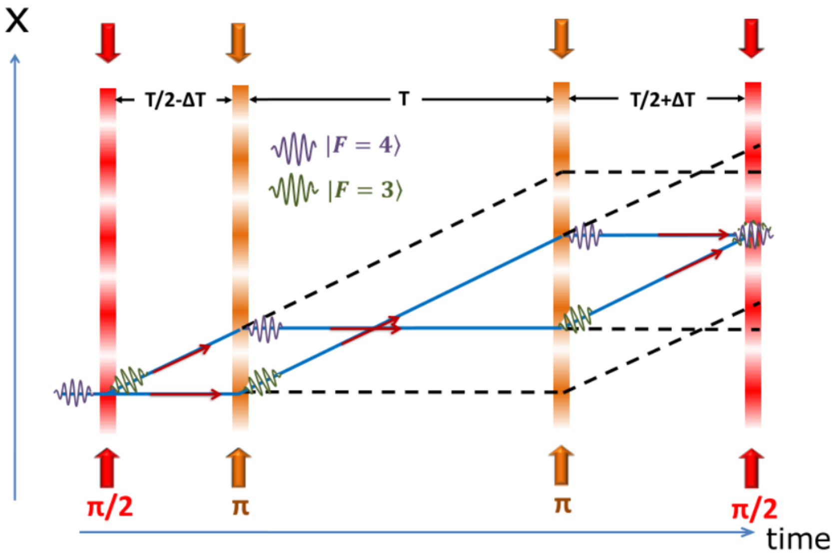

Figure 3.7: Illustration of the parasitic interferometers occuring because of the imperfect transfer at the π pulses.

corresponds to effective dead times since the interferometer is not phase sensitive at these points. Such dead times also prevent from observing a stability scaling faster than $\tau^{-1/2}$. In the Supplementary Materials of Ref. [66], we analyzed (by numerical simulations) the limitations to the τ^{-1} scaling of the stability associated with the non-linearity of the interferometer. The simulations are reported in Fig. 3.8. They show the importance of restricting the operation of the interferometer to its central, linear region, in order to benefit from the correlations between successive measurements associated with the joint operation.

The next section will present the results corresponding to the improvements on these limitations.

3.2.2 High-sampling rate gyroscope with interleaved interferometry

The extension of the applications of cold-atom inertial sensors to the measurement of time-varying signals has been confronted to their reduced sampling rate, which originates from their sequential operation and from the long interrogation time of the atoms that is required to achieve high inertial sensitivity. This limitation is, for example, an obstacle for applications to inertial navigation [69] or gravitational wave astronomy [70], [71]. In Ref. [72], we increased the sampling rate of our gyroscope by interleaving 3 joint experimental cycles, yielding a cycling time $T_c = 2T/3 = 267$ ms. We also implemented technical upgrades as solutions of the problems identified in our previous study. The main technical improvements were:

1. reduction of the detection noise to an equivalent phase noise of 70 mrad per shot (8 nrad.s^{-1}.Hz$^{-1/2}$ rotation rate sensitivity in triple joint);

2. implementation of seismometers (model Trillium from Nanometrics) as vibration sensors, featuring a noise floor 30 times lower than the accelerometers in the frequency band of interest to our experiment (0.01-10 Hz);

3. real time compensation of the vibration noise via a feedback on the Raman laser relative phase, in order to operate the interferometer as much as possible in its linear range. To this aim, we adapted the method previously demonstrated in our team on a cold-atom gravimeter [73].

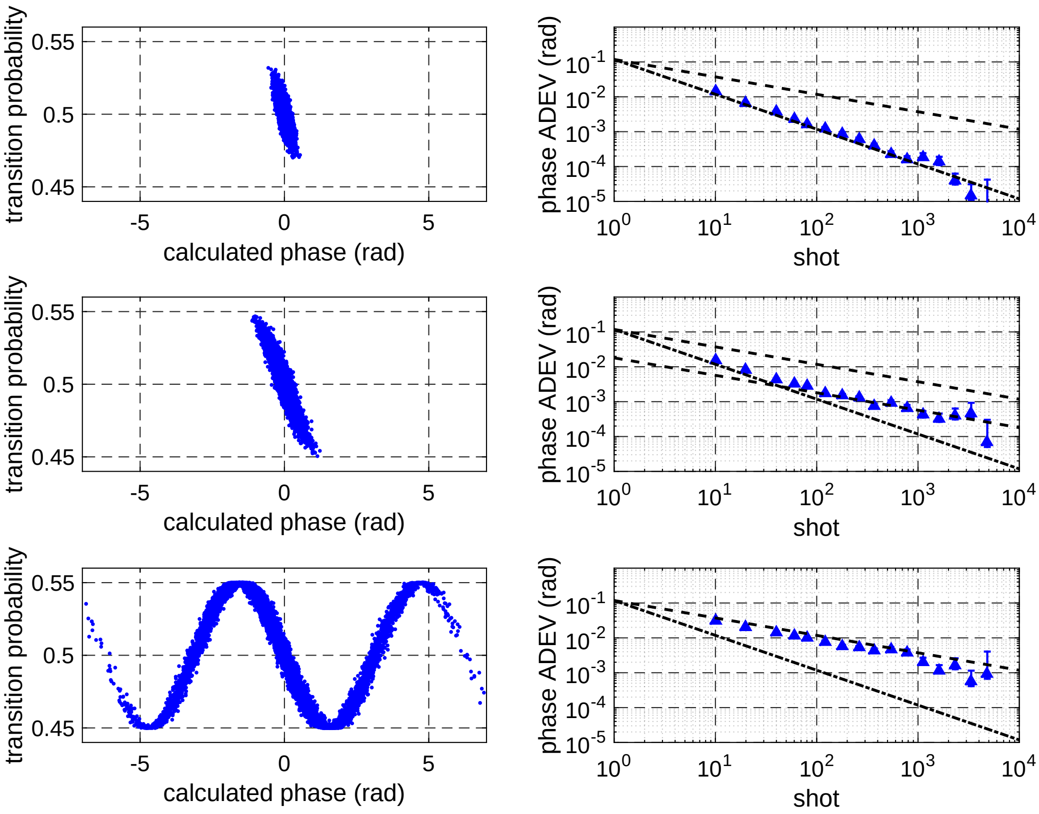

Figure 3.8: **Impact of the operation beyond the linear range.** Simulation of the gyroscope phase stability when fitting the interferometer fringes by packets of 10 points. The interferometer was simulated without probability noise (detection noise), 120 mrad of correlated phase noise between the successive cycles, and various levels σ_{vib} of vibration induced phase noise (assumed to be perfectly measured by the vibration sensors). Top, $\sigma_{vib} = 0.13$ rad; middle: $\sigma_{vib} = 0.32$ rad; bottom: $\sigma_{vib} = 2.1$ rad. The left columns show the synthetic correlation of the atom interferometer with the calculated vibration phase; the right columns show the Allan deviation of the fitted phases, together with lines indicating the τ^{-1} (dash-dotted) and $\tau^{-1/2}$ (dashed) scaling.

Fig. 3.9(a) shows the trajectories of the atom cloud in the interleaved configuration. Panel (b) shows the Allan deviation of rotation rates. In this work, we could observe the τ^{-1} scaling to the sensitivity predicted to occur due to the correlations between successive cycles. As such a scaling brings an important improvement to the short term sensitivity of the sensor, it is important to understand its origin:

Following Eq. (3.6), and assuming that the Raman lasers are oriented purely in the x direction, the 4-light-pulse atom interferometer phase shift is given by :

$$\Phi = k_{\text{eff}} \left[x_b(0) - 2x_t(T/2) + 2x_t(3T/2) - x_b(2T) \right], \tag{3.18}$$

with $x_{b,t}(t)$ the position of the bottom and top retro-mirrors with respect to the free-falling atom cloud. The phase shift can be re-written as

$$\begin{aligned} \Phi &= k_{\text{eff}} \left[x_t(0) - 2x_t(T/2) + 2x_t(3T/2) - x_t(2T) \right] + k_{\text{eff}} \Big([x_b(0) - x_t(0)] - [x_b(2T) - x_t(2T)] \Big) \\ &= \Phi_t^{\text{acc}} + k_{\text{eff}} L \left(\theta_b(0) - \theta_b(2T) \right), \end{aligned} \tag{3.19}$$

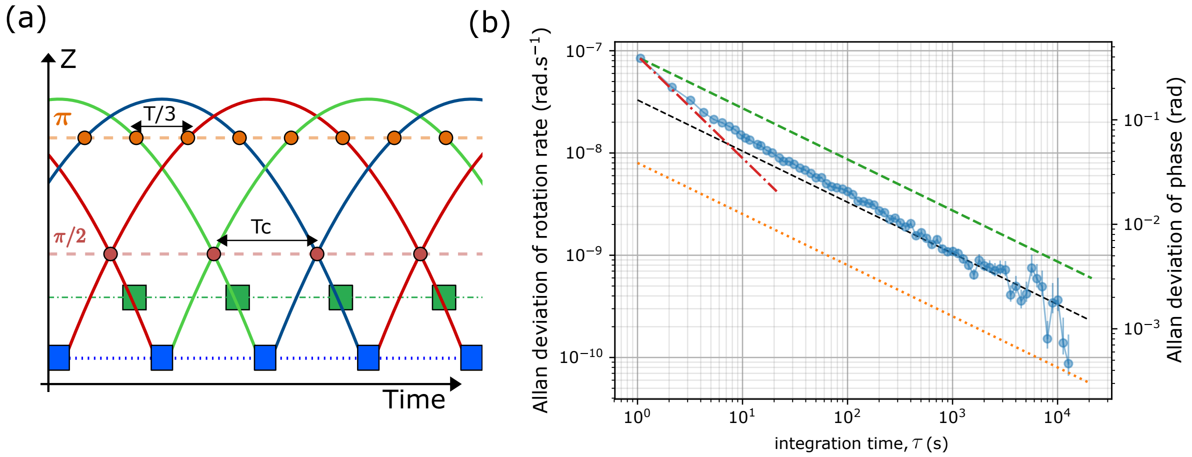

Figure 3.9: **Interleaved atom interferometry.** Adapted from Ref. [72]. (a) Trajectories of the successively launched atom clouds in interleaved operation. Each interferometer has an interrogation time $2T = 801$ ms and the cycle time is $T_c = 2T/3 = 267$ ms. The $\pi/2$ pulses are shared between the atom clouds entering and exiting the interferometer. (b) Stability analysis of a night acquisition of rotation rates [72]. Dashed black line: 3.3×10^{-8} rad.s$^{-1} \times \tau^{-1/2}$. Green dashed line: $\tau^{-1/2}$ scaling from the one shot Allan deviation. Red dotted-dashed line: τ^{-1} scaling from the one shot Allan deviation. Orange dotted line: detection noise limit corresponding to 8×10^{-9} rad.s$^{-1} \times \tau^{-1/2}$.

with $L = \frac{3}{8} g T^2$ the distance between the bottom and top mirrors, and Φ_t^{acc} the term associated to the linear acceleration of the top mirror. The second term represents pure rotation of the bottom mirror about the position of the top one. Recalling that $T_c = 2T/3$ and writting as $\Phi_i = \Phi(iT_c)$ the atom interferometer phase at cycle i, the mean phase after N measurement reads

$$\bar{\Phi}_N = \frac{1}{N} \sum_{i=0}^{N-1} \Phi_i = \frac{1}{N} \sum_{i=0}^{N-1} \left(k_{\mathrm{eff}} L \left[\theta_b(iT_c) - \theta_b((i+3)T_c) \right] + \delta \tilde{\phi_i} \right). \tag{3.20}$$

The term $\delta \tilde{\phi_i}$ encompasses contributions of detection noise, uncompensated linear acceleration noise and laser phase noise. When expanding the sum in Eq. (3.20), the θ_b terms mutually cancel, such that the mean phase reads

$$\bar{\Phi}_N = k_{\mathrm{eff}} L \frac{\theta_b(0) - \theta_b((N+2)T_c)}{N} + \frac{1}{N} \sum_{i=0}^{N-1} \delta \tilde{\phi_i}. \tag{3.21}$$

This equation shows that the random rotation noise averages as N^{-1} (first term). The second term represents the uncorrelated noise contributions of standard deviation $\sigma_{\delta\phi}$. Their sum equals $\sqrt{N} \times \sigma_{\delta\phi}$, which corresponds to a scaling of the phase sensitivity as as $N^{-1/2}$.

Besides rotation noise, uncompensated linear accelerations in the frequency range $[0.1 - 1]$ Hz contribute to a large part the interferometer phase noise. This contribution, estimated to typically about 500 mrad per shot, dominates the noise budget and may prevent from observing a clear τ^{-1} scaling of the gyroscope sensitivity. Interleaving, however, allows to over-sample these fluctuations, thus introducing correlations between successive measurements, which also contributes to the τ^{-1} dependence of the instrument sensitivity.

The sensitivity of 3.3×10^{-8} rad.s$^{-1} \times \tau^{-1/2}$ reported in Ref. [72] represents the state-of-the art for cold-atom gyroscopes as of 2018.

Systematic effects and long-term stability. As introduced earlier, a systematic shift specific to the interleaved interrogation originates from the light scattered from the MOT towards the atoms interrogated in the interferometer [60]. The MOT scattered light is close to resonance and induces a loss of contrast and a differential light shift (AC Stark shift). The influence of induced light shifts is reduced by the spin-echo-like four-pulse sequence, and by the use of $\vec{k}_{\text{eff}}$ reversal: alternating $\pm\hbar\vec{k}_{\text{eff}}$ momentum transfers changes the sign of the inertial phase shift but not the one of the clock-terms (e.g. differential light shift), which are rejected when taking the half-difference of two measurements. We measured the residual effect, and showed that it corresponds to an instability below 7×10^{-11} rad.s^{-1}(see Supplementary Materials of Ref. [72]).

The most important systematic effects in atom interferometers with separated Raman beams originate from relative wavefront mismatch coupled to deviations of the atom trajectories with respect to the ideal one [74], [75]. In our system, a relative angular misalignement $\vec{\delta\theta}$ between the top and bottom mirrors used to retro-reflect the Raman beams, coupled with an error of launch velocity $\vec{\delta v}$ (with respect to a velocity of $-\vec{g}\,T$ at the first Raman pulse) in the (y, z) plane results in a phase shift

$$\Delta\Phi = 2Tk_{\text{eff}}\left(\delta v_y\delta\theta_y + \delta v_z\delta\theta_z\right) = 12\ \text{mrad} \times \left(\frac{\delta v_{y,z}}{1\ \text{mm.s}^{-1}}\right) \times \left(\frac{\delta\theta_{y,z}}{1\ \mu\text{rad}}\right). \tag{3.22}$$

We explain in the Methods of Ref. [72] how we set the parallelism between the two Raman beams and the velocity of the atoms to approach the ideal trajectory, in order to achieve an uncertainty on the residual systematic shift of 21 mrad (i.e. 4.6 nrad.s^{-1}).

After this systematic analysis and the corresponding fine-tuning of the apparatus, we could demonstrate a **long term stability of 3×10^{-10} rad.s^{-1}, which represents the state of the art for atomic gyroscopes.**

Dynamic rotation rate measurements. To illustrate the potential of interleaved interferometry, we performed measurements of dynamic rotation rates. To this end, we modulate the orientation of the experiment around the y axis. This was performed by applying a force on the bottom plate linking the experimental frame to the vibration isolation platform (see Fig. 3.1), via the voice-coil actuator controlling the tilt θ of the apparatus. We apply sinusoidal modulations of the form $\theta(t) = \theta_0\sin(\omega t)$ with a period $2\pi/\omega$ and with an amplitude θ_0 of few 10^{-7} rad. The resulting rotation rate is of the form $\vec{\Omega}(t) = \Omega_0\cos(\omega t)\hat{u}_y$, with $\Omega_0 = \omega\theta_0$.

The measurements are reported in Fig. 3.10 for modulation periods of 5 s and 10 s. The respective modulation amplitudes are 2.3×10^{-7} rad and 3.4×10^{-7} rad. Panels A and B show the atomic phase extracted from the transition probability, $P(t)$, which follows the sinusoidal modulation. The total phase signal from the atom interferometer is the sum of this atomic phase and of the phase compensated in real time. A Fourier analysis of the total signal is shown in panel C. Within our frequency resolution, we find that the amplitude of the reconstructed rotation rate signal agrees with the expectation of Ω_0 with a relative precision of 5%. A more detailed analysis is presented in the Supplementary Materials of Ref. [72] (section S5).

3.3 Conclusion and perspectives

Since my arrival at SYRTE in September 2013, about 60% of my research activity has been related to the gyroscope-accelerometer experiment (performing measurements, training the students and postdocs, scheduling the improvements to the setup, analyzing the data, writing the articles, organizing collaborations). With this setup, we have demonstrated new techniques (zero dead time operation, interleaving) which are important to the atom interferometry community, especially regarding future applications of cold-atom interferometers to the measurement of time varying signals, as it is the case in inertial navigation or gravitational wave detection. Moreover,

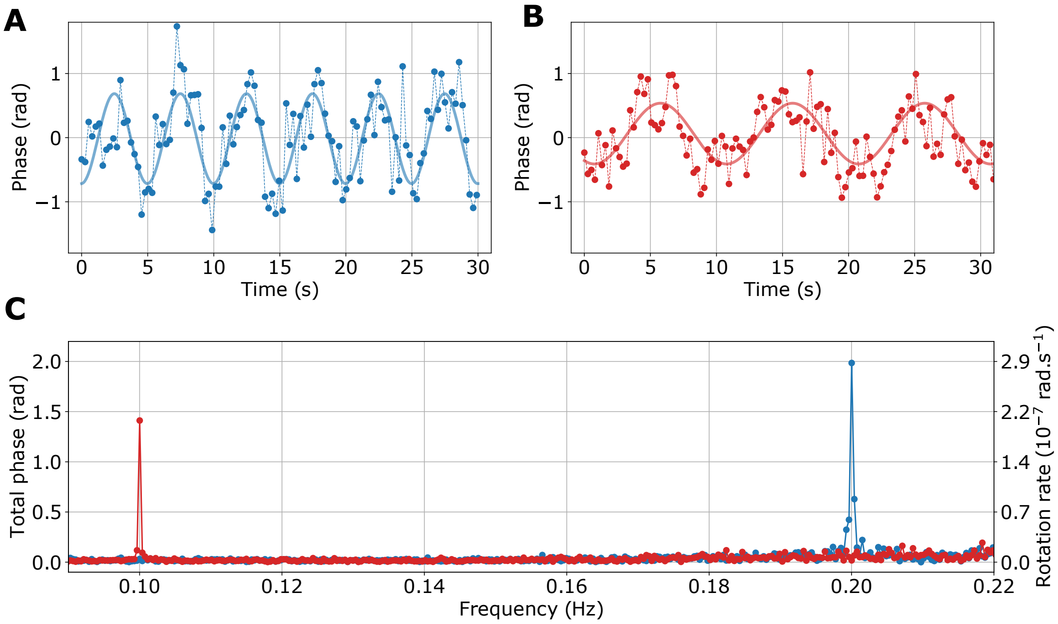

Figure 3.10: From Ref. [72]. **Measurement of dynamic rotation rates.** Atom interferometer phase deduced from the transition probability, for rotation rate modulations of 5 s period (A) and 10 s period (B). Plain line: sinusoidal fit to guide the eye. C): Fourier analysis of the total rotation rate signal, with a frequency resolution is 0.37 mHz.

we have pushed the metrological study of our sensor: our gyroscope now represents the state-of-the-art of atomic gyroscopes in terms of stability, and competes with the best fiber-optics gyroscopes [76].

Perspectives. I have planned several projects for the near future (4 years):

- *An accurate measurement of the Earth rotation rate and a test of the Sagnac effect for matter-waves at the* 10^{-4} *relative accuracy level.* In December 2018, we implemented a rotation stage below the experiment to control the orientation to North (in principle with a resolution below 1 μrad) and vary it over a large range (180°). This will allow us to measure the bias and the scale factor of our gyroscope. Consequently, we will be able to verify the validity of the Sagnac effect for matter waves. Reaching an accuracy of 10 nrad.s^{-1}would already represent an improvement of more than one order of magnitude compared to previous experiments involving matter-waves such as neutrons [77], [78] or atoms [74]. A collaboration with the theory team of SYRTE has started to investigate the impact of such measurements on a test of Lorentz invariance in the so-called matter-gravity sector of the Standard Model Extension [79].
- *Measurements along two axis.* Our setup offers the possibility to measure rotation rates and accelerations along two horizontal axis, and to interleave such measurements. Setting up the Raman lasers for the second direction (orthogonal to the current one) is ongoing. The experiment can also be used to perform a 2 dimensional interferometer as presented in [80], without modification to the fluorescence detection system.
- *An improvement of the vibration noise rejection.* I am collaborating with the team of Christophe Collette at *Université Libre de Bruxelles* in order to engineer a system to actively compensate vibration noise (linear acceleration noise along $\vec{e}_x$ and rotation noise along $\vec{e}_y$), by using the signals of our seismometers and applying a feedback to our vibration isolation platform.
- The design of a new experiment to implement degenerate Raman sideband cooling (to reach temperatures $\sim$ 200 nK in 3D [81]), with an arrangement of the atom preparation and detec-

tion zones compatible with interleaved interferometry at a 20 Hz rate. This project will be of high relevance for resolving time-varying signals as in gravitational wave detection (see chapter 5) or gravity gradiometry (for, e.g., the early detection of Earthquakes) [82], or rotational semismology [83], [84].

- *A test of gravitational decoherence models* following the proposal of Ref. [85], in collaboration with the theory team of M. Zych at the University of Queensland (Australia).

3.3.1 Publications linked with the gyroscope-accelerometer project:

1. *The Sagnac effect: 20 years of development in matter-wave interferometry*
   Brynle Barrett, **Remi Geiger**, Indranil Dutta, Matthieu Meunier, Benjamin Canuel, Alexandre Gauguet, Philippe Bouyer, Arnaud Landragin
   Comptes Rendu Physique 15, 875-883 (2014), Ref. [86]

2. *Stability enhancement by joint phase measurements in a single cold atomic fountain*
   M. Meunier, I. Dutta, **R. Geiger**, C. Guerlin, C. L. Garrido Alzar, and A. Landragin, Ref. [60]

3. *Gyromètre à atomes froids de grande sensibilité - High sensitivity cold atom gyroscope*
   Remi Geiger, Indranil Dutta, Denis Savoie, Bess Fang, Carlos L. Garrido-Alzar, Christine Guerlin, Matthieu Meunier, Thomas Lévèque, Bertrand Venon, Michel Lours et Arnaud Landragin Revue Français de Métrologie 41, Vol. 2016-1, 21-27, Ref. [87]

4. *Metrology with Atom Interferometry: Inertial Sensors from Laboratory to Field Applications*
   Bess Fang, Indranil Dutta, Pierre Gillot, Denis Savoie, Jean Lautier, Bing Cheng, Carlos L Garrido Alzar, **Remi Geiger**, Sebastien Merlet, Franck Pereira Dos Santos, Arnaud Landragin
   Journal of Physics: Conference Series, Volume 723, conference 1, Ref. [88]

5. *Continuous Cold-atom Inertial Sensor with 1 nrad/sec Rotation Stability*
   I. Dutta, D. Savoie, B. Fang, B. Venon, C.L. Garrido Alzar, **R. Geiger**, A. Landragin
   Phys. Rev. Lett. 116, 183003 (2016), Ref. [66]

6. *Improving the phase response of an atom interferometer by means of temporal pulse shaping*
   Bess Fang, Nicolas Mielec, Denis Savoie, Matteo Altorio, Arnaud Landragin, and **Remi Geiger**
   New J. Phys. 20 023020 (2018), Ref. [89]

7. *Interleaved Atom Interferometry for High Sensitivity Inertial Measurements*
   D. Savoie, M. Altorio, B. Fang, L. A. Sidorenkov, **R. Geiger**, A. Landragin
   Science Advances 21 Dec 2018: Vol. 4, no. 12, eaau7948, Ref. [72].

3.3.2 Students and postdocs supervised on the gyroscope-accelerometer experiment.

- Indranil Dutta, PhD student until November 2015;
- Denis Savoie, Master and PhD student from March 2014 to Nov. 2017;
- Matteo Altorio, PhD student since Oct. 2016;
- Romain Gautier, Master and PhD student since March 2018;
- Bess Fang, postdoc from November 2014 to August 2017;
- Leonid Sidorenkov since November 2017;
- Interns: Guillaume Payet, Yasmina Dahmani, Williamn Dubosclard, Nicolas Gibelin, Mehdi Ait-Yahia.

3.3.3 Funding

Since 2013, I obtained several grants to conduct the research on the cold-atom gyroscope-accelerometer :

- a grant for the PhD thesis of Denis Savoie from *Délégation Générale pour l'Armement*-DGA;
- a grant from the city of Paris (project HSENS-MWGRAV) over the period 2014-2018 (240 k€);
- two postdoc grants from the Scientific Council of Paris Observatory for Bess Fang (2015-2017) and Leonid Sidorenkov (2018-2020);
- a grant from *Sorbonne Universités* for small equipment and the start of the contract of L. Sidorenkov (LORINVACC project, 60 k€);
- two PhD thesis grants from the EDPIF doctoral school (for Matteo Altorio and Romain Gautier);
- a grant from the French Research Agency-ANR (project PIMAI-Precision Inertial Measurements with Atom Interferometers) will allow me to conduct the projects mentioned above over the period 2019-2023 (310 k€).

Chapter 4

Optical systems for atom interferometry experiments

Large momentum transfer (LMT) beam splitters represent a key concept to enhance the sensitivity, compactness and sampling frequency of cold-atom inertial sensors [22], [90]–[95]. This technique consists in transferring a large momentum to the atoms (larger than two recoils) in order to increase the interferometer area and thus its sensitivity. LMT could be used to reduce the time T of interrogation of the atoms in the interferometer, and thus reduce the size of the sensor which scales as T^2. It therefore appears as a promising solution both for applications aiming at high sensitivity (e.g. gradiometry or gravitational wave detection), or for applications requiring compactness of the setup (gravimetry or navigation).

However, benefiting from the potential of LMT requires large laser intensities and low wavefront distortions, which explains why LMT techniques have not yet been able to improve the inertial sensitivity of cold-atom accelerometers or gyroscopes. An appealing solution to this problem is to use an optical resonator, which can provide power amplification at resonance, as well as an interferometric control of the beam wavefront. To be efficient, the resonator should support a laser beam featuring a large enough waist (> 1 cm) to interact with the whole atomic cloud, which is challenging. My objective is to realize a cavity with an optical gain exceeding 20 and which is resonant for a beam of 2 cm of diameter featuring a flat intensity profile at its top (so-called flattop or top-hat beam [96], [97]). This chapter summarizes such optical developments.

4.1 Generation of collimated flattop (top-hat) laser beams

4.1.1 Context

The sensitivity and accuracy cold-atom inertial sensors crucially depend on the relative phase uniformity of the laser beams realizing the atom-optics functionalities. Inhomogeneities in the laser intensity across the atom cloud degrade the atom optics efficiency, which causes a decrease of interferometer contrast and hence a lower signal to noise ratio, as well as systematic effects [74]. Such detrimental effects are amplified in interferometers employing large momentum transfer (LMT) techniques, in particular because of diffraction phase shifts [98]. The problem of intensity inhomogeneity can be mitigated by employing Gaussian beams with a size much larger than that of the atom cloud, at the cost of a reduced peak intensity. *My objective was to develop a solution for a collimated top-hat laser beam (a beam with a uniform intensity distribution in the central part [96]) as a solution to circumvent the problems encountered in atom interferometers employing Gaussian beams.*

I started this activity in 2015, with the analysis that, to the best of my knowledge, no commercial solution did exist for producing a laser beam with a top-hat intensity profile which could propagate over several meters, while many solutions for shaping the intensity profile in a given plane did exist. Based on the work of Jefferson and Hoffnagle [97], Nicolas Mielec and myself started to design a refractive telescope made of two aspheric lenses (sag of few μm) to produce a collimated top-hat beam. The idea of this design is the following [99]: a first aspheric lens transforms a Gaussian beam in a top-hat beam in a plane; the second aspheric lens corrects the wavefront of the beam to flatten it.

The company (*QED Techologies*) who realized the aspheric lenses in [97] stopped this activity and could not assist us in the design. They could only propose us to realize the lenses that we would request (for about 10 k€ per lens), which did not appear to us as a satisfactory solution. In order to benefit from the expertise in optics of the GEPI department of Paris Observatory, we thus started a collaboration with David Horville to design effective aspheric lenses consisting of a simple lens and a ion-etched phase plate ensuring the required dephasing, which could be realized in house. While this work did not lead to a good enough quality of the generated top-hat beam, we learned on the method and on some of the problems that can be encountered. This work is presented in chapter 2 of the PhD thesis of Nicolas Mielec [99].

In order to better control the wavefront of the beam, we investigated a solution based on a double passage on a spatial light modulator, where each reflection on the SLM plays the role of the phase plate of the refractive telescope. This method had the advantage to offer us the possibility to vary the parameters. We could produce a top-hat beam of 20 mm diameter (region where the intensity deviates by less than 10%) that could propagate without significant distortion over 3 m [99]. As we were starting the optimization of this method (transmission efficient, stability, improvement of the intensity noise), I became aware of a commercial solution proposed by the *Asphericon* company (Germany) for a collimated top-hat beam shaper (released in Summer 2017). With the expertise acquired in beamshaping techniques, we could judge about the suitability of the commercial product and retained this solution, which presents key advantages over the SLM for implementation on an atom-interferometer: it is compact and passive. I will present here the main result obtained with this solution, corresponding to the publication [100].

4.1.2 Top-hat collimator

Our top-hat collimator solution presented in Fig. 4.1a) is based on the beamshaper TSM-25-10-S-B from Asphericon. The beamshaper shall receive at its input a Gaussian beam of 10 mm $1/e^2$-diameter and produce a top-hat beam of 15 mm full width at half maximum (FWHM), with a region of about 14 mm where the intensity varies by less than 10%. The advertized uniformity of intensity plateau is 0.056 rms, with a phase inhomogeneity of $\lambda/3$ peak-valley and $\sim \lambda/20$ rms, allowing the beam to propagate without deformation on distances of several meters. We inject the beamshaper with a home-made fiber collimator made of 3 simple lenses, to produce a Gaussian beam of 9.95 ± 0.05 mm $1/e^2$ diameter. At the output of the beamshaper, the top-hat beam is magnified by a factor of two with two achromatic doublets, in order to reach a useful region of 28 mm. The optical system can be mounted conveniently on an experiment. The power transmission of the input collimator plus the beamshaper is 91%, while that of the full system is 85%. The quality of the generated top-hat beam mainly depends on the input beam size (which must fall within the 10 mm diameter specification at the 10% level, and of its collimation.

Fig 4.1b) shows the beam imaged on a paper screen at the output of the expander. While this method is convenient for the alignment procedure, it is not suited for a precise measurement of the intensity uniformity of the beam because of the speckle produced on the paper screen. We use a large-area beamprofiler (11.3×6.0 mm^2) to measure the uniformity of the plateau. Fig 4.1c) shows the stitched images acquired by scanning the beamprofiler in front of the beam after 40 cm of propagation. The uniformity of the plateau over a diameter of 28 mm is 0.11 rms, and the FWHM is 31.7 ± 0.2 mm. Fig 4.1d) shows a profile of the vertical cut through the middle of the beam (along the blue line). The orange line is a moving average over 1 mm of the profile, shown here to illustrate lower frequency inhomogeneities. For comparison, the green line shows a Gaussian beam with 40 mm diameter at $1/e^2$ (as used on the gyroscope-accelerometer experiment) and same peak intensity as the top-hat beam.

In an atom interferometer, the relative phase between two counter-propagating laser beams is imprinted on the atomic wave-function during the light pulses. This relative phase contains a term associated with the free propagation, $\varphi(x, y, 0) - \varphi(x, y, 2L)$, where L the distance between the atom cloud and the retro-mirror [101]. We measured such relative phase field for our top-hat beam using an asymmetric Michelson interferometer with the difference of its arms set to $2L$. The relative phase map in a pupil of 28 mm diameter corresponding to the useful part of the beam is shown Fig 4.1e), for a difference in propagation distance $2L = 70$ cm. We find relative phase inhomogeneities of $\lambda/5$ PV and a $\lambda/28$ rms. This represents an upper bound, as it is compatible with the imperfect planeity of the optics used in the Michelson interferometer. Additional characterizations are presented in the Supplementary materials of [100] and in [99].

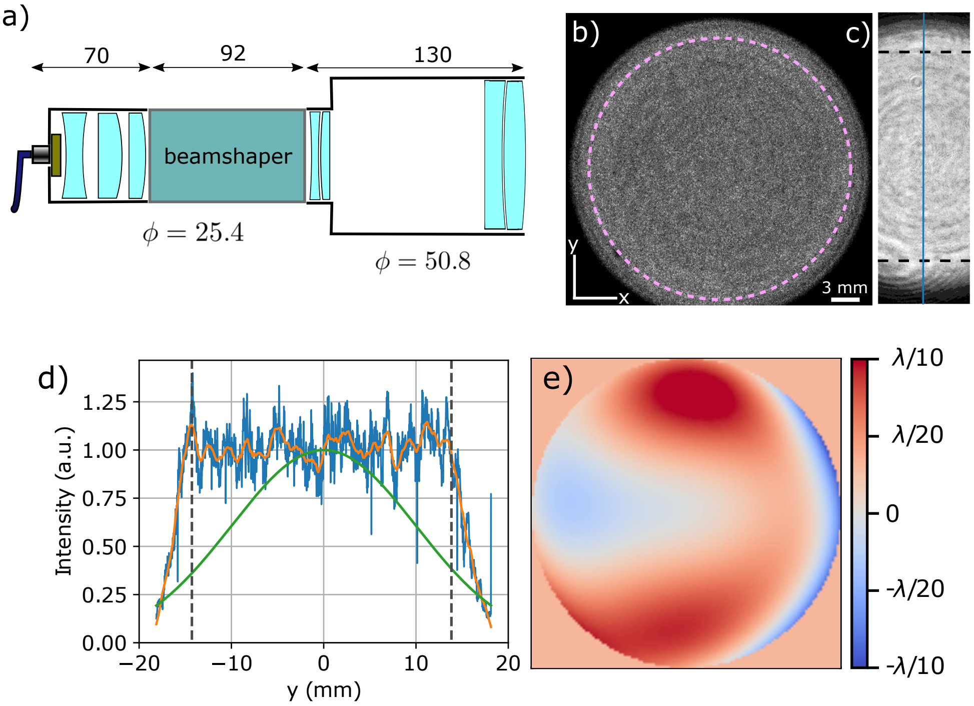

Figure 4.1: From [100]. a) Schematic view of the optical system with the input collimator, the beamshaper, and the expander (dimensions in mm, ϕ denoting the diameter of the optics). b) Image of the top-hat beam on a paper screen. The dashed purple line is a circle of 28 mm diameter. c) Image obtained with a beamprofiler, after 40 cm of propagation. Between the 2 dashed lines separated by 28 mm, the uniformity of the plateau is 0.11 rms. d) (blue) Vertical line profile of the top-hat beam shown in c); the intensity has been normalized to the mean plateau intensity. (orange) Moving average over 1 mm. (green) Theoretical profile of a Gaussian beam with 40 mm $1/e^2$ diameter. e) Relative phase of the top-hat beam with 70 cm propagation difference, in a disk of 28 mm; the deviation is $\lambda/5$ (PV) and $\lambda/28$ (rms).

4.1.3 Atom interferometry with a top-hat beam

We implemented the top-hat beam on the cold-atom gyroscope-accelerometer experiment described in chapter 3. The top-hat collimator was set up at the position of the second window (from the bottom, see Fig. 3.1), while the beam at the bottom window was the usual Gaussian beam of 40 mm diameter at $1/e^2$.

To assess the limitations to the gain in atom-optics efficiency offered by our top-hat beam over our Gaussian beam, we recorded Rabi oscillations after various time-of-flight (TOF), when the launched atom cloud crosses the beams on its way up and on its way down. Fig 4.2a) shows the Rabi oscillations on the way up after a TOF of 170 ms and on the way down after TOF of 855 ms for the top-hat and Gaussian beams. On the way up, the cloud size is smaller than the beam sizes, and the Rabi oscillations have a similar shape for the Gaussian and top-hat beams, as expected. The transfer efficiency of $\sim 70\%$ is limited by the velocity selectivity of the two-photon transition, given by the finite Rabi frequency (i.e. laser power) and velocity spread of the atoms in the direction of the beams. On the contrary, on the way down, the Rabi oscillation in the top-hat beam (green) is significantly improved with respect to that in the Gaussian beam (red), owing to the homogeneity of the two-photon Rabi frequency from the top-hat beam.

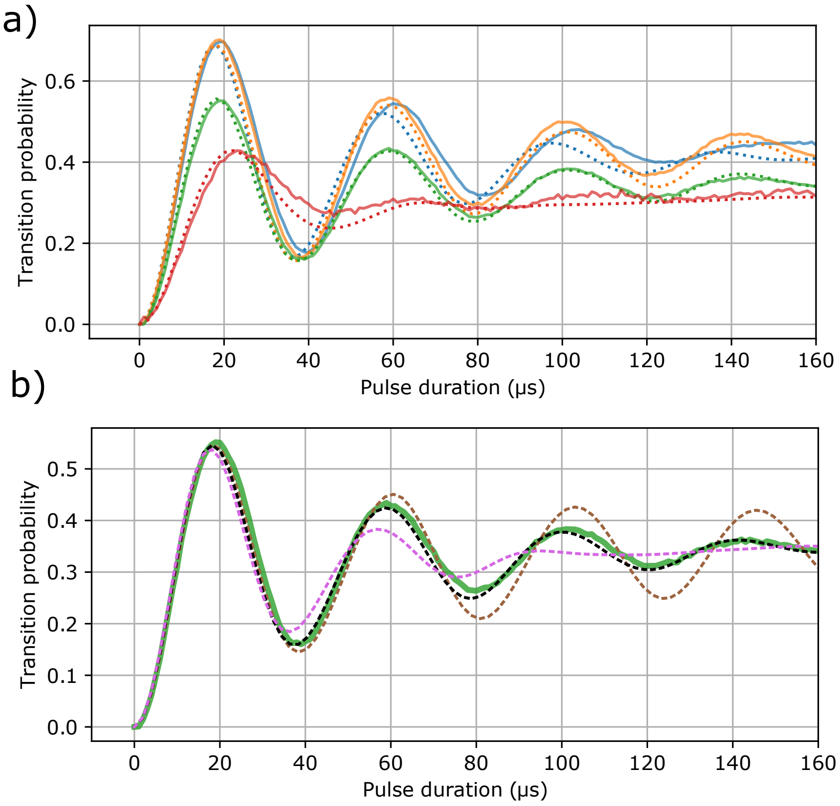

Figure 4.2: From [100]. **Rabi oscillations.** a) Plain lines: measured oscillations on the way up after 170 ms of TOF (blue and orange for Gaussian and top-hat, respectively), and on the way down after 855 ms of TOF (red and green). Dotted lines: numerical simulation. b) Green plain line: measured Rabi oscillation in the top-hat beam after 855 ms of TOF (the same as in a)). Dashed: numerical simulation for various level of rms intensity noise on the top-hat (brown: 0%, black: 8.3%, violet: 15%).

We modeled the Rabi oscillations with a Monte-Carlo simulation where we generated an ensemble of atoms with individual velocities following the distribution measured with the Doppler-sensitive Raman transitions (corresponding to a 3D temperature of 1.2 μK), and propagate them in the Raman beams. The model reproduces well the data, and allows to assess the residual intensity inhomogeneities of the top-hat beam. Fig. 4.2b) shows the measured Rabi oscillation confronted to a simulation where intensity noise of various levels is added on the top-hat profile. The data match best the numerical simulation assuming an inhomogeneity of 8.3% rms, consistent with the optical characterization of the intensity inhomogeneities of 11% reported in Fig. 4.1.

We performed additional experiments to show the suitability of the top-hat beam for cold-atom interferometry, which are presented in Ref. [100].

4.2 Large beam optical resonator for atom interferometry

4.2.1 Context

An essential aspect of optical cavities in several applications is the possibility to enhance the power of the light when the resonance condition is maintained. In the most common case, optical resonators are formed by an ensemble of mirrors, whose curvature defines the geometry and spectral properties of the resonating mode, the optical enhancement factor being essentially determined by the losses of the optics. In some applications, it is desirable to obtain large diameters (several mm or cm) for the resonating beam, which translates in increased resonator length and radii of curvature of the mirrors (up to km).

Enhancement cavities have been proposed for cold-atom interferometry experiments, as a way to relax the requirements on the laser power required to operate atom interferometers [102], [103]. This application most commonly requires two counter propagating beams of the same shape and with sizes of several mm, in order to efficiently interrogate clouds of atoms at a temperature of typically few μK. Reaching such large beam sizes in compact setups (< 1 m) introduces severe constraints on the resonator design. Large mode enhancement cavities have been studied in various configurations. For example, optical power enhancement factors of 2000 were demonstrated for a beam radius of 5 mm in Ref. [104] which used a four-mirror cavity. Ref. [105] studied a three-mirror resonator in a telescope-based configuration achieving beam waists of about 2 mm. In the context of atom interferometry, the need to accommodate the enhancement cavity in the vacuum system enclosing the atom interferometer leads to considering linear resonators as the easiest-to-implement configuration. For that purpose, we proposed in Ref. [106] to employ a linear, degenerate, resonator consisting of two mirrors located at the focal planes of a lens to achieve large beam waists in a compact geometry.

I will summarize here our experimental results (not yet published [107]) on the degenerate optical resonator proposed in Ref. [106], in a compact geometry of 44 cm. This study started in 2015 with the PhD thesis of Nicolas Mielec, funded by the city of Paris. Ranjita Sapam joined the team as a postdoc in Mai 2016 and worked mainly on the experimental aspects (while Nicolas Mielec mainly developed the simulation tools). In such a degenerate resonator, an arbitrary input field distribution (e.g. flattop) should reproduce after two round-trips, and a large beam can in principle resonate when a laser beam of large waist in injected in the cavity. However, due to its degeneracy, achieving the resonance of a Gaussian beam critically depends on the alignment of the resonator.

4.2.2 Presentation of the degenerate resonator and results

Setup

A simplified view of our experimental set-up is illustrated in Fig. 4.3. The resonator is made of two plane mirrors of diameter 50.8 mm (M1) and 12.7 mm (M2), placed approximately in the focal planes of a plano-convex lens of focal distance f. The two mirrors are spaced by $L \simeq 2f \simeq 456$ mm. A collimated Gaussian beam of variable waist, w_{in} is sent into the cavity from M1 and is focused on M2 by the lens with a waist, $w_{out} = \lambda f/\pi w_{in}$. In the study reported here, the input waist was varied between three different values, $w_{in} = 1.4,\ 2.6,\ 5.6$ mm.

Denoting as E_{in} the incident field in the cavity, E_{cir} as the circulating field inside the cavity, the optical gain is given by $G = |\frac{E_{cir}}{E_{in}}|^2$. The theoretical expression of G and finesse ,$\mathcal{F}$ evaluated at a plane between the lens and M2 are given by

$$G = \frac{r_2(1-r_1^2)(1-r_L^2)}{[1-r_1 r_2(1-r_L^2)]^2} \tag{4.1a}$$

$$\mathcal{F} = \frac{\pi\sqrt{r_1 r_2(1-r_L^2)}}{1-r_1 r_2(1-r_L^2)} \tag{4.1b}$$

where r_1, r_2 and r_L are the amplitude reflection coefficients of M1, M2 and lens, respectively. We measured $r_1 = r_2 = 0.994(5)$ for the mirrors but the measurement of r_L was impacted by a larger error. As its value has a stronger impact on the estimates of the finesse and gain, we adjusted its value by the measurement of the cavity finesse at small beam size (as explained in Fig. 4.5 below).

Due to the degeneracy of this cavity, the spectral and spatial characteristics of the beam that will resonate will critically depend on the relative alignment of the optical elements (i.e. the normal to the surface of the lens and of the mirrors) and of the input beam direction and position. The theoretical response of the resonator to various types of misalignment drove our alignment procedure. The detailed alignment procedure is presented in Ref. [107].

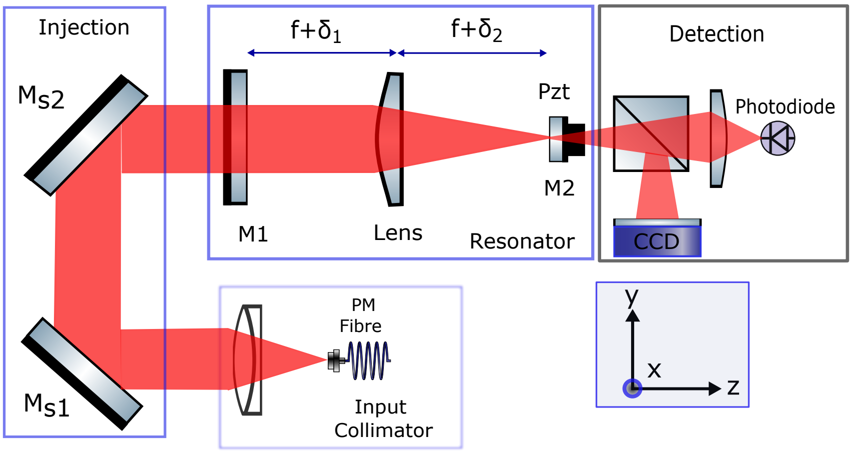

Figure 4.3: **Schematic of the degenerate optical resonator setup** (simplified and not to scale) consisting of two flat mirrors M1 (input) and M2 (output) at the focal planes of a plano-convex lens of focal distance $f = 228$ mm. $\delta_{1,2}$ are the longitudinal misalignment of mirrors M1 and M2 from the focal planes. M_{s1} and M_{s2} are the two input beam steering mirrors, PZT is a cylindrical piezo electric actuator tube attached to the back of M2.

Resonances

To analyze the behavior of our resonator, we measured its transmission spectrum for different values of its length around the $f-f$ configuration. The resonances were measured by scanning the voltage of the PZT actuator holding M_2, for different values of δ_2. Fig. 4.4(a) shows the variations in the transmission spectrum for an input beam of w_{in}=1.4 mm, for different values of $\delta_2 > 0$. When increasing δ_2, the spectrum becomes more and more asymmetric and features a long tail on one side.

Fig. 4.4 d) is the corresponding theoretically calculated spectra using the ABCD transfer matrix method presented in Ref. [106]. The calculation reproduces well the broadening and the asymmetric feature of the resonance, which can be interpreted with the standard modal theory of optical resonators as follows: in the case of a stable resonator, the frequencies of the eigenmodes indexed by $\{q, m, m\}$ (q for longitudinal, (m, n) for transverse) are given by

$$\nu_{qmn} = \frac{c}{2L}\left(q + (m+n+1)\frac{\phi_G}{\pi}\right), \tag{4.2}$$

where ϕ_G is the Gouy phase. In the case of our resonator, the perfect $f - f$ configuration ($\delta_2 = 0$) implies $\phi_G = \pi/2$ [106]. Any combination of even modes ($m + n$ even) resonate at one set of frequencies, and any combination of odd modes ($m + n$ odd) at another, shifted by $c/4L$.

When the resonator is off from the $f - f$ configuration ($\delta_2 \neq 0$), the degeneracy between the transverse and longitudinal modes is lifted, and a fundamental mode ($m = n = 0$) is well defined, corresponding to $\phi_G \neq \pi/2$. Injecting the cavity with a beam of different waist than that of the resonator mode results in a decomposition of the input beam over several transverse modes, which resonate at different frequencies according to Eq. (4.2). When $\delta_2 \ll f$ is small enough for the different resonance curves to partially overlap (within the resonance linewidth given by the resonator finesse), the resulting projection yields an asymmetric resonance, which is what we observe (for a more detailed explanation, see Fig. 4.17 on page 79 of the PhD thesis of N. Mielec [99]).

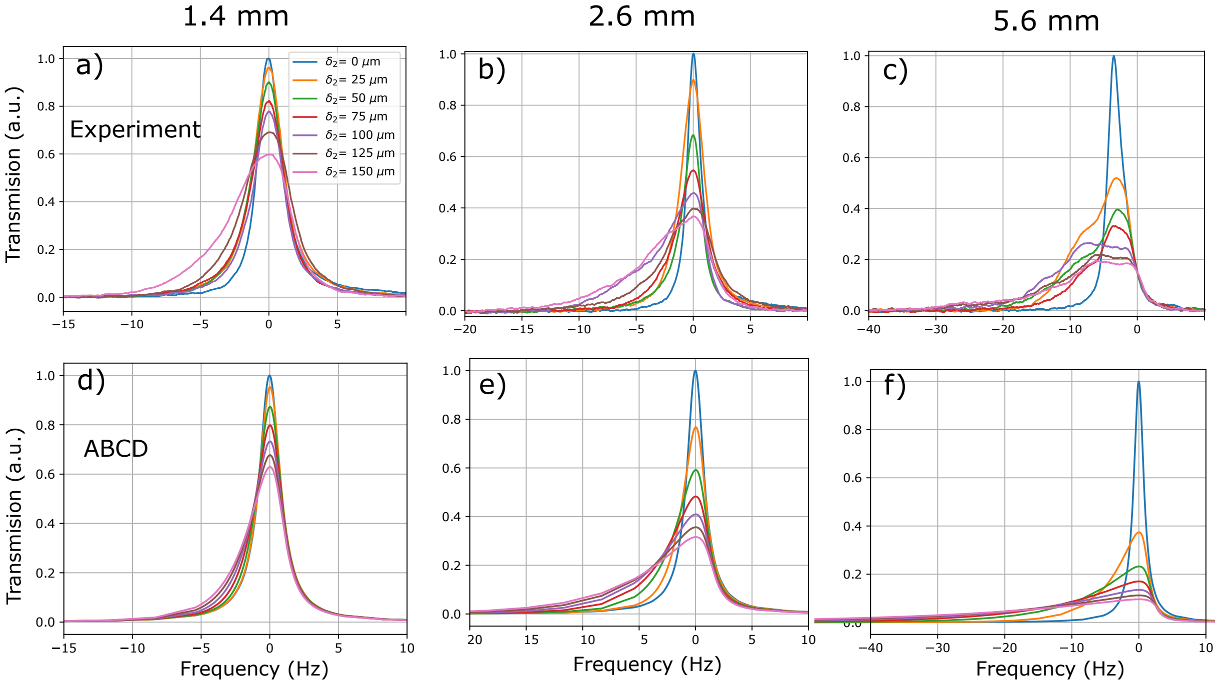

Figure 4.4: **Transmission spectra for different values of the longitudinal misalignement** δ_2. (a)-(c) are experimental spectra for input beam waists w_{in} = 1.4, 2.6, 5.6 mm, respectively. (d)-(f) are the corresponding spectra calculated with the ABCD transfer matrix method (i.e. assuming aberration-free optics).

The resonance spectra for w_{in}=2.6 mm and 5.6 mm are respectively are shown in Fig. 4.4 (b) and (c). We observe that the spectrum has a higher degree of asymmetry and a lower optical gain than for the case of w_{in} = 1.4 mm, for equivalent values of displacement δ_2. This behavior is qualitatively reproduced by the ABCD matrix calculation (panels (e) and (f)), and can be explained by the higher number of transverse modes over which the input beam projects when the input waist increases, for a given value of δ_2. For the largest input beam size, we observe the appearance of additional structures in the resonance profile (dips and bumps on the elongated tail), which are not captured by the ABCD matrix calculation. Extending the ABCD matrix propagation to the generalized calculation taking into account tilts of the optics and transverse misalignment [108] could also not explain these features. This suggested that the imperfections of the optics (e.g. optical aberrations) should have an influence on the resonating beam, and called for a more advanced modeling of our resonator.

Optical gain

We measured the finesse and the optical gain of the resonator when aligned in its best configuration, i.e. at the closest point to the ideal $f-f$ case that is experimentally achievable. The results are presented in Fig. 4.5. We observed that the finesse and the optical gain decrease while increasing w_{in}, in contradiction with the prediction of the ABCD transfer matrix calculation, which predicts a constant value (Eq. (4.1)) for all values of w_{in}. This discrepancy confirmed that a more advanced modeling of our resonator was necessary. To this end, Nicolas Mielec developed a set of numerical calculations based on the angular spectrum propagation of fields, with the same numerical methods as in the OSCAR cavity simulation software [109]. As described in Ref. [110], the angular spectrum method (ASM) is limited by computational memory constraints derived from the grid size and the number of round trips to consider (about $3 \times \mathcal{F} \simeq 600$ round-trips for our resonator). In our application, simulating beams with larger input waists translates into the need to use a calculation grid with a smaller step in order to sample correctly the smaller beam sizes at M_2. Finite computer memory resources (~ 16 GBytes) limited our simulations to beams with waists smaller than typically 2.5 mm. To overcome this issue in the particular case of problems with cylindrical symmetry, we performed calculations using the Hankel transform.

We measured the optical aberrations of each optical component of our resonator using a ZYGO interferometer. The spherical aberration is the greatest source of wavefront distortion (1.3λ over 50 mm). As studying its influence is computationally less demanding (using Hankel transforms), we could manage to numerically simulate its influence for all beam sizes. The red points in Fig. 4.5 present the results of the numerical calculation based on the ASM taking into account the measured third order spherical aberration of the lens. The trend is reproduced qualitatively, suggesting that optical aberrations play an important role in our resonator, owing to its degeneracy.

Beam shape

We recorded the profile of the resonating beams using a CCD camera in transmission of the cavity. Figs. 4.6(a), (b) and (c) show the profiles of the beam at resonance, respectively for w_{in} = 1.4 mm, 2.6 mm and 5.6 mm. Structural deviations with respect to the shape of a Gaussian profile can clearly be observed for w_{in} = 5.6 mm, and indicate the presence of aberrations without cylindrical symmetry, such as astigmatism.

In order to calculate the effects of aberrations without cylindrical symmetries, such as astigmatism, a complete 2D calculation is required. Due to our implementation of the ASM calculation and the computer memory constraints, we could only investigate its impact on beams of relatively small waists, up to 2.6 mm. To illustrate its influence, we introduced a degree of astigmatism larger than the one measured on the ZYGO interferometer: 0.2λ over the 50 mm pupil of the lens. Fig. 4.6(d) and (e) show the result of the ASM calculation for $w_{in} = 1.4$ mm and 2.6 mm respectively. While the astigmatism has almost no effect for $w_{in} = 1.4$ mm, it strongly modifies the beam shape for $w_{in} = 2.6$ mm. Moreover, the calculation reproduces qualitatively the beam shape observed experimentally for w_{in} = 5.6 mm in panel (c). Work is currently in progress to modify the numerical methods in order to simulate larger beam sizes under the presence of astigmatism.

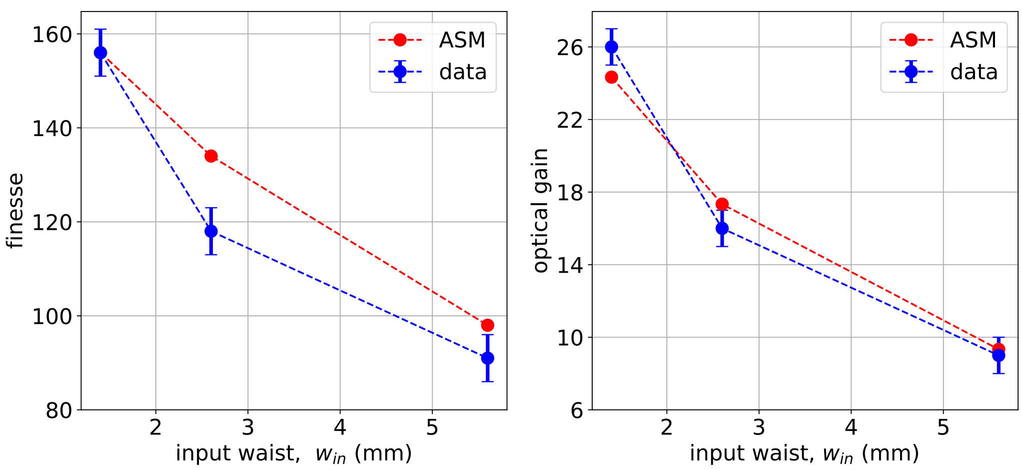

Figure 4.5: **Dependence of the finesse and optical gain on the size of the input beam**. The red points are the result of the numerical calculation based on the angular spectrum method taking into account the measured third order spherical aberration of 1.3λ of the lens. The measurement of the finesse for $w_{in} = 1.4$ mm has been used to adjust the value of the reflection coefficient of the lens, r_L, appearing in Eq. (4.1), yielding $T_L = 1 - r_L^2 = 0.992$.

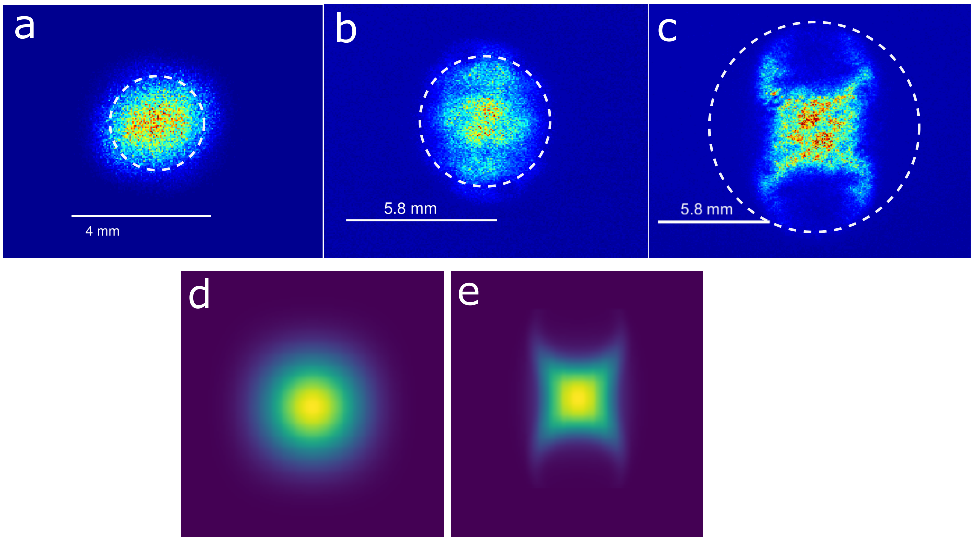

Figure 4.6: **Images of the transmitted beam** for $w_{in} = 1.4$ mm (a), 2.6 mm (b) and 5.6 mm (c). The dashed circles indicate the $1/e^2$ diameter of the input beams. (d) and (e) show the calculated profile on resonance with the angular spectrum method for $w_{in} = 1.4$ mm (d) and 2.6 mm (e), for a value of astigmatism of 0.2λ and a value of third order spherical aberration of 1.3λ.

4.3 Conclusion

In this chapter, I have presented two optical developments aimed at improving the atom-optics efficiency in cold-atom interferometers: generating top-hat laser beams and realizing a large mode optical cavity. The latter project was motivated by the potential interest of using an enhancement cavity for cold-atom interferometers, which requires beam sizes of several millimeters. In that context, reaching an optical gain of 26 for a gaussian beam of 1.4 mm waist in a linear, 44 cm long, cavity already constitutes an encouraging result. Our studies on both developments are still ongoing and I aim at answering the following questions:

- The intensity noise of our top-hat beam is currently 10% rms, while the specified intensity noise of the Asphericon beam-shaper is 6%. These levels are not sufficient to control diffraction phase shifts in LMT interferometers at the mrad level for the interferometer phase. The beam-shaper contains 7 optical elements (14 surfaces), our input collimator 3 simple lenses (6 surfaces) and the expander 2 doublets (8 surfaces). Scattered light from the optics should contribute to the intensity noise. To reduce its level, we anticipate to implement optics of lower rugosity in the collimator and to order a beam shaper with a narrow band coating. We will also study the effect of spectral filtering, which compromises the intensity noise level and the sharpness of the top-hat beam on its edges.
- We are working on the extension of the numerical calculations in order to explain quantitatively the drop of performance in our cavity (optical gain, beam shape distortions) observed at large beam waists, and to derive constraints on the alignment and requirements on the wavefront distortions introduced by the optics. For this purpose, we plan to implement band-limited ASM [111] or grid adaptation techniques [112].
- Owing to its degeneracy, beams of arbitrary shape can in principle resonate in our cavity. I therefore plan to realize a top-hat resonator suited to atom interferometry.

4.3.1 Publications linked with the development of optical systems

1. *Atom interferometry in a marginally stable optical resonator*
   I. Riou, N. Mielec, G. Lefèvre, M. Prevedelli, A. Landragin, P. Bouyer, A. Bertoldi, **R. Geiger**, B. Canuel
   J. Phys. B: At. Mol. Opt. Phys. 50 155002 (2017), Ref. [106]

2. *Système et procédé d'interféromètre atomique à cavité optique résonnante*
   B. Canuel, A. Bertoldi, I. Riou, P. Bouyer, **R. Geiger**, N. Mielec
   French patent FR3054773

3. *Atom interferometry with top-hat laser beams*
   N. Mielec, M. Altorio, R. Sapam, D. Horville, D. Holleville, L.A. Sidorenkov, A. Landragin, **R. Geiger**
   Appl. Phys. Lett. 113, 161108 (2018), Ref. [100]

4. *Study of a compact, large-mode, degenerate optical resonator*
   R. Sapam, N. Mielec, B. Canuel, A. Landragin, **R. Geiger**
   in preparation (March 2019), Ref. [107].

4.3.2 Students and postdocs supervised on the gyroscope-accelerometer experiment.

- Nicolas Mielec, Master and PhD student from March 2015 to September 2018;
- Ranjita Sapam, postdoc from Mai 2016 to July 2018.
- Interns: Enrique Morrell, Nicolas Février.

4.3.3 Funding

This activity was partly funded by the Emergence Programme from the city of Paris (project HSENS-MWGRAV) and additional grants

- a Marie Sklodowska-Curie postdoc grant from the European Commission (for Ranjita Sapam);
- a grant from the FIRST-TF labex for equipment (37 k€);
- a grant from CNES for equipment (40 k€).

Chapter 5

Gravitational wave detection with atom interferometers

5.1 Context, objectives, theory

The detection of gravitational waves (GWs) radiated from merging black holes [113] or neutron stars [114], respectively in 2015 and 2017, by the LIGO and VIRGO collaborations has triggered the field of gravitational wave astronomy. These first observations of the amplitude and phase of GWs occured nearly 100 years after their prediction from the theory of General Relativity (GR), and about 30 years after the demonstration of the existence of GW through the observation of energy loss in a binary pulsar system matching with the prediction of GR [115]. Detecting GWs represent one of the most important scientific discoveries and has been made possible by a tremendous effort of researchers in various communities, both on the experimental and theoretical sides. GW detectors provide a new way to observe the universe and thereby to assess the fundamental laws of Physics. In less than four years, the detection of 11 GW events (as of February 2019, see Ref. [116]) has already shed light on several problems in astrophysics and gravitational physics (see, for example, the LIGO Caltech website [117] for an overview).

Still, the field of GW astronomy is still in its infancy, as one could expect that this new type of astronomy shall bring as many discoveries as brought by the development of new means of observations of electromagnetic waves since the refracting telescopes of the early 1600s. To this end, the broadest spectrum of GWs must be probed, which requires the development of dedicated detectors sensitive in other frequency bands than the current 10 Hz – 2 kHz of terrestrial laser interferometers such as advanced LIGO or VIRGO. The *GW plotter online tool* (Ref. [118]) shows how different methods complement each other and can be used to probe various sources of GWs. The mostly employed methods to date are the Pulsar Timing Array to probe the nHz corner, space-based laser interferometers such as LISA to detect mHz radiation, and third generation terrestrial laser interferometers (such as the Einstein Telescope) improving over aLIGO, aVIRGO or KAGRA.

As I will now explain, detectors based on atom interferometry have the potential to cover the frequency band below 1 Hz and therefore to complement existing or planned optical detectors. I will concentrate on a particular atom interferometer configuration which has retained most attention in the last 10 years, the so-called **long-baseline atom gradiometer configuration**. The introduction of Ref. [119] presents an historical perspective on the field.

Principle and limitations of current laser interferometer detectors in a nutshell. The principle of GW detection by laser interferometers consists in measuring the variation of the relative phase between two electromagnetic waves propagating in an interferometer induced by the strain $h(t)$ of the GW. To ease the interpretation, the effect of the GW is commonly pictured as equivalent to a relative variation of the optical path length $h(t)L$ inducing a variation of phase $\Delta\phi(t) = h(t)kL$ between two waves of wavevector k, where L is the interferometer arm length. This interpretation helps to physically understand the effect of the GW but one has to keep in mind that only the phase difference $\Delta\phi$ is physically meaningful (it is the observable), while L and k are dependent on the choice of coordinate system.

In order to observe the effect of the GW, the optical elements serving as phase reference in the interferometer shall follow geodesics of space-time, i.e. be free falling in the frequency band of interest to the detector (e.g. 10 Hz – 2 kHz). Differential deviations from the free fall (i.e. differential accelerations) translate into equivalent strain noise (in unit of $\text{Hz}^{-1/2}$) and must therefore be mitigated. In other words, spurious forces acting on the interferometer mirrors must be sufficiently reduced. Given the typical strain amplitudes of GWs from the first detections, the strain noise level of the interferometer must be below $10^{-22}/\sqrt{\text{Hz}}$. The reduction of noise sources in advanced LIGO and advanced VIRGO is described in Ref. [120] and [121]. Position noise of the interferometer mirrors requires particular care and originates from several sources, the most important one being the impact of seismic noise for a detector on ground. Above 10 Hz, seismic noise is reduced by 14 orders of magnitude with a sophisticated set of pendulums acting as second order filters above their cutoff frequency. Importantly, the limit at low frequency (few Hz) of terrestrial laser interferometer detectors originates from the difficulty to attenuate the mirrors' position noise at a sufficiently low level. Such limitations are usually of fundamental nature (e.g. thermal noise in the mirrors coatings or in the suspension system, photon shot noise), but can be lowered by technological upgrades (e.g. by using cryogenics, different coatings, squeezed light) as it will be the case in third generation interferometers [122].

The idea behind using atom interferometers for GW detection, in the lines presented below, is to benefit from the inherently free falling nature of the test mass in a cold-atom inertial sensor, in order to alleviate some of the constraints present in laser interferometer detectors at low frequency.

5.1.1 Principle of GW detection with two distant atom interferometers

This section is based on section 2 of the book chapter of Ref. [119]. I recall the calculations for the completeness of the presentation, but the reader can skip the details and go directly to Eq. (5.17) which gives the influence of a GW on the relative phase between two counter-propagating lasers.

Atom interferometer phase shift in the presence of a GW.

I present here a derivation of the light-pulse atom interferometer (AI) phase shift in the presence of a GW. I will concentrate on the effect of the GW on the phase of the lasers, which is impinted on the atomic wavepacket at the diffraction events. I will not consider the effect of the GW on the phase of the atomic waves themselves, as it is negligible compared to the laser induced phase in the configuration which will be considered. I refer, e.g., to Ref. [123] [Eq. (24)] for the full expression with both the laser induced phase and the AI phase contributions.

The scheme of the laser interrogation is shown in Fig. 5.1(a), where the laser beam is retroreflected. I recall that the phase difference between the two arms in the AI essentially originates from the local phase of the lasers which is imprinted onto the diffracted wave-packet at the interaction points [57]. Therefore, the calculation of the AI phase reduces to the calculation of the laser phase of the two counterpropagating beams. I will use the Einstein Coordinates to describe the experiment, where the GW affects the propagation of light and the atoms are freely falling, i.e. used as phase discriminators. The same result is obtained when considering a different coordinate system [123], [124].

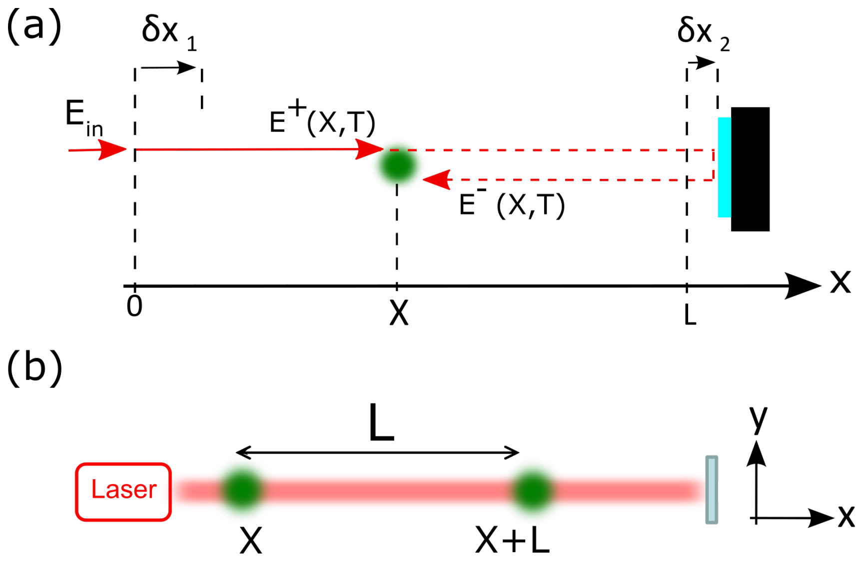

Figure 5.1: (a) Laser interrogation scheme and notations used in the calculation of the AI phase shifts. $\delta x_1(t)$ and $\delta x_2(t)$ are the position fluctuations of the input optics and of the retroreflecting mirror with respect to the fixed baseline L, respectively. (b) Gradiometer configuration: two distant AIs (green clouds) are interrogated by the same laser beam.

(a) Calculation of the phase of the lasers. I decompose the electromagnetic field as a superposition of two counterpropagating waves, $E^{\pm}(t)$, respectively propagating towards positive and negative x (see Fig. 5.1(a)). The AI phase shift is determined by the *relative* phase between $E^{+}(t)$ and $E^{-}(t)$, which is imprinted on the atoms at position X. I will determine this relative phase as a function of the mirror position, the frequency of the laser, and the gravitational wave (GW) amplitude.

I consider the effect of a GW propagating in the direction perpendicular to the plane of Fig. 5.1 and polarized along the laser propagation direction (x). I describe the propagation of electromagnetic (EM) waves in the x direction. The relativistic invariant is given by [125]:

$$ds^2 = c^2dt^2 - dx^2 + h(t)dx^2 = 0, \tag{5.1}$$

where $h(t)$ is the amplitude of the GW. For weak GW, the solution is

$$dx = \pm[1 + \frac{1}{2}h(t)]cdt, \tag{5.2}$$

where the plus (minus) sign corresponds to the light propagating from left to right (right to left). The EM wave is emitted at time t^+ from the left input optics (position $\delta x_1(t^+)$) and arrives at time T at the position X, where it interacts with the atoms. The emission time t^+ is given from the integration of Eq. (5.2) by the following equation:

$$\int_{\delta x_1(t^+)}^{X} dx = c[T - t^+] + \frac{c}{2}\int_{t^+}^{T} h(t)dt. \tag{5.3}$$

Using perturbation theory with $t^+ \approx T - X/c$, we obtain at first order in $(\delta x_1, h)$:

$$t^+ \approx T - \frac{X - \delta x_1(T - \frac{X}{c})}{c} + \frac{1}{2}\int_{T-\frac{X}{c}}^{T} h(t)dt. \tag{5.4}$$

In a similar way, we can obtain the emission time t^- of the EM wave which propagates to the right mirror, is reflected, and propagates back in opposite direction to arrive at position X at time T, where it interacts with the atoms. Taking into account the propagation from the right mirror to the atoms, t^- is given by:

$$t^- = T - \frac{1}{c}[2L - X + 2\delta x_2(T - \frac{L-X}{c}) - \delta x_1(T - \frac{2L-X}{c})] + \frac{1}{2}\int_{T-\frac{2L-X}{c}}^{T} h(t)dt. \tag{5.5}$$

At the space-time event (X, T), the atoms interact with two counterpropagating fields $E^{\pm}(X, T)$, which we define by

$$E^{\pm}(X, T) \equiv E(t^{\pm}). \tag{5.6}$$

The relative phase $\Delta\varphi = \varphi^+ - \varphi^-$ imprinted on the atoms during the atom diffraction is thus determined by the time delay $t^+ - t^-$ between the two emission events, which is obtained from Eqs. (5.4) and (5.5) .

I now consider only slow fluctuations of $\delta x_i(t)$ and $h(t)$ corresponding to frequencies $\omega/2\pi \ll (2L/c)^{-1}$ (50 kHz for a baseline of 3 km). In particular, I neglect the position fluctuations on a time-scale smaller than the light round-trip time from the atoms to the retroreflecting mirror. This condition can be ensured by the use of a dedicated suspension system of the optics. In this approximation the fluctuations in Eqs. (5.4) and (5.5) are evaluated at time T and become:

$$t^+ \approx T - \frac{X}{c} + \frac{\delta x_1(T)}{c} + \frac{X}{2c}h(T) \tag{5.7}$$

$$t^- \approx t^+ - \frac{2(L-X)}{c} - \frac{2\delta x_2(T)}{c} + \frac{2(L-X)}{2c}h(T). \tag{5.8}$$

To account for laser phase noise, I write the EM field as

$$E(t) = E_{in}(t)e^{i\alpha(t)} \tag{5.9}$$

where $E_{in}(t)$ is the amplitude of the EM field just after the input optics and

$$\alpha(t) = 2\pi\nu_0 t + \tilde{\phi}(t) \tag{5.10}$$

is the laser phase. Here ν_0 is the injection laser frequency and $\tilde{\phi}(t)$ is the laser phase noise. Assuming that the phase noise is small and slowly varying, it can be expressed as

$$\tilde{\phi}(t + \Delta t) \approx \phi_0 + 2\pi\delta\nu(t)\Delta t, \tag{5.11}$$

where $\delta\nu(t)$ is the frequency noise of the laser. This approximation is valid as long as Δt is smaller than the typical inverse bandwidth of the noise, meaning that in a sufficiently small region of time around t, the phase is proportional to the instantaneous frequency $(\nu_0 + \delta\nu(t))$ of the laser field.

With this model for the phase noise, I obtain the following expression for the EM field at the point of interaction with the atoms:

$$E^+(X, T) \equiv E(t^+) = E_{in}(t^+)e^{i\alpha(t^+)}, \tag{5.12}$$

with

$$\alpha(t^+) \approx 2\pi\nu_0 t^+ + \phi_0 + 2\pi\delta\nu(T)(t^+ - T). \tag{5.13}$$

Using the above equation for t^+, I thus obtain:

$$E^+(X, T) \approx E_{in}(T)e^{2i\pi T[\nu_0 + \delta\nu(T)] + i\phi_0}e^{i\varphi^+(X,T)} \tag{5.14}$$

with

$$\varphi^+(X, T) = -\frac{2\pi\nu_0}{c}X + \frac{2\pi\nu_0}{c}\delta x_1(T) + \frac{2\pi}{c}[-\delta\nu(T) + \frac{\nu_0}{2}h(T)]X. \tag{5.15}$$

From now on, I will omit the time argument (T) in the variables $\{\delta x_i, \delta\nu, h\}$ for clarity of the equations. A similar calculation for the E^- field yields the phase

$$\varphi^-(X) = -\frac{2\pi\nu_0}{c}(2L - X) + \frac{2\pi\nu_0}{c}[\delta x_1 - 2\delta x_2] + \frac{2\pi}{c}[-\delta\nu + \frac{\nu_0}{2}h](2L - X). \tag{5.16}$$

The relative phase $\Delta\varphi = \varphi^+ - \varphi^-$ imprinted on the atoms during the diffraction is thus:

$$\Delta\varphi(X) = 2k\left[(L - X) + \delta x_2 + \left[\frac{\delta\nu}{\nu_0} - \frac{h}{2}\right](L - X)\right], \tag{5.17}$$

where $k = 2\pi\nu_0/c$ is the laser wavevector. **In the retroreflecting configuration, the position noise δx_1 of the input optics is common to both beam and is therefore not present in Eq. (5.17).**

(b) Sensitivity function of the atom interferometer. The AI phase is determined by the relative phase of the EM fields given by Eq. (5.17), and by the sensitivity function $s(t)$ of the three light-pulse AI, as introduced in Ref. [59] and in chapter 3.

Besides the sensitivty function, AIs operate sequentially and deliver a measurement every cycle of duration $T_c = T_{\text{prep}} + 2T + T_{\text{det}}$ during which the atoms are prepared (e.g. laser cooled during a period T_{prep}), interrogated in the AI (duration $2T$) and detected at the AI output (duration T_{det}). The AI output signal at cycle m is then given by the convolution product

$$s_\varphi(X, mT_c) = \Delta\varphi(X, t) \otimes s(t - mT_c), \tag{5.18}$$

with $s(t) \approx \delta(t - 2T) - 2\delta(t - T) + \delta(t)$ and $\delta(t)$ the Dirac distribution. For simplification, I neglected in this expression of the sensitivity function the finite duration of the light pulse (the full expression can be found in [59]). This approximation corresponds to neglecting the phase fluctuations (e.g. due to $\{\delta x_i(t), \delta\nu(t), h(t)\}$) of frequencies higher than the Rabi frequency of the two-photon transition, which typically lies in the tens of kHz range.

(c) Full expression of the AI phase. Using Eqs. (5.18) and (5.17), the output signal of the AI at cycle m reads

$$s_\varphi\left(X, mT_c\right) = 2k\left[-\delta x\left(X, t\right) + \delta x_2(t) + \left(\frac{\delta\nu(t)}{\nu_0} - \frac{h(t)}{2}\right)(L - X)\right] \otimes s(t - mT_c). \tag{5.19}$$

Here, $\delta x(X, t)$ represents the relative motion of the atoms along the laser beam direction due to the fluctuations of the local gravitational acceleration. This contribution corresponds to the first term $2k(L - X)$ appearing in Eq. (5.17) which I rewrote as follows for more clarity: *(i)* as L is a constant, it does not contribute to the AI signal and disapears ; *(ii)* to highlight the fact that X might fluctuate because of temporal variations of the local gravitational field in the x direction, I change for the notation $\delta x(X, t)$. I will focus on this contribution below when discussing gravity gradient noise reduction techniques 5.1.2.

Gradiometer configuration

I now consider the gradiometer configuration sketched in Fig. 5.1(b). Taking the differential signal $\psi(X, mT_c) = s_\varphi\left(X, mT_c\right) - s_\varphi\left(X + L, mT_c\right)$ between two AIs separated by the distance L yields:

$$\psi(X, mT_c) = 2k\left[L\left(\frac{h(t)}{2} - \frac{\delta\nu(t)}{\nu_0}\right) + \delta X\left(X + L, t\right) - \delta X\left(X, t\right)\right] \otimes s(t - mT_c). \tag{5.20}$$

This equation can be rewritten in terms of the local gravity acceleration as

$$\psi(X,mT_c) = 2k\left[L\left(\frac{\ddot{h}(t)}{2} - \frac{\delta\ddot{\nu}(t)}{\nu_0}\right) + a_x\left(X+L,t\right) - a_x\left(X,t\right)\right] \otimes s_\alpha(t-mT_c) \tag{5.21}$$

where $a_x(X,t) = \partial_t^2[\delta x(X,t)]$ is the local gravity acceleration in the x direction and $s_\alpha(t)$ is the AI sensitivity function to acceleration, given by $\ddot{s}_\alpha(t) = s(t)$.

The very important aspect in this equation is that the position noise $\delta x_2(t)$ of the retroreflecting mirror has been rejected by the gradiometer configuration. To be more precise, position fluctuations of frequencies smaller that $(2L/c)^{-1}$ are rejected, which represents the major part of the position noise in optical GW detectors. Rejection of the vibration noise in gradiometer configuration has already been measured in AIs (rejection by 140 dB was demonstrated in [126]). This important immunity to position noise of the AI gradiometer makes such instruments good candidates for GW detectors operating at lower frequencies than ground based optical interferometers, which sensitivity are limited at frequencies below ~ 10 Hz by position noise of the optics (vibration noise, thermal noise, etc).

Eq. (5.21) also shows that fluctuations of the local gravity field result in an acceleration signal $a_x(X,t)$ whose spatial gradient will have the same signature as that of the GW. **Therefore, it is impossible to distinguish the effect of a GW from that of a fluctuating gravity gradient with such an observable: Fundamentally, a gravity gradient and a GW induce equivalent strain effects**. This equivalence at a fundamental level can be made more clear with a general relativistic treatment of the gravity gradient, as shown for example in the PhD thesis of P. Delva (comparing equations (2.71) and (2.87)). This limitation to GW detection is known as the gravity gradient noise limit, or Newtonian Noise limit, and has been raised at the early stages of the set up of ground-based optical detectors [127].

Quantum limited strain sensitivity curve

To illustrate the potential performance of the AI detector, I will assume in this paragraph that the detector is limited by the quantum noise, i.e. neglect the contribution of laser frequency noise and Newtonian noise which appear in Eq. (5.21). The power spectral density (PSD) of the gradiometer output is then given by

$$S_\psi(\omega) = (2nkL)^2\omega^4\frac{S_h(\omega)}{4}|\hat{s}_\alpha(\omega)|^2 + 2S_\phi(\omega), \tag{5.22}$$

where S_h is the PSD of the GW, S_ϕ is the PSD of the AI phase noise (the factor 2 accounts for the 2 AIs involved in the gradiometer), and $\hat{s}_\alpha(\omega) = \mathrm{FT}[s_\alpha(t)] = 4\sin^2\left(\omega T/2\right)/\omega^2$ is the Fourier transform of the sensitivity function of a 3 pulse AI.

The factor n in Eq. (5.24) denotes the number of momenta transfered to the atom during the diffraction process, which amplifies the phase signal by a factor of n. It is analogous to the use of Fabry-Perot cavities which amplify the phase signal in laser interferometers. Such process called large momentum transfer (LMT) beam splitters is now frequently used in AI experiments to enhance the sensitivity of the interferometer (AIs with $n = 100$ have been reported).

The phase noise PSD for an AI limited by quantum noise can be written as

$$S_\phi(\omega) = \frac{\eta}{\dot{N}_{at}}\left(\frac{\mathrm{rad}^2}{\mathrm{Hz}}\right) \tag{5.23}$$

where $\dot{N}_{at}$ is the cold atom flux (in s^{-1}) and $\eta \leq 1$ is a factor which accounts for a possible measurement noise reduction with respect to the standard quantum limit ($\eta \approx 0.01$ has ben reported in [128]). If we consider a minimum sensitivity with a signal to noise ratio of 1, we obtain the strain sensitivity function:

$$\left(S_h\left(\omega\right)\right)^{1/2} = \left(\frac{2\eta}{\dot{N}_{at}}\right)^{1/2} \frac{1}{4Lnk\sin^2\left(\omega T/2\right)}. \tag{5.24}$$

I plot in Fig. 5.2 the strain sensitivity function for various parameters of the AI gradiometer. The blue line corresponds to an optimized AI combining several state of the art techniques, i.e. with a phase noise of $10^{-6}\ \frac{\mathrm{rad}^2}{\mathrm{Hz}}$, a 20 photon LMT beam splitter ($n = 10$), and a gradiometer baseline $L = 1$ km. The red curve corresponds to the much more ambitious scenario which could be obtained in the future with $10^{-14}\ \frac{\mathrm{rad}^2}{\mathrm{Hz}}$ phase noise, $n = 1000$ and $L = 10$ km. In both cases, I considered an interrogation time $2T = 0.6$ s, which determines the frequency $f_0 = 1/2T$ corresponding to the minimum of the sensitivity curve. Such interrogation time is typical and would allow to cover the frequency band $\sim 0.1 - 10$ Hz. Using longer interrogation times T does not change the value of the peak sensitivity but shifts the operating bandwith to lower frequencies. Long (> 10 s) interrogation times in AIs using ultracold atoms (temperature < 10 nK) could then be used to design space-based detectors operating in the mHz regime [129]. Finally, I neglected here the sequential operation of the AI, i.e. I neglected the possible aliasing effects due to the finite sampling period T_c of the AI. The interleaving technique presented in chapter 3 is a promising way to speed up the sampling rate in AIs without compromising their interrogation time.

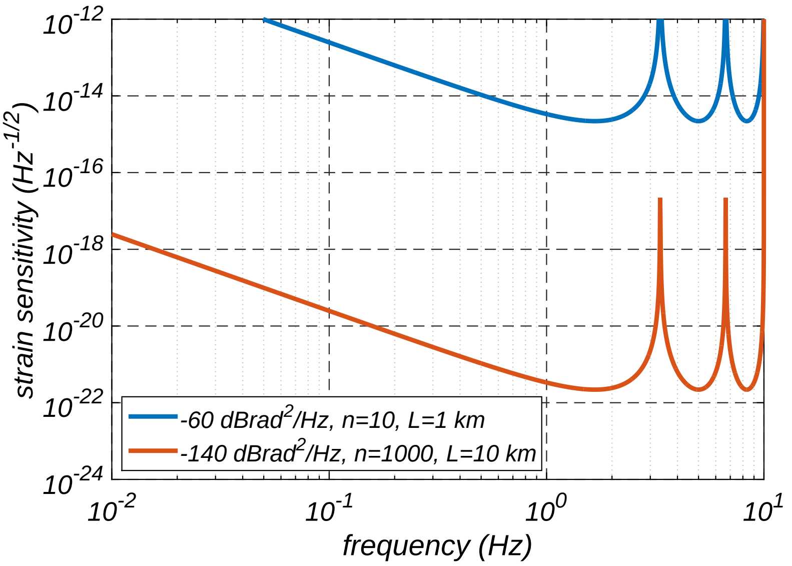

Figure 5.2: Quantum limited strain sensitivity curve of the GW detector for different parameters of the AI gradiometer: basic configuration (blue) and advanced configuration (red). In both cases $T = 0.3$ s.

5.1.2 Beating the Newtonian noise limit with an array of atom interferometers

As shown by Eq. 5.21, the effect of the GW cannot be distinguished from that of a fluctuating gravity gradient by using two AIs. This problem is similar to optical GW detectors which use two test masses (the two cavity mirrors of one interferometer arm). This fundamental limit for GW detectors operating on Earth in known as the Newtonian Noise (NN) limit. For ground based detectors, it represents a fundamental limit which prevents from observing GW at frequencies below few Hz, because the NN starts to dominate at these frequencies [127], [130].

NN originates from density fluctuations in the surrounding of the detector, which translate in gravity field fluctuations at the position of the test masses. Sources of NN are, for example, seismic noise triggerring stochastic fluctuations of the ground density and resulting in fluctuations of the gravity field (so called seismic NN), or air density fluctuations in the atmosphere caused by turbulence (so called infrasound NN).

Through a collaboration with Walid Chaibi from Observatoire de la Côte d'Azur, we proposed a method to go beyond the NN limit in GW detectors based on atom interferometry [70]. The method relies on the fact that the spatial properties of the NN are different than the spatial properties of the GW: while the wavelength c/f of the GW at $f = 1$ Hz is 3×10^8 m, the characteristic correlation length $v/2f$ of the NN at such frequency is of order 1 km [127] (v is the velocity of seismic waves for the seismic NN, or the speed of sound in air for infrasound NN). Therefore, by operating an array of spatially distributed AI gradiometer interrogated by the same laser beam, it is possible to average the NN to zero. This idea is sketched in Fig. 5.3.

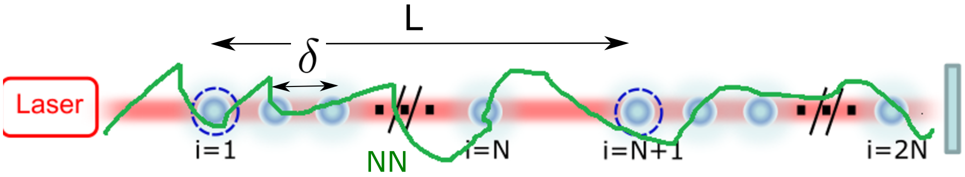

Figure 5.3: Principle of the rejection of the Newtonian Noise (NN) with an array of spatially distributed AIs. L is the gradiometer baseline and δ is the spatial sampling period.

More precisely, the detector consists of N gradiometers of baseline L, which sample the NN with a spatial step δ. The average signal reads

$$H_N(t) = \frac{1}{N}\sum_{i=1}^{N}\psi(t, X_i), \tag{5.25}$$

with $\psi(X)$ given by Eq. (5.21). This procedure yields the GW signal and a residue of the NN which standard deviation is reduced by $\sqrt{N}$ compared to the single gradiometer case, if the N measurements are uncorrelated. Using the spatial behavior of the NN correlation function, we showed that a rejection of the NN greater than $\sqrt{N}$ can be obtained. For a scenario with $N = 80$, we showed that rejection efficiencies of up to 30 for the infrasound NN could be achieved at 1 Hz.

Comparison with other GW detectors.

The window opened by the AI array proposition described in Ref. [70] would enable to cover the frequency band between LISA and third generation ground based laser interferometers, as shown in Fig. 5.4. The parameters of the AI detector (red line) are those of Ref. [70]: a phase noise level of 10^{-7} rad/$\sqrt{\text{Hz}}$, LMT beam splitters with $n = 1000$ and a gradiometer baseline $L = 16$ km. The quantum noise is moreover reduced by a factor $\sqrt{N}$ thanks to the array of N gradiometers. In Fig. 5.4, we show strain sensitivity functions for different detectors (plain lines) and simple estimates for the GW signal (dashed lines) corresponding to compact binaries as sources of the GW. We parametrized the binaries by the mass of the stars and their luminosity distance, and assumed a detection with signal to noise ratio of 1. To obtain the estimate of the signal strength for the compact binary, we followed the simple model of [133] [Eq.(11) to (18)] yielding

$$\sqrt{[S_h(\omega)]} \simeq 0.3 \times \eta^{1/2} c^{-3/2} f^{-2/3} (GM)^{5/6} r^{-1} \tag{5.26}$$

with $\eta = m_1 m_2/M^2$ the symmetric mass ratio ($M = m_1 + m_2$), f the GW frequency and r the luminosity distance.

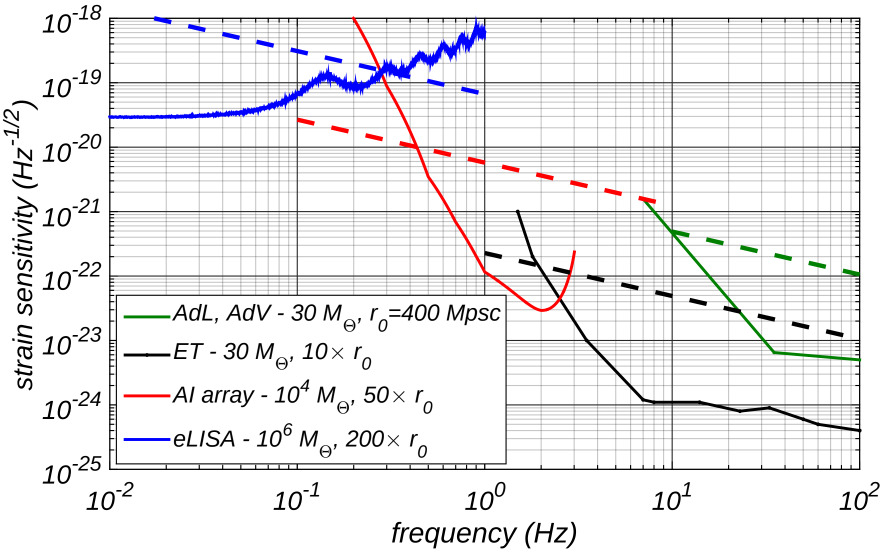

Figure 5.4: From [119]. Strain sensitivity curves of current and possible future GW detectors (plain lines). Dashed lines indicate the required senitivity to detect the GW from a compact binary following Eq. (5.26); M_Θ is the mass of the sun and $r_0 = 400\ Mpsc$. We assumed a detection with a signal to noise ratio of 1. AdV: Advanced VIRGO [121], AdL: Advanced LIGO [120]; ET (Einstein Telescope) [131]. eLISA [132] is a space-based laser interferometer proposal. The AI array is the proposal [70].

While the arguments presented so far motivate the development of detectors based on atom interferometry for sub-Hz GW astronomy, current atom interferometry sensors feature performances which are far from the expected one illustrated in Fig. 5.4. Demonstrators at small scale must therefore be set up and new techniques investigated. The MIGA project, which I will now describe, targets these objectives.

5.2 The Matter wave laser Interferometric Gravitation Antenna (MIGA) project

5.2.1 General description of MIGA

The MIGA project started in 2013 with an initial funding from the French national research agency (ANR), and involves 15 laboratories with expertise in atomic physics, metrology, gravitational physics and geosciences. The goal of the project is to design and realize an instrument capable of serving as a demonstrator for a future GW detector based on atom interferometry. The instrument will also be used for precision gravity field measurements, with important applications in geosciences, in particular hydrology [134]. The initial idea of the instrument is based on the gradiometer configuration described in the previous section, with a baseline $L = 150$ m, and the possibility to correlate several AIs interrogated by the same laser beam. Ref. [135] presents in details the project and the subsystems. I will briefly describe here the main elements of the instrument.

Fig. 5.5 shows the geometry of the MIGA instrument where the optical mode of two optical cavities interrogate simultaneously 3 AIs seperated by a distance of 75 m. The optical cavity will allow to enhance the optical power at the cavity resonance by the optical gain ($\simeq 10$ in the initial design) in order to improve the efficiency of LMT beam splitters which require large laser

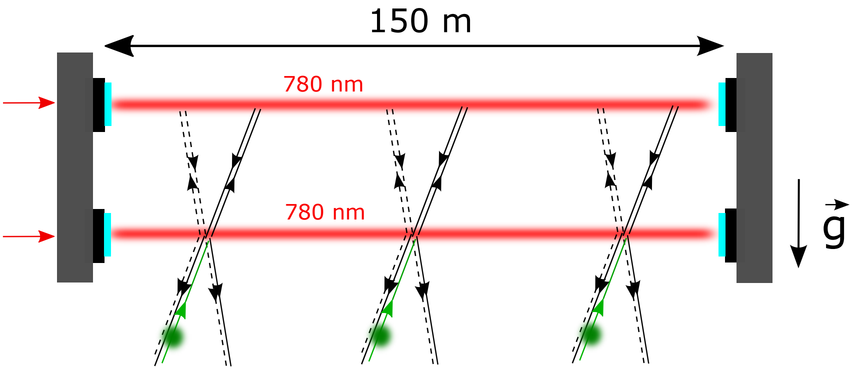

Figure 5.5: **Geometry of the MIGA instrument** (not to scale). The atoms are launched from below from the magneto-optical trap (not shown). Bragg diffraction on lasers resonating in an optical cavity is used as matter-wave optics, which requires to enter the AI with the correct (Bragg) angle with respect to the (horizontal) direction of the cavity beam (the Bragg angle is exaggerated here for clarity). The interrogation time is $2T = 500$ ms for a 3 light-pulse AI with apogee of the atom trajectory at the top beam.

powers [136]. The length of the cavity will be stabilized using an external pre-stabilized 1560 nm wavelength laser (laboratory in charge : CELIA, Bordeaux). The AIs use Bragg diffraction of ^{87}Rb on the light standing wave in the cavity (wavelength 780 nm), where momentum states $|-n\hbar k\rangle$ and $|+n\hbar k\rangle$ are coupled by the (high order) Bragg diffraction. LMT beam splitters with n up to 5 are initially planned for atom sources with temperature in the μK range.

The instrument will be installed at the low noise underground laboratory LSBB loacted in the South-East of France [137], see Fig. 5.6. Two 150 m galleries will be dug dedicate for the detector. Besides the vacuum tube, the optical systems and the AI sensors, various environmental instruments are deployed in order to monitor the hydrological environment around the detector and assess applications in hydrology: one superconducting gravimeter, an array of several seismometers, a mobile broadband radar and muon detectors.

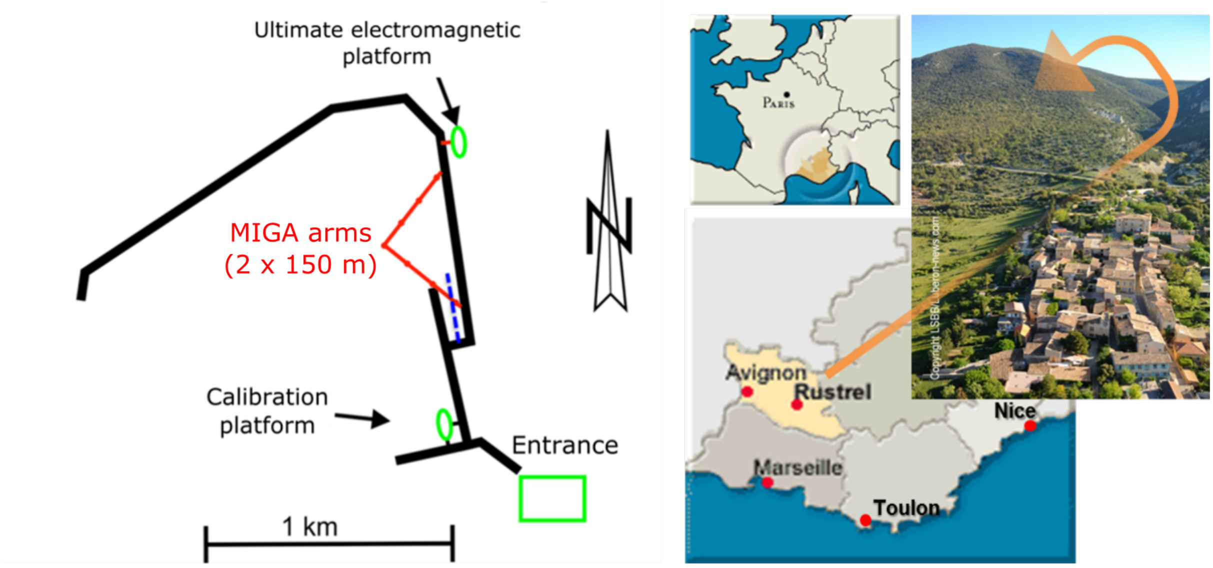

Figure 5.6: Installation site of the MIGA instrument at the low noise underground laboratory in the South-East of France.

While the MIGA instrument has not been designed for GW detection applications because of its relatively small (150 m) baseline and the lack of maturity of cold atom technology at the start of the project, it will serve as a first demonstrator for a future larger detector, at the European or international scale. Among the first tests which will be performed, correlations between distant AI sensors, gravity gradient measurements at the $10^{-13}\ \mathrm{s}^{-2}/\sqrt{\mathrm{Hz}}$ level, and validation of the state of the art AI technology in a large detector will have an important impact on the design of a future instrument. Of particular interest will be the characterization of the infrasound gravity gradient noise, which we plan to resolve by averaging differential AI measurements during few hours, as described in Ref. [138].

5.2.2 Cold-atom interferometer systems realized at SYRTE

My primary role is to coordinate the design and the realization of an important subsystem of MIGA, the cold-atom fountains. More precisely, the role of SYRTE in the MIGA collaboration is to deliver 5 systems with the following functionalities: preparation of a source of cold ^{87}Rb atoms, preparation of the quantum state of the atoms (magnetic sub level and velocity class) before the interferometer, detection of the output momentum state of the atom after the Bragg interferometer. Five systems were planned: 3 for the LSBB, and 2 for the 6 m gradiometer prototype based at the LP2N laboratory in Talence. A view of the system is presented in Fig. 5.7.

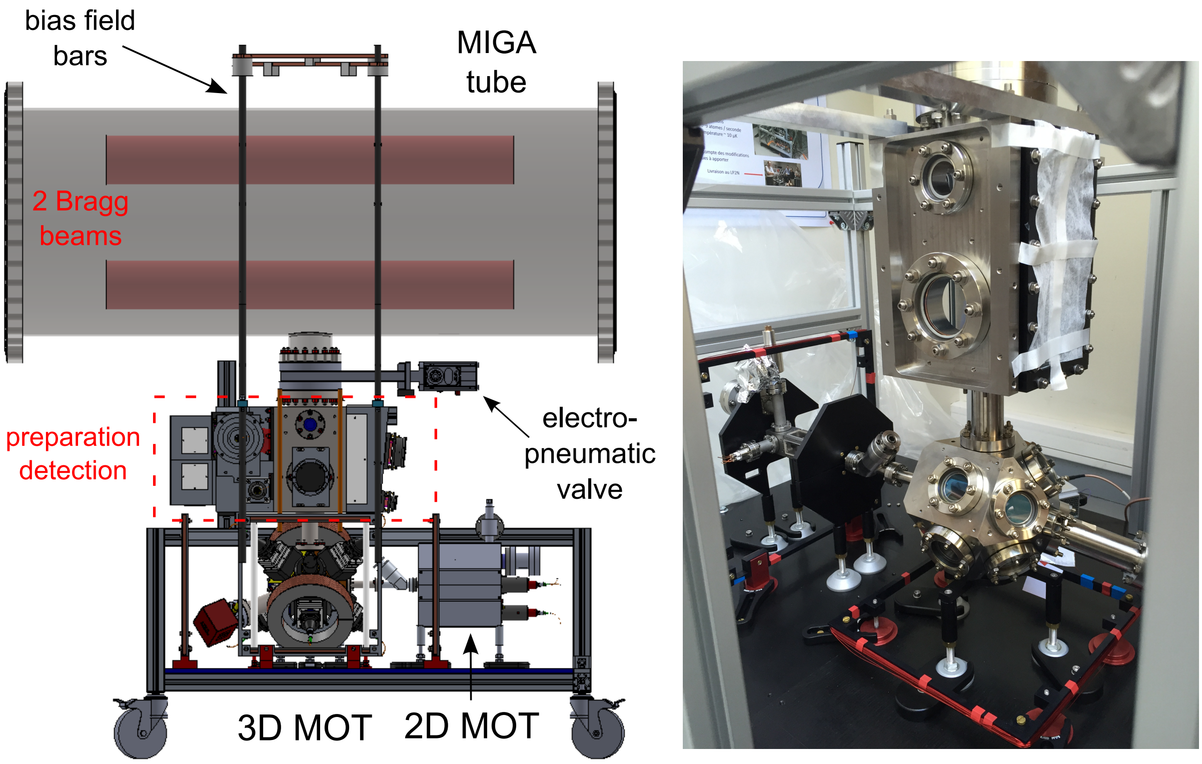

Figure 5.7: **Cold-atom interferometer systems realized at SYRTE.** Left: Global view of the cold-atom interferometer fountain. Right: Photograph of the vacuum system (with the 2D MOT on the left).

Preparation of the atoms before the interferometer.

In order to optimize the contrast of the interferometer, the quantum state of the atoms is prepared on their way up, before the interrogation region. A first counter-propagating velocity-selective Raman pulse (beam 'Raman 1' in Fig. 5.8) is used to select the atoms in the $m_F = 0$ Zeeman sub-level of the $F = 2$ hyperfine state, with a relatively narrow velocity class (e.g. width of 1 photon recoil, corresponding to a temperature of ≈ 400 nK in the direction of the Raman lasers). The atoms which are not transfered to $|F = 1\rangle$ by the Raman transition are then pushed by a laser tuned on resonance with the cycling transition ('push 1' in Fig. 5.8). This Raman/push procedure is repeated a second time to clean the remaining unwanted atoms produced by spontaneous emission on the first Raman selection pulse. For this purpose, we use a second Raman light pulse ('Raman 2') which slightly is more velocity selective than the first Raman beam to transfer the atoms back to the $F = 2$ state with a narrower velocity distribution. The remaining atoms in the $F = 1$ state are pushed with an orthogonal beam tuned on the $F = 1 \rightarrow F' = 0$ transition ('push 2').

The angle of the Raman beams with respect to the direction perpendicular to gravity is set to few degrees in order to introduce a Doppler effect and thus lift the degeneracy between the $|p\rangle \rightarrow |p + 2\hbar k\rangle$ and $|p\rangle \rightarrow |p - 2\hbar k\rangle$ transitions. In this way, the atoms will enter the interferometer in a well-defined momentum state. The atoms must enter the interrogation region with a well defined velocity in order to fulfill the resonance condition in the Bragg interferometer where the laser beams are horizontal (wavevector $\vec{k} = k\vec{e}_x$). For a $2n\hbar k$ transition coupling the momentum states $|\vec{p}_0\rangle \rightarrow |\vec{p}_0 + 2n\hbar\vec{k}\rangle$, the input momentum must fulfill $p_{0x} = -n\hbar k$. The vertical velocity at the first Bragg pulse is $gT \simeq 2.5$ m.s^{-1}, resulting in an angle $\theta = n\hbar k/MgT \simeq n \times 3.2$ mrad of the atom trajectory with respect to gravity. The control of this angle can be obtained by adjusting the ratios of intensity or the directions of the 3D MOT Raman beams. Alternatively, a non-zero horizontal velocity class can be selected with the two step Raman selection by using different two-photon detunings for the 'Raman 1' and 'Raman 2' beams, at the cost of a loss of atoms.

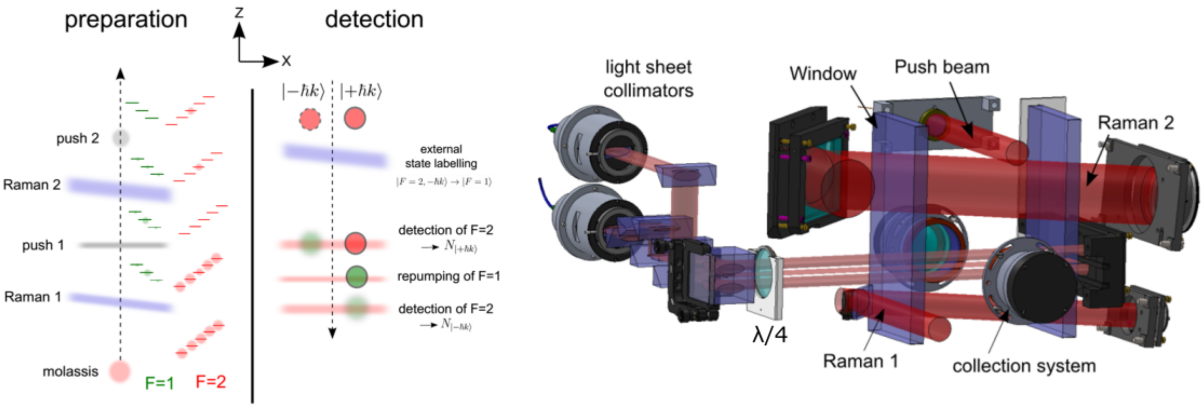

Figure 5.8: **MIGA detection system.** Left: principle. Right: view of the optomechanical system. A homogeneous bias magnetic field is applied along the direction of the Raman and detection beams.

Detection system.
After their interrogation by the Bragg beams in the interferometer, the two different momentum states $|\pm n\hbar k\rangle$ of the atoms are labeled to two different internal states with the 'Raman 2' laser beam. More precisely, the velocity selective feature of the Raman transition is used to transfer the $|F = 2, n\hbar k\rangle$ atoms to the $F = 1$ internal state, while the $|F = 2, -n\hbar k\rangle$ atoms remain in the $F = 2$ internal state. The internal state of the atoms can then be resolved by fluorescence detection, in a similar way as used in the gyroscope-accelerometer presented in chapter 3. Detection of the atoms labeled in $F = 2$ is first realized with a light sheet beam (see Fig. 5.8) tuned on resonance on the $F = 2 \rightarrow F' = 3$ transition. The beam is partially blocked at the retroreflection mirror so that the atoms acquire a net momentum in the beam direction and will therefore not be resonant with the following light beams. The $F = 1$ atoms are re-pumped to the $F = 2$ state using a thinner intermediate light sheet, before these $F = 2$ atoms enter the third light sheet. The fluorescence light emitted by the atoms in the two light sheets is collected by a 2% collection efficiency lens and imaged on a two-quadrant photodiode. The fluorescence signal is used to reconstruct the normalized atomic populations and then the

transition probability, yielding the AI phase.

Laser System.
The different lasers used to cool and manipulate the atoms are delivered from an all-fibered laser module developed by the company μQuans [139]. The laser architecture is based on frequency doubled telecom lasers. A Master laser is locked using a Rubidium 85 saturated absorption spectroscopy signal and references 3 slave lasers which are respectively used for the 2D MOT cooling laser, the 3D MOT cooling/Raman 2 laser, and the 3D MOT repumper/Raman 1 laser. The 3 slave lasers are all phase locked to the Master laser. The repumping light for the 2D MOT is generated by a fiber electro-optic phase modulator at 1560 nm fed with the appropriate microwave frequency.

After amplification of the 1560 nm light emitted by laser diodes in Erbium doped fiber amplifiers and second harmonic generation in PPLN waveguide cristals, the 780 nm light is sent to optical splitters and guided to the experiment chamber using several optical fibers. The laser module nominally delivers 300 mW total power for the 2D MOT, 150 mW total power for the 3D MOT, 350 mW in the Raman 1 beam and up to 700 mW in the Raman 2 beam. The relative power and polarization fluctuations at the fiber outputs have been measured to be below one percent rms on a timescale of 100 hours. The phase lock signals are controlled by radio and microwave frequency sources all referenced to a stable 100 MHz quartz oscillator. The full laser system is hosted in a $1.7 \times 0.5 \times 0.5$ m^3 transportable rack.

Status.
The design of the first system was elaborated by Louis Amand from summer 2013 to mid 2014. The vacuum system was then prepared in 2014, followed by the characterizations of the laser systems (in particular the fiber splitters) and of the control system (realized at LP2N), and the setup of the optomechanical systems. The MOT was obtained in January 2015, followed by a preliminary characterization of the launching phase and detection system. A magnetic shield hosting the system and a 2.4 meter portion of the tube above the fountain was also designed and realized. For this first system, the choice was made to deliver it as soon as possible (June 2015) to LP2N such that they could start to interface the fountain with a 1 m test optical cavity. Since 2016, we have entered the 'production phase' of the systems, i.e. the ordering and realization of the 4 subsequent fountains. Upgrades to the laser system (in particular the fiber splitters) and the fountain design have been operated, on the basis of problems identified in the first prototype.

5.3 Conclusion and perspectives

Atom interferometry represents an interesting perspective for GW detection below few Hz, by using free falling atom clouds as the probes to measure the relative optical phase shift induced by a GW on a laser beam traveling between two distant points. I have concentrated my research since 2013 on terrestrial GW detection with alkaline atoms. The MIGA instrument is a prototype of GW detector using standard cold atom technology and a moderate baseline of 150 m, with the aim to achieve strain sensitivities of $10^{-13}/\sqrt{\text{Hz}}$ at 2 Hz by 2022. Advanced versions of MIGA (with $10^{-15}/\sqrt{\text{Hz}}$ sensitivity) envisioned for 2027 should allow us to characterize the gravity gradient noise, which represents a fundamental problem for ground based detectors.

Reaching the strain sensitivities below $10^{-20}/\sqrt{\text{Hz}}$ level at 1 Hz that are interesting to GW astronomy is a challenge, which will require dedicated studies. The MIGA consortium and particularly SYRTE is engaged in a proposal for a design study intended to be supported by the European Union and gathering the main European actors in atom interferometry and GW detection (ELGAR project - European Laboratory for Atom interferometric Research). Among the numerous aspects to be studied, our team at SYRTE will be particularly engaged in the metrological study of atom interferometers, i.e. the understanding of systematic effects so far unexplored in the target sensitivity range for atom interferometers (phase sensitivity below the $\mu\text{rad}/\sqrt{\text{Hz}}$ level). Future GW detectors based on the architecture presented in this chapter will need to feature large fluxes (10^{12} ultracold atoms per second) and high order LMT atom optics ($n \sim 1000$). Whether these performances will be reached or not is an open question that deserves to be investigated, given the impact that atom interferometry could have on other fields (for example, gravity gradiometry for early Earthquake warning systems [140]).

Much interest has been drawn towards interferometers using alkaline-Earth atoms and single photon transitions on their clock transitions to alleviate the requirements on the laser frequency stability. Several proposals for space based mission have been put forward in this context [71], [141]–[143], as a possible way to complement planned space-based detectors such as LISA. While being difficult from the technological point of view [144], the long baselines offered by space ($\sim$ 100 km) reduces the need for high order large momentum transfer atom optics and atom flux that have not been demonstrated so far. This type of atom interferometry with alkaline-Earth atoms has started recently [95], [145] and is expected to attract more and more interest in a near future.

5.3.1 Publications related to my research on gravitational wave detection

1. *Characterizing Earth gravity field fluctuations with the MIGA antenna for future Gravitational Wave detectors*
   J. Junca, A. Bertoldi, D. O. Sabulsky, G. Lefèvre, X. Zou, J.-B. Decitre, **R. Geiger**, A. Landragin, S. Gaffet, P. Bouyer, and B. Canuel
   submitted to Phys. Rev. D (2019), Ref. [138]

2. *Exploring gravity with the MIGA large scale atom interferometer*
   B. Canuel, A. Bertoldi, L. Amand, E. Borgo di Pozzo, B. Fang, **R. Geiger**, J. Gillot, S. Henry, J. Hinderer, D. Holleville, G. Lefèvre, M. Merzougui, N. Mielec, T. Monfret, S. Pelisson, M. Prevedelli, S. Reynaud, I. Riou, Y. Rogister, S. Rosat, E. Cormier, A. Landragin, W. Chaibi, S. Gaffet, P. Bouyer
   Scientific Reports 8, 14064 (2018), Ref. [135]

3. *Low Frequency Gravitational Wave Detection With Ground Based Atom Interferometer Arrays*
   W. Chaibi, **R. Geiger**, B. Canuel, A. Bertoldi, A. Landragin, P. Bouyer
   Phys. Rev. D 93, 021101(R), 2016, Ref. [70]

4. *Future Gravitational Wave Detectors Based on Atom Interferometry*
   Remi Geiger
   Published in the book ”An Overview of Gravitational Waves: Theory and Detection”, edited by G. Auger and E. Plagnol (World Scientific, 2017), arxiv: 1611.09911, Ref. [119]

5. *MIGA: Combining laser and matter wave interferometry for mass distribution monitoring and advanced geodesy*
   B. Canuel, S. Pelisson, L. Amand, A. Bertoldi, E. Cormier, B. Fang, S. Gaffet, **R. Geiger**, J. Harms, D. Holleville, A. Landragin, G. Lefèvre, J. Lhermite, N. Mielec, M. Prevedelli, I. Riou, P. Bouyer
   Proceedings of SPIE Photonics Europe conference, Brussels (Belgium), 3-7 April 2016, arXiv:1604.02072, Ref. [146]

6. Matter-wave laser Interferometric Gravitation Antenna (MIGA): New perspectives for fundamental physics and geosciences
   R. Geiger, L. Amand, A. Bertoldi, B. Canuel, W. Chaibi, C. Danquigny, I. Dutta, B. Fang, S. Gaffet, J. Gillot, D. Holleville, A. Landragin, M. Merzougui, I. Riou, D. Savoie,

P. Bouyer
Proceedings of the 50th Rencontres de Moriond ”100 years after GR”, La Thuile (Italy), 21-28 March 2015, arXiv:1505.07137, Ref. [134]

7. *The matter-wave laser interferometer gravitation antenna (MIGA): New perspectives for fundamental physics and geosciences*
B. Canuel, L. Amand, A. Bertoldi, W. Chaibi, **R. Geiger**, J. Gillot, A. Landragin, M. Merzougui, I. Riou, S.P. Schmid and P. Bouyer
E3S Web of Conferences, Volume 4, 01004 (2014) i-DUST 2014, Ref. [147]

5.3.2 People supervised in the context of the MIGA project

- Louis Amand, mechanical engineer, 2013-2016
- Thomas Chantrait, mechnical engineer, 2017-2018

Chapter 6

Testing the weak equivalence principle with entangled atom interferometers

This chapter will be different than the others of this manuscript as it relates to a theoretical proposal not yet linked to an experimental activity. While the core of the results are presented in Ref. [148], I would like to present here what is not written in the publication: some elements of context behind this study, which I have presented at various seminars (listed on my personal page) and that I judge of interest to illustrate the progress of the ideas towards the published proposal.

6.1 Episode 1: Birth of the idea in Vienna (April 2013)

As I was postdoctoral fellow in Vienna, my colleague Michael Trupke presented during a group meeting an interesting *gedanken Experiment* aimed at entangling two atoms of different species. He started the meeting by recalling the paper of the Heidelberg team entitled *Single spontaneous photon as a coherent beamsplitter for an atomic matter-wave* [149]. In this work, a coherent superposition of two momentum states of an Argon atom is created by the spontaneous emission of a single photon in front of a mirror: by placing a photon detector close to the atom, the detector can click if the photon is emitted directly towards the detector (resulting in a recoil of the atom in a given direction), or click if the photon is emitted towards the mirror and reflected to the detector (resulting in a recoil in the opposite direction). If the two possibilities cannot be distinguished, a superposition of momentum states is created. The authors then use an interferometer to prove the coherence of this superposition state.

Based on that work, M. Trupke proposes the following idea: imagine sending a single photon towards a single atom (in free space) and looking with a photon detector at the photon coming back in the opposite direction from which it was sent. Then, detection of a click projects the atom into a $2\hbar k$ momentum state ($1\hbar k$ from the absorption, $1\hbar k$ from the emission in the direction of the detector). Imagine now, as sketched in Fig. 6.1(a) from M. Trupke' group meeting slides, that we send two photons and place two detectors in opposite directions. Then, the detection of a click on each detector will project the atomic state onto a state where one atom has been pushed and the other left unperturbed. If one cannot distinguish which atom emitted the photon, then an entangled state of the following form is created:

$$|\Psi\rangle = |\text{atom 1 pushed; atom 2 free}\rangle + |\text{atom 1 free; atom 2 pushed}\rangle. \tag{6.1}$$

To prove that the state is entangled, i.e. that there is a well defined phase relationship between the two parts of the state in Eq. (6.1), an interferometer may be used, as sketeched in Fig. 6.1(b). M. Trupke concludes his talk by saying that performing such an experiment would be of great interest as one could entangle atoms of different species in free fall, and maybe look for some measurement of gravity acceleration on that state.

I was seduced by this idea. As Michael and I were sharing the same office, we immediately started to talk about this idea. At that time, I was not so much interested in the entanglement part of the proposal rather than by the possibility to perform a new type of test of the equivalence principle (I was biased by my PhD thesis linked to a prospect for testing the universality of free fall with a two species atom interferometer). Therefore, I started to do some calculations about the phase shift in such an interferometer. However, as we were both busy with our respective activities (not linked at all to this idea), not much more than this rough (though interesting) idea came out at that time. And I then left Vienna for Paris...

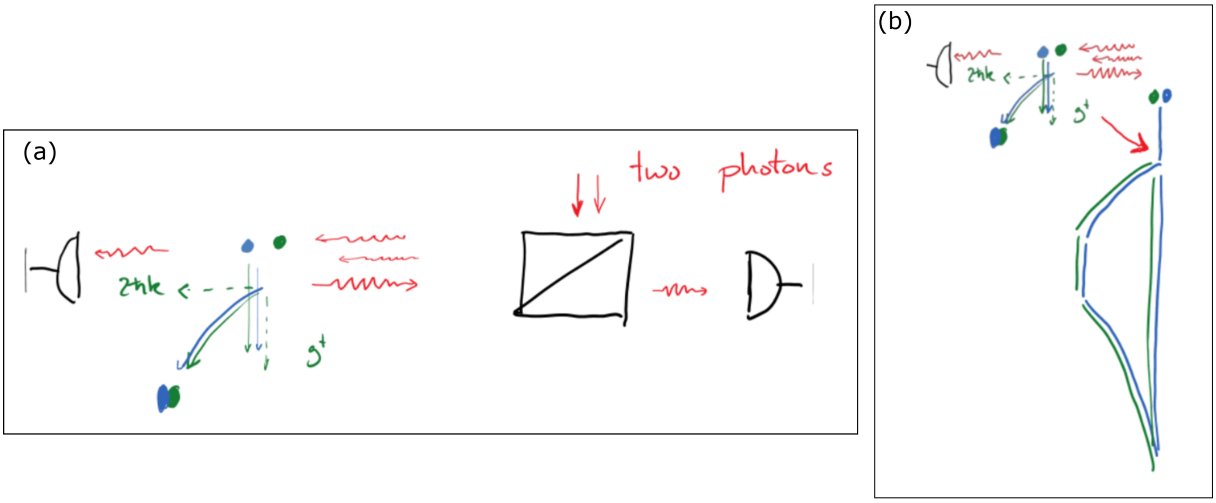

Figure 6.1: *Gedanken Experiment* proposed by Michael Trupke for entangling two atoms of different species, at the atomchip group meeting of the Atom Institut (Vienna, Austria) on 2$^{\text{nd}}$ of April, 2013 (credit: M. Trupke). The two colors (blue and green) represent two different atomic species.

6.2 Episode 2: rebirth of the idea in Paris (Summer 2016)

Although I was recruited at SYRTE to work on standard atom interferometers, my role was to strengthen the activity related to tests of fundamental physics. Therefore, I thought that giving again attention to this idea was my duty. In summer 2016, I thus started to brainstorm about it, and try to come closer to a possible experimental implementation. To simplify the protocol, I modeled it as follows: two atoms $\mathcal{A}$ and $\mathcal{B}$ are in free space and a photon is emitted by one of them, with the impossibility to distinguish which atom emitted the photon; detection of the photon projects the atoms-photon state to an atomic state of the form of Eq. (6.1):

$$|\psi\rangle = \frac{1}{\sqrt{2}}\left(|\mathcal{A},\hbar\vec{k};\mathcal{B},\vec{0}\rangle + |\mathcal{A},\vec{0};\mathcal{B},\hbar\vec{k}\rangle\right). \tag{6.2}$$

One requirement was heralded entanglement, which I understood as a way to know, for sure, that if the photon is detected, then it corresponds to the target state. The seminal papers by Cabrillo *et al*, *Creation of entangled states of distant atoms by interference* [150] (proposal), and by the Blatt group [151], *Atom-Atom Entanglement by Single-Photon Detection* (experiment), gave us a starting point. In this work, the detection of a photon emitted by one of two trapped Calcium ions characterized by a Λ Raman-type interrogation scheme creates an entangled state of the form $\Psi\rangle = |e;g\rangle + |g;e\rangle$, where e and g are two internal states of the ion. Using microwave radiation coupling the two internal states, the authors reveal the coherence of the state using a Ramsey sequence.

The question was then to adapt this idea to free space atoms with a transfer of momentum. By studying the work of the Rempe team in Munich [152], [153], I came to the idea to use the vacuum Stimulated Raman Adiabatic Passage (VSTIRAP) protocol. In this protocol, an atom with two hyperfine states in its ground state (e.g. alkaline) interacts with two light fields; a Raman process is performed by coupling the atom to a laser field and to the vacuum field of an optical cavity, such that the frequency difference between the laser and the cavity mode equals the internal state energy difference. Sweeping the Rabi frequency of the laser allows to adiabatically transfer the atom from one state to the other, by emitting a photon in the cavity mode. The Rempe group extensively studied this technique with atoms in free fall and with trapped atoms to generate polarization entangled photons [154], and to entangle distant atomic systems by the exchange of a single photon [155].

Regarding the production of our target state, my idea was to benefit from the momentum imparted on a free space atom from the photon emission in the VSTIRAP process, and from the fact that the emitted photon is defined by the cavity. Roughly speaking, the idea was to place two different atomic species in a cavity and to drive such a VSTIRAP process, in order to ensure that the emitted photon was indistinguishable as emitted in the same cavity mode. By driving weakly the VSTIRAP process (as in the Cabrillo *et al* proposal [150]) to ensure that the probability of emission of a photon was small ($\sim 10^{-1}$), we could ensure that the probability of two photon emissions would be lower ($\sim 10^{-2}$). With this more realistic scenario in hand, we then studied the details of the implementation in order to come to realistic estimates for the success of production of our target state (choice of atoms, cavity design, evaluation of success rates, etc.).

My wish was to use such an entangled state of two different atomic species in a new type of test of the weak equivalence principle (WEP). To this aim, it required to measure the gravitational acceleration of the two-atom state (by atom interferometry), thereby requiring a vertical accelerometer. Therefore, at least one of the light beams realizing the Raman transition must have a projection on the gravity direction (z).

6.3 Episode 3: publication of our proposal (June-December 2017)

It took us about one year, starting from this idea of implementation based on VSTIRAP, to come to a plausible proposal from the experimental side, which we submitted to Physical Review Letters at the end of June 2017. I was delighted to read, on January 2^{nd} of 2018, that our paper was accepted for publication. I invite the reader to directly study our publication entitled *Proposal for a Quantum Test of the Weak Equivalence Principle with Entangled Atomic Species.* A sketch of the proposed setup is shown in Fig. 6.2 for completeness of the presentation.

As I thought that this idea deserved further attention, I gave a series of seminars in Paris area to discuss our proposal with people from different communities: *(i)* laboratories specialized in AMO physics or quantum optics for feedback on the interest of such generation of entanglement between atoms in free fall and on the feasibility (Institut d'Optique in Palaiseau, Laboratory for laser physics in Villetaneuse); *(ii)* theoretical institutes for the feedback on the relevance of a test of the WEP with a new kind of probe mass, namely a state of entangled atoms (theory group of the Astrophysics institute of Paris, Laboratory for Universe and Theory of Paris Observatory). In general, researchers were enthusiastic about the idea. Regarding the WEP test, Michael

Trupke and myself discussed with several theorists who gave us the same answer as the one which we fairly provided to the reviewers of our paper and write in conclusion of [148]: *To the best of our knowledge, there is currently no theoretical model which addresses the question of whether or not the presence of entanglement in a system could lead to a violation of the WEP at a given level of accuracy. In general, WEP tests involving new types of physical objects, such as matter waves or antimatter, are motivated by the qualitatively different nature of the involved proof masses, rather than by a consensual theoretical argument predicting a violation in such systems. Our proposal follows this approach by aiming for a test of a foundational principle of physics with a qualitatively new system not considered before.*

The objectives of our proposal can be thoroughly stated in the terms of a recent review article on gravitational quantum physics [156]: *"It is fair to say that with the current state of physics the question concerning the quantum nature of gravity is entirely open. Ultimately, its answer is likely to be decided by experiment. It is therefore of much interest to test the foundational principles of general relativity, like the equivalence principle, on systems in non-classical states."*

These considerations thus called me for further studies.

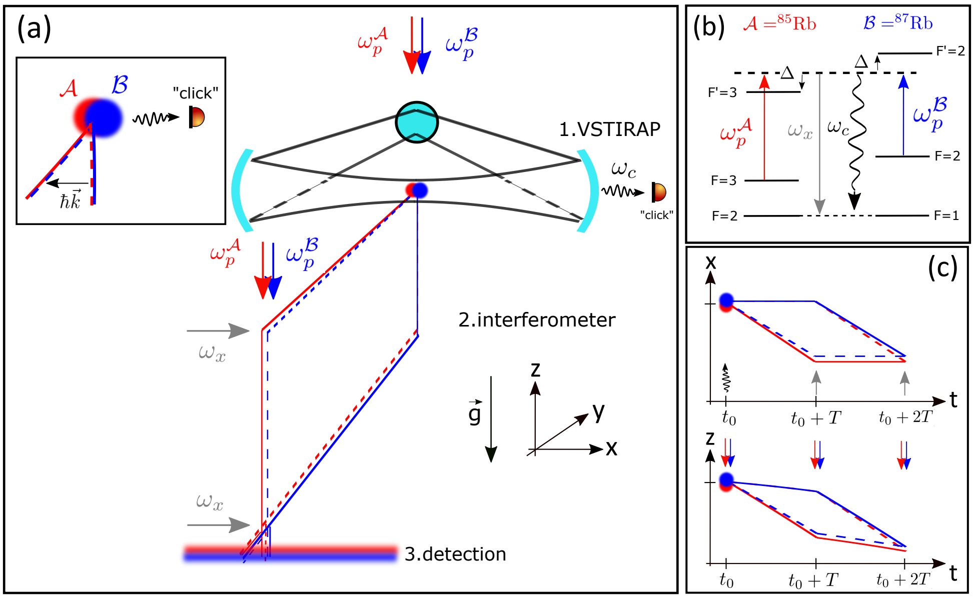

Figure 6.2: **Sketch of the proposed experiment consisting of a two-atom gravimeter using ^{85}Rb and ^{87}Rb. Inset of (a): Principle of the entanglement generation.** (a) Schematical overview (not to scale): after laser cooling, the atoms are released and interrogated in a high finesse optical cavity made of three mirrors lying in the (xy) plane. During the VSTIRAP process, a photon is extracted from the pump beams (red and blue arrows, $\omega_p^{\mathcal{A},\mathcal{B}}$, respectively for ^{85}Rb and ^{87}Rb), and a photon is emitted into the cavity mode (angular frequency ω_c). The emitted photon is detected in output of the cavity ('click'). (b) Energy levels of the atoms subject to two-photon Raman transitions (D_1 line of Rubidium). The gray arrow represents a laser beam (angular frequency $\omega_x = \omega_c$) used to perform the Raman transitions in the mirror pulse ($t = t_0 + T$) and final beam splitter pulse ($t = t_0 + 2T$) of the interferometer. (c) Space-time diagrams of the atom interferometer in the x and z directions.

6.4 Episode 4: further details, towards an experiment setup ?

In this last section, I will present unpublished work regarding a possible implementation of the experiment, following a grant application that I submitted in 2018 to pursue this project (project entitled **GENTLE**– Probing Gravity with ENTangLEd atomic species – not yet funded).

The key elements of the experiment are:

1. the production of two single cold (μK) atoms of ^{85}Rb and ^{87}Rb in a high finesse optical resonator, and the deterministic production of the entangled state $|\psi\rangle$ by VSTIRAP;
2. the manipulation of the two-atom state $|\psi\rangle$ in an atomic gravimeter;
3. the detection of the two-atom state in free fall.

6.4.1 Element 1: Preparation of the atoms, optical resonator, and production of the entangled state.

As a starting point for the design of the experiment, I followed the seminal work of the group of. G. Rempe on VSTIRAP. The group first used atoms free falling from a Magneto-Optical-Trap (MOT) through a high finesse optical cavity [153], and later single atoms trapped directly in the cavity [154]. I considered two key requirements for the success of the protocol:

- *Determinism.* Two and only two single ^{85}Rb and ^{87}Rb atoms must deterministically be present in the cavity.
- *Temperature.* The two atoms must see the same atom-cavity coupling constant in order to make the photon emission process as indistinguishable as possible. Given a typical waist $w_0 \sim 40\ \mu$m of the fundamental mode in the resonator, the separation between the two atoms at the time of the VSTIRAP process must be smaller than w_0 in the transverse direction (y and z), and smaller than the Rayleigh length $z_R = \pi w_0^2/\lambda \sim 6$ mm in the longitudinal (x) direction. This sets stringent bounds on the maximum temperature Θ of the two atoms, and on the time t_0 between the atom release (from their preparation) and the VSTIRAP pulse: $\sigma_v t_0 \ll w_0$, where $\sigma_v = \sqrt{k_B\Theta/m}$. For typical temperatures $\Theta \sim 5\ \mu$K ($\sigma_v \simeq 2.2$ cm.s^{-1}), the VSTIRAP pulse must occur within less than 1 ms after the atom release.

These two requirements point towards preparing the cold two atoms in the cavity mode as in [154] and releasing them shortly before the VSTIRAP pulse, rather than extracting them from a MOT located above the cavity as in [153].

Interferometer duration. The atoms need to escape the cavity in the vertical direction in order to perform the second and third pulses of the atom interferometer, as shown in Fig. 6.2(a) (performing these pulses in the cavity would add unnecessary complexity). This implies a free fall distance $h \sim 2$ cm after the VSTIRAP pulse in order to escape from the mirror. In the case where the atoms are dropped shortly after the VSTIRAP pulse ($t_0 < 1$ ms), this condition sets the minimum interferometer pulse duration $T = \sqrt{2h/g} \simeq 63$ ms. The link between interferometer phase and acceleration is $\Phi = \vec{k}_{\text{eff}}.\vec{a}\ T^2$ [57]. The phase shift associated with Earth' gravity is 3×10^5 rad.

Cavity geometry.
The experiments of [153], [154] used a two-mirror Fabry-Perot cavity, with one mirror of higher transmission than the other for a preferred direction of escape of the photon. In such a geometry, the direction of emission of the photon ($+x$ or $-x$) is unknown. In the present case, the direction of emission must be known, as it determines the atom' recoil direction and hence the resonance condition for the subsequent interferometer beams. I therefore propose to use a three-mirror cavity with one flat mirror of higher transmission T_1 and two concave mirrors of low transmission $T_2, T_3 \ll T_1$. The direction of the photon' emission can then be determined from the output direction at the flat mirror. Regarding the feasibility, a three-mirror cavity of high finesse (1.7×10^5 at 799 nm) has already been used in cold atom experiments [157].

Cavity parameters for VSTIRAP and trade-offs.
Several parameters govern the VSTIRAP process: the atom-cavity coupling g (half vacuum Rabi-frequency), the cavity decay rate κ, the atom decay rate γ, and the Rabi frequency Ω_p of

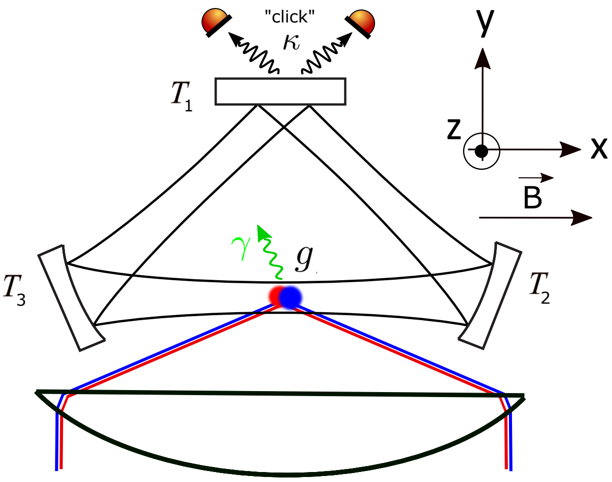

Figure 6.3: **Schematic of the optical resonator and of the preparation of the atoms** (view from the top). The cavity decay rate is κ, the atom-cavity coupling is g, and the atom decay rate is γ (see Table 6.1). The two atoms (red and blue balls) will be loaded in the cavity by optical tweezers formed by a high numerical aperture objective lens. A magnetic field $\vec{B}$ along the x direction is applied to produce a Zeeman splitting larger than the cavity decay rate κ.

the pump beam. The latter, together with g and the detuning Δ from the excited state (see Fig. 6.2(b)), determines the characteristic duration $\Delta\tau$ of the Raman adiabatic passage. As explained in [158], VSTIRAP will be effective for a given parameter range.

Trade-offs have to be operated. The atom-cavity coupling $g = d_{ge}\sqrt{\frac{\omega_c}{2\epsilon_0\hbar V_{\rm mode}}}$ is essentially determined by the mode volume[1] $V_{\rm mode} = \pi w_0^2 L/2$, i.e. by the cavity total length L and the waist w_0. $d_{ge} \simeq 1.89 \times 10^{-29}$ C.m is the dipole matrix element of the relevant transition on the D_1 line of ^{85}Rb [159]. The larger g, the better; in other words, the smaller L and w_0, the better. However, L and w_0 (set by the radius of curvature of the mirrors) constrain the optical access to prepare the atoms in the cavity. Second, the cavity decay rate $\kappa = \pi{\rm FSR}/\mathcal{F}$ is set by the free spectral range ${\rm FSR} = c/L$, and by the finesse $\mathcal{F}$. Following [157], a reasonable starting point for the finesse is $\mathcal{F} = 1 \times 10^5$. Finally, the figure of merit for our entangling protocol is determined by the probability of stimulated emission (in the cavity mode), P_{stim}, and the probability of spontaneous emission, P_{sp}. These shall be tuned to achieve a workable success probability $P_S = 2 \times P_{stim} \times (1 - P_{stim}) \times P_{coll} \times (1 - P_{spon})^2$, where $P_{\rm coll}$ indicates the probability for photon detection [148]. The probability for false-positive detection (i.e. both atoms emit a photon, but only one is detected) is $P_F = P_{stim}^2 \times P_{coll} \times (1 - P_{coll})$, where I assume number-resolving photon detectors.

The atoms will respectively be prepared in the $|F = 3, m_F = 3\rangle$ state for ^{85}Rb and $|F = 2, m_F = 2\rangle$ state for ^{87}Rb, with pump Raman fields π polarized (linear polarization parallel to the magnetic field). If the Zeeman splitting is larger than the cavity linewidth κ, then a photon of well-defined polarization (σ^+ or σ^-) will be emitted in the cavity [153].

For the tuning of the cavity parameters, I numerically solved the 3-level master equation governing the VSTIRAP process. The power envelopes of the photons emitted by the two atomic species can be made indistinguishable by tuning the Rabi frequencies of the two processes (see also Refs. [160], [161]). The parameters of the cavity and VSTIRAP protocol are summarized in Table 6.1. **I expect a success probability (before-last line in the table) of 1%.**

---

[1] For simplicity, I refer here to the geometric average of the waists which are slightly different in the two directions, due to the angle of incidence of 22.5° on the curved mirrors.

detuning from the excited state $\Delta/2\pi$ (MHz)	1360
Rb atom decay rate $\gamma/2\pi$ (MHz)	2.9
resonator length L (mm)	6
mirrors' radii of curvature (mm)	∞, 50, 50
transmission coefficients T_i(ppm)	50, 5, 5
waist w_0 (μm)	46
finesse $\mathcal{F}$	105 000
cavity decay rate $\kappa/2\pi$ (MHz)	0.24
atom-cavity coupling $g/2\pi$ (MHz)	0.76
stimulated emission probability P_{stim}	0.018
spontaneous emission probability P_{sp}	0.011
photon detection efficiency P_{coll}	0.3
success probability P_S	0.010
false positive probability P_F	7×10^{-5}

Table 6.1: **Cavity and VSTIRAP parameters**. The calculation is done for the D_1 line of ^{85}Rb, according to the level structure in Fig. 6.2(b). The dipole matrix element for ^{87}Rb is 0.95 times that of ^{85}Rb for the relevant transitions [159]. The Rabi frequency of the pump laser was set to 20 MHz.

Characterization of the emitted photon.

The detection efficiency of the emitted photon is given [162] by the product of the output directionality of the cavity (83% for the parameters in Tab. 6.1), the transmission of the optical path (e.g. fiber coupling ~ 70% [163]), and the quantum efficiency of the single photon counting module (~ 60% at 780 nm [164]), leading to an estimate of 34% in both output ports (i.e. 17% in each port). I assumed a detection efficiency of 30% in the above table. Noise from the dark count of the detector and from the background photons (scattering on optics or blackbody radiation) is not expected to be problematic since the detector can be gated with the μs-long Raman pump pulse.

The single photon nature of the source can be assessed with a Hanbury Brown and Twiss setup, by looking at intensity correlations between two detectors placed after a 50 : 50 beam splitter as a function of the delay time between the detections [163]. This could be done for each atom independently driven by its own pump beam, and then when both atoms are driven. Indistinguishibility of the two photons can be assessed in a time-resolved two-photon interference experiment (Hong-Ou-Mandel-like setup).

Atom preparation in optical tweezers.

The preparation of two single atoms of ^{85}Rb and ^{87}Rb in the cavity mode could build on the rapid progresses in trapping, cooling, and manipulating single atoms in optical tweezers, demonstrated in several groups **Schlosser2001**, [165]–[169]. A high numerical aperture (NA) optical system is used to focus a far-off resonance laser beam (waist ~ 1 μm) in which the atom is trapped owing to the dipole force. The same high-NA optical system can be used to image the single atom on a camera, by employing a dichroic element to separate the dipole trapping laser and the scattered light from the atom during imaging. Regarding state of the art and feasibility, single atom imaging has already been performed in cavity-QED (e.g. [154]), and a single-atom interferometer using the techniques of single atom preparation based on the collisional blockage regime has already been demonstrated for Cesium in [170], where the measured temperature was 4 μK.

Trapping the two isotopes. Here, we need to prepare two single atoms of ^{85}Rb and ^{87}Rb in the cavity, and to release them with a temperature of only few μK compatible with atom interferometry, and with the requirements of single atom detection in time-of-flight (section 6.4.3).

Preparation of two single atoms of ^{85}Rb and ^{87}Rb with 95% probability has been demonstrated and characterized in [167]. I plan to implement a similar optical system for trapping the two atoms at the same place in the cavity mode, i.e. by using a single high-NA objective to create a static tweezer (to trap, e.g., ^{85}Rb) and a movable tweezer to bring one atom (e.g. ^{87}Rb) in contact with the first one. The high-NA objective will be designed in close combination with the cavity system, as it requires enough optical access, which is constrained by the cavity frame. This is the reason why I started the estimation of cavity and VSTIRAP parameters with a distance of 2 mm between the mirrors.

Temperature. An important requirement for the success of the subsequent experiments is the atoms' temperature after their release from the tweezers. The energy of the atom can be (non-deterministically) reduced to low micro-Kelvin temperatures by adiabatic cooling and by truncating the Botzmann distribution of the atom [170], [171]. For deterministic cooling, polarization gradient cooling in the tweezer can reach $\sim 10\ \mu$K temperatures [165], and Raman sideband cooling can bring to lower temperatures determined by the trap depth (e.g. 3.6 μK in [165]). Finally, transport and transfer of a single cold atom can be performed without heating as shown in [172], which is important for bringing ^{85}Rb in the same tweezer as ^{87}Rb after cooling. My aim is to achieve a probability of 50% for the preparation and release of the two single atoms, with a temperature of 5 μK.

6.4.2 Element 2: Two-atom interferometer.

Interferometer geometry and realization.

Following the VSTIRAP entangling pulse, the core of the proposal relies on a two-atom interferometer sensitive to gravity acceleration of the two-atom state. The atom interferometer geometry is similar to the traditional 3 light-pulse interferometer for single atoms ([53] and Fig. 6.2(c)), with the first beam splitter replaced by the VSTIRAP pulse occuring at time t_0. A mirror pulse for the atomic waves occuring at a time $t_0 + T$ will redirect the two interferometer arms towards each other, before their recombination at the third light pulse occuring at time $t_0 + 2T$. The light pulses which diffract the matter waves are stimulated two photon Raman transitions, where the atoms absorb a photon in one beam and stimulatedly emit a photon in the other beam. The special feature of the interferometer is that it operates along two dimensions (x and z). Three phase-locked lasers will be involved in the experiment: the pair ω_x/ω^{85} (resp. ω_x/ω^{87}) to induce the Raman transition for the ^{85}Rb (resp. ^{87}Rb) atom, sketched by the horizontal gray arrow and the vertical red (resp. blue) arrows in Fig. 6.2(a)).

Wave-packet separation. As mentionned at the beginning of section 6.4.1, the interrogation time T must be such that the atoms can escape from the cavity before the mirror pulse, where one of the two Raman lasers (ω_x) is sent horizontally (see Fig.6.2(a)). This sets a minimum total interrogation time $2T \simeq 120$ ms, corresponding to a total free fall distance $H = 2gT^2 \simeq 70$ mm. The displacement between the two interferometer arms at the mirror pulse will be $\Delta x, \Delta z = \hbar kT/m \simeq 0.35$ mm. This displacement is sufficiently small compared to the distance between the two concave mirrors of the cavity (~ 2 mm) to send the $\omega_z^{85,87}$ beams from above, as shown in Fig. 6.2(a). Addressing the two arms of the interferometer with the same effective Rabi frequency requires the Raman beam waists to be larger than $\Delta x, \Delta z$.

Doppler effect. The Raman transitions are velocity sensitive. The Doppler effect $kgt/2\pi$ associated with the free fall of the atoms must therefore be corrected to stay on Raman resonance. The frequency of the lasers will be sweeped during the interferometer, since the Doppler effect (~ 1.5 MHz for $2T = 120$ ms) will be larger than the pulse effective Rabi frequency (typically few tens of kHz). Such frequency sweeps are routinely done in atom interferometers via the phase-lock-loop on the lasers [66].

Two-atom interferometer signal and phase shift.

At the interferometer output, the 4 possible states associated to 8 possible paths [148] are:

$$|85,\vec{0},F=3,m_F=3;\ 87,\vec{0},F=2,m_F=2\rangle \quad ; \quad |85,\vec{0},F=3,m_F=3;\ 87,\hbar\vec{k}_{\rm eff},F=1,m_F=1\rangle$$
$$|85,\hbar\vec{k}_{\rm eff},F=2,m_F=2;\ 87,\vec{0},F=2,m_F=2\rangle \quad ; \quad |85,\hbar\vec{k}_{\rm eff},F=2,m_F=2;\ 87,\hbar\vec{k}_{\rm eff},F=1,m_F=1\rangle.$$

Each state contains the contribution from two path in the interferometer. The detection of these 4 possible states at the interferometer output will be performed by fluorescence detection (as described in subsection 6.4.3 below), which resolves the two hyperfine states of each atom [52].

For example, the probability of detecting the two atoms in the output port corresponding to $\vec{0}$ momentum (^{85}Rb in $F=3$ and ^{87}Rb in $F=2$) is given by [148]

$$P_{00} = \frac{1}{8}\left|1+e^{i(\Phi_{85}-\Phi_{87})}\right|^2. \tag{6.3}$$

Here $\Phi_\alpha = \phi^\alpha(t_0) - 2\phi^\alpha(t_0+T) + \phi^\alpha(t_0+2T)$ is the phase shift that would be measured on independent single-species interferometers ($\alpha = 85, 87$), where $\phi^\alpha(t) = -k_x x_\alpha(t) - k_z^\alpha z_\alpha(t)$ is the relative phase between the light fields involved in the two photon Raman processes [57]. **Remarquably, the two-atom interference signal is determined by the phase shifts of each single atom loop, as in two-photon interferometers [173], [174].**

The main signal of the interferometer, $\Delta\Phi = \Phi_{85} - \Phi_{87}$, can be computed following standard techniques [148] and reads:

$$\Delta\Phi = k_z(g_z^{85} - g_z^{87})T^2 + k_x(a_x^{85} - a_x^{87})T^2, \tag{6.4}$$

which reflects the bidirectional acceleration sensitivity of the interferometer (along x and z). Provided that the experiment is not constantly accelerated in the horizontal direction with respect to the freely falling atoms ($a_x^\alpha = 0$), the second term vanishes on average. The main phase shift of the interferometer, $\Delta\Phi_{\rm WEP} \equiv k_z(g_z^{85} - g_z^{87})T^2$, represents a coherent measurement of the difference in the gravitational acceleration between the two atoms. More precisely, **the interferometer measures the gravity acceleration of the two-entangled-atom state**.

Entanglement verification.
The entanglement between the two species can be directly assessed by applying controlled phase shifts on the relative phase of the (phase-locked) Raman lasers: while a phase shift applied to only one pair of lasers (say for ^{85}Rb) affects the joint signal P_{00}, the same phase shift applied on both pairs of lasers should not affect P_{00}. Quantifying the entanglement fidelity could be done in a similar way as in the two-ion experiment of [151], i.e. by applying global rotations to the two-atom state (here with the Raman transitions) for different phases $\Delta\Phi$.

6.4.3 Element 3: Detection of the two-atom state in time-of-flight.

The principle of the detection of the internal states of the atoms at the interferometer output will be analog to the fluorescence detection made in atomic fountains [66], [175], [176], but will operate here at the single atom level. Four states need to be resolved, i.e. the two hyperfine states for each atom.

Requirements and comparison with previous experiments.
While many groups have reported high detection fidelity levels for trapped single atoms, only few experiments have performed the detection of single atoms in time-of-flight. In terms of time-of-flight duration, the closest realization to the scheme anticipated for the project was performed in my previous postdoc group in Vienna [177]. The challenge in this project lies in the large volume of rms radius $\sigma_r \simeq \sigma_v \times 2T$ occupied by the atom in the detection light sheet, given by the total time of flight after release $2T \simeq 120$ ms, and the finite rms velocity of the 5 μK-cold atoms $\sigma_v = \sqrt{k_B\Theta/m} \simeq 2.2$ cm.s^{-1}. This leads to a volume of rms diameter $2\sigma_r \simeq 5.2$ mm.

Previous experiments with trapped single atoms [170], [178] used single mode fibers (core diameter $c \sim$ few μm) with a high NA optical system ($NA \sim 0.3 - 0.5$) to collect the light scattered by the atoms and to strongly reduce contributions from background light scattered in the chamber. However, this is not a good solution in this project because it would require very low magnifications $c/2\sigma_r \sim 10^{-3}$, which would compromise the field of view and depth of field of the system, yielding a too low atom detection probability ($\sim 10^{-5}$). Large detectors of few mm^2 area capable of detecting few photons are thus preferable, such as photomulitplier tubes.

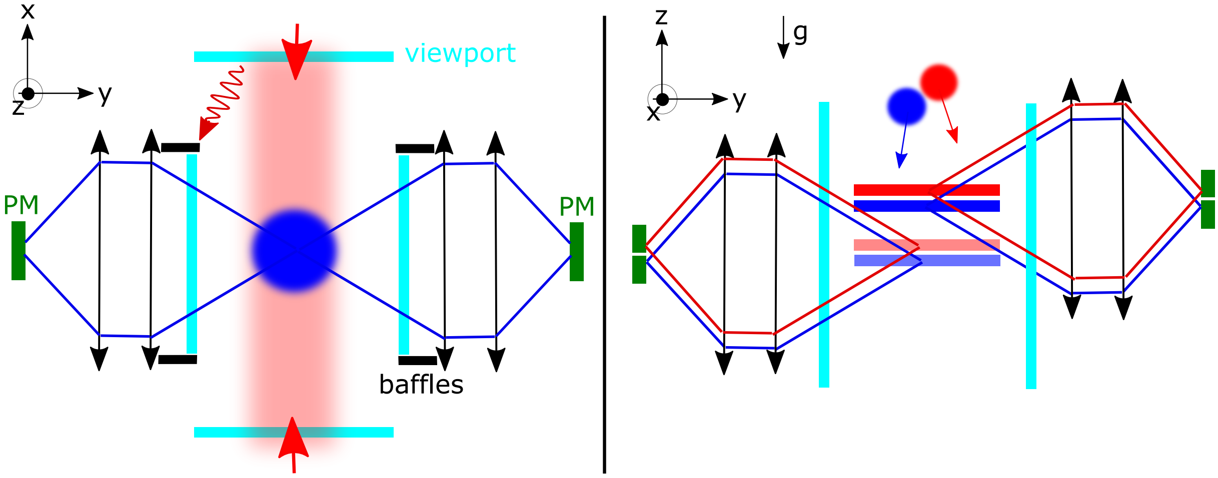

Figure 6.4: **Schematic of the detection system.** Left: view from the top. Right: view from the side. Four light sheets are used, to detect each possible hyperfine state for each atom. PM: photomultipler tube. Two optical systems are used to collect the light scattered by the atom in each zone and focus it on a dedicated PM. Baffles are used to reduce the contribution from scattered light from the viewports.

Description of the anticipated detection system.
The detection system is sketched in Fig. 6.4, with a view from the top (left panel) and from the side (right panel). The optical design is similar to systems which I already implemented on previous experiments [66], [134]. Four elliptical light sheets of $2w_z \simeq 1$ mm thickness and $2w_y \simeq 2\sigma_r = 5$ mm width will be sent through the chamber in the x direction. An optical system of $NA \simeq 0.3$ and magnification $|m| \simeq 0.5$ will collect the light and focus it on photomultiplier tubes. The sensitive area $\mathcal{A} = a_z \times a_x$ of each photomultiplier tube must be large enough to collect the photons from the detection volume, corresponding to a field of view of $2\sigma_r$ in the x direction, and a depth of field of $2\sigma_r$ in the y direction (in object space). This yields a detector size $a_x = 2\sigma_r \times |m| \simeq 2.5$ mm and $a_z \simeq 2NA \times |m| \times 2\sigma_r \simeq 1.5$ mm.

Each light sheet will be used to detect the atom in each possible hyperfine state. The top light sheets will address the cycling transitions (D_2 line, $F = 3 \rightarrow F' = 4$ for ^{85}Rb and $F = 2 \rightarrow F' = 3$ for ^{87}Rb), and the bottom light sheets will contain the cooling and repumping light for each atom. An atom in the upper hyperfine level will therefore be detected at the top and at the bottom, while an atom in the lower hyperfine state will be detected at the bottom only.

SNR estimation.
I propose here an estimation of the signal to noise ratio (SNR) to illustrate the challenge of the proposed detection scheme. The signal is given by $\mathcal{S} = \frac{\Gamma}{2}\frac{s}{1+s}\eta \times QE \times \Delta t \times G$ where $\Gamma \simeq 3.7 \times 10^7$ s^{-1} is the inverse excited state lifetime, $s \simeq 1$ the saturation parameter, $\eta = NA^2/4 \simeq 2.2\%$ the collection efficiency, $QE \simeq 3\%$ the photomultiplier quantum efficiency, $\Delta t = 2w_z/2gT$ the duration spent by the atom of speed $2gT$ is the light sheet of thickness $2w_z = 1$ mm, and $G \simeq 10^5$ the photomultiplier gain [179]. The noise is given by quadratic sum of the shot noise of

the signal, the shot noise of the background light (mainly due to scattering on viewports), and the shot noise of the dark count rate of the photomultiplier. The largest expected contribution to the noise is that from background light, given by $\sigma_b = G \times [\epsilon_{sc} \times QE \times \eta \times P\Delta t/\hbar\omega]^{1/2}$, where $\hbar\omega$ is the energy of the 780 nm photons, $P \simeq s \times \pi w_z w_y I_{sat}/2$ the power in the light sheet beam for a saturation parameter s, with $2w_y = 5$ mm the total width of the light sheet and $I_{sat} \simeq 1.7$ mW.cm^{-2} the saturation intensity of the cycling transition [159]. With a saturation parameter $s = 1$, the required power is 30 μW. The key parameter is ϵ_{sc}, the scattered amplitude in the viewport reduced by the use of baffles. **For a level of scattered light, ϵ_{sc}, as low as 1 ppm, the expected SNR only equals 3.5, which illustrates the challenge of the single atom detection after such a long time-of-flight**.

6.4.4 WEP test: sensitivity, protocol, accuracy.

Sensitivity.
Various ways exists to measure the phase shift in an atom interferometer. The most simple one is to reconstruct the interferometer fringes shot after shot by varying the Raman laser relative phase before the last light-pulse, which will allow us to extract $\Delta\Phi_{\mathrm{WEP}}$. Assuming a single-atom quantum projection noise limited sensitivity corresponding to 1 rad for a single atom [170], the acceleration sensitivity is given by $\sigma_{\mathrm{WEP}} \simeq 1/(k_z T^2 \sqrt{N})$, where N is the number of measurements. To conservatively estimate a number of successful measurements, I assume:

- a cycle time of 2 seconds for preparing the two cold atoms in the cavity at 10 μK temperature, with a two-atom preparation probability $\mathcal{P}_{prep} = 50\%$;
- a success probability of $\mathcal{P}_S = 1\%$ for the VSTIRAP entangling process (see Table 6.1);
- a limited detection efficiency of the two atoms of $\mathcal{P}_{det} = 50\%$.

This yields a global success probability of the experimental run of $\mathcal{P}_{tot} = \mathcal{P}_{prep} \times \mathcal{P}_S \times \mathcal{P}_{det} = 2.5 \times 10^{-3}$, corresponding to about 100 useful data points in one full day of measurement. A total number $N = 100$ of successful measurements is therefore realistic, corresponding to a phase sensitivity of 100 mrad and to an acceleration sensitivity of 4×10^{-6} m.s^{-2}. This means that a potential sensitivity of 4×10^{-7} on the Eötvös parameter can be reached.

The main noise source in precision inertial measurements is vibration noise. Here, the measurement is differential, so that vibration noise is expected to have a negligible effect (see Eq. (6.4)), as in other works on differential atom interferometry.

Measurement protocol.
A convincing test of the WEP must involve the comparison with a reference, i.e. it requires two differential acceleration measurements with at least three proof masses; for example, the comparison of the measurement $a_1 - a_2$ with that of $a_1 - a_3$ [180]. With the experimental apparatus described in the previous sections, the following sequences can be implemented and interleaved to remove and characterize long term varying systematic effects:

1. Measurement on the ^{85}Rb–^{87}Rb two-atom state.
2. Measurement on a ^{85}Rb–^{85}Rb two-atom state, i.e. same as (1) but with two ^{85}Rb atoms and the VSTIRAP process (detection of one photon → superposed two-atom state).
3. Same as (2) but with a ^{87}Rb–^{87}Rb two-atom state.
4. Measurement with only one ^{85}Rb atom, without the VSTIRAP process. In that case, the interferometer is performed by doing a standard $\pi/2$ beam splitter pulse instead of VSTIRAP (e.g. by sending ω_x in the cavity).
5. Same as (4) with one ^{87}Rb atom.

Steps (4) and (5) can be performed simultaneously as in standard cold atom WEP tests.

Using these sequences yields numerous pieces of information:

- Steps (4) and (5) are similar to current tests of the WEP with cold atoms, but here at the single atom level. This measurement will be used as a reference as the difference $a_{85} - a_{87}$ is known to be zero at the level of 10^{-8} on the Eötvös parameter [14].
- Comparing the outcomes of (2) and (3) with (4) and (5) allows to assess the role of entanglement between the two same species on the free fall.
- Comparing the outcome of (1) with (2) and (3) allows to assess the influence of entanglement between two different species on the free fall.

Systematic effects and accuracy of the test.
Two categories of systematics are expected: well-studied effects encountered in single particle atom interferometers, such as differential AC Stark shifts, gravity gradients, optical wave-front aberrations, or effects of magnetic field gradients. New types of systematics associated with two-particle interferometry could arise, in particular a possible phase shift associated with the VSTIRAP process, which could be isotope-dependent. Such phase shifts have not been experimentally studied previously, and shall be characterized. They are interesting by their own as they inform on the exact mechanisms occuring during VSTIRAP. Other isotope-dependents phase-shifts are expected to impact the measurement, such as the impact of magnetic field gradients associated with the difference in magnetic field response of the two isotopes (^{85}Rb arms are on $|F = 3, m_F = 3\rangle$ and $|F = 2, m_F = 2\rangle$, and ^{87}Rb arms are on $|F = 2, m_F = 2\rangle$ and $|F = 1, m_F = 1\rangle$). Reaching an accuracy at the 10^{-6} level on the Eötvös parameter is a reasonable estimate.

6.5 Conclusion

This chapter presented the proposal of an experiment to entangle two atoms of different species in free space and to test the validity of the weak equivalence principle (WEP) for an entangled state of matter. I presented the context of the proposal and a possibility of experimental implementation, with more details than in the publication [148]. While the paper focuses on the application to a test of the WEP, entangling *in free space* two atoms would be of high interest. Two teams are already actively working on a test of Bell' inequalities on free metastable Helium atoms in France [181] and Australia [182].

While no particular violation of the WEP is predicted, the system is qualitatively sufficiently different than other tests involving classically distinct proof masses to deserve interest. I have tried to attract theorists to the subject, in order to come to a possible parametrization of the experiment and a broader theoretical treatment. A possible simple empirical parametrization of a violation in terms of Eötvös parameter would be, for example, $\eta(\mathcal{A}, \mathcal{B}) = \epsilon(\mathcal{A}, \mathcal{B}) \times \mathcal{F}(\mathcal{A}, \mathcal{B})$, with $\epsilon(\mathcal{A}, \mathcal{B})$ a measure for the difference in composition of the two atoms (e.g. number of nucleons) and $\mathcal{F}(\mathcal{A}, \mathcal{B})$ the entanglement fidelity of the state, which can be experimentally measured.

Our proposed experiment is based on a VSTIRAP process to entangle the two species. A Chinese team has demonstrated the entanglement of ^{85}Rb and ^{87}Rb using Rydberg blockade in a trap [183]. It would be interesting to study whether their setup could be an easier starting point for producing the pair of entangled atoms in free space, e.g. with Raman transitions following the entanglement generation. Moreover, a more detailed analysis of the detection of the single atoms in time-of-flight should be carried out, in order to alleviate the needs for the challenging levels of scattered light assumed in this chapter.

Publication.
Proposal for a Quantum Test of the Weak Equivalence Principle with Entangled Atomic Species
Remi Geiger and Michael Trupke
Phys. Rev. Lett. 120, 043602 (2018), Ref. [148]

Bibliography

[1] S. Lepoutre, A. Gauguet, G. Trénec, M. Büchner, and J. Vigué, He-McKellar-Wilkens Topological Phase in Atom Interferometry. en, *Physical Review Letters*, vol. 109, no. 12, Sep. 2012.

[2] P. Asenbaum, C. Overstreet, T. Kovachy, D. D. Brown, J. M. Hogan, and M. A. Kasevich, Phase Shift in an Atom Interferometer due to Spacetime Curvature across its Wave Function. en, *Physical Review Letters*, vol. 118, no. 18, May 2017.

[3] H. Müller, S.-w. Chiow, S. Herrmann, S. Chu, and K.-Y. Chung, Atom-Interferometry Tests of the Isotropy of Post-Newtonian Gravity. en, *Physical Review Letters*, vol. 100, no. 3, Jan. 2008.

[4] P. Hamilton, M. Jaffe, P. Haslinger, Q. Simmons, H. Müller, and J. Khoury, Atom-interferometry constraints on dark energy. *Science*, vol. 349, no. 6250, pp. 849–851, 2015.

[5] M. Jaffe, P. Haslinger, V. Xu, P. Hamilton, A. Upadhye, B. Elder, J. Khoury, and H. Müller, Testing sub-gravitational forces on atoms from a miniature in-vacuum source mass. *Nature Physics*, vol. 13, no. 10, pp. 938–942, Jul. 2017.

[6] R. Bouchendira, P. Cladé, S. Guellati-Khélifa, F. Nez, and F. Biraben, New Determination of the Fine Structure Constant and Test of the Quantum Electrodynamics. en, *Physical Review Letters*, vol. 106, no. 8, Feb. 2011.

[7] R. H. Parker, C. Yu, W. Zhong, B. Estey, and H. Mueller, Measurement of the fine-structure constant as a test of the standard model. *Science*, vol. 360, no. 6385, p. 191, Apr. 2018.

[8] J. B. Fixler, G. T. Foster, J. M. McGuirk, and M. A. Kasevich, Atom interferometer measurement of the newtonian constant of gravity. *Science*, vol. 315, no. 5808, pp. 74–77, 2007. eprint: `http://science.sciencemag.org/content/315/5808/74.full.pdf`.

[9] G. Rosi, F. Sorrentino, L. Cacciapuoti, M. Prevedelli, and G. M. Tino, Precision measurement of the Newtonian gravitational constant using cold atoms. en, *Nature*, vol. 510, no. 7506, pp. 518–521, Jun. 2014.

[10] S. Fray, C. A. Diez, T. W. Hänsch, and M. Weitz, Atomic interferometer with amplitude gratings of light and its applications to atom based tests of the equivalence principle. *Phys. Rev. Lett.*, vol. 93, no. 24, p. 240 404, Dec. 2004.

[11] M. G. Tarallo, T. Mazzoni, N. Poli, D. V. Sutyrin, X. Zhang, and G. M. Tino, Test of einstein equivalence principle for 0-spin and half-integer-spin atoms: Search for spin-gravity coupling effects. *Phys. Rev. Lett.*, vol. 113, p. 023 005, 2 Jul. 2014.

[12] D. Schlippert, J. Hartwig, H. Albers, L. L. Richardson, C. Schubert, A. Roura, W. P. Schleich, W. Ertmer, and E. M. Rasel, Quantum test of the universality of free fall. *Phys. Rev. Lett.*, vol. 112, p. 203 002, 20 May 2014.

[13] L. Zhou, S. Long, B. Tang, X. Chen, F. Gao, W. Peng, W. Duan, J. Zhong, Z. Xiong, J. Wang, Y. Zhang, and M. Zhan, Test of equivalence principle at 1e-8 level by a dual-species double-diffraction raman atom interferometer. *Phys. Rev. Lett.*, vol. 115, p. 013 004, 1 Jul. 2015.

[14] A. Bonnin, N. Zahzam, Y. Bidel, and A. Bresson, Characterization of a simultaneous dual-species atom interferometer for a quantum test of the weak equivalence principle. *Phys. Rev. A*, vol. 92, p. 023 626, 2 Aug. 2015.

[15] X.-C. Duan, X.-B. Deng, M.-K. Zhou, K. Zhang, W.-J. Xu, F. Xiong, Y.-Y. Xu, C.-G. Shao, J. Luo, and Z.-K. Hu, Test of the universality of free fall with atoms in different spin orientations. *Phys. Rev. Lett.*, vol. 117, p. 023 001, 2 Jul. 2016.

[16] B. Barrett, L. Antoni-Micollier, L. Chichet, B. Battelier, T. Lévèque, A. Landragin, and P. Bouyer, Dual matter-wave inertial sensors in weightlessness. *Nature Communications*, vol. 7, p. 13 786, Dec. 2016.

[17] G. Rosi, G. D'Amico, L. Cacciapuoti, F. Sorrentino, M. Prevedelli, M. Zych, C. Brukner, and G. M. Tino, Quantum test of the equivalence principle for atoms in coherent superposition of internal energy states. *Nat. Commun.*, vol. 8, p. 15 529, Jun. 2017.

[18] S. Dimopoulos, P. W. Graham, J. M. Hogan, and M. A. Kasevich, Testing general relativity with atom interferometry. *Phys. Rev. Lett.*, vol. 98, p. 111 102, 11 Mar. 2007.

[19] G. Varoquaux, R. A. Nyman, R. Geiger, P. Cheinet, A. Landragin, and P. Bouyer, How to estimate the differential acceleration in a two-species atom interferometer to test the equivalence principle. *New Journal of Physics*, vol. 11, no. 11, p. 113 010, 2009.

[20] B. Altschul, Q. G. Bailey, L. Blanchet, K. Bongs, P. Bouyer, L. Cacciapuoti, S. Capozziello, N. Gaaloul, D. Giulini, J. Hartwig, L. Iess, P. Jetzer, A. Landragin, E. Rasel, S. Reynaud, S. Schiller, C. Schubert, F. Sorrentino, U. Sterr, J. D. Tasson, G. M. Tino, P. Tuckey, and P. Wolf, Quantum tests of the einstein equivalence principle with the ste???quest space mission. *Advances in Space Research*, vol. 55, no. 1, pp. 501–524, Jan. 2015.

[21] M. Dupont-Nivet, R. Demur, C. I. Westbrook, and S. Schwartz, Experimental study of the role of trap symmetry in an atom-chip interferometer above the bose-einstein condensation threshold. *New Journal of Physics*, vol. 20, no. 4, p. 043 051, Apr. 2018.

[22] K. Kotru, D. L. Butts, J. M. Kinast, and R. E. Stoner, Large-area atom interferometry with frequency-swept raman adiabatic passage. en, *Physical Review Letters*, vol. 115, no. 10, Aug. 2015.

[23] Z. Fu, B. Wu, B. Cheng, Y. Zhou, K. Weng, D. Zhu, Z. Wang, and Q. Lin, A new type of compact gravimeter for long-term absolute gravity monitoring. *Metrologia*, vol. 56, no. 2, p. 025 001, Feb. 2019.

[24] S.-K. Wang, Y. Zhao, W. Zhuang, T.-C. Li, S.-Q. Wu, J.-Y. Feng, and C.-J. Li, Shift evaluation of the atomic gravimeter nim-agrb-1 and its comparison with fg5x. *Metrologia*, vol. 55, no. 3, pp. 360–365, Apr. 2018.

[25] T. Akatsuka, T. Takahashi, and H. Katori, Optically guided atom interferometer tuned to magic wavelength. *Applied Physics Express*, vol. 10, no. 11, p. 112 501, Oct. 2017.

[26] I. Bloch, J. Dalibard, and S. Nascimbène, Quantum simulations with ultracold quantum gases. *Nature Physics*, vol. 8, p. 267, Apr. 2012.

[27] T. Langen, R. Geiger, and J. Schmiedmayer, Ultracold atoms out of equilibrium. *Annual Review of Condensed Matter Physics*, vol. 6, no. 1, pp. 201–217, 2015. eprint: `http://dx.doi.org/10.1146/annurev-conmatphys-031214-014548`.

[28] M. Srednicki, Chaos and quantum thermalization. *Phys. Rev. E*, vol. 50, pp. 888–901, 1994.

[29] J. M. Deutsch, Quantum statistical mechanics in a closed system. *Phys. Rev. A*, vol. 43, pp. 2046–2049, 4 Feb. 1991.

[30] M. Rigol, V. Dunjko, and M. Olshanii, Thermalization and its mechanism for generic isolated quantum systems. *Nature*, vol. 452, pp. 854–858, 2008.

[31] M. Cramer, C. M. Dawson, J. Eisert, and T. J. Osborne, Exact relaxation in a class of nonequilibrium quantum lattice systems. *Phys. Rev. Lett.*, vol. 100, p. 030 602, 2008.

[32] A. Imambekov, I. E. Mazets, D. S. Petrov, V. Gritsev, S. Manz, S. Hofferberth, T. Schumm, E. Demler, and J. Schmiedmayer, Density ripples in expanding low-dimensional gases as a probe of correlations. *Phys. Rev. A*, vol. 80, no. 3, p. 033 604, Sep. 2009.

[33] S. Manz, R. Bücker, T. Betz, C. Koller, S. Hofferberth, I. E. Mazets, A. Imambekov, E. Demler, A. Perrin, J. Schmiedmayer, and T. Schumm, Two-point density correlations of quasicondensates in free expansion. *Physical Review A*, vol. 81, no. 3, Mar. 2010.

[34] T. Schumm, S. Hofferberth, L. M. Andersson, S. Wildermuth, S. Groth, I. Bar-Joseph, J. Schmiedmayer, and P. Krüger, Matter-wave interferometry in a double well on an atom chip. *Nature Physics*, vol. 1, p. 57, Sep. 2005.

[35] T. Betz, S. Manz, R. Bücker, T. Berrada, C. Koller, G. Kazakov, I. E. Mazets, H.-P. Stimming, A. Perrin, T. Schumm, and J. Schmiedmayer, Two-point phase correlations of a one-dimensional bosonic josephson junction. *Phys. Rev. Lett.*, vol. 106, no. 2, p. 020 407, Jan. 2011.

[36] D. A. Smith, M. Gring, T. Langen, M. Kuhnert, B. Rauer, R. Geiger, T. Kitagawa, I. Mazets, E. Demler, and J. Schmiedmayer, Prethermalization revealed by the relaxation dynamics of full distribution functions. *New Journal of Physics*, vol. 15, no. 7, p. 075 011, 2013.

[37] M. Gring, M. Kuhnert, T. Langen, T. Kitagawa, B. Rauer, M. Schreitl, I. Mazets, D. A. Smith, E. Demler, and J. Schmiedmayer, Relaxation and prethermalization in an isolated quantum system. *Science (New York, N.Y.)*, vol. 337, no. 6100, pp. 1318–22, Sep. 2012.

[38] J. Berges, S. Borsányi, and C. Wetterich, Prethermalization. *Phys. Rev. Lett.*, vol. 93, p. 142 002, 2004.

[39] S. Hofferberth, I. Lesanovsky, B. Fischer, T. Schumm, and J. Schmiedmayer, Non-equilibrium coherence dynamics in one-dimensional Bose gases. *Nature*, vol. 449, pp. 324–327, Sep. 2007.

[40] M. Kuhnert, R. Geiger, T. Langen, M. Gring, B. Rauer, T. Kitagawa, E. Demler, D. A. Smith, and J. Schmiedmayer, Multimode dynamics and emergence of a characteristic length scale in a one-dimensional quantum system. *Physical review letters*, vol. 110, no. 9, p. 090 405, 2013.

[41] R. Geiger, T. Langen, I. Mazets, and J. Schmiedmayer, Local relaxation and light-cone-like propagation of correlations in a trapped one-dimensional bose gas. *New Journal of Physics*, vol. 16, no. 5, p. 053 034, 2014.

[42] T. Langen, R. Geiger, M. Kuhnert, B. Rauer, and J. Schmiedmayer, Local emergence of thermal correlations in an isolated quantum many-body system. en, *Nature Physics*, vol. 9, no. 10, pp. 640–643, Oct. 2013.

[43] P. Calabrese and J. Cardy, Time dependence of correlation functions following a quantum quench. *Phys. Rev. Lett.*, vol. 96, p. 136 801, 13 Apr. 2006.

[44] M. Cramer, C. M. Dawson, J. Eisert, and T. J. Osborne, Exact relaxation in a class of nonequilibrium quantum lattice systems. *Phys. Rev. Lett.*, vol. 100, p. 030 602, 3 Jan. 2008.

[45] M. Cheneau, P. Barmettler, D. Poletti, M. Endres, P. S. T. Fukuhara, C. Gross, I. Bloch, C. Kollath, and S. Kuhr, Light-cone-like spreading of correlations in a quantum many-body system. *Nature*, vol. 481, p. 484, 2012.

[46] T. Langen, S. Erne, R. Geiger, B. Rauer, T. Schweigler, M. Kuhnert, W. Rohringer, I. E. Mazets, T. Gasenzer, and J. Schmiedmayer, Experimental observation of a generalized gibbs ensemble. *Science*, vol. 348, no. 6231, pp. 207–211, 2015. eprint: `http://science.sciencemag.org/content/348/6231/207.full.pdf`.

[47] T. Langen, Experimental observation of a generalized gibbs ensemble. In *Non-equilibrium Dynamics of One-Dimensional Bose Gases*, T. Langen, Ed., Cham: Springer International Publishing, 2015, pp. 111–121.

[48] B. Rauer, S. Erne, T. Schweigler, F. Cataldini, M. Tajik, and J. Schmiedmayer, Recurrences in an isolated quantum many-body system. *Science*, eaan7938, Feb. 2018.

[49] T. Schweigler, V. Kasper, S. Erne, I. Mazets, B. Rauer, F. Cataldini, T. Langen, T. Gasenzer, J. Berges, and J. Schmiedmayer, Experimental characterization of a quantum many-body system via higher-order correlations. *Nature*, vol. 545, p. 323, May 2017.

[50] B. Rauer, Gri šins, I. E. Mazets, T. Schweigler, W. Rohringer, R. Geiger, T. Langen, and J. Schmiedmayer, Cooling of a one-dimensional bose gas. *Phys. Rev. Lett.*, vol. 116, p. 030 402, 3 Jan. 2016.

[51] T. Langen, M. Gring, M. Kuhnert, B. Rauer, R. Geiger, D. A. Smith, I. E. Mazets, and J. Schmiedmayer, Prethermalization in one-dimensional bose gases: Description by a stochastic ornstein-uhlenbeck process. *The European Physical Journal Special Topics*, vol. 217, no. 1, pp. 43–53, 2013.

[52] C. Bordé, Atomic interferometry with internal state labelling. *Physics Letters A*, vol. 140, no. 1Ãâ âœ2, pp. 10–12, Sep. 1989.

[53] M. Kasevich and S. Chu, Atomic interferometry using stimulated raman transitions. *Phys. Rev. Lett.*, vol. 67, pp. 181–184, 2 Jul. 1991.

[54] D. Savoie, Continuous and interleaved operation of a cold atom gyroscope and improvement of its stability. PhD thesis, Université Pierre et Marie Curie, 2017.

[55] E. Gourgoulhon, *Special Relativity in General Frames: From Particles to Astrophysics*, ser. Graduate Texts in Physics. Springer Berlin Heidelberg, 2013.

[56] T. Lévèque, Development of a high sensitivity cold atom gyroscope based on a folded geometry. Theses, Université Pierre et Marie Curie - Paris VI, Sep. 2010.

[57] P. Storey and C. Cohen-Tannoudji, The feynman path integral approach to atomic interferometry. *J. Phys. II France*, vol. 4, p. 1999, 1994.

[58] K. Takase, Precision rotation rate measurements with a mobile atom interferometer. PhD thesis, Stanford University, 2008.

[59] P. Cheinet, B. Canuel, F. P. D. Santos, A. Gauguet, F. Yver-Leduc, and A. Landragin, Measurement of the sensitivity function in a time-domain atomic interferometer. *IEEE Transactions on Instrumentation and Measurement*, vol. 57, no. 6, pp. 1141–1148, Jun. 2008.

[60] M. Meunier, I. Dutta, R. Geiger, C. Guerlin, C. L. Garrido Alzar, and A. Landragin, Stability enhancement by joint phase measurements in a single cold atomic fountain. *Phys. Rev. A*, vol. 90, p. 063 633, 6 Dec. 2014.

[61] R. Legere and K. Gibble, Quantum Scattering in a Juggling Atomic Fountain. *Phys. Rev. Lett.*, vol. 81, no. 26, pp. 5780–5783, Dec. 1998.

[62] Z.-K. Hu, X.-C. Duan, M.-K. Zhou, B.-L. Sun, J.-B. Zhao, M.-M. Huang, and J. Luo, Simultaneous differential measurement of a magnetic-field gradient by atom interferometry using double fountains. *Physical Review A*, vol. 84, no. 1, p. 013 620, 2011.

[63] B. Canuel, F. Leduc, D. Holleville, A. Gauguet, J. Fils, A. Virdis, A. Clairon, N. Dimarcq, C. J. Bordé, A. Landragin, and P. Bouyer, Six-axis inertial sensor using cold-atom interferometry. *Phys. Rev. Lett.*, vol. 97, p. 010 402, 1 Jul. 2006.

[64] G. Rosi, F. Sorrentino, L. Cacciapuoti, M. Prevedelli, and G. M. Tino, Precision measurement of the newtonian gravitational constant using cold atoms. *Nature*, vol. 510, no. 7506, pp. 518–521, Jun. 2014.

[65] G. W. Biedermann, K. Takase, X. Wu, L. Deslauriers, S. Roy, and M. A. Kasevich, Zero-Dead-Time Operation of Interleaved Atomic Clocks. *Phys. Rev. Lett.*, vol. 111, no. 17, p. 170 802, Oct. 2013.

[66] I. Dutta, D. Savoie, B. Fang, B. Venon, C. L. Garrido Alzar, R. Geiger, and A. Landragin, Continuous Cold-Atom Inertial Sensor with 1 nrad / sec Rotation Stability. en, *Physical Review Letters*, vol. 116, no. 18, May 2016.

[67] S. Merlet, J. L. Gouët, Q. Bodart, A. Clairon, A. Landragin, F. P. D. Santos, and P. Rouchon, Operating an atom interferometer beyond its linear range. *Metrologia*, vol. 46, no. 1, pp. 87–94, Jan. 2009.

[68] J. K. Stockton, K. Takase, and M. A. Kasevich, Absolute Geodetic Rotation Measurement Using Atom Interferometry. *Phys. Rev. Lett.*, vol. 107, no. 13, p. 133 001, Sep. 2011.

[69] C. Jekeli, Navigation Error Analysis of Atom Interferometer Inertial Sensor. en, *Navigation*, vol. 52, no. 1, pp. 1–14, Mar. 2005.

[70] W. Chaibi, R. Geiger, B. Canuel, A. Bertoldi, A. Landragin, and P. Bouyer, Low frequency gravitational wave detection with ground-based atom interferometer arrays. *Phys. Rev. D*, vol. 93, p. 021 101, 2 Jan. 2016.

[71] P. W. Graham, J. M. Hogan, M. A. Kasevich, and S. Rajendran, Resonant mode for gravitational wave detectors based on atom interferometry. *Phys. Rev. D*, vol. 94, p. 104 022, 10 Nov. 2016.

[72] D. Savoie, M. Altorio, B. Fang, L. A. Sidorenkov, R. Geiger, and A. Landragin, Interleaved atom interferometry for high-sensitivity inertial measurements. *Sci Adv*, vol. 4, no. 12, eaau7948, Dec. 2018.

[73] J. Lautier, L. Volodimer, T. Hardin, S. Merlet, M. Lours, F. Pereira Dos Santos, and A. Landragin, Hybridizing matter-wave and classical accelerometers. *Appl. Phys. Lett.*, vol. 105, no. 14, p. 144 102, Oct. 2014.

[74] A. Gauguet, B. Canuel, T. Leveque, W. Chaibi, and A. Landragin, Characterization and limits of a cold-atom sagnac interferometer. *Phys. Rev. A*, vol. 80, p. 063 604, 2009.

[75] G. Tackmann, P. Berg, C. Schubert, S. Abend, M. Gilowski, W. Ertmer, and E. M. Rasel, Self-alignment of a compact large-area atomic sagnac interferometer. *New Journal of Physics*, vol. 14, no. 1, p. 015 002, Jan. 2012.

[76] H. C. Lefévre, The fiber-optic gyroscope, a century after Sagnac's experiment: The ultimate rotation-sensing technology? *Comptes Rendus Physique*, The Sagnac effect: 100 years later / L'effet Sagnac : 100 ans apr??s, vol. 15, no. 10, pp. 851–858, Dec. 2014.

[77] S. A. Werner, J. .-.-L. Staudenmann, and R. Colella, Effect of earth's rotation on the quantum mechanical phase of the neutron. *Phys. Rev. Lett.*, vol. 42, pp. 1103–1106, 17 Apr. 1979.

[78] D. K. Atwood, M. A. Horne, C. G. Shull, and J. Arthur, Neutron phase shift in a rotating two-crystal interferometer. *Phys. Rev. Lett.*, vol. 52, pp. 1673–1676, 19 May 1984.

[79] V. A. Kostelecky and J. D. Tasson, Matter-gravity couplings and lorentz violation. en, *Physical Review D*, vol. 83, no. 1, Jan. 2011.

[80] B. Barrett, P. Cheiney, B. Battelier, F. Napolitano, and P. Bouyer, Multidimensional atom optics and interferometry. *Phys. Rev. Lett.*, vol. 122, p. 043 604, 4 Feb. 2019.

[81] P. Treutlein, K. Y. Chung, and S. Chu, High-brightness atom source for atomic fountains. en, *Physical Review A*, vol. 63, no. 5, Apr. 2001.

[82] M. Vallée, J. P. Ampuero, K. Juhel, P. Bernard, J.-P. Montagner, and M. Barsuglia, Observations and modeling of the elastogravity signals preceding direct seismic waves. *Science*, vol. 358, no. 6367, p. 1164, Dec. 2017.

[83] K. U. Schreiber and J.-P. R. Wells, Invited review article: Large ring lasers for rotation sensing. *Rev. Sci. Instrum.*, vol. 84, no. 4, 041101, 2013.

[84] Website of the project ROtational Motions in seismologY: `https://www.geophysik.uni-muenchen.de/ROMY/`.

[85] N. Altamirano, P. Corona-Ugalde, R. B. Mann, and M. Zych, Gravity is not a pairwise local classical channel. *Classical and Quantum Gravity*, vol. 35, no. 14, p. 145 005, Jun. 2018.

[86] B. Barrett, R. Geiger, I. Dutta, M. Meunier, B. Canuel, A. Gauguet, P. Bouyer, and A. Landragin, The Sagnac effect: 20 years of development in matter-wave interferometry.

Comptes Rendus Physique, The Sagnac effect: 100 years later / L'effet Sagnac : 100 ans après, vol. 15, no. 10, pp. 875–883, Dec. 2014.

[87] R. Geiger, I. Dutta, D. Savoie, B. Fang, C. Garrido Alzar, C. Guerlin, M. Meunier, T. Leveque, B. Venon, M. Lours, and A. Landragin, Gyromètre à atomes froids de grande sensibilité. *Revue française de métrologie*, no. 41, pp. 21–27, Apr. 2016.

[88] B. Fang, I. Dutta, P. Gillot, D. Savoie, J. Lautier, B. Cheng, C. L. G. Alzar, R. Geiger, S. Merlet, F. P. D. Santos, and A. Landragin, Metrology with atom interferometry: Inertial sensors from laboratory to field applications. *J. Phys. Conf. Ser.*, vol. 723, no. 1, p. 012 049, Jul. 2016.

[89] B. Fang, N. Mielec, D. Savoie, M. Altorio, A. Landragin, and R. Geiger, Improving the phase response of an atom interferometer by means of temporal pulse shaping. *New Journal of Physics*, vol. 20, no. 2, p. 023 020, 2018.

[90] H. Muller, S.-w. Chiow, Q. Long, S. Herrmann, and S. Chu, Atom Interferometry with up to 24-Photon-Momentum-Transfer Beam Splitters. en, *Physical Review Letters*, vol. 100, no. 18, May 2008.

[91] T. Lévèque, A. Gauguet, F. Michaud, F. Pereira Dos Santos, and A. Landragin, Enhancing the Area of a Raman Atom Interferometer Using a Versatile Double-Diffraction Technique. *Phys. Rev. Lett.*, vol. 103, no. 8, p. 080 405, Aug. 2009.

[92] P. Cladé, S. Guellati-Khélifa, F. Nez, and F. Biraben, Large momentum beam splitter using bloch oscillations. *Phys. Rev. Lett.*, vol. 102, p. 240 402, 24 Jun. 2009.

[93] S.-w. Chiow, T. Kovachy, H.-C. Chien, and M. A. Kasevich, $102\hbar k$ large area atom interferometers. *Phys. Rev. Lett.*, vol. 107, p. 130 403, 13 Sep. 2011.

[94] G. D. McDonald, C. C. N. Kuhn, S. Bennetts, J. E. Debs, K. S. Hardman, M. Johnsson, J. D. Close, and N. P. Robins, 80 hbar k momentum separation with Bloch oscillations in an optically guided atom interferometer. en, *Physical Review A*, vol. 88, no. 5, Nov. 2013.

[95] T. Mazzoni, X. Zhang, R. Del Aguila, L. Salvi, N. Poli, and G. M. Tino, Large-momentum-transfer bragg interferometer with strontium atoms. *Phys. Rev. A*, vol. 92, p. 053 619, 5 Nov. 2015.

[96] F. Gori, Flattened gaussian beams. *Optics Communications*, vol. 107, no. 5, pp. 335–341, May 1994.

[97] J. A. Hoffnagle and C. M. Jefferson, Design and performance of a refractive optical system that converts a gaussian to a flattop beam. *Appl. Opt.*, vol. 39, no. 30, pp. 5488–5499, Oct. 2000.

[98] M. Büchner, R. Delhuille, A. Miffre, C. Robilliard, J. Vigué, and C. Champenois, Diffraction phases in atom interferometers. en, *Physical Review A*, vol. 68, no. 1, Jul. 2003.

[99] N. Mielec, Studies for a top-hat optical resionatorand its application to atom interferometry. PhD thesis, Observatoire de Paris, Université PSL, Sept. 2018.

[100] N. Mielec, M. Altorio, R. Sapam, D. Horville, D. Holleville, L. A. Sidorenkov, A. Landragin, and R. Geiger, Atom interferometry with top-hat laser beams. *Appl. Phys. Lett.*, vol. 113, no. 16, p. 161 108, Oct. 2018.

[101] A. Louchet-Chauvet, T. Farah, Q. Bodart, A. Clairon, A. Landragin, S. Merlet, and F. Pereira Dos Santos, The influence of transverse motion within an atomic gravimeter. *New J. Phys.*, vol. 13, p. 065 025, 2011.

[102] P. Hamilton, M. Jaffe, J. M. Brown, L. Maisenbacher, B. Estey, and H. Müller, Atom interferometry in an optical cavity. *Phys. Rev. Lett.*, vol. 114, p. 100 405, 10 Mar. 2015.

[103] M. Dovale-Álvarez, D. D. Brown, A. W. Jones, C. M. Mow-Lowry, H. Miao, and A. Freise, Fundamental limitations of cavity-assisted atom interferometry. *Phys. Rev. A*, vol. 96, p. 053 820, 5 Nov. 2017.

[104] .

[105] D. Fiorucci, A. Hreibi, and W. Chaibi, Telescope-based cavity for negative ion beam neutralization in future fusion reactors. *Appl. Opt.*, vol. 57, no. 7, B122–B134, Mar. 2018.

[106] I. Riou, N. Mielec, G. Lefèvre, M. Prevedelli, A. Landragin, P. Bouyer, A. Bertoldi, R. Geiger, and B. Canuel, A marginally stable optical resonator for enhanced atom interferometry. *Journal of Physics B: Atomic, Molecular and Optical Physics*, vol. 50, no. 15, p. 155 002, 2017.

[107] R. Sapam, N. Mielec, B. Canuel, A. Landragin, R. Geiger, *Study of a compact, large-mode, degenerate optical resonator*, in preparation (March 2019).

[108] A. A. Tovar and L. W. Casperson, Generalized beam matrices: Gaussian beam propagation in misaligned complex optical systems. *JOSA A*, vol. 12, no. 7, pp. 1522–1533, Jul. 1995.

[109] J. Degallaix, Oscar a matlab based optical fft code. *Journal of Physics: Conference Series*, vol. 228, no. 1, p. 012 021, 2010.

[110] T. Kozacki, Numerical errors of diffraction computing using plane wave spectrum decomposition. *Optics Communications*, vol. 281, no. 17, pp. 4219–4223, Sep. 2008.

[111] K. Matsushima and T. Shimobaba, Band-limited angular spectrum method for numerical simulation of free-space propagation in far and near fields. *Opt. Express*, vol. 17, no. 22, pp. 19 662–19 673, Oct. 2009.

[112] V. c. J.-Y. Vinet, *The virgo physics book, vol. ii, optics and related topics, chapter 3 numerical methods, page 179*, 2006.

[113] LIGO Scientific Collaboration and Virgo Collaboration, Observation of gravitational waves from a binary black hole merger. *Phys. Rev. Lett.*, vol. 116, p. 061 102, 6 Feb. 2016.

[114] ——, Gw170817: Observation of gravitational waves from a binary neutron star inspiral. *Phys. Rev. Lett.*, vol. 119, p. 161 101, 16 Oct. 2017.

[115] J. H. Taylor and J. M. Weisberg, A new test of general relativity - Gravitational radiation and the binary pulsar PSR 1913+16. *Astrophysics Journal*, vol. 253, pp. 908–920, Feb. 1982.

[116] Detection of gravitational waves, website of the LIGO Scientific Collaboration, `https://www.ligo.org/detections.php` (accessed Feb. 2019).

[117] LIGO Caltech website at `https://www.ligo.caltech.edu/page/science-impact`.

[118] Christopher Moore, Robert Cole and Christopher Berry, Gravitational Wave Detectors and Sources, `http://gwplotter.com/`, accessed Feb. 2019.

[119] R. Geiger, in *Future Gravitational Wave Detectors Based on Atom Interferometry,* May 2016, pp. 285–313.

[120] The LIGO Scientific Collaboration, Advanced ligo. *Classical and Quantum Gravity*, vol. 32, no. 7, p. 074 001, Mar. 2015.

[121] The VIRGO Collaboration, Advanced virgo: A second-generation interferometric gravitational wave detector. *Classical and Quantum Gravity*, vol. 32, no. 2, p. 024 001, Dec. 2014.

[122] Website of the Einstein Telescope at `http://www.et-gw.eu/` (February 2019).

[123] G. Tino and F. Vetrano, Atom interferometers for gravitational wave detection: A look at a simple configuration. English, *General Relativity and Gravitation*, vol. 43, no. 7, pp. 2037–2051, 2011.

[124] C. J. Bordé, Quantum theory of atom-wave beam splitters and application to multidimensional atomic gravito-inertial sensors. *General Relativity and Gravitation*, vol. 36, no. 3, pp. 475–502, 2004.

[125] J.-Y. Vinet, The VIRGO physics book, Chapter 2: Optics and related topics, available at `http://www.virgo-gw.eu/vpb/`., 2016.

[126] J. M. McGuirk, G. T. Foster, J. B. Fixler, M. J. Snadden, and M. A. Kasevich, Sensitive absolute-gravity gradiometry using atom interferometry. *Phys. Rev. A*, vol. 65, p. 033 608, 3 Feb. 2002.

[127] P. R. Saulson, Terrestrial gravitational noise on a gravitational wave antenna. *Phys. Rev. D*, vol. 30, pp. 732–736, 4 Aug. 1984.

[128] O. Hosten, N. J. Engelsen, R. Krishnakumar, and M. A. Kasevich, Measurement noise 100 times lower than the quantum-projection limit using entangled atoms. *Nature*, vol. 529, no. 7587, pp. 505–508, Jan. 2016.

[129] S. Dimopoulos, P. W. Graham, J. M. Hogan, M. A. Kasevich, and S. Rajendran, Atomic gravitational wave interferometric sensor. *Phys. Rev. D*, vol. 78, p. 122 002, 12 Dec. 2008.

[130] M. Beccaria, M. Bernardini, S. Braccini, C. Bradaschia, A. Bozzi, C. Casciano, G. Cella, A. Ciampa, E. Cuoco, G. Curci, E. D'Ambrosio, V. Dattilo, G. D. Carolis, R. D. Salvo, A. D. Virgilio, A. Delapierre, D. Enard, A. Errico, G. Feng, I. Ferrante, F. Fidecaro, F. Frasconi, A. Gaddi, A. Gennai, G. Gennaro, A. Giazotto, P. L. Penna, G. Losurdo, M. Maggiore, S. Mancini, F. Palla, H. B. Pan, F. Paoletti, A. Pasqualetti, R. Passaquieti, D. Passuello, R. Poggiani, P. Popolizio, F. Raffaelli, S. Rapisarda, A. ViceríÃ©, and Z. Zhang, Relevance of newtonian seismic noise for the virgo interferometer sensitivity. *Classical and Quantum Gravity*, vol. 15, no. 11, pp. 3339–, 1998.

[131] ET - Einstein gravitational wave Telescope - Design Study, A joint European Project; Web: `http://www.et-gw.eu`.

[132] P. Amaro-Seoane et al, Low-frequency gravitational-wave science with elisa/ngo. *Classical and Quantum Gravity*, vol. 29, no. 12, p. 124 016, 2012.

[133] J. Harms, B. J. J. Slagmolen, R. X. Adhikari, M. C. Miller, M. Evans, Y. Chen, H. Müller, and M. Ando, Low-frequency terrestrial gravitational-wave detectors. *Phys. Rev. D*, vol. 88, p. 122 003, 12 Dec. 2013.

[134] R. Geiger et al, Matter-wave laser interferometric gravitation antenna (miga): New perspectives for fundamental physics and geosciences. In *Proceedings of the 50th Rencontres de Moriond*, E. Augé, J. Dumarchez, and J. Trân Thanh Vân, Eds., La Thuile, Italy: ARISF, 21-28 March 2015 2015.

[135] B. Canuel, A. Bertoldi, L. Amand, E. Pozzo di Borgo, T. Chantrait, C. Danquigny, M. Dovale Álvarez, B. Fang, A. Freise, R. Geiger, J. Gillot, S. Henry, J. Hinderer, D. Holleville, J. Junca, G. Lefèvre, M. Merzougui, N. Mielec, T. Monfret, S. Pelisson, M. Prevedelli, S. Reynaud, I. Riou, Y. Rogister, S. Rosat, E. Cormier, A. Landragin, W. Chaibi, S. Gaffet, and P. Bouyer, Exploring gravity with the miga large scale atom interferometer. *Scientific Reports*, vol. 8, no. 1, p. 14 064, Sep. 2018.

[136] H. Müller, S. Chiow, and S. Chu, Atom-wave diffraction between the Raman-Nath and the Bragg regime: Effective Rabi frequency, losses, and phase shifts. *Phys. Rev. A*, vol. 77, no. 2, p. 023 609, Feb. 2008.

[137] LSBB, *Low noise underground laboratory*, 2016.

[138] J. Junca, A. Bertoldi, D. O. Sabulsky, G. Lefèvre, X. Zou, J.-B. Decitre, **R. Geiger**, A. Landragin, S. Gaffet, P. Bouyer, and B. Canuel, Characterizing Earth gravity field fluctuations with the MIGA antenna for future Gravitational Wave detectors, submitted to Phys. Rev. D (2019).

[139] Muquans laser systems, `https://www.muquans.com/index.php/products/laser-systems` (February 2019).

[140] Workshop on future instruments for gravity-based earthquake early warning, APC laboratory, Paris, 10th of January 2018, `https://indico.in2p3.fr/event/16950/`.

[141] N. Yu and M. Tinto, Gravitational wave detection with single-laser atom interferometers. English, *General Relativity and Gravitation*, vol. 43, no. 7, pp. 1943–1952, 2011.

[142] P. W. Graham, J. M. Hogan, M. A. Kasevich, and S. Rajendran, New method for gravitational wave detection with atomic sensors. *Phys. Rev. Lett.*, vol. 110, p. 171 102, 17 Apr. 2013.

[143] J. M. Hogan and M. A. Kasevich, Atom-interferometric gravitational-wave detection using heterodyne laser links. *Phys. Rev. A*, vol. 94, p. 033 632, 3 Sep. 2016.

[144] P. L. Bender, Comparison of atom interferometry with laser interferometry for gravitational wave observations in space. *Phys. Rev. D*, vol. 89, p. 062 004, 6 Mar. 2014.

[145] L. Hu, N. Poli, L. Salvi, and G. M. Tino, Atom interferometry with the sr optical clock transition. *Phys. Rev. Lett.*, vol. 119, p. 263 601, 26 Dec. 2017.

[146] B. Canuel, S. Pelisson, L. Amand, A. Bertoldi, E. Cormier, B. Fang, S. Gaffet, R. Geiger, J. Harms, D. Holleville, A. Landragin, G. Lefèvre, J. Lhermite, N. Mielec, M. Prevedelli, I. Riou, and P. Bouyer, MIGA: Combining laser and matter wave interferometry for mass distribution monitoring and advanced geodesy., J. Stuhler and A. J. Shields, Eds., Apr. 2016, p. 990 008.

[147] B. Canuel, L. Amand, A. Bertoldi, W. Chaibi, R. Geiger, J. Gillot, A. Landragin, M. Merzougui, I. Riou, S. Schmid, and P. Bouyer, The matter-wave laser interferometer gravitation antenna (MIGA): New perspectives for fundamental physics and geosciences. *E3S Web of Conferences*, vol. 4, P. Febvre, E. P. di Borgo, and K. Coulié-Castellani, Eds., p. 01 004, 2014.

[148] R. Geiger and M. Trupke, Proposal for a quantum test of the weak equivalence principle with entangled atomic species. *Phys. Rev. Lett.*, vol. 120, p. 043 602, 4 Jan. 2018.

[149] J. Tomkovic, M. Schreiber, J. Welte, M. Kiffner, J. Schmiedmayer, and M. K. Oberthaler, Single spontaneous photon as a coherent beamsplitter for an atomic matter-wave. *Nat Phys*, vol. 7, no. 5, pp. 379–382, May 2011.

[150] C. Cabrillo, J. I. Cirac, P. Garcıa-Fernández, and P. Zoller, Creation of entangled states of distant atoms by interference. *Phys. Rev. A*, vol. 59, pp. 1025–1033, 2 Feb. 1999.

[151] L. Slodicka, G. Hétet, N. Röck, P. Schindler, M. Hennrich, and R. Blatt, Atom-atom entanglement by single-photon detection. *Phys. Rev. Lett.*, vol. 110, p. 083 603, 8 Feb. 2013.

[152] A. Kuhn, M. Hennrich, T. Bondo, and G. Rempe, Controlled generation of single photons from a strongly coupled atom-cavity system. *Applied Physics B*, vol. 69, no. 5, pp. 373–377, Dec. 1999.

[153] T. Wilk, S. C. Webster, H. P. Specht, G. Rempe, and A. Kuhn, Polarization-controlled single photons. *Physical Review Letters*, vol. 98, no. 6, Feb. 2007.

[154] B. Weber, H. P. Specht, T. Müller, J. Bochmann, M. Mücke, D. L. Moehring, and G. Rempe, Photon-Photon Entanglement with a Single Trapped Atom. en, *Physical Review Letters*, vol. 102, no. 3, Jan. 2009.

[155] M. Lettner, M. Mücke, S. Riedl, C. Vo, C. Hahn, S. Baur, J. Bochmann, S. Ritter, S. Dürr, and G. Rempe, Remote entanglement between a single atom and a bose-einstein condensate. *Phys. Rev. Lett.*, vol. 106, p. 210 503, 21 May 2011.

[156] M. Aspelmeyer, C. Brukner, D. Giulini, and G. Milburn, Focus on gravitational quantum physics. *New Journal of Physics*, vol. 19, no. 5, p. 050 401, 2017.

[157] D. Kruse, M. Ruder, J. Benhelm, C. von Cube, C. Zimmermann, P. W. Courteille, T. Elsässer, B. Nagorny, and A. Hemmerich, Cold atoms in a high- Q ring cavity. en, *Physical Review A*, vol. 67, no. 5, May 2003.

[158] M. Hennrich, T. Legero, A. Kuhn, and G. Rempe, Vacuum-stimulated raman scattering based on adiabatic passage in a high-finesse optical cavity. *Phys. Rev. Lett.*, vol. 85, pp. 4872–4875, 23 Dec. 2000.

[159] Daniel Adam Steck, Rubidium 87 and Rubidium 85 D Line Data, January 2015.

[160] G. S. Vasilev, D. Ljunggren, and A. Kuhn, Single photons made-to-measure. *New Journal of Physics*, vol. 12, no. 6, p. 063 024, 2010.

[161] N. V. Vitanov, A. A. Rangelov, B. W. Shore, and K. Bergmann, Stimulated raman adiabatic passage in physics, chemistry, and beyond. *Reviews of Modern Physics*, vol. 89, no. 1, p. 015 006, 2017.

[162] M. Mücke, J. Bochmann, C. Hahn, A. Neuzner, C. Nölleke, A. Reiserer, G. Rempe, and S. Ritter, Generation of single photons from an atom-cavity system. *Phys. Rev. A*, vol. 87, p. 063 805, 6 Jun. 2013.

[163] T. Wilk, Quantum interface between an atom and a photon. Dissertation, Technische Universität München, München, 2008.

[164] *See, for example, the single photon couting modules from Excelitas.*

[165] A. M. Kaufman, B. J. Lester, and C. A. Regal, Cooling a Single Atom in an Optical Tweezer to Its Quantum Ground State. en, *Physical Review X*, vol. 2, no. 4, Nov. 2012.

[166] J. D. Thompson, T. G. Tiecke, A. S. Zibrov, V. Vuletić, and M. D. Lukin, Coherence and Raman Sideband Cooling of a Single Atom in an Optical Tweezer. en, *Physical Review Letters*, vol. 110, no. 13, Mar. 2013.

[167] P. Xu, J. Yang, M. Liu, X. He, Y. Zeng, K. Wang, J. Wang, D. J. Papoular, G. V. Shlyapnikov, and M. Zhan, Interaction-induced decay of a heteronuclear two-atom system. *Nature Communications*, vol. 6, p. 7803, Jul. 2015.

[168] D. Stuart and A. Kuhn, Single-atom trapping and transport in DMD-controlled optical tweezers. *ArXiv e-prints*, Aug. 2017. arXiv: `1708.06672 [physics.atom-ph]`.

[169] P. Sompet, Y. H. Fung, E. Schwartz, M. D. J. Hunter, J. Phrompao, and M. F. Andersen, Zeeman-insensitive cooling of a single atom to its two-dimensional motional ground state in tightly focused optical tweezers. *Phys. Rev. A*, vol. 95, p. 031 403, 3 Mar. 2017.

[170] L. P. Parazzoli, A. M. Hankin, and G. W. Biedermann, Observation of free-space single-atom matter wave interference. *Phys. Rev. Lett.*, vol. 109, p. 230 401, 23 Dec. 2012.

[171] C. Tuchendler, A. M. Lance, A. Browaeys, Y. R. P. Sortais, and P. Grangier, Energy distribution and cooling of a single atom in an optical tweezer. *Phys. Rev. A*, vol. 78, p. 033 425, 3 Sep. 2008.

[172] J. Beugnon, C. Tuchendler, H. Marion, A. Gaëtan, Y. Miroshnychenko, Y. R. P. Sortais, A. M. Lance, M. P. A. Jones, G. Messin, A. Browaeys, and P. Grangier, Two-dimensional transport and transfer of a single atomic qubit in optical tweezers. en, *Nature Physics*, vol. 3, no. 10, pp. 696–699, Oct. 2007.

[173] M. A. Horne, A. Shimony, and A. Zeilinger, Two-particle interferometry. *Phys. Rev. Lett.*, vol. 62, pp. 2209–2212, 19 May 1989.

[174] J. G. Rarity and P. R. Tapster, Experimental violation of bell's inequality based on phase and momentum. *Phys. Rev. Lett.*, vol. 64, pp. 2495–2498, 21 May 1990.

[175] G. Santarelli, P. Laurent, P. Lemonde, A. Clairon, A. G. Mann, S. Chang, A. N. Luiten, and C. Salomon, Quantum projection noise in an atomic fountain: A high stability cesium frequency standard. *Phys. Rev. Lett.*, vol. 82, pp. 4619–4622, 23 Jun. 1999.

[176] G. W. Biedermann, X. Wu, L. Deslauriers, K. Takase, and M. A. Kasevich, Low-noise simultaneous fluorescence detection of two atomic states. *Opt. Lett.*, vol. 34, no. 3, pp. 347–349, Feb. 2009.

[177] R. Bücker, A. Perrin, S. Manz, T. Betz, C. Koller, T. Plisson, J. Rottmann, T. Schumm, and J. Schmiedmayer, Single-particle-sensitive imaging of freely propagating ultracold atoms. *New Journal of Physics*, vol. 11, no. 10, p. 103 039, 2009.

[178] A. Fuhrmanek, R. Bourgain, Y. R. P. Sortais, and A. Browaeys, Free-space lossless state detection of a single trapped atom. *Phys. Rev. Lett.*, vol. 106, p. 133 003, 13 Mar. 2011.

[179] *Hamamatsu photomultiplier tubes.*

[180] T. A. Wagner, S. Schlamminger, J. H. Gundlach, and E. G. Adelberger, Torsion-balance tests of the weak equivalence principle. *Classical and Quantum Gravity*, vol. 29, no. 18, p. 184 002, 2012.

[181] P. Dussarrat, M. Perrier, A. Imanaliev, R. Lopes, A. Aspect, M. Cheneau, D. Boiron, and C. I. Westbrook, Two-particle four-mode interferometer for atoms. *Phys. Rev. Lett.*, vol. 119, p. 173 202, 17 Oct. 2017.

[182] D. K. Shin, B. M. Henson, S. S. Hodgman, T. Wasak, J. Chwedenczuk, and A. G. Truscott, A strong Bell correlation witness between spatially separated pairs of atoms. *arXiv e-prints*, arXiv:1811.05681, arXiv:1811.05681, Nov. 2018. arXiv: `1811.05681 [quant-ph]`.

[183] Y. Zeng, P. Xu, X. He, Y. Liu, M. Liu, J. Wang, D. J. Papoular, G. V. Shlyapnikov, and M. Zhan, Entangling Two Individual Atoms of Different Isotopes via Rydberg Blockade. en, *Physical Review Letters*, vol. 119, no. 16, Oct. 2017.

Curriculum Vitae

Remi GEIGER

Date of birth : 14th of February 1985
French nationality
Married, 3 children
Researcher ID: M-4231-2016
Web page: https://sites.google.com/site/researchgeiger/

Current position

since 2013	Associate Professor (Maître de Conférences), Sorbonne Université and SYRTE laboratory, Paris Observatory, France.

Previous positions

2011-2013	Postdoctoral fellow, quantum optics group of J. Schmiedmayer, Vienna University of Technology, Austria.
2008-2011	PhD fellow, atom optics group of A. Aspect, Laboratoire Charles Fabry, Institut d'Optique, Palaiseau, France. Fellowship of the French space agency (CNES).

Education

2011	PhD in Physics, supervision of P. Bouyer, Institut d'Optique, Palaiseau, France. Thesis: *Airborne matter-wave inertial sensor.*
2008	Master in Physics, group of S. Klapp, Technische Universität Berlin, Germany. Thesis: *Long-range order in quasi two-dimensional dipolar fluids: a Density Functional Theory study.*
2008	Engineering degree from Ecole Supérieure d'Electricité, Gif-sur-Yvette, France.

Fellowships and prizes

2015	Laureate of the Edouard Branly prize for young researchers in Physical Sciences from the federation of the French scientific societies and IEEE France.
2012	Laureate of the ParisTech doctoral thesis prize.
2011	Lise Meitner Fellowship of the Austrian Science Fund (project FWF-LM1423).
2010	Young researcher prize of the French space agency (CNES).
2010	Prize of the *Waves and Matter* doctoral school of University Paris Saclay.
2008	Doctoral fellowship from the French space agency.

Teaching activities [hyperlink]

since 2018	Lecturer at Mines-Paris-Tech engineering school (atoms and lasers, Master level) .
since 2013	Full teaching duty of Associate Professor (192 hours per year) at the Physics Department of Sorbonne Université. Courses at Bachelor and Master levels in various fields of Physics.
2014	Course on atom interferometry at the summer school *Frontiers On Matter-wave Optics (FOMO)*, Greece.
2012	Lecture on Laser Cooling and Trapping, Vienna Technical University (Master level).
2012	Course on atom interferometry and atom chips at the summer school *Introductory Course on Ultra-cold Quantum Gases*, Innsbruck, Austria.
2008-2011	Teaching assistant at Supélec (Statistical and solid state Physics - Master) and at Institut d'Optique (Electrodynamics - Bachelor 3).

Reviewing activities

Referee for the journals Physical Review Letters, Physical Review X, Physical Review D, Physical Review Applied, Review of Scientific Instruments.

Institutional responsibilities

since 2018	Co-coordinator of the working group *development of detectors* of the national network for research on gravitational waves of CNRS
since 2015	Co-cordinator of the *Gravitation and Fundamental Physics* research programme of Paris Observatory (6 laboratories).

Collaborations

- Prof. Christophe Collette, Université Libre de Bruxelles, Belgium. Topic: inertial control;
- Dr. Benjamin Canuel, LP2N laboratory, Talence, France. Topic: Experimental developments of a 150-meters cold-atom gradiometer, design of optical cavities;
- Dr. Walid Chaibi ARTEMIS laboratory, Nice, France. Topic: models for gravitational wave detectors based on atom interferometry, design of optical cavities;
- Dr. Michael Trupke, University of Vienna, Austria. Topic: quantum optics and entangled atom interferometry.

Selected publications

LETTERS
nature physics

| DOI: 10.1038/NPHYS2739

Local emergence of thermal correlations in an isolated quantum many-body system

T. Langen*, R. Geiger, M. Kuhnert, B. Rauer and J. Schmiedmayer*

Understanding the dynamics of isolated quantum many-body systems is a central open problem at the intersection between statistical physics and quantum physics. Despite important theoretical effort[1], no generic framework exists yet to understand when and how an isolated quantum system relaxes to a steady state. Regarding the question of how, it has been conjectured[2,3] that equilibration must occur on a local scale in systems where correlations between distant points can establish only at a finite speed. Here, we provide the first experimental observation of this local equilibration hypothesis. In our experiment, we quench a one-dimensional Bose gas by coherently splitting it into two parts. By monitoring the phase coherence between the two parts we observe that the thermal correlations of a prethermalized state[4,5] emerge locally in their final form and propagate through the system in a light-cone-like evolution. Our results underline the close link between the propagation of correlations[2,3,6,7] and relaxation processes in quantum many-body systems.

It has been theoretically suggested that relaxation in generic isolated quantum many-body systems proceeds through the dephasing of the quantum states populated at the onset of the non-equilibrium evolution[8,9]. It is generally believed that this dynamically leads to relaxed states that can be well described either by the usual thermodynamical ensembles or by generalized Gibbs ensembles that take into account dynamical constraints[10]. However, it remains an open question how these relaxed states form dynamically, and in particular, whether they emerge gradually on a global scale, or appear locally and then spread in space and time[3].

Ultracold atomic gases offer an ideal test bed to explore such quantum dynamics. Their almost perfect isolation from the environment and the many available methods to probe their quantum states make it possible to reveal the dynamical evolution of a many-body system at a very detailed level[4,7,11–16].

In our experiment, a phase-fluctuating ultracold one-dimensional (1D) Bose gas[17] is split coherently[18]. The splitting creates a non-equilibrium state consisting of two gases with almost identical phase profiles. Interactions in the many-body system drive the relaxation of this highly phase-correlated state to a prethermalized state, characterized by thermal phase correlations[4,19]. The dynamics is monitored by time-resolved measurements of the relative phase field using matter-wave interferometry[20].

The experimental procedure starts with a 1D degenerate gas of 4,000–12,000 ^{87}Rb atoms trapped at temperatures between 30–110 nK in a magnetic trap, formed 100 µm below the trapping wires of an atom chip[21]. By applying radiofrequency fields through additional wires on the chip, we rapidly transform the initial harmonic trapping potential into a double well, thereby realizing the matter-wave analogue of a coherent beamsplitter[18] (see Methods).

The system is allowed to evolve in the double well for a variable time t, before the gases are released by switching off the trapping potential. They expand and interfere after a time-of-flight of 15.7 ms. The resulting interference pattern allows us to extract the relative phase $\phi(z,t)=\theta_1(z,t)-\theta_2(z,t)$ along the length of the system (Fig. 1). Here, $\theta_1(z,t)$ and $\theta_2(z,t)$ are the phase profiles of the two individual gases. Repeating this procedure approximately 150 times for each value of t, we determine the two-point relative phase correlation function

$$C(\bar{z}=z-z',t)=\mathrm{Re}\,\langle \mathrm{e}^{i\phi(z,t)-i\phi(z',t)}\rangle$$

It measures the degree of correlation between the phases at two arbitrary points z and z', separated by a distance $\bar{z}$ (refs 22,23). In contrast to the integrated visibility of the interference pattern, which was used in a previous experiment to identify the prethermalized state[4], the phase correlation function provides a sensitive probe for the local dynamics, and is therefore ideally suited to study the propagation of correlations.

Typical experimental data are presented in Fig. 2a. Directly after the quench, the phase correlation function $C(\bar{z},t)$ is close to unity for any distance $\bar{z}$. This is a direct manifestation of the long-range phase coherence produced by the splitting process. After a given evolution time t, the phase correlation function decays exponentially up to a characteristic distance $\bar{z}_c$ and stays nearly constant afterwards: $C(\bar{z}>\bar{z}_c,t)=C(\bar{z}_c,t)$. This means that beyond the distance $\bar{z}_c$ long-range phase coherence is retained across the system. With longer evolution time, the position of $\bar{z}_c$ shifts to larger distances and the value of $C(\bar{z}>\bar{z}_c,t)$ gradually decreases. This evolution continues until the system reaches a quasi-steady state, where the correlations decay exponentially throughout the entire system[19]. This prethermalized state corresponds to the relaxed state of the 1D system and can be described by a generalized Gibbs ensemble[4,10]. Our observation that the exponentially decreasing parts of the dynamical phase correlation functions match the exponential decay of the relaxed, prethermalized state for $\bar{z}<\bar{z}_c$ allows us to conclude that equilibration occurs locally in our system.

From the experimental data, we extract the crossover points $\bar{z}_c$ through the level of long-range phase coherence. To this end, we consider for each t the region where the correlation function is constant, extrapolate the constant value to smaller $\bar{z}$ and determine the position $\bar{z}_c$ where it crosses the prethermalized correlation function (Supplementary Information). The result of this procedure is shown in Fig. 2b. We observe a clear linear scaling of the position $\bar{z}_c=2ct$, characterizing the local decay of correlations

---

Vienna Center for Quantum Science and Technology, Atominstitut, TU Wien, Stadionallee 2, 1020 Vienna, Austria. *e-mail: tlangen@ati.ac.at; schmiedmayer@atomchip.org

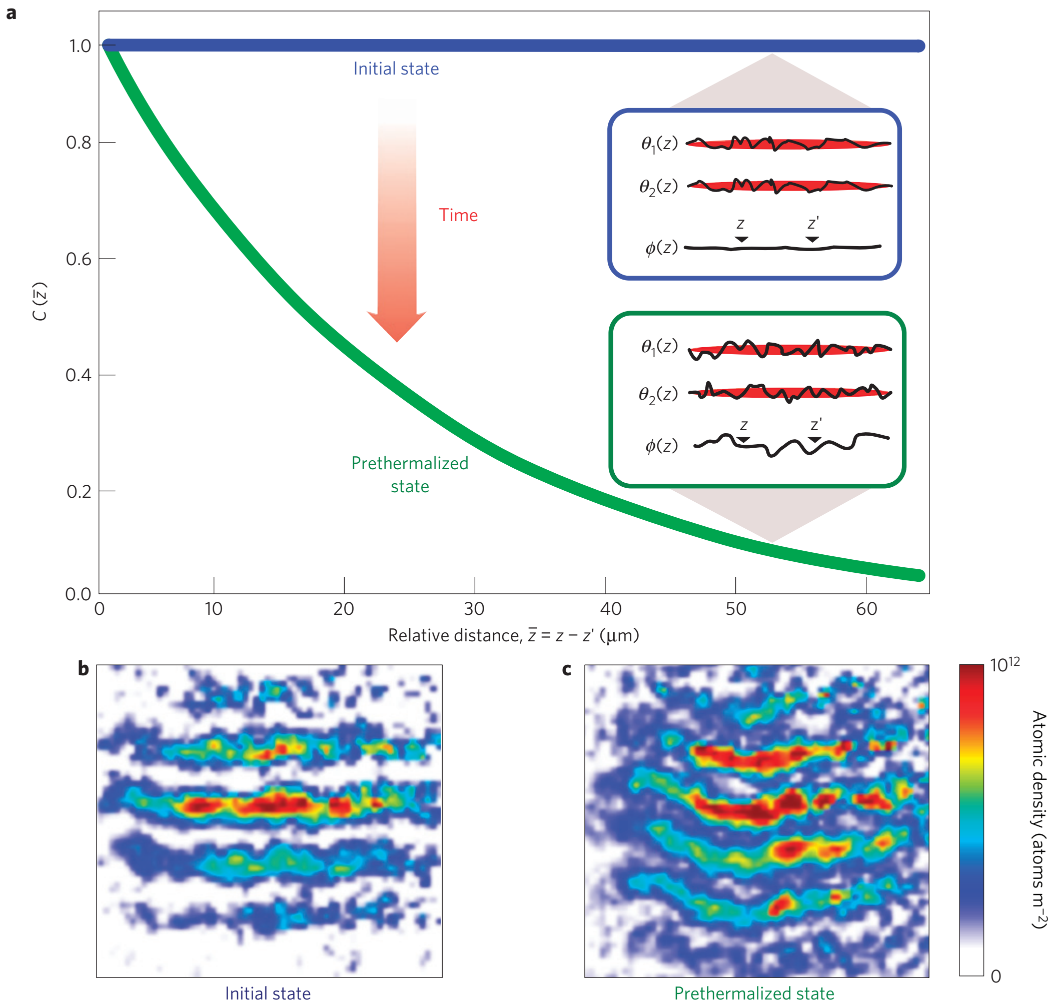

Figure 1 | Characterizing the dynamics of correlations in a coherently split 1D Bose gas. a, The splitting process creates two 1D gases with almost identical longitudinal phase profiles $\theta_1(z)$ and $\theta_2(z)$, corresponding to long-range phase coherence in the relative phase field $\phi(z)=\theta_1(z)-\theta_2(z)$. The degree of relative phase correlations between two arbitrary points z and z' along the length of the system is characterized by the two-point correlation function $C(\bar{z},t)$. Initially, it is close to unity for any distance $\bar{z}=z-z'$ between the points. Over time, this strongly phase-correlated state relaxes towards a prethermalized state, characterized by thermal (exponentially decaying) correlations. The aim of this study is to investigate how the thermal correlations locally emerge in time. In the experiment, the relative phase field is probed using matter-wave interferometry between the two gases. **b**,**c**, Example interference pictures in the initial (**b**) and in the prethermalized state (**c**). In these pictures, the relative phase $\phi(z)$ is directly extracted from the local position of the interference fringes. The phase correlation function is then calculated from an average over approximately 150 interference pictures.

with time. This observation reveals that an arbitrary point in the gas loses its correlations with other points up to a certain separation $\bar{z}_c$, whereas long-range phase coherence persists outside this horizon. The experimental data thus show that the prethermalized state locally emerges in a light-cone-like evolution, where c plays the role of a characteristic velocity for the propagation of correlations in the quantum many-body system. For the data presented in Fig. 2b a linear fit allows us to extract a velocity of $c=1.2\pm0.1\ \mathrm{mm\,s^{-1}}$.

Light-cone-like effects in quantum many-body dynamics have been previously predicted using results from conformal field theory[2], and for 2D superfluids[24]. Similarly, it is known that some quantum spin models exhibit an intrinsic maximum velocity[6] that limits the propagation of correlations and entanglement to an effective light cone[7,25,26]. It has been conjectured that this leads to a local establishment of thermal properties[3].

The light-cone-like emergence of thermal correlations that we observe in this work can be understood using a homogeneous Luttinger-liquid model that effectively describes the interacting many-body system in terms of low-energy excitations[27]. Within the Luttinger-liquid model, these excitations are superpositions of phase and density fluctuations. They are characterized by a linear dispersion relation $\omega_k=c_0|k|$, with k being the momentum of the excitation and c_0 the speed of sound, the latter defining the characteristic velocity in the homogeneous system.

The coherent splitting process equally distributes energy among the excitations, resulting in a $1/k$ dependence of their occupation numbers[28]. Each excitation is initialized with small relative phase fluctuations and high relative density fluctuations. Over time, the amplitude of the phase (density) fluctuations increases (decreases), resulting in a progressive randomization of the relative phase field $\phi(z)$. Eventually, the energy associated with the phase fluctuations equilibrates with the energy associated with the density fluctuations, leading to the thermal phase correlations of the prethermalized state[28].

For a given evolution time t, the dephasing of the excitations with different wavelengths $(2\pi/k)$ randomizes the relative phase field only up to a characteristic distance $\bar{z}_c=2c_0t$. This effect can be understood in the following way (see Methods for mathematical details): the degree of randomization of the phase is related to the amplitude of the contributing phase fluctuations. For

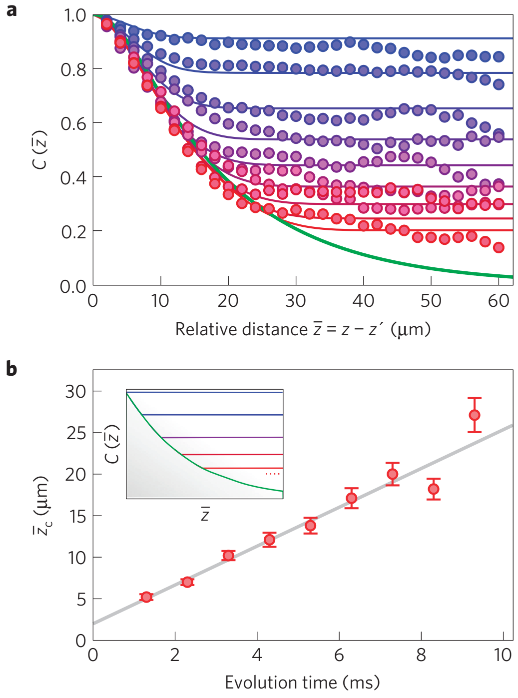

Figure 2 | Local emergence of thermal correlations in a light-cone-like evolution. **a**, Experimental phase correlation functions $C(\bar{z},t)$ (filled circles) compared to theoretical calculations (solid lines). From top to bottom, the evolution time t increases from 1 to 9 ms in steps of 1 ms. The bottom (green) line is the theoretical correlation function of the prethermalized state. For each t, the constant values of $C(\bar{z},t)$ at large $\bar{z}$ can be used to determine the crossover distance $\bar{z}_c(t)$ up to which the system forgets the initial long-range phase coherence (see text for details). **b**, Position of the crossover distance $\bar{z}_c$ as a function of evolution time t, revealing the light-cone-like decay of correlations. Error bars denote the uncertainty in $\bar{z}_c$, following from the standard deviation of the constant values of $C(\bar{z},t)$ and the uncertainty in the effective temperature of the prethermalized state (see Supplementary Information). The solid line is a linear fit, the slope of which corresponds to twice the characteristic velocity of correlations. Inset: schematic visualization of the dynamics with increasing evolution time from top to bottom as in **a**. The decay of correlations is characterized by a front moving with a finite velocity: for a given time t, $C(\bar{z},t)$ is exponential (thermal) only up to the characteristic distance $\bar{z}_c(t)$. Beyond this horizon, long-range phase coherence is retained. Note that in the experimental data shown in **a**, the sharp transitions are smeared out by the finite experimental imaging resolution.

large distances they are associated with the highly occupied long-wavelength excitations that take a long time ($\sim 1/\omega_k$) to be converted from the initial density fluctuations into phase fluctuations. At time t, there exists a characteristic distance beyond which the contribution of these long-wavelength fluctuations to the randomization of the phase is compensated by a decrease of the contribution from the faster short-wavelength fluctuations (see Supplementary Fig. S3 for an illustration). Therefore, the phase does not randomize any further and long-range phase coherence remains beyond $\bar{z}_c$. The sharpness of the transition at $\bar{z}_c$ results from the interference of the many excitations with different momenta.

Alternatively, the excitations in the Luttinger-liquid model can also be identified as pairs of quasi-particles, which propagate in opposite directions with momenta k and $-k$, respectively[2,7]. This interpretation naturally leads to the light-cone condition, as two points separated by $\bar{z}$ can establish thermal correlations if quasi-particles originating from these points meet after a time $t=\bar{z}/2c_0$.

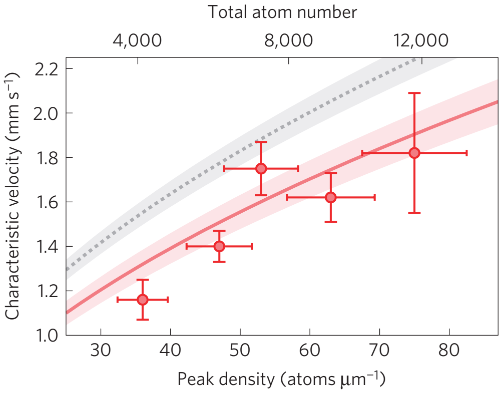

Figure 3 | Scaling of the characteristic velocity with particle number. The solid red (dashed grey) line is the calculated velocity of correlations for a trapped (homogeneous) system. The peak densities are given for each gas. Shaded areas correspond to the uncertainty on the measured trap frequencies. Error bars denote one standard deviation.

In Fig. 2a we compare the results of the Luttinger-liquid calculation to our measured data, taking into account the finite resolution of the imaging system (Supplementary Information). We find good agreement, using independently measured experimental parameters as the input for the theory. This quantitative agreement validates our interpretation of the observations as the local emergence of thermal correlations.

When increasing the number of particles in our quantum many-body system, we expect interaction effects to play a more important role, leading to a faster local relaxation. In the homogeneous limit this is captured by the scaling of the speed of sound $c_0 \sim \sqrt{\rho}$ with the 1D density ρ of each gas[17]. To investigate the scaling of the characteristic velocity, we perform the experiment for a varying number of atoms N in the system. We observe the light-cone-like emergence of the thermal correlations over the whole range of probed atom numbers ($N \sim 4{,}000$–$12{,}000$). In the experimentally realized trapped system, the density varies along the length of the gases, resulting in a spatially dependent speed of sound. Nevertheless, the superposition of many excitations still leads to a single characteristic velocity for the dynamics, which is slightly reduced with respect to the homogeneous case (Supplementary Information). In Fig. 3 we show the measured characteristic velocities. A Luttinger-liquid calculation including the trapping potential describes the experimental data within the experimental error, whereas a purely homogeneous calculation clearly overestimates the characteristic velocity.

In our experiment thermal correlations emerge locally in their final prethermalized form. This supports the local relaxation hypothesis[3] and indicates a general pathway for the emergence of classical properties in isolated quantum many-body systems. In our system, interactions manifest themselves in excitations with a linear dispersion relation (in the homogeneous limit), resulting in a decay of quantum coherence that takes the form of an effective light cone. Whether this scenario holds also for systems with nonlinear dispersion relations, long-range interactions[29] or systems that are subject to disorder[30] remains a topic of intense study.

Methods

Splitting process. The splitting is performed by linearly increasing the amplitude of the radiofrequency current in the chip wires to 24 mA within 12 ms. To minimize longitudinal excitations during the splitting, the initial gas is prepared in a slightly dressed radiofrequency trap that has the same longitudinal confinement as the final double-well potential (see Supplementary Information for more details). The increase of radiofrequency current results in a rapid decay of the tunnel coupling between the two gases. Simulations of the chip potential and experiments with quasi-condensates in thermal equilibrium[23] indicate that the decoupling of the two gases happens within less than 500 µs. This is faster than the characteristic timescale of the dynamics (~10 ms; ref. 19) and therefore realizes a quench.

Relative phase measurement. The interference patterns are recorded after a time-of-flight expansion of 15.7 ms using absorption imaging. The point spread function of the optical system has a measured r.m.s. width of 3.6 µm. The phase $\phi(z)$ of the interference patterns is extracted by fitting each pixel line (of size $\sigma_{\rm px} = 2\,\mu$m) with a cosine-modulated Gaussian function.

Theoretical model. Within the Luttinger Liquid theory the phase correlation function can be written as $C(z,z',t) = \exp(-(1/2)\langle\Delta\phi_{zz'}(t)^2\rangle)$, with $\Delta\phi_{zz'}(t) = \phi(z,t) - \phi(z',t)$. In the homogeneous limit, the local relative phase variance is given by[28,31]

$$\langle\Delta\phi_{zz'}(t)^2\rangle = \frac{\pi^2\rho}{LK^2}\sum_{k\neq 0}\frac{\sin(\omega_k t)^2}{k^2}(1-\cos(k\bar{z})) \qquad (1)$$

with L being the length of the system, $k = 2\pi n/L$ the momentum of the excitations ($n \neq 0$ integer) and K the Luttinger parameter. The amount of fluctuations is thus determined by the interference of several longitudinal modes of the 1D system.

The first term in the sum (1) represents the growth and subsequent oscillations in the amplitude of the phase fluctuations as they get converted from the initial density fluctuations. The factor $1/k^2$ in the amplitude reflects the $1/k$ scaling of the excitation occupation numbers associated with the equipartition of energy induced by the fast splitting. The second term in the sum corresponds to the spatial fluctuations. Expression (1) is the Fourier decomposition of a trapezoid with a sliding edge at $\bar{z}_c = 2c_0 t$, which explains the two-step feature of the phase correlation function.

A similar expression can be derived for the trapped system probed in the experiment (Supplementary Information).

Received 15 May 2013; accepted 29 July 2013; published online 8 September 2013

References

1. Polkovnikov, A., Sengupta, K., Silva, A. & Vengalattore, M. Nonequilibrium dynamics of closed interacting quantum systems. *Rev. Mod. Phys.* **83,** 863–883 (2011).
2. Calabrese, P. & Cardy, J. Time dependence of correlation functions following a quantum quench. *Phys. Rev. Lett.* **96,** 011368 (2006).
3. Cramer, M., Dawson, C. M., Eisert, J. & Osborne, T. J. Exact relaxation in a class of nonequilibrium quantum lattice systems. *Phys. Rev. Lett.* **100,** 030602 (2008).
4. Gring, M. *et al.* Relaxation and prethermalization in an isolated quantum system. *Science* **337,** 1318–1322 (2012).
5. Berges, J., Borsányi, S. & Wetterich, C. Prethermalization. *Phys. Rev. Lett.* **93,** 142002 (2004).
6. Lieb, E. H. & Robinson, D. W. The finite group velocity of quantum spin systems. *Commun. Math. Phys.* **28,** 251–257 (1972).
7. Cheneau, M. *et al.* Light-cone-like spreading of correlations in a quantum many-body system. *Nature* **481,** 484–487 (2012).
8. Rigol, M., Dunjko, V. & Olshanii, M. Thermalization and its mechanism for generic isolated quantum systems. *Nature* **452,** 854–858 (2008).
9. Srednicki, M. Chaos and quantum thermalization. *Phys. Rev. E* **50,** 888–901 (1994).
10. Rigol, M., Dunjko, V., Yurovsky, V. & Olshanii, M. Relaxation in a completely integrable many-body quantum system: An *ab initio* study of the dynamics of the highly excited states of 1d lattice hard-core bosons. *Phys. Rev. Lett.* **98,** 050405 (2007).
11. Kinoshita, T., Wenger, T. & Weiss, D. A quantum newton's cradle. *Nature* **440,** 900–903 (2006).
12. Gaunt, A. L., Fletcher, R. J., Smith, R. P. & Hadzibabic, Z. A superheated Bose-condensed gas. *Nature Phys.* **9,** 271–274 (2013).
13. Sadler, L. E., Higbie, J. M., Leslie, S. R., Vengalattore, M. & Stamper-Kurn, D. M. Spontaneous symmetry breaking in a quenched ferromagnetic spinor Bose-Einstein condensate. *Nature* **443,** 312–315 (2006).
14. Ritter, S. *et al.* Observing the formation of long-range order during Bose-Einstein condensation. *Phys. Rev. Lett.* **98,** 090402–090402 (2007).
15. Trotzky, S. *et al.* Probing the relaxation towards equilibrium in an isolated strongly correlated one-dimensional Bose gas. *Nature Phys.* **8,** 325–330 (2012).
16. Gerving, C. S. *et al.* Non-equilibrium dynamics of an unstable quantum pendulum explored in a spin-1 Bose-Einstein condensate. *Nature Commun.* **3,** 1169 (2012).
17. Petrov, D., Shlyapnikov, G. & Walraven, J. Regimes of quantum degeneracy in trapped 1d gases. *Phys. Rev. Lett.* **85,** 3745–3749 (2000).
18. Schumm, T. *et al.* Matter-wave interferometry in a double well on an atom chip. *Nature Phys.* **1,** 57–62 (2005).
19. Kuhnert, M. *et al.* Multimode dynamics and emergence of a characteristic length scale in a one-dimensional quantum system. *Phys. Rev. Lett.* **110,** 090405 (2013).
20. Cronin, A. D., Schmiedmayer, J. & Pritchard, D. Optics and interferometry with atoms and molecules. *Rev. Mod. Phys.* **81,** 1051–1129 (2009).
21. Reichel, J. & Vuletic, V. (eds) *Atom Chips* (Wiley, 2011).
22. Whitlock, N. K. & Bouchoule, I. Relative phase fluctuations of two coupled one-dimensional condensates. *Phys. Rev. A* **68,** 053609 (2003).
23. Betz, T. *et al.* Two-point phase correlations of a one-dimensional bosonic Josephson junction. *Phys. Rev. Lett.* **106,** 020407 (2011).
24. Mathey, L. & Polkovnikov, A. Light cone dynamics and reverse Kibble-Zurek mechanism in two-dimensional superfluids following a quantum quench. *Phys. Rev. A* **81,** 60033 (2010).
25. Bravyi, S., Hastings, M. B. & Verstraete, F. Lieb-Robinson bounds and the generation of correlations and topological quantum order. *Phys. Rev. Lett.* **97,** 050401 (2006).
26. Läuchli, A. M. & Kollath, C. Spreading of correlations and entanglement after a quench in the one-dimensional Bose-Hubbard model. *J. Stat. Mech.* P05018 (2008).
27. Giamarchi, T. *Quantum Physics in One Dimension* (Oxford Univ. Press, 2004).
28. Kitagawa, T., Imambekov, A., Schmiedmayer, J. & Demler, E. The dynamics and prethermalization of one dimensional quantum systems probed through the full distributions of quantum noise. *New J. Phys.* **13,** 073018 (2011).
29. Hauke, P. & Tagliacozzo, L. Spread of correlations in long-range interacting systems. Preprint at http://arxiv.org/abs/1304.7725 (2013).
30. Burrell, C. K. & Osborne, T. J. Bounds on the speed of information propagation in disordered quantum spin chains. *Phys. Rev. Lett.* **99,** 167201 (2007).
31. Langen, T. *et al.* Prethermalization in one-dimensional Bose gases: description by a stochastic Ornstein-Uhlenbeck process. *Eur. Phys. J. Special Top.* **217,** 43–53 (2013).

Acknowledgements

We would like to thank D. Adu Smith and M. Gring for contributions in the early stage of the experiment, I. Mazets, V. Kasper and J. Berges for discussions and J-F. Schaff and T. Schumm for comments on the manuscript. This work was supported by the Austrian Science Fund (FWF) through the Wittgenstein Prize and the EU through the projects QIBEC and AQUTE. T.L. and M.K. thank the FWF Doctoral Programme CoQuS (W1210); R.G. is supported by the FWF through the Lise Meitner Programme M 1423.

Author contributions

T.L. and R.G. performed the experiment, analysed the data and carried out the theoretical modelling. J.S. conceived the experiment and the leading scientific questions. All authors contributed to the interpretation of the data and the writing of the manuscript.

Additional information

Supplementary information is available in the online version of the paper. Reprints and permissions information is available online at www.nature.com/reprints. Correspondence and requests for materials should be addressed to T.L. or J.S.

Competing financial interests

The authors declare no competing financial interests.

PHYSICS

Interleaved atom interferometry for high-sensitivity inertial measurements

D. Savoie*, M. Altorio*, B. Fang, L. A. Sidorenkov, R. Geiger†, A. Landragin

Cold-atom inertial sensors target several applications in navigation, geoscience, and tests of fundamental physics. Achieving high sampling rates and high inertial sensitivities, obtained with long interrogation times, represents a challenge for these applications. We report on the interleaved operation of a cold-atom gyroscope, where three atomic clouds are interrogated simultaneously in an atom interferometer featuring a sampling rate of 3.75 Hz and an interrogation time of 801 ms. Interleaving improves the inertial sensitivity by efficiently averaging vibration noise and allows us to perform dynamic rotation measurements in a so far unexplored range. We demonstrate a stability of 3×10^{-10} rad s^{-1} , which competes with the best stability levels obtained with fiber-optic gyroscopes. Our work validates interleaving as a key concept for future atom-interferometry sensors probing time-varying signals, as in on-board navigation and gravity gradiometry, searches for dark matter, or gravitational wave detection.

INTRODUCTION

Quantum sensing relies on the manipulation of internal or external degrees of freedom in atoms, molecules, optomechanical devices, and photonic or solid-state systems and covers various applications such as magnetometry (*1*–*3*), the definition of frequency standards (*4*, *5*), short-range force measurements (*6*), or electromagnetic measurements (*7*, *8*). Inertial sensors based on the coherent manipulation of superpositions of momentum states in atom interferometers have been developed for more than 25 years (*9*–*11*), with the goal of addressing various applications. Examples of remarkable achievements are tests of fundamental physics (*12*–*16*), metrology (*17*), or absolute gravimetry (*18*–*21*). These precision measurements of gravito-inertial effects directly take benefit from the inherent accuracy and long-term stability of cold-atom sensors. These two properties can eventually be combined with the high bandwidth of relative sensors, which is at the basis of sensor fusion (*22*). This approach is reminiscent of atomic clocks, where probing the stable atomic energy structure is used for stabilizing a microwave or optical oscillator (*4*, *5*) or for tests of fundamental physics.

The extension of applications of cold-atom inertial sensors to measurement of time-varying signals has been challenged by their reduced sampling rate, which originates from their sequential operation and from the long interrogation time of the atoms that is required to achieve high inertial sensitivity. This limitation is, for example, an obstacle for applications to inertial navigation (*23*) or to fundamental research related to dark matter detection (*24*) or gravitational wave astronomy (*25*, *26*). In this study, we report on the interleaved operation of a cold-atom inertial sensor, which operates with a sampling frequency of 3.75 Hz and features a high inertial sensitivity, as given by the 801-ms interrogation time of the atoms in the interferometer. The method of interleaving, which we demonstrate for both static and dynamic rotation rate measurements, can be generalized to other atom interferometer architectures and therefore paves the way to the development of high-bandwidth and high-sensitivity cold-atom inertial sensors.

Besides an increase in sensor bandwidth, we show that interleaving allows us to efficiently average vibration noise (as $1/\tau$, where τ is the integration time), which represents the most important noise source in cold-atom inertial sensors. As a consequence, we demonstrate a record rotation rate sensitivity of 3×10^{-8} rad s^{-1} $Hz^{-1/2}$. Such a high-sensitivity level allows us to characterize the systematic effects of a cold-atom gyroscope in a so far unexplored range (*27*, *28*) and to stabilize them at the few 10^{-10} rad s^{-1} level. Previous research on atomic beam gyroscopes has already demonstrated excellent sensitivities (*29*) and long-term stabilities close to the state-of-the-art optical gyroscopes (*30*). As the long-term instability of gyroscopes is a limiting factor in inertial navigation systems, achieving the performance of the best fiber-optic gyroscopes (*31*) was a long-standing goal, which we attain for the first time with a cold-atom sensor.

RESULTS

Experimental setup

Experimental sequence and principle of the gyroscope

The core of the experimental setup used in this work has been described in (*32*) and is sketched in Fig. 1. The essential techniques are given in Materials and Methods, with further details in the Supplementary Materials. In short, we laser-cool cesium atoms to a temperature of 1.2 μK and launch them vertically at a velocity of 5.0 m s^{-1}. After a selection step of the $m_F = 0$ magnetic sublevel, we interrogate the atoms in the interferometer and finally detect their state at the output of the interferometer, on their way down, using fluorescence detection. We realize the light-pulse atom interferometer using two-photon stimulated Raman transitions with counter-propagating laser beams, which couple the $|F = 3, m_F = 0\rangle$ and $|F = 4, m_F = 0\rangle$ clock states of the cesium atom.

According to the Sagnac effect, the rotation sensitivity is proportional to the area between the two arms of the interferometer. Our gyroscope is based on a fountain configuration with four light pulses to create a folded geometry owing to gravity (*33*). The symmetric four-pulse fountain configuration allows us to achieve a large area (11 cm^2 in this work) and leads to a vanishing sensitivity to constant linear accelerations. The interferometer phase shift, Φ, can be calculated from the relative phase between the two Raman lasers, $\Delta\varphi_{\text{laser}}(t) = \vec{k}_{\text{eff}} \cdot \vec{r}_{\text{b,t}}(t) + \Delta\varphi(t)$, which is imprinted on the diffracted part of the matter wave at the time t of the pulse. It reads

$$\Phi = \vec{k}_{\text{eff}} \cdot \left[\vec{r}_{\text{b}}(0) - 2\vec{r}_{\text{t}}\left(\frac{T}{2}\right) + 2\vec{r}_{\text{t}}\left(\frac{3T}{2}\right) - \vec{r}_{\text{b}}(2T)\right] + \Delta\Phi^0 \quad (1)$$

LNE-SYRTE, Observatoire de Paris, Université PSL, CNRS, Sorbonne Université, 61 Avenue de l'Observatoire, 75014 Paris, France.
*These authors contributed equally to this work.
†Corresponding author. Email: remi.geiger@obspm.fr.

where $\vec{k}_{\text{eff}}$ is the two-photon wave vector, $\vec{r}_{\text{b,t}}(t)$ is the position of the mirror retroreflecting the Raman lasers with respect to the center of mass of the free-falling atoms (subscripts {b, t} for bottom and top mirror; see Fig. 1), and $2T$ is the total interrogation time. The last term $\Delta\Phi^0$ is a controllable laser phase shift independent of inertial effects. The phase shift associated to the stationary Earth rotation rate $\vec{\Omega}_{\text{E}}$ is given by

$$\Phi_\Omega = \frac{1}{2}\vec{k}_{\text{eff}}\cdot(\vec{g}\times\vec{\Omega}_{\text{E}})T^3 \tag{2}$$

where $\vec{g}$ is the acceleration of gravity (*34*).

Interleaved operation

We use a sequence of joint interrogation of successive interferometers, which is obtained by using the same π/2 Raman pulse for the atom clouds entering and exiting the interferometer zone (*32*). Consequently, the sensor can operate without dead times. The interleaved operation, which is reminiscent from the atom juggling technique of (*35*), is then implemented by extending this joint sequence to a multiple-joint sequence, as proposed in (*36*). The sequence of Raman pulses is given in Fig. 1. If we denote $2T = 801$ ms as the total duration of the interferometer, then we launch an atom cloud every $T_c = 2T/3 = 267$ ms, which supposes that a cloud is laser cooled while three previously launched clouds are interrogated in the interferometer. Because of timing constraints, the loading time of the magneto-optical trap (MOT) is limited. The atoms are loaded in the MOT during 55 ms, and we detect 2×10^5 atoms at the end of the interferometer. The light scattered from the MOT atoms causes incoherent photon absorption and emission from the interrogated atoms and therefore a loss of contrast (*36*). The contrast of the interferometer is 7.4%, limited by the expansion of the cloud during the free fall in the Raman beams of Gaussian profile and by the light scattered from the MOT.

Technical upgrades

We implemented several key upgrades of our setup compared to (*32*). First, we improved the detection noise, which was limiting the sensitivity in (*32*). The equivalent one-shot phase noise is now 71 mrad, corresponding to a rotation noise of 8 nrad s^{-1} $\text{Hz}^{-1/2}$. Second, we implemented a real-time compensation of linear acceleration noise (*22*) and a servo loop to operate the interferometer at mid-fringe, i.e., in its linear range. These techniques are described in Materials and Methods. These upgrades result in a sensor that effectively operates without dead times, as statistically very few points sit on the top or bottom of a fringe, where the sensitivity vanishes.

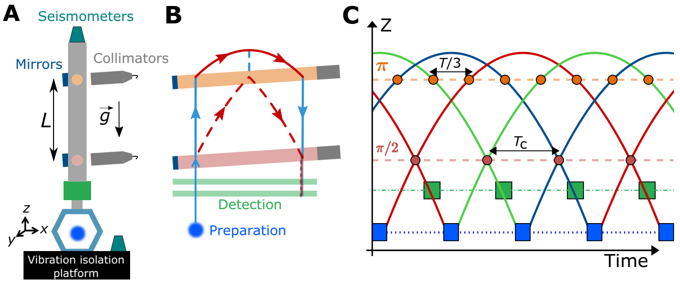

Fig. 1. Principle of the experiment. (**A**) Sketch of the experiment, where the atoms are laser cooled (blue cloud) and launched vertically, interrogated by two Raman beams (brought from the gray collimators and retroreflected on the blue mirrors), and detected on their way down (green box). The distance between the Raman beams is $L = \frac{3}{8}gT^2 \simeq 59$ cm. (**B**) Diagram of the atom interferometer in the (*xz*) plane (not to scale), with the blue and red lines labeling the $|\vec{0}\rangle$ and $\hbar\vec{k}_{\text{eff}}$ momentum states, respectively. The dashed and plain lines show the two paths of the matter waves in the interferometer, which enclose an area of 11 cm^2. (**C**) Trajectories of the successively launched atom clouds in interleaved operation. Each interferometer has an interrogation time $2T = 801$ ms, and the cycle time is $T_c = 2T/3 = 267$ ms. The π/2 pulses are shared between the atom clouds entering and exiting the interferometer.

Rotation rate acquisition

Figure 2 shows a 32.5-hour acquisition of rotation rate measurements obtained between 23 and 25 September 2017. To obtain this series of data, we alternated the direction of the Raman wave vector ($\pm\vec{k}_{\text{eff}}$) and computed the half-difference of two successive measurements to reject noninertial ($\vec{k}_{\text{eff}}$-independent) effects, such as AC Stark shifts (see Materials and Methods and section S1 for the details of the sequence and section S2 for the raw data). In the following, we will analyze the sensitivity and the stability of the gyroscope from this acquisition.

Efficient averaging of vibration noise and record sensitivity

Vibration noise is the most important source of sensitivity degradation in cold-atom inertial sensors of large area [i.e., using long interrogation time and/or large momentum transfer techniques (*37*)]. Efficient vibration isolation at low frequencies (below a few hertz) is technically challenging [e.g., (*38*)] and not suited for field applications. We will show that interleaving allows us to reduce the impact of this key noise source.

In our sensor, the impact of inertial noise can be analyzed by con sidering a center of rotation located at the top Raman beam: Inertial noise then appears as linear acceleration noise of both mirrors plus rotation noise of the bottom mirror. The rotation noise translates into random variations of the angle $\theta_{\text{B}}(t)$ of the Raman beam with respect to a geostationary reference frame (*34*) and affects the interferometer phase as $[\theta_{\text{B}}(2T) - \theta_{\text{B}}(0)]$ (Eq. 1). In joint measurements, in which π/2 pulses are shared (occurring at times 0 and $2T$), the contribution of rotation noise cancels out when averaging N successive measurements (see Materials and Methods for a derivation). Therefore, the gyroscope sensitivity should improve as τ^{-1}, where $\tau = 2NT$ is the integration time, instead of $\tau^{-1/2}$ in the case of uncorrelated measurements affected by rotation noise.

Besides averaging rotation noise, the interleaved operation of our sensor allows us to reduce the impact of residual linear acceleration noise: Because our sampling frequency ($1/T_c = 3.75$ Hz) is higher than the frequencies at which the acceleration noise mostly contributes (around 0.5 Hz; see table S1), correlations appear between successive

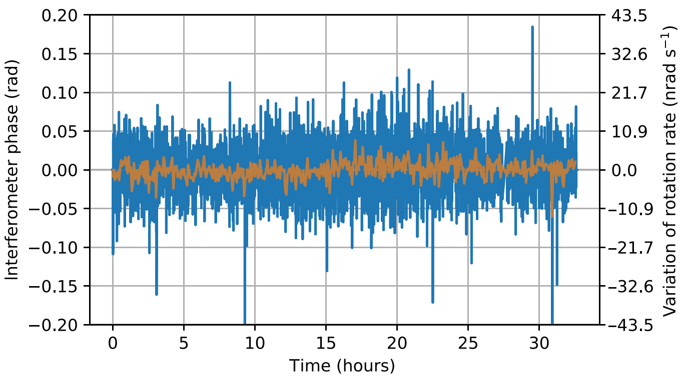

Fig. 2. Rotation rate measurement during 32.5 hours. In the blue (orange) trace, each data point is the average over segments of 26.7 s (267 s) of raw inertial phase measurements. The right axis translates inertial phase to rotation rate using the scale factor of the gyroscope to stationary Earth rotation (from Eq. 2).

measurements, yielding a scaling of the sensitivity that approaches τ^{-1} (rather than $\tau^{-1/2}$).

Figure 3 shows the Allan deviation of the gyroscope stability for an 11.3-hour portion of night data of Fig. 2. The improvement of the sensitivity as τ^{-1} for integration times up to $\simeq 7$ s is clear. The stability then gradually enters the $\tau^{-1/2}$ regime characteristic of uncorrelated white noise, corresponding to a sensitivity of 3×10^{-8} rad s^{-1} Hz$^{-1/2}$. This sensitivity, which improves by more than a factor of 3 on our previous result (*32*), establishes the new record for cold-atom gyroscopes. As a comparison, our short-term sensitivity competes favorably with that of the best fiber-optic gyroscopes (*31*). This sensitivity enables us to study several systematic effects affecting a cold-atom gyroscope for the first time in the range of low 10^{-9} rad s^{-1}.

Systematic effects and gyroscope long-term stability

A systematic shift specific to the interleaved interrogation originates from the light scattered from the MOT toward the atoms interrogated in the interferometer (*36*). The MOT scattered light is close to resonance and induces a loss of contrast and a differential light shift (AC Stark shift). The influence of induced light shifts is reduced by the spin-echo–like four-pulse sequence and by the use of $\vec{k}_{\mathrm{eff}}$ reversal: Alternating $\pm\hbar\vec{k}_{\mathrm{eff}}$ momentum transfers changes the sign of the inertial phase shift but not the one of the clock terms (e.g., differential light shift), which are rejected when taking the half-difference of two measurements (as done in Fig. 2). We measured the residual effect and showed that it corresponds to an instability below 7×10^{-11} rad s^{-1} (see Supplementary Materials). Although currently negligible, this effect is purely technical and could be resolved by having the MOT and the detection region out of view from the atom interferometer region in future designs.

The most important systematic effects in atom interferometers with separated Raman beams originate from relative wavefront mismatch coupled to deviations of the atom trajectories with respect to the ideal one (*27*, *39*). In our system, a relative angular misalignment $\vec{\delta\theta}$ between the top and bottom mirrors used to retroreflect the Raman beams (Fig. 1), coupled with an error of launch velocity $\vec{\delta v}$ (with respect to a velocity of $-\vec{g}\,T$ at the first Raman pulse) in the (y, z) plane, results in a phase shift

$$\Delta\Phi = 2Tk_{\mathrm{eff}}(\delta v_y\delta\theta_y + \delta v_z\delta\theta_z)$$
$$= 12\mathrm{mrad} \times \left(\frac{\delta v_{y,z}}{1\mathrm{mm.s}^{-1}}\right) \times \left(\frac{\delta\theta_{y,z}}{1\mu\mathrm{rad}}\right) \qquad (3)$$

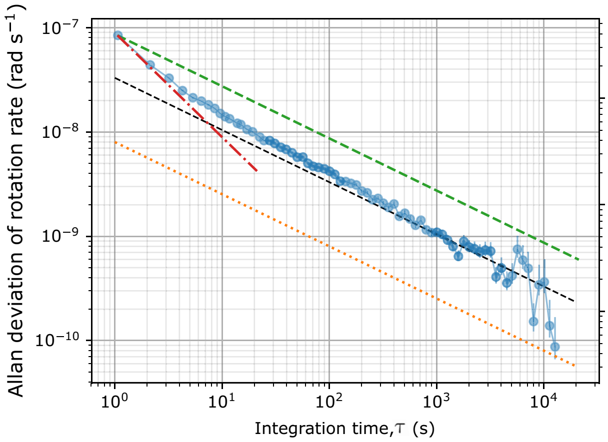

Fig. 3. Gyroscope sensitivity. Stability analysis of an 11.3-hour portion of rotation rate measurements of Fig. 2, between 1:22 a.m. and 12:47 p.m. on 24 September 2017. The error bars represent the 68% confidence intervals on the estimation of the Allan deviation. Dashed black line, 3.3×10^{-8} rad s^{-1} × $\tau^{-1/2}$; green dashed line, $\tau^{-1/2}$ scaling from the one-shot Allan deviation; red dotted-dashed line, τ^{-1} scaling from the one-shot Allan deviation; orange dotted line, detection noise limit corresponding to 8×10^{-9} rad s^{-1} × $\tau^{-1/2}$.

We explain in Materials and Methods how we set the parallelism between the two Raman beams and the velocity of the atoms to approach the ideal trajectory to achieve an uncertainty on the residual systematic shift of 21 mrad (i.e., 4.6 nrad s^{-1}, from Eq. 2).

After this systematic analysis and the corresponding fine-tuning of the apparatus, we recorded the rotation rate acquisition displayed on Fig. 2. The stability of the gyroscope over the entire acquisition is analyzed in the Supplementary Materials (fig. S5) and is in agreement with that read from Fig. 3 for shorter integration times.

Dynamic rotation rate measurements

We use the unprecedented sampling rate and inertial sensitivity of our gyroscope to perform measurements of weak dynamic rotation rates. To this end, we modulate the orientation of the experiment around the y axis. This was performed by applying a force on the bottom plate linking the experimental frame to the vibration isolation platform via the voice-coil actuator controlling the tilt θ_x of the apparatus. We apply sinusoidal modulations of the form $\theta_x(t) = \theta_0 \sin(\omega t)$ with a period $2\pi/\omega$ and with an amplitude θ_0 of a few 10^{-7} rad. The resulting rotation rate is of the form $\vec{\Omega}(t) = \Omega_0\cos(\omega t)\hat{u}_y$, with $\Omega_0 = \omega\theta_0$. The measurements are reported in Fig. 4 for modulation periods of 5 and 10 s. The respective modulation amplitudes are 2.3×10^{-7} and 3.4×10^{-7} rad. Figure 4 (A and B) shows the atomic phase extracted from the transition probability, $P(t)$, which follows the sinusoidal modulation. The total rotation signal from the atom interferometer is the sum of this atomic phase and the phase compensated in real time. A Fourier analysis of the total signal is shown in Fig. 4C. Within our frequency resolution, we find that the amplitude of the reconstructed rotation rate signal agrees with the expectation of Ω_0 with a relative precision of 5%. A more detailed analysis is presented in section S5. Our proof-of-principle experiment, performed in a so far unexplored range of time resolution and inertial sensitivity for a cold-atom sensor, demonstrates the impact of interleaved atom interferometry for dynamic measurements.

DISCUSSION

We have demonstrated the method of interleaving in a large-area atom interferometer, as a way to reach high sampling frequencies and high inertial sensitivities together. Interleaving enables us to efficiently average vibration noise (the largest noise source in cold-atom inertial sensors) and is thus a promising way of reaching the quantum projection noise limit, a necessary condition before increasing the atom flux or implementing schemes to approach the Heisenberg limit. As a result, we demonstrated record short-term sensitivities for a cold-atom gyroscope and could thus characterize systematic effects in a so far unexplored range. The rotation rate sensitivity and stability that we achieved competes with that of the best strategic-grade fiber-optic gyroscopes [long-term stability in the range of 5×10^{-10} rad s^{-1} (*31*)]. Our results thus pave the way for a change of technology in future high-precision inertial navigation systems.

In our setup, the maximum number of interleaved measurements is technically limited to three because of the arrangement of our detection

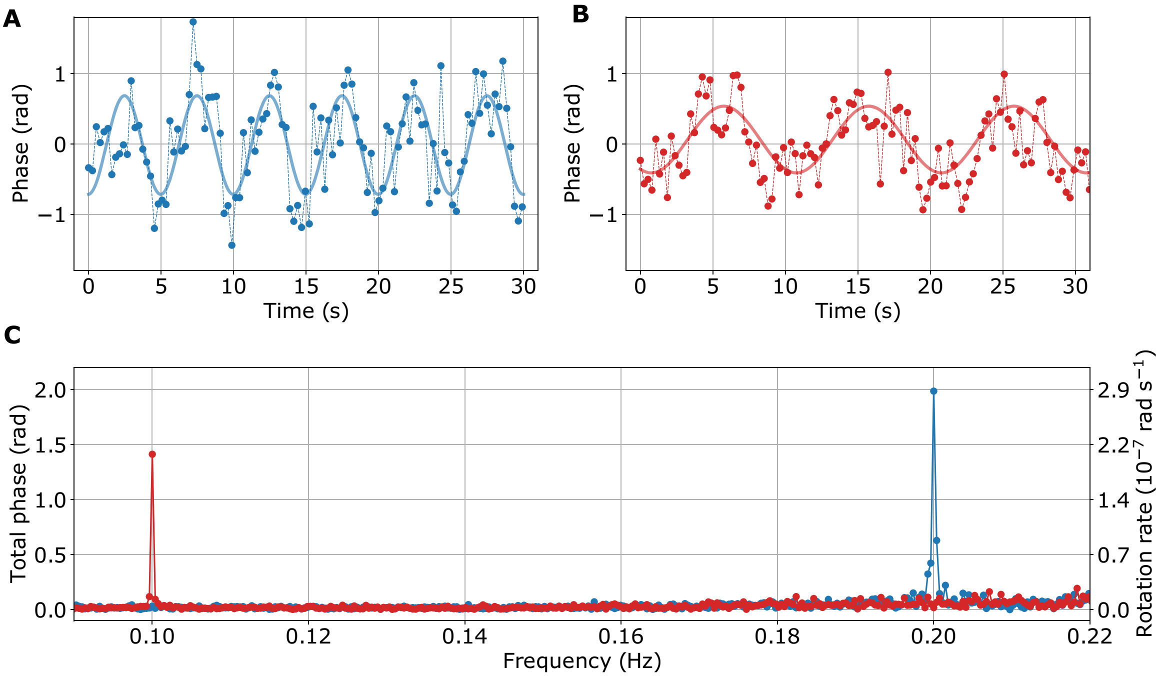

Fig. 4. Measurement of dynamic rotation rates. Atom interferometer phase deduced from the transition probability, for rotation rate modulations of 5-s period (**A**) and 10-s period (**B**). Plain line, sinusoidal fit to guide the eye. (**C**) Fourier analysis of the total rotation rate signal, with a frequency resolution of 0.37 mHz.

system with respect to the MOT region (see Materials and Methods). In a dedicated design, e.g., where the detection region would be out of view from the upcoming clouds, sampling frequencies of 20 Hz or higher could be reached. As an alternative, the use of atoms characterized by different transition wavelengths for the cooling/detection/atom interferometer would be beneficial to circumvent the effects associated with the scattered light from the source or the detected atoms. Our technique is thus well suited for ongoing developments of atom interferometers with alkaline-earth atoms (*40*).

Interleaving ties well with laser-cooling techniques, which are able to rapidly (in less than 100 ms) produce cold samples with more than 10^7 atoms. Laser cooling beyond optical molasses such as degenerate Raman sideband cooling appears as a suitable solution for an increased brightness without compromising the cycling frequency. Interleaving is, in principle, also compatible with the production of ultracold, collimated, atom sources (*16*), provided that they can be produced (*41*) or extracted at sufficiently high (several hertz) repetition rates.

The method of interleaved atom interferometry can be applied to different sensor architectures, such as multi-axis accelerometers (by alternating measurements along different axes at a high repetition rate), gavimeters, or gradiometers. For example, interleaving can be exploited to realize a gravimeter of both high accuracy and high sensitivity in a single instrument, potentially allowing to surpass superconducting gravimeters that currently feature record sensitivities but require regular calibrations. Hence, interleaving is representative of the flexibility of cold atoms for realizing versatile inertial sensors, as compared to architectures involving macroscopic masses and electromechanical systems. Regarding fundamental physics applications, achieving high sampling rates is a prerequisite for future studies on dark matter with atomic accelerometers (*24*), as well as for gravitational wave detection with atom interferometers (*25*, *26*). Interleaving is therefore a key concept for future applications of cold-atom inertial sensors.

MATERIALS AND METHODS

Details of the experiment

Cesium atoms loaded from a two-dimensional (2D) MOT were trapped and laser cooled in a 3D MOT. We launched the atoms vertically at a velocity of 5.0 m s^{-1} using moving molasses with a (3D) cloud temperature of 1.2 μK. After the MOT and before the interrogation, the atoms were prepared in the $|F = 4, m_F = 0\rangle$ state using a selection scheme based on the Stern-Gerlach effect (magnetic deflection of the atoms in $m_F \neq 0$ states). Light pulse interferometry is realized using two phase-locked Raman lasers that couple the cesium clock states (hyperfine splitting of 9.192 GHz). The Raman lasers have a wavelength close to the D_2 line (wavelength $\lambda \simeq 852$ nm) and are detuned by 470 MHz from the excited state to reduce incoherent scattering. The impact of residual relative Raman laser phase noise has been estimated to 50 mrad per shot of atom interferometer phase. The Raman lasers were sent to the atoms through two optical windows separated by $L = \frac{3}{8} g T^2 \simeq 59$ cm, with an interrogation time $2T = 801$ ms. We used Gaussian Raman beams with $1/e^2$ diameter equal to 40 mm and about 120 mW of total power. The interferometer output signal was determined by the probability of transition, P, from the $F = 4$ to the $F = 3$ state, which is read out via fluorescence detection of the two levels' populations after the atom interferometer light-pulse sequence. The probability of transition was modulated according to $P = P_0 + A \sin \Phi$, where $C = 2A$ is the interferometer contrast and Φ is the interferometer phase.

Our experiment uses retroreflected Raman beams, such as to form two pairs of Raman beams inducing two transitions: one in the $+\vec{k}_{\text{eff}}$ direction and another in the $-\vec{k}_{\text{eff}}$ direction. Selectivity of the $\pm\vec{k}_{\text{eff}}$ transitions is provided by tilting the Raman beams by an angle $\theta \simeq 3.80°$ with respect to the horizontal to introduce a Doppler shift ($\pm\, k_{\text{eff}} g T \sin \theta / 2\pi \simeq \pm 611$ kHz at the first and last $\pi/2$ pulses), which is much larger than the width of the atom Doppler distribution (~ 40 kHz). To follow the resonance condition at each Raman pulse, we stepwise changed the relative frequency between the two Raman lasers during the sequence, to match the values given by the underlying frequency chirp pattern (see details in fig. S2). To apply the frequency steps, we used a direct digital synthesizer driven by an FPGA (field-programmable gate array).

Real-time compensation of vibration noise and mid-fringe lock

We measured the vibrations of the setup with two broadband seismometers (model Trillium Compact 120 s from Nanometrics) located at the bottom and top of the experimental frame (see Fig. 1). From the measured signal, we estimated the interferometer phase shift due to vibrations and applied a corresponding phase jump to the relative phase of the Raman lasers 15 ms before the last pulse. This allows us to reduce the standard deviation (SD) of the interferometer phase from about 3.2 to 0.5 rad. To work within the linear regime where the sensitivity is maximal, we alternated measurements on both sides of a fringe and computed an error signal from two successive measurements of the transition probability. This error signal was integrated and used to servo-lock the interferometer at mid-fringe via a feedback on the Raman laser relative phase. More details are given in section S1.

Efficient averaging of vibration noise

Following Eq. 1 and assuming that the Raman lasers are oriented purely in the x direction, the four-light-pulse atom interferometer phase shift is given by (we neglect the duration of the Raman pulse)

$$\Phi = k_{\text{eff}}[x_{\text{b}}(0) - 2x_{\text{t}}(T/2) + 2x_{\text{t}}(3T/2) - x_{\text{b}}(2T)] \tag{4}$$

with $x_{\text{b,t}}(t)$ as the position of the bottom and top retro-mirrors with respect to the free-falling atom cloud. The phase shift can be rewritten as

$$\begin{aligned}\Phi &= k_{\text{eff}}[x_{\text{t}}(0) - 2x_{\text{t}}(T/2) + 2x_{\text{t}}(3T/2) - x_{\text{t}}(2T)] \\ &\quad + k_{\text{eff}}([x_{\text{b}}(0) - x_{\text{t}}(0)] - [x_{\text{b}}(2T) - x_{\text{t}}(2T)]) \\ &= \Phi_{\text{t}}^{\text{acc}} + k_{\text{eff}}L(\theta_{\text{b}}(0) - \theta_{\text{b}}(2T))\end{aligned} \tag{5}$$

with $L = \frac{3}{8}gT^2$ as the distance between the bottom and top mirrors and Φ_t^{acc} as the term associated to the linear acceleration of the top mirror. The second term represents pure rotation of the bottom mirror about the position of the top one. Recalling that $T_{\text{c}} = 2T/3$ and writing as $\Phi_i = \Phi(iT_{\text{c}})$ the atom interferometer phase at cycle i, the mean phase after N measurement reads

$$\begin{aligned}\bar{\Phi}_N = \frac{1}{N}\sum_{i=0}^{N-1}\Phi_i = \frac{1}{N}\sum_{i=0}^{N-1}(k_{\text{eff}}L[\theta_{\text{b}}(iT_{\text{c}}) - \theta_{\text{b}}((i+3)T_{\text{c}})] \\ + \delta\tilde{\phi}_i)\end{aligned} \tag{6}$$

The term $\delta\tilde{\phi}_i$ encompasses contributions of detection noise, uncompensated linear acceleration noise, and laser phase noise. When expanding the sum in Eq. 6, most of the θ_{b} terms mutually cancel such that the mean phase reads

$$\bar{\Phi}_N = k_{\text{eff}}L\frac{\theta_{\text{b}}(0) - \theta_{\text{b}}((N+2)T_{\text{c}})}{N} + \frac{1}{N}\sum_{i=0}^{N-1}\delta\tilde{\phi}_i \tag{7}$$

This equation shows that the random rotation noise averages as N^{-1} (first term). The second term represents the uncorrelated noise contributions of SD $\sigma_{\delta\phi}$. Their sum equals $\sqrt{N} \times \sigma_{\delta\phi}$, which corresponds to a scaling of the phase sensitivity as $N^{-1/2}$.

Besides rotation noise, uncompensated linear accelerations in the frequency range [0.1 – 1] Hz contribute, to a large part, to the interferometer phase noise (see section S3 for details). This contribution, estimated to typically about 500 mrad per shot, dominates the noise budget and may prevent from observing a clear τ^{-1} scaling of the gyroscope sensitivity. Interleaving, however, allows us to oversample these fluctuations, thus introducing correlations between successive measurements, which also contribute to the τ^{-1} dependence of the instrument sensitivity.

Alignment of the two Raman beams and atom trajectory

We set the parallelism between the top and bottom Raman beams by means of a two-axis piezo-motorized mirror mount with a resolution of 0.7 μrad. By optimizing the contrast of the interferometer, we approached the parallelism with an uncertainty of about 3 μrad, which is required for the matter waves to recombine at the output of the interferometer. For the fine adjustment, we measured the dependence of the phase shift of Eq. 3, $\Delta\Phi = 2Tk_{\text{eff}}(\delta v_y\delta\theta_y + \delta v_z\delta\theta_z)$, on $\delta\theta_{y,z}$ and $\delta v_{y,z}$ (as defined in the main text). To this end, we set the atom trajectory in the (y, z) directions by varying the tilt of the experiment (y direction) and the launch velocity during the moving molasses phase (z direction). In the z direction, we could zero the systematic effect with an uncertainty of 5 mrad. This amounts to set the velocity of the atoms at the first Raman pulse to the ideal velocity ($v_z = gT$) with an uncertainty of 0.6 mm s^{-1} and to set the parallelism between two mirrors in the z direction with an uncertainty of 0.7 μrad.

The minimization of the systematic shift in the y direction was technically more difficult to achieve than in the z direction: recording the dependence of the phase shift on $\delta\theta_y$ for various velocities required to tilt the entire apparatus by several mrad to vary δv_y by several mm s^{-1}. This procedure required to manually move masses on the base plate of the experiment sitting on a floating vibration isolation platform, which introduced instabilities. We managed to set the y velocity close to the ideal velocity ($v_y = 0$) with an uncertainty of 1.8 mm s^{-1}. The residual shift corresponds to a phase variation of 21 mrad per microradian of $\delta\theta_y$ variation.

Limitation to the number of interleaved interferometers

When trying five interleaved cycles, we observed a marked loss of contrast of the interferometer. The reason is that when a (descending) atom cloud at the output of the interferometer enters the detection region, a part of the light scattered by the atoms is directed toward the (ascending) cloud, which optically pumps atoms to unwanted magnetic states and heats them before they enter the interferometer.

SUPPLEMENTARY MATERIALS

Supplementary material for this article is available at http://advances.sciencemag.org/cgi/content/full/4/12/eaau7948/DC1
Section S1. Real-time compensation of vibration noise, mid-fringe lock, and details of the sequence
Section S2. Raw data
Section S3. Analysis of vibration noise
Section S4. Stability analysis
Section S5. Analysis of the dynamic rotation rate measurements
Section S6. Systematic effect from the scattered light
Fig. S1. Histogram of the vibration phase and of the interferometer phase with real-time compensation of vibration.
Fig. S2. Details of the sequence.
Fig. S3. Raw interferometer measurements corresponding to the data presented in Fig. 2.

Fig. S4. Analysis of vibration noise.
Fig. S5. Stability analysis of the gyroscope.
Table S1. Contribution of the linear acceleration noise to the interferometer phase noise by frequency band.
Reference (*42*)

REFERENCES AND NOTES

1. D. Sheng, S. Li, N. Dural, M. V. Romalis, Subfemtotesla scalar atomic magnetometry using multipass cells. *Phys. Rev. Lett.* **110**, 160802 (2013).
2. I. Gross, W. Akhtar, V. Garcia, L. J. Martínez, S. Chouaieb, K. Garcia, C. Carrétéro, A. Barthélémy, P. Appel, P. Maletinsky, J.-V. Kim, J. Y. Chauleau, N. Jaouen, M. Viret, M. Bibes, S. Fusil, V. Jacques, Real-space imaging of non-collinear antiferromagnetic order with a single-spin magnetometer. *Nature* **549**, 252–256 (2017).
3. R. Jiménez-Martínez, J. Kołodyński, C. Troullinou, V. G. Lucivero, J. Kong, M. W. Mitchell, Signal tracking beyond the time resolution of an atomic sensor by Kalman filtering. *Phys. Rev. Lett.* **120**, 040503 (2018).
4. M. Takamoto, F.-L. Hong, R. Higashi, H. Katori, An optical lattice clock. *Nature* **435**, 321–324 (2005).
5. R. Le Targat, L. Lorini, Y. Le Coq, M. Zawada, J. Guéna, M. Abgrall, M. Gurov, P. Rosenbusch, D. G. Rovera, B. Nagórny, R. Gartman, P. G. Westergaard, M. E. Tobar, M. Lours, G. Santarelli, A. Clairon, S. Bize, P. Laurent, P. Lemonde, J. Lodewyck, Experimental realization of an optical second with strontium lattice clocks. *Nat. Commun.* **4**, 2109 (2013).
6. M. G. Tarallo, T. Mazzoni, N. Poli, D. V. Sutyrin, X. Zhang, G. M. Tino, Test of einstein equivalence principle for 0-spin and half-integer-spin atoms: Search for spin-gravity coupling effects. *Phys. Rev. Lett.* **113**, 023005 (2014).
7. T. Bagci, A. Simonsen, S. Schmid, L. G. Villanueva, E. Zeuthen, J. Appel, J. M. Taylor, A. Sørensen, K. Usami, A. Schliesser, E. S. Polzik, Optical detection of radio waves through a nanomechanical transducer. *Nature* **507**, 81–85 (2014).
8. A. Facon, E.-K. Dietsche, D. Grosso, S. Haroche, J.-M. Raimond, M. Brune, S. Gleyzes, A sensitive electrometer based on a Rydberg atom in a Schrödinger-cat state. *Nature* **535**, 262–265 (2016).
9. Ch. J. Bordé, Atomic interferometry with internal state labelling. *Phys. Lett. A* **140**, 10–12 (1989).
10. M. Kasevich, S. Chu, Atomic interferometry using stimulated Raman transitions. *Phys. Rev. Lett.* **67**, 181–184 (1991).
11. F. Riehle, Th. Kisters, A. Witte, J. Helmcke, Ch. J. Bordé, Optical Ramsey spectroscopy in a rotating frame: Sagnac effect in a matter-wave interferometer. *Phys. Rev. Lett.* **67**, 177–180 (1991).
12. R. Bouchendira, P. Cladé, S. Guellati-Khélifa, F. Nez, F. Biraben, New determination of the fine structure constant and test of the quantum electrodynamics. *Phys. Rev. Lett.* **106**, 080801 (2011).
13. S. Lepoutre, A. Gauguet, G. Trénec, M. Büchner, J. Vigué, He-Mckellar-Wilkens topological phase in atom interferometry. *Phys. Rev. Lett.* **109**, 120404 (2012).
14. L. Zhou, S. Long, B. Tang, X. Chen, F. Gao, W. Peng, W. Duan, J. Zhong, Z. Xiong, J. Wang, Y. Zhang, M. Zhan, Test of equivalence principle at 10^{-8} level by a dual-species double-diffraction Raman atom interferometer. *Phys. Rev. Lett.* **115**, 013004 (2015).
15. M. Jaffe, P. Haslinger, V. Xu, P. Hamilton, A. Upadhye, B. Elder, J. Khoury, H. Müller, Testing sub-gravitational forces on atoms from a miniature in-vacuum source mass. *Nat. Phys.* **13**, 938–942 (2017).
16. P. Asenbaum, C. Overstreet, T. Kovachy, D. D. Brown, J. M. Hogan, M. A. Kasevich, Phase shift in an atom interferometer due to spacetime curvature across its wave function. *Phys. Rev. Lett.* **118**, 183602 (2017).
17. G. Rosi, F. Sorrentino, L. Cacciapuoti, M. Prevedelli, G. M. Tino, Precision measurement of the Newtonian gravitational constant using cold atoms. *Nature* **510**, 518–521 (2014).
18. A. Peters, K. Y. Chung, S. Chu, High-precision gravity measurements using atom interferometry. *Metrologia* **38**, 25 (2001).
19. C. Freier, M. Hauth, V. Schkolnik, B. Leykauf, M. Schilling, H. Wziontek, H.-G. Scherneck, J. Müller, A. Peters, Mobile quantum gravity sensor with unprecedented stability. *J. Phys. Conf. Ser.* **723**, 012050 (2016).
20. Y. Bidel, N. Zahzam, C. Blanchard, A. Bonnin, M. Cadoret, A. Bresson, D. Rouxel, M. F. Lequentrec-Lalancette, Absolute marine gravimetry with matter-wave interferometry. *Nat. Commun.* **9**, 627 (2018).
21. R. Karcher, A. Imanaliev, S. Merlet, F. Pereira Dos Santos, Improving the accuracy of atom interferometers with ultracold sources. *New J. Phys.* **20**, 113041 (2018).
22. J. Lautier, L. Volodimer, T. Hardin, S. Merlet, M. Lours, F. Pereira Dos Santos, A. Landragin, Hybridizing matter-wave and classical accelerometers. *Appl. Phys. Lett.* **105**, 144102 (2014).
23. C. Jekeli, Navigation error analysis of atom interferometer inertial sensor. *Navigation* **52**, 1–14 (2005).
24. P. W. Graham, D. E. Kaplan, J. Mardon, S. Rajendran, W. A. Terrano, Dark matter direct detection with accelerometers. *Phys. Rev. D* **93**, 075029 (2016).
25. W. Chaibi, R. Geiger, B. Canuel, A. Bertoldi, A. Landragin, P. Bouyer, Low frequency gravitational wave detection with ground-based atom interferometer arrays. *Phys. Rev. D* **93**, 021101 (2016).
26. P. W. Graham, J. M. Hogan, M. A. Kasevich, S. Rajendran, Resonant mode for gravitational wave detectors based on atom interferometry. *Phys. Rev. D* **94**, 104022 (2016).
27. A. Gauguet, B. Canuel, T. Lévèque, W. Chaibi, A. Landragin, Characterization and limits of a cold-atom Sagnac interferometer. *Phys. Rev. A* **80**, 063604 (2009).
28. P. Berg, S. Abend, G. Tackmann, C. Schubert, E. Giese, W. P. Schleich, F. A. Narducci, W. Ertmer, E. M. Rasel, Composite-light-pulse technique for high-precision atom interferometry. *Phys. Rev. Lett.* **114**, 063002 (2015).
29. T. L. Gustavson, A. Landragin, M. A. Kasevich, Rotation sensing with a dual atom-interferometer Sagnac gyroscope. *Class. Quantum Gravity* **17**, 2385 (2000).
30. D. S. Durfee, Y. K. Shaham, M. A. Kasevich, Long-term stability of an area-reversible atom-interferometer Sagnac gyroscope. *Phys. Rev. Lett.* **97**, 240801 (2006).
31. H. C. Lefèvre, The fiber-optic gyroscope, a century after Sagnac's experiment: The ultimate rotation-sensing technology? *C. R. Phys.* **15**, 851–858 (2014); for recent performances, see, e.g., iXblue ultimate-performance Fiber-Optic Gyroscope (FOG) (http://web.ixblue.com/cn/aw6ym/fiberoptic-gyroscope).
32. I. Dutta, D. Savoie, B. Fang, B. Venon, C. L. Garrido Alzar, R. Geiger, A. Landragin, Continuous cold-atom inertial sensor with 1 nrad / sec rotation stability. *Phys. Rev. Lett.* **116**, 183003 (2016).
33. B. Canuel, F. Leduc, D. Holleville, A. Gauguet, J. Fils, A. Virdis, A. Clairon, N. Dimarcq, Ch. J. Bordé, A. Landragin, P. Bouyer, Six-axis inertial sensor using cold-atom interferometry. *Phys. Rev. Lett.* **97**, 010402 (2006).
34. J. K. Stockton, K. Takase, M. A. Kasevich, Absolute geodetic rotation measurement using atom interferometry. *Phys. Rev. Lett.* **107**, 133001 (2011).
35. R. Legere, K. Gibble, Quantum scattering in a juggling atomic fountain. *Phys. Rev. Lett.* **81**, 5780–5783 (1998).
36. M. Meunier, I. Dutta, R. Geiger, C. Guerlin, C. L. Garrido Alzar, A. Landragin, Stability enhancement by joint phase measurements in a single cold atomic fountain. *Phys. Rev. A* **90**, 063633 (2014).
37. S. M. Dickerson, J. M. Hogan, A. Sugarbaker, D. M. S. Johnson, M. A. Kasevich, Multiaxis inertial sensing with long-time point source atom interferometry. *Phys. Rev. Lett.* **111**, 083001 (2013).
38. J. M. Hensley, A. Peters, S. Chu, Active low frequency vertical vibration isolation. *Rev. Sci. Instrum.* **70**, 2735–2741 (1999).
39. G. Tackmann, P. Berg, C. Schubert, S. Abend, M. Gilowski, W. Ertmer, E. M. Rasel, Self-alignment of a compact large-area atomic Sagnac interferometer. *New J. Phys.* **14**, 015002 (2012).
40. L. Hu, N. Poli, L. Salvi, G. M. Tino, Atom interferometry with the Sr optical clock transition. *Phys. Rev. Lett.* **119**, 263601 (2017).
41. J. Rudolph, W. Herr, C. Grzeschik, T. Sternke, A. Grote, M. Popp, D. Becker, H. Müntinga, H. Ahlers, A. Peters, C. Lämmerzahl, K. Sengstock, N. Gaaloul, W. Ertmer, E. M. Rasel, A high-flux BEC source for mobile atom interferometers. *New J. Phys.* **17**, 065001 (2015).
42. P. Cheinet, B. Canuel, F. Pereira Dos Santos, A. Gauguet, F. Yver-Leduc, A. Landragin, Measurement of the sensitivity function in a time-domain atomic interferometer. *IEEE Trans. Instrum. Meas.* **57**, 1141–1148 (2008).

Acknowledgments: We thank F. Pereira Dos Santos for careful reading of the manuscript. **Funding:** We acknowledge the financial support from Ville de Paris (project HSENS-MWGRAV), FIRST-TF (ANR-10-LABX-48-01), Centre National d'Etudes Saptiales (CNES), Sorbonne Universités (project SU-16-R-EMR-30, LORINVACC), and Action Spécifique du CNRS Gravitation, Références, Astronomie et Métrologie (GRAM). B.F. was funded by Conseil Scientifique de l'Observatoire de Paris, D.S. by Direction Générale de l'Armement, and M.A. by the EDPIF doctoral school. **Author contributions:** D.S., M.A., and B.F. performed the experiments, and L.A.S. contributed to the dynamic rotation rate measurements. D.S., R.G., and M.A. analyzed the data. R.G. and D.S. wrote the manuscript. A.L. conceived the experiment. R.G. and A.L. supervised the research. All authors discussed the manuscript. **Competing interests:** The authors declare that they have no competing interests. **Data and materials availability:** All data needed to evaluate the conclusions in the paper are present in the paper and/or the Supplementary Materials. Additional data related to this paper may be requested from the authors.

Submitted 17 July 2018
Accepted 19 November 2018
Published 21 December 2018
10.1126/sciadv.aau7948

Citation: D. Savoie, M. Altorio, B. Fang, L. A. Sidorenkov, R. Geiger, A. Landragin, Interleaved atom interferometry for high-sensitivity inertial measurements. *Sci. Adv.* **4**, eaau7948 (2018).

APPLIED PHYSICS LETTERS **113**, 161108 (2018)

Atom interferometry with top-hat laser beams

N. Mielec,[1] M. Altorio,[1] R. Sapam,[1] D. Horville,[2] D. Holleville,[1] L. A. Sidorenkov,[1]
A. Landragin,[1] and R. Geiger[1,a)]
[1]*LNE-SYRTE, Observatoire de Paris, Université PSL, CNRS, Sorbonne Université, 61 Avenue de l'Observatoire, 75014 Paris, France*
[2]*GEPI, Observatoire de Paris, Université PSL, CNRS, 5 Place Jules Janssen, 92190 Meudon, France*

(Received 10 August 2018; accepted 6 October 2018; published online 18 October 2018)

The uniformity of the intensity and the phase of laser beams is crucial to high-performance atom interferometers. Inhomogeneities in the laser intensity profile cause contrast reductions and systematic effects in interferometers operated with atom sources at micro-Kelvin temperatures and detrimental diffraction phase shifts in interferometers using large momentum transfer beam splitters. We report on the implementation of a so-called top-hat laser beam in a long-interrogation-time cold-atom interferometer to overcome the issue of inhomogeneous laser intensity encountered when using Gaussian laser beams. We characterize the intensity and relative phase profiles of the top-hat beam and demonstrate its gain in atom-optic efficiency over a Gaussian beam, in agreement with numerical simulations. We discuss the application of top-hat beams to improve the performance of different architectures of atom interferometers. *Published by AIP Publishing.*
https://doi.org/10.1063/1.5051663

Inertial sensors based on light-pulse atom interferometry address various applications ranging from inertial navigation,[1–3] metrology,[4–6] gravimetry,[7–13] gradiometry,[14,15] and tests of fundamental physics,[16–21] to gravitational wave astronomy.[22,23] Light-pulse atom interferometers rely on the coherent transfer of momentum from the photons of counter-propagating laser beams to free falling atoms in order to split, deflect and recombine the matter-waves. The sensitivity and the accuracy of the instruments thus crucially depend on the relative phase uniformity of the laser beams realizing these atom-optic functionalities. State-of-the-art cold-atom sensors typically use sources at few μK temperatures, interrogation times of several hundreds of milliseconds, and two-photon transitions.[5,10,24] Inhomogeneities in the laser intensity across the atom cloud degrade the atom optic efficiency, which causes a decrease in interferometer contrast and hence a lower signal to noise ratio, as well as systematic effects.[25] Such detrimental effects are amplified in interferometers employing large momentum transfer (LMT) techniques (in which several momenta are transferred to the atoms),[21,26] in particular, because of diffraction phase shifts.[27] The problem of intensity inhomogeneity can be mitigated by employing Gaussian beams with a size much larger than that of the atom cloud, at the cost of reduced peak intensity.

In this work, we report on the implementation of a *collimated* top-hat laser beam (i.e., with uniform intensity distribution in the central part[28]) as a solution to circumvent the problems encountered in atom interferometers employing Gaussian beams.

Beamshaping is a topic of intense development, with applications ranging from micro-lithography, optical data storage, to optical tweezers, where different approaches are followed to produce structured light patterns. For application in atom interferometry, the requirement for the relative phase homogeneity motivates a scheme where the counter-propagating beam pair is obtained by retro-reflection (the retro-distance typically lying in the ten-centimeters-to-meter scale). The interrogation laser beams are thus required to be well collimated over such distances. This requirement of the beam shaping technique amounts to achieving a flat phase profile.

The simplest form of shaping the intensity distribution of a laser beam, apodization, results in significant loss of optical power (for example, the optimal transformation of a Gaussian beam into a beam with a flat intensity profile sacrifices 64% of power). More efficient techniques involve diffractive optical elements, such as spatial light modulators (SLMs), in order to produce focused light patterns[29] or collimated structured beams when multiple SLMs are cascaded.[30] However, the bulkiness of the optical setup, the potential drift of the beam-shaping performance linked to the use of an active material, and the limited incident peak intensity make such solutions cumbersome for atom interferometry experiment. Instead, passive refractive techniques based on aspheric optical elements[31] seem favorable, owing to their compactness, stability, and efficiency.

Our passive top-hat collimator solution is based on a recently released commercial beamshaper from the Asphericon Company (model TSM-25–10-S-B), see Fig. 1(a). The beamshaper shall receive at its input a Gaussian beam of 10 mm $1/e^2$-diameter and produce a top-hat beam of 15 mm full width at half maximum (FWHM), with a region of about 14 mm where the intensity varies by less than 10% (Ref. 32). The beamshaping is done with multiple aspheric optics, based on principles similar to those of Ref. 31. The advertized uniformity of the intensity plateau is 0.056 rms, with a phase inhomogeneity of $\lambda/3$ peak-valley (PV) and $\sim\lambda/20$ rms, allowing the beam to propagate without deformation on distances of several meters.[32] We inject the beamshaper with a home-made fiber collimator made of 3 simple lenses, to produce a Gaussian beam of 9.95 ± 0.05 mm $1/e^2$ diameter. At the output of the beamshaper, the top-hat beam is

---

[a)] Electronic mail: remi.geiger@obspm.fr

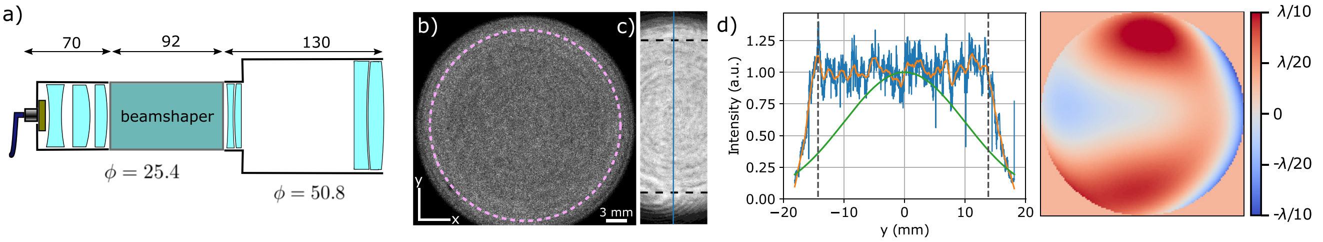

FIG. 1. (a) Schematic view of the optical system with the input collimator, the beamshaper, and the expander (dimensions in mm, ϕ denoting the diameter of the optics). (b) Image of the top-hat beam on a paper screen. The dashed purple line is a circle of 28 mm diameter. (c) Image obtained with a beamprofiler, after 40 cm of propagation. Between the 2 dashed lines separated by 28 mm, the uniformity of the plateau is 0.11 rms. (d) (blue) Vertical line profile of the top-hat beam shown in (c); the intensity has been normalized to the mean plateau intensity (orange). Moving average over 1 mm (green). Theoretical profile of a Gaussian beam with 40 mm $1/e^2$ diameter. (e) Relative phase of the top-hat beam with 70 cm propagation difference, in a disk of 28 mm; the deviation is $\lambda/5$ (PV) and $\lambda/28$ (rms).

magnified by a factor of two with two achromatic doublets, in order to reach a useful region of 28 mm. The optical system can be mounted conveniently during an experiment. The power transmission of the input collimator plus the beamshaper is 91%, while that of the full system is 85%. The quality of the generated top-hat beam mainly depends on the input beam size (which must fall within the 10 mm diameter specification at the 10% level[32]) and its collimation.

To align the top-hat collimator, we image the beam on a paper screen and optimize the intensity profile by moving the input fiber placed on a 5-axis mount. We target a flat circular intensity profile maintained over a propagation distance of at least 150 cm. Figure 1(b) shows the beam imaged on the paper screen at the output of the expander. While this method is convenient for the alignment procedure, it is not suited for a precise measurement of the intensity uniformity of the beam because of the speckle produced on the paper screen. We use a large-area beamprofiler ($11.3 \times 6.0\,\mathrm{mm}^2$) to measure the uniformity of the plateau. Figure 1(c) shows the stitched images acquired by scanning the beamprofiler in front of the beam after 40 cm of propagation. The beam exhibits a qualitatively flat plateau. Large diameter rings concentric to the beam are attributed to the beamshaper. The uniformity of the plateau over a diameter of 28 mm is 0.11 rms and the FWHM is 31.7 ± 0.2 mm. Figure 1(d) shows a profile of the vertical cut through the middle of the beam (along the blue line). The orange line is a moving average over 1 mm of the profile, shown here to illustrate lower frequency inhomogeneities. For comparison, the green line shows a Gaussian beam with 40 mm diameter at $1/e^2$ (as used in Ref. 24) and same peak intensity as the top-hat beam.

In an atom interferometer, the relative phase between two counter-propagating laser beams is imprinted on the atomic wave-function during the light pulses. This relative phase contains a term associated with the free propagation, $\varphi(x, y, 0) - \varphi(x, y, 2L)$, where L is the distance between the atom cloud and the retro-mirror.[33] We measured such a relative phase field for our top-hat beam using an asymmetric Michelson interferometer with the difference of its arms set to $2L$. At the output, the interference pattern carries the 2D relative phase map, which we recover using Fourier analysis.[34] A lower bound on the accuracy is set by the planarity of the mirrors and the beamsplitter used in the interferometer, specified to be $\lambda/10$ peak-valley (PV). The relative phase map in a pupil of 28 mm diameter corresponding to the useful part of the beam is shown in Fig. 1(e), for a difference in propagation distance $2L = 70$ cm. We find relative phase inhomogeneities of $\lambda/5$ PV and a $\lambda/28$ rms. Additional phase maps for further propagation distances are given in the supplementary material. Our characterization shows that the top-hat beam is suitable for high-precision atom interferometry, where relative wavefront inhomogeneities are an issue.[13,25,33,35]

We implemented the top-hat beam on a cold-atom gyroscope-accelerometer experiment. The setup has been described in previous works[24,36] and we recall here the main features which are relevant to this study. Laser-cooled cesium atoms (at a temperature of 1.2 μK) are launched vertically with a velocity of up to $5.0\,\mathrm{m\,s^{-1}}$. After a selection step of the $m_F = 0$ magnetic sublevel, we realize the atom interferometer by means of two-photon stimulated Raman transitions from counter-propagating laser beams, which couple the $|F = 3, m_F = 0\rangle$ and $|F = 4, m_F = 0\rangle$ clock states. The direction of the Raman beams is nearly horizontal. We use two beams separated vertically by a distance of 211 mm. The top-hat collimator was set up at the position of the top beam, while the bottom beam is a Gaussian beam of 40 mm diameter at $1/e^2$ [Fig. 2(a)]. The state of the atoms at the output of the interferometer is finally read out using fluorescence detection.

We first probe the intensity profile of the top-hat beam by applying a Raman pulse of fixed duration τ at different

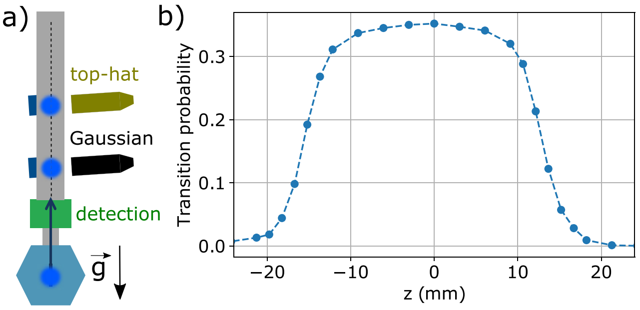

FIG. 2. (a) Sketch of the experiment. (b) Measurement of the local Raman lasers intensity with a cold atom cloud, by recording the transition probability versus time-of-flight. The duration of the Raman pulse is fixed ($\tau = 9\,\mu$s) and set close to that of a $\pi/2$ pulse, where the sensitivity to intensity fluctuations on the plateau is maximum. The horizontal axis (z) is obtained by multiplying the TOF with the mean velocity of atoms in the beam ($3.0\,\mathrm{m\,s^{-1}}$).

times as the atoms travel on their way up. The atoms are launched with a velocity of 4.7 m s^{-1} and their mean trajectory intersects the center of the beam after a time of flight (TOF) of 170 ms. After this relatively short TOF, the size of the cloud is still close to that of the initially launched atoms ($\simeq$1.5 mm rms radius) and much smaller than the beam size. The transition probability, $P \propto \sin^2(\Omega(z)\tau/2)$, is determined by the local value of the two-photon Rabi frequency, $\Omega(z)$, and can thus be used as a probe of the local intensity of the beam (here, z denotes the direction parallel to gravity). Figure 2(b) shows the transition probability versus the relative position of the cloud inside the beam. We observe a qualitatively flat intensity profile in the center, with a width consistent with the optical characterization reported in Fig. 1.

The size of a cold atom cloud increases over free propagation due to finite temperature. This results in an inhomogeneous atom-light coupling when the cloud size approaches the waist of the Gaussian beam, thereby decreasing the interferometer contrast. The intensity homogeneity of the top-hat beam allows in principle to improve on this effect. To illustrate this improvement, we operate a 3 light-pulse interferometer sequence with a pulse separation time $T = 1$ ms, after a long TOF of 855 ms to bring forward the effect of the atom cloud expansion. For a quantitative comparison, the difference in height between the two beams (211 mm) was matched by the respective change in launch velocity, in order to obtain nearly the same TOFs when crossing the Gaussian and top-hat beams. Figure 3 presents the comparison and shows the advantage of the top-hat beam.

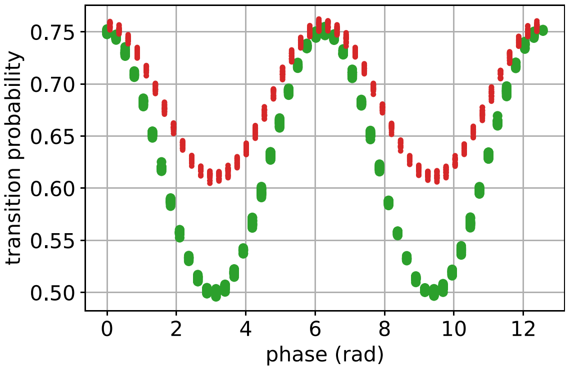

FIG. 3. Interference fringes for a 3-pulse interferometer sequence with a pulse separation time $T = 1$ ms, after a TOF of 855 ms. Red: Gaussian beam. Green: top-hat beam. The interference fringes are scanned by varying the relative Raman laser phase at the third light pulse. The same optical power was used for the Gaussian and the top-hat beams.

To assess the limitations to the gain in atom-optic efficiency offered by our top-hat beam over our Gaussian beam, we recorded Rabi oscillations after various TOFs, when the launched atom cloud crosses the beams on its way up and on its way down. Figure 4(a) shows the Rabi oscillations on the way up after a TOF of 170 ms and on the way down after a TOF of 855 ms for the top-hat and Gaussian beams. On the way up, the cloud size is smaller than the beam sizes and the Rabi oscillations have a similar shape for the Gaussian and top-hat beams, as expected. The transfer efficiency of ~70% is limited by the velocity selectivity of the two-photon transition, given by the finite Rabi frequency (i.e., laser power) and the velocity spread of the atoms in the direction of the beams. On the contrary, on the way down, the Rabi oscillation in the top-hat beam (green) is significantly improved with respect to that in the Gaussian beam (red), owing to the homogeneity of the two-photon Rabi frequency from the top-hat beam. To model the Rabi oscillations, we employ a Monte-Carlo simulation where we generate an ensemble of atoms with individual velocities following the distribution measured with the Doppler-sensitive Raman transitions (corresponding to a 3D temperature of 1.2 μK), and propagate them in the Raman beams. The details of the model are given in the supplementary material. The model reproduces well the data and allows one to assess the residual intensity inhomogeneities of the top-hat beam. Figure 4(b) shows the measured Rabi oscillation confronted to a simulation where the intensity noise of various levels is added on the top-hat profile.[37] The data match best with the numerical simulation assuming an inhomogeneity of 8.3% rms, consistent with the optical characterization of the intensity inhomogeneities of 11% reported in Fig. 1.

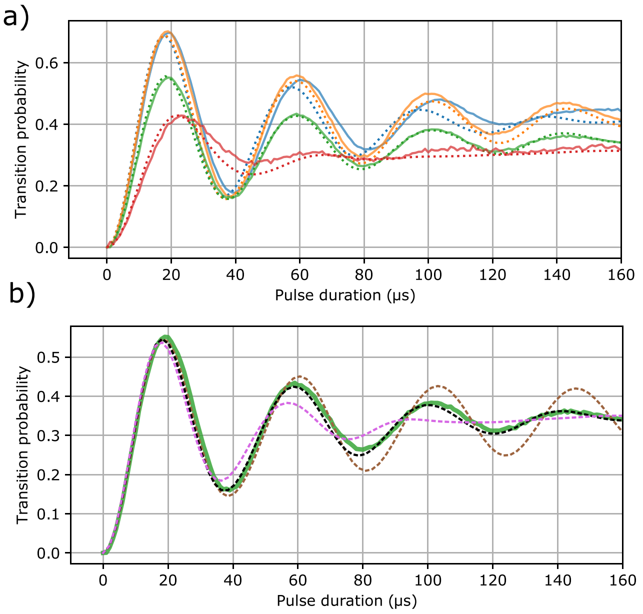

FIG. 4. Rabi oscillations. (a) Plain lines: measured oscillations on the way up after 170 ms of TOF (blue and orange for Gaussian and top-hat, respectively) and on the way down after 855 ms of TOF (red and green). Dotted lines: numerical simulation. (b) Green plain line: measured Rabi oscillation in the top-hat beam after 855 ms of TOF [the same as in (a)]. Dashed: numerical simulation for various levels of rms intensity noise on the top-hat (brown: 0%, black: 8.3%, violet: 15%).

Finally, we demonstrate that the top-hat beam is suited for high-sensitivity atom interferometry, by running a 3-pulse atom interferometer sequence with a pulse separation time $T = 147$ ms. The first $\pi/2$ pulse is realized in the Gaussian beam (on the way up, TOF = 170 ms), while the second and third pulses are realized in the top-hat beam (TOF = 317 and 464 ms). For such long interrogation time, the interferometer is highly sensitive to vibration noise producing at its output a typical rms phase shift of more than π rad. Running the interferometer results in a random sampling of the fringe pattern by vibration noise, which appears blurred without additional knowledge on the vibration noise at each run. To extract the contrast, we follow the method of

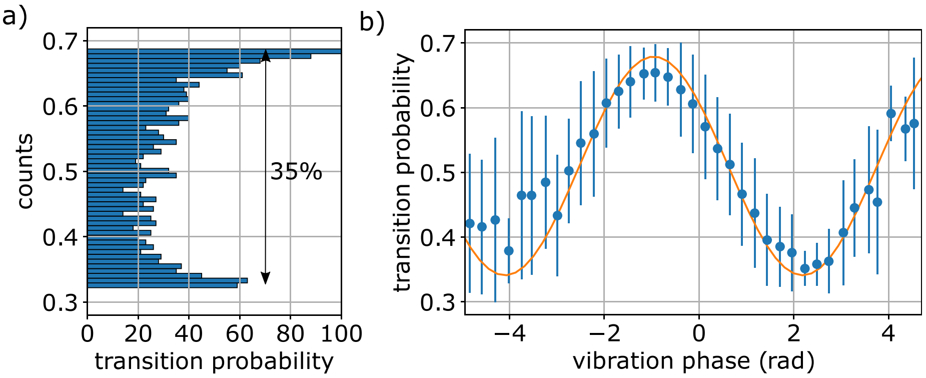

FIG. 5. Performance of the 3-pulse interferometer with $2T = 294\,\text{ms}$. (a) Histogram of the transition probability showing a contrast of 35%. (b) Transition probability versus the vibration phase calculated from the data for a broadband seismometer. The data points are sorted along the x-axis and binned in intervals of 262 mrad width. The imperfect estimation of the vibration phase by the seismometer translates into phase noise and consequently into probability noise when binning. Error bars denote a standard deviation of 1. The orange plain curve shows a sinusoidal fit where the fringe amplitude is set to the value of 35% extracted from (a).

Ref. 2 and compute the histogram of the transition probability data [Fig. 5(a)], from which we extract a contrast of 35%. Furthermore, we recover the interference fringes by correlating the atom interferometer output with the phase calculated from vibration data acquired with two broadband seismometers,[24,38] see Fig. 5(b). The uncertainty (1σ) on the fitted phase is 80 mrad, corresponding to a horizontal acceleration uncertainty of $2.5 \times 10^{-7}\ \text{m}\,\text{s}^{-2}$. Although the measurement sensitivity is limited by residual vibration noise, this experiment shows that the top-hat beam is compatible with high-sensitivity inertial measurements based on long-interrogation-time cold-atom interferometry.

In conclusion, we have set up and characterized a collimated top-hat laser beam and reported on its implementation for a long interrogation time cold-atom interferometer. Our top-hat beam features a constant intensity over a region of 28 mm with rms variations of about 10%. We expect that the intensity homogeneity offered by top-hat beams compared to Gaussian beams will be beneficial to various atom interferometer geometries which we discuss below. We present additional advantages in the supplementary material.

The intensity homogeneity of the interrogation beams will allow reducing or canceling important systematic effects in cold-atom interferometers, such as the two photon light shift.[39] It can also be used to improve the efficiency and the stability of atom launching techniques based on the coherent transfer of photon momenta, such as in Bloch oscillations.[4,6,21] Moreover, this beamshaping solution could be adapted for atom interferometers with baselines of several meters as in Ref. 21.

Employing a single top-hat beam can be used to build compact, yet precise, cold-atom inertial sensors. For example, a $D = 28\,\text{mm}$ a wide homogeneous intensity profile should allow one to run a fountain interferometer with a total interferometer time of $2T \simeq 2 \times \sqrt{2D/g} = 151$ ms, if the atoms are launched from the bottom of the beam. Moreover, the design of gyroscopes, where the atoms travel through successive laser beams with a velocity transverse to the momentum transfers[25,40,41] could be simplified with a single top-hat beam.

Homogeneity of the intensity profile should reduce the diffraction phase shifts encountered in LMT Bragg diffraction.[42–44] For example, a variation of 1% of laser intensity in $4\hbar k$ Bragg diffraction amounts to a variation in the diffraction phase of about 84 mrad.[27] The rms intensity uniformity of our top-hat beam is between 8% and 11% over a region of 28 mm [Fig. 1(c)]. Keeping a 10% rms intensity variation within a Gaussian beam requires working within a reduced portion around the center, which translates into using only 25% of the total power. This suggests that the efficiency and the accuracy of LMT beam splitters should be significantly improved by employing top-hat beams.

See supplementary material for additional data regarding intensity profiles (Fig. S1) and relative phase maps (Fig. S2) for various propagation distances, for the impact of relative phase inhomogeneities on the atom interferometer bias, for the details of the model of Rabi oscillations, and for numerical examples of the gain in contrast with top-hat beams compared to Gaussian beams for specific interferometer geometries.

We thank Josiane Firminy and Faouzi Boussaha for their realization of engraved aspheric phase plates in an early design of the beamshaper conducted in the beginning of this project. This work was supported by Ville de Paris (Project No. HSENS-MWGRAV), FIRST-TF (ANR-10-LABX-48-01), Centre National d'Etudes Saptiales (CNES), Sorbonne Universités (project LORINVACC), Action Spécifique du CNRS Gravitation, Références, Astronomie et Métrologie (GRAM), and the European Union's Horizon 2020 research and innovation programme under the Marie Sklodowska-Curie Grant Agreement No. 660081. We thank Laurence Pruvost for fruitful discussions.

[1] B. Canuel, F. Leduc, D. Holleville, A. Gauguet, J. Fils, A. Virdis, A. Clairon, N. Dimarcq, C. J. Bordé, A. Landragin, and P. Bouyer, Phys. Rev. Lett. **97**, 010402 (2006).

[2] R. Geiger, V. Ménoret, G. Stern, N. Zahzam, P. Cheinet, B. Battelier, A. Villing, F. Moron, M. Lours, Y. Bidel, A. Bresson, A. Landragin, and P. Bouyer, Nat. Commun. **2**, 474 (2011).

[3] P. Cheiney, L. Fouché, S. Templier, F. Napolitano, B. Battelier, P. Bouyer, and B. Barrett, Phys. Rev. Applied **10**, 034030 (2018).

[4] R. Bouchendira, P. Cladé, S. Guellati-Khlifa, F. Nez, and F. Biraben, Phys. Rev. Lett. **106**, 080801 (2011).

[5] G. Rosi, F. Sorrentino, L. Cacciapuoti, M. Prevedelli, and G. M. Tino, Nature **510**, 518 (2014).
[6] R. H. Parker, C. Yu, W. Zhong, B. Estey, and H. Müller, Science **360**, 191 (2018).
[7] A. Peters, K. Y. Chung, and S. Chu, Metrologia **38**, 25 (2001).
[8] Z.-K. Hu, B.-L. Sun, X.-C. Duan, M.-K. Zhou, L.-L. Chen, S. Zhan, Q.-Z. Zhang, and J. Luo, Phys. Rev. A **88**, 043610 (2013).
[9] P. Gillot, O. Francis, A. Landragin, F. P. D. Santos, and S. Merlet, Metrologia **51**, L15 (2014).
[10] C. Freier, M. Hauth, V. Schkolnik, B. Leykauf, M. Schilling, H. Wziontek, H.-G. Scherneck, J. Müller, and A. Peters, J. Phys. Conf. Ser. **723**, 012050 (2016).
[11] S.-K. Wang, Y. Zhao, W. Zhuang, T.-C. Li, S.-Q. Wu, J.-Y. Feng, and C.-J. Li, Metrologia **55**, 360 (2018).
[12] Y. Bidel, N. Zahzam, C. Blanchard, A. Bonnin, M. Cadoret, A. Bresson, D. Rouxel, and M. F. Lequentrec-Lalancette, Nat. Commun. **9**, 627 (2018).
[13] R. Karcher, A. Imanaliev, S. Merlet, and F. Pereira dos Santos, pre-print arXiv:1804.04909 (2018). [physics.atom-ph].
[14] J. M. McGuirk, G. T. Foster, J. B. Fixler, M. J. Snadden, and M. A. Kasevich, Phys. Rev. A **65**, 033608 (2002).
[15] F. Sorrentino, A. Bertoldi, Q. Bodart, L. Cacciapuoti, M. de Angelis, Y.-H. Lien, M. Prevedelli, G. Rosi, and G. M. Tino, Appl. Phys. Lett. **101**, 114106 (2012).
[16] S. Dimopoulos, P. W. Graham, J. M. Hogan, and M. A. Kasevich, Phys. Rev. Lett. **98**, 111102 (2007).
[17] S. Lepoutre, A. Gauguet, G. Trénec, M. Büchner, and J. Vigué, Phys. Rev. Lett. **109**, 120404 (2012).
[18] D. N. Aguilera, H. Ahlers, B. Battelier, A. Bawamia, A. Bertoldi, R. Bondarescu, K. Bongs, P. Bouyer, C. Braxmaier, L. Cacciapuoti *et al.*, Classical Quantum Gravity **31**, 115010 (2014).
[19] L. Zhou, S. Long, B. Tang, X. Chen, F. Gao, W. Peng, W. Duan, J. Zhong, Z. Xiong, J. Wang, Y. Zhang, and M. Zhan, Phys. Rev. Lett. **115**, 013004 (2015).
[20] M. Jaffe, P. Haslinger, V. Xu, P. Hamilton, A. Upadhye, B. Elder, J. Khoury, and H. Mller, Nat. Phys. **13**, 938 (2017).
[21] P. Asenbaum, C. Overstreet, T. Kovachy, D. D. Brown, J. M. Hogan, and M. A. Kasevich, Phys. Rev. Lett. **118**, 183602 (2017).
[22] W. Chaibi, R. Geiger, B. Canuel, A. Bertoldi, A. Landragin, and P. Bouyer, Phys. Rev. D **93**, 021101 (2016).
[23] J. M. Hogan and M. A. Kasevich, Phys. Rev. A **94**, 033632 (2016).
[24] I. Dutta, D. Savoie, B. Fang, B. Venon, C. Garrido Alzar, R. Geiger, and A. Landragin, Phys. Rev. Lett. **116**, 183003 (2016).
[25] A. Gauguet, B. Canuel, T. Lévèque, W. Chaibi, and A. Landragin, Phys. Rev. A **80**, 063604 (2009).
[26] T. Mazzoni, X. Zhang, R. Del Aguila, L. Salvi, N. Poli, and G. M. Tino, Phys. Rev. A **92**, 053619 (2015).
[27] M. Büchner, R. Delhuille, A. Miffre, C. Robilliard, J. Vigué, and C. Champenois, Phys. Rev. A **68**, 013607 (2003).
[28] F. Gori, Opt. Commun. **107**, 335 (1994).
[29] V. Pal, C. Tradonsky, R. Chriki, N. Kaplan, A. Brodsky, M. Attia, N. Davidson, and A. A. Friesem, Appl. Opt. **57**, 4583 (2018).
[30] H. Ma, Z. Liu, P. Zhou, X. Wang, Y. Ma, and X. Xu, J. Opt. **12**, 045704 (2010).
[31] J. A. Hoffnagle and C. M. Jefferson, Appl. Opt. **39**, 5488 (2000).
[32] See https://www.asphericon.com/en/asphere/shape-it-til-you-make-it-top-hat-beam-shaping-with-aspheres/ for "Asphericon Website" (last accessed October 9, 2018).
[33] A. Louchet-Chauvet, T. Farah, Q. Bodart, A. Clairon, A. Landragin, S. Merlet, and F. P. D. Santos, New J. Phys. **13**, 065025 (2011).
[34] M. Takeda, H. Ina, and S. Kobayashi, J. Opt. Soc. Am. **72**, 156 (1982).
[35] V. Schkolnik, B. Leykauf, M. Hauth, C. Freier, and A. Peters, Appl. Phys. B **120**, 311 (2015).
[36] M. Meunier, I. Dutta, R. Geiger, C. Guerlin, C. L. Garrido Alzar, and A. Landragin, Phys. Rev. A **90**, 063633 (2014).
[37] We varied the spatial frequencies of the added intensity noise and found no substantial difference in the simulation results as long as the spatial period was smaller than about 1/10 of the beam size. In the simulation reported in Fig. 3, the spatial period of the noise is 1/100 of the beam size.
[38] S. Merlet, J. LeGouët, Q. Bodart, A. Clairon, A. Landragin, F. Pereira Dos Santos, and P. Rouchon, Metrologia **46**, 87 (2009).
[39] A. Gauguet, T. E. Mehlstäubler, T. Lévèque, J. Le Gouët, W. Chaibi, B. Canuel, A. Clairon, F. P. Dos Santos, and A. Landragin, Phys. Rev. A **78**, 043615 (2008).
[40] G. Tackmann, P. Berg, C. Schubert, S. Abend, M. Gilowski, W. Ertmer, and E. M. Rasel, New J. Phys. **14**, 015002 (2012).
[41] Z.-W. Yao, S.-B. Lu, R.-B. Li, J. Luo, J. Wang, and M.-S. Zhan, Phys. Rev. A **97**, 013620 (2018).
[42] S.-W. Chiow, T. Kovachy, H.-C. Chien, and M. A. Kasevich, Phys. Rev. Lett. **107**, 130403 (2011).
[43] P. A. Altin, M. T. Johnsson, V. Negnevitsky, G. R. Dennis, R. P. Anderson, J. E. Debs, S. S. Szigeti, K. S. Hardman, S. Bennetts, G. D. McDonald, L. D. Turner, J. D. Close, and N. P. Robins, New J. Phys. **15**, 023009 (2013).
[44] B. Estey, C. Yu, H. Müller, P.-C. Kuan, and S.-Y. Lan, Phys. Rev. Lett. **115**, 083002 (2015).

RAPID COMMUNICATIONS

PHYSICAL REVIEW D **93,** 021101(R) (2016)

Low frequency gravitational wave detection with ground-based atom interferometer arrays

W. Chaibi,[1,*] R. Geiger,[2,†] B. Canuel,[3] A. Bertoldi,[3] A. Landragin,[2] and P. Bouyer[3]

[1]*ARTEMIS, Université Côte d'Azur, CNRS and Observatoire de la Côte d'Azur, F-06304 Nice, France*
[2]*LNE-SYRTE, Observatoire de Paris, PSL Research University, CNRS, Sorbonne Universités,*
UPMC Univ. Paris 06, 61 avenue de l'Observatoire, 75014 Paris, France
[3]*LP2N, Laboratoire Photonique, Numérique et Nanosciences Université Bordeaux-IOGS-CNRS:UMR*
5298, rue Mitterrand, F-33400 Talence, France

(Received 23 June 2015; published 15 January 2016)

We propose a new detection strategy for gravitational waves (GWs) below a few hertz based on a correlated array of atom interferometers (AIs). Our proposal allows us to reduce the Newtonian noise (NN), which limits all ground based GW detectors below a few hertz, including previous atom interferometry-based concepts. Using an array of long baseline AI gradiometers yields several estimations of the NN, whose effect can thus be reduced via statistical averaging. Considering the km baseline of current optical detectors, a NN rejection of a factor of 2 could be achieved and tested with existing AI array geometries. Exploiting the correlation properties of the gravity acceleration noise, we show that a tenfold or more NN rejection is possible with a dedicated configuration. Considering a conservative NN model and the current developments in cold atom technology, we show that strain sensitivities below $1 \times 10^{-19}/\sqrt{\mathrm{Hz}}$ in the $0.3 - 3$ Hz frequency band can be within reach, with a peak sensitivity of $3 \times 10^{-23}/\sqrt{\mathrm{Hz}}$ at 2 Hz. Our proposed configuration could extend the observation window of current detectors by a decade and fill the gap between ground-based and space-based instruments.

DOI: 10.1103/PhysRevD.93.021101

I. INTRODUCTION

Gravitational wave (GW) detection remains one of the challenges in fundamental physics and astrophysics. State-of-the-art GW detectors consisting of giant Fabry-Perot Michelson interferometers [1–5] now reach a sensitivity that justifies the expectations for a direct detection of GWs in the next few years [6]. Nevertheless, low frequency GW sources will remain hidden for ground based detectors for which the observation bandwidth will be limited to frequencies above a few Hz [7]. Reaching sub-Hz sensitivities would provide a decisive asset to GW astronomy as the sources in this band produce more powerful and durable signals [8]. For this purpose, hybrid detectors based on two distant atom interferometers (AIs) interrogated by a laser propagating over a long baseline have been proposed (see, e.g., Ref. [9]). Using as test masses free falling atoms instead of suspended mirrors could resolve most of the technical limitations presented by optical GW detectors at low frequency, such as residual seismic noise or thermal noise of suspension systems.

Like all ground based detectors, current atom interferometry proposals will nevertheless suffer from the so-called Newtonian noise (NN) [10]. NN consists in fluctuations of the terrestrial gravity field which creates a tidal effect on separated test masses and is indiscernible from the effect of a GW [10,11]. NN is therefore considered as a fundamental limit for any ground based GW detectors at frequencies below a few Hz. Various methods have been considered to circumvent this problem [12–15]. In this paper we propose a new concept which uses an array of AIs configured to reject the NN.

Unlike previous single strainmeter or gradiometer proposals where the NN and the GW signal are indiscernible, the array of AIs allows us to extract the GW signal by averaging over several realizations of the NN. The NN rejection can be further enhanced by exploiting the correlation spatial behavior of the gravity acceleration. With the $3 - 4$ km baseline of current best optical detectors, our method reaches a NN rejection of about 2; this factor is comparable to what was obtained by other passive methods (e.g., Ref. [14]). The principle of such rejection can be tested in current AI array projects [16]. We focus here on a 16 km baseline detector that takes full advantage of our method and enables strong NN rejection by more than a decade. This could complement the current optical interferometers development program by opening the $\sim 0.3 - 3$ Hz observation window.

II. PRINCIPLE

A single AI gradiometer [Fig. 1(a)] consists of two AIs separated by a baseline L and interrogated by a common laser beam of frequency ν close to the atomic transition frequency (see, e.g., Ref. [9]). We consider a three light-pulse AI (with T the time between the successive pulses) using Bragg diffraction of atoms from a standing wave produced by retroreflecting the interrogation laser. The

---

[*] chaibi@oca.eu
[†] remi.geiger@obspm.fr

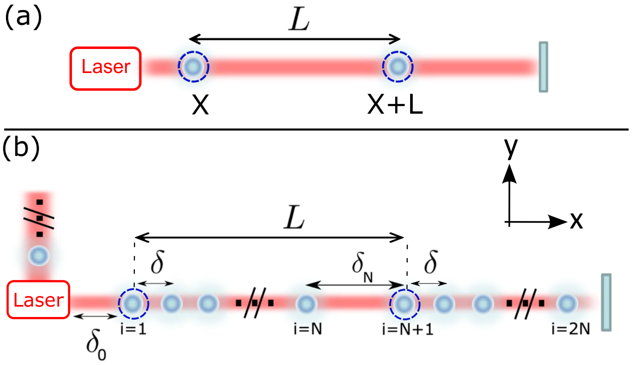

FIG. 1. (a) A single gradiometer using two AIs at positions X and $X + L$, interrogated by a common laser beam. (b) An array of N AI gradiometers used for sampling the spatial variations of the NN. The separation between the gradiometers is δ. The array allows one to repeat the experiment sketched in (a) N times and average the NN. The use of two orthogonal arms injected by a common laser enables one to reject laser frequency noise (the second arm in the y direction is only partially represented here for clarity).

output phase of each AI originates from the local phase difference $\Delta\varphi$ between the two counterpropagating beams at the time of the pulse and the position of the atom [17]. The retroreflection configuration gives immunity to laser phase noise induced by position noise of the input laser system. We consider large momentum transfer (LMT) diffraction [18], where the atom absorbs n photons from one beam and emits n photons in the counterpropagating beam. When the interrogation laser is pulsed, the atom undergoes diffraction with a momentum change of $n \times 2\hbar k$ along the laser propagation direction ($k = 2\pi\nu/c$ is the laser wave vector). A phase $n\Delta\varphi(X,t)$ is imprinted on the diffracted component.

After the three pulses, the output phase of the AI reads

$$\Delta\phi_x(X,t) = \epsilon(X,t) + 2nk\left[\left(\frac{\Delta\nu(t)}{\nu} + \frac{h(t)}{2}\right)(L - X) + \Delta x_2(t) - \Delta x(X,t)\right] \otimes s(t) \tag{1}$$

where $\epsilon(X,t)$ represents the detection noise (e.g., atom shot noise) on the output phase of an AI using atoms placed at position X. Here, $s(t)$ is the sensitivity function of the three pulse AI [19], and it relates the AI output phase to the second temporal derivative of the local laser phase difference $\Delta\varphi$. $\Delta x_2(t)$ is the position noise of the retroreflecting mirror, and $\Delta x(X,t)$ represents the motion of the atoms along the laser beam direction due to the fluctuations of the local gravitational acceleration.

Taking the differential phase $\psi(X,t) = \Delta\phi_x(X,t) - \Delta\phi_x(X+L,t)$ between two AIs separated by the distance L and neglecting laser frequency noise yields

$$\psi(X,t) = 2nk\left[\frac{L\ddot{h}(t)}{2} + a_x(X+L,t) - a_x(X,t)\right] \otimes s_\alpha(t) + \epsilon(X,t) - \epsilon(X+L,t), \tag{2}$$

where $s_\alpha(t)$ is the AI sensitivity function to acceleration, given by $\ddot{s}_\alpha(t) = s(t)$. Importantly, position noise $\Delta x_2(t)$ of the retroreflecting mirror has been rejected in this gradiometer configuration. Equation (2) shows that fluctuations of the local gravity field result in an acceleration signal $a_x(X,t) = \Delta\ddot{x}(X,t)$ whose gradient will have the same signature as that of the GW (see Ref. [17] for a more rigorous calculation).

The differential phase of Eq. (2) can be written as $\psi(\tilde{\eta}) = H(t) + \tilde{\eta}(t)$, where $H(t)$ is the GW signal and $\tilde{\eta}(t)$ the noise (detection noise and NN) at position X. Our idea is to extract $H(t)$ using a Monte Carlo method: The GW signal is obtained by averaging over several samples of the noise $\tilde{\eta}(t)$, which formally reads $H = \int \Psi(\tilde{\eta})\mathrm{d}\tilde{\eta}$. To this aim, we consider N realizations $\{\psi(X_i,t) \equiv \psi_i(t)\}_{i=1..N}$ of the single gradiometer and compute the average signal

$$H_N(t) = \frac{1}{N}\sum_{i=1}^{N}\psi_i(t), \tag{3}$$

which represents a nonbiased approximation to the GW signal of interest, i.e., $Lh(t)/2$. Assuming that the N realizations are independent, the residual noise on the GW measurement is reduced by $\sqrt{N}$,

$$\sigma_{H_N} = \frac{\sqrt{2}\sigma_\eta}{\sqrt{N}}, \tag{4}$$

with $\sigma_\eta = \sqrt{\sigma_a^2 + \sigma_\epsilon^2}$ the standard deviation (s.d.) resulting from the NN and detection noise which we considered as independent variables of s.d., σ_a and σ_ϵ, respectively. We assumed uncorrelated noise between the 2 AIs of a single gradiometer, yielding $\sqrt{2}$. This is always valid for the detection noise and applies for the NN when the gradiometer baseline L is much larger than the NN correlation length. Since the GW signal increases with L, a very long gradiometer baseline will be considered in the following, which validates the assumption of uncorrelated NN between the two AIs. As the N gradiometer measurements are assumed to be independent, the AI array brings a $\sqrt{N}$ rejection factor for the NN (and for the detection noise).

We study an implementation of this Monte Carlo sampling method in which N different gradiometer measurements are simultaneously realized in parallel thanks to an array of spatially distributed AIs. The proposed configuration is chosen to enhance the NN reduction via variance reduction [20]. For that, we optimize the AI array distribution, i.e., the signal spatial sampling, in order to benefit from the spatial behavior of NN correlations. We show that, in a given frequency band, a significant additional rejection factor can be gained with respect to the standard $\sqrt{N}$ of Eq. (4).

III. IMPLEMENTATION AND SENSITIVITY OF THE DETECTOR

The implementation is sketched in Fig. 1(b). We consider a symmetric configuration consisting of two orthogonal arms of the same length and interrogated by the same laser. For a GW with (+) polarization, laser frequency noise is therefore rejected (see Appendix A for more details). Each arm of total length L_a consists in a series of gradiometers of baseline $L = X_{N+i} - X_i$ which are separated by the distance δ. The geometrical parameter δ_N reflects that the baseline L and the separation δ between the gradiometers are independent. For $1 \leq i \leq N$ we define

$$\psi_i(t) = [\Delta\phi_x(X_i, 0, t) - \Delta\phi_x(X_{N+i}, 0, t)] - [\Delta\phi_y(0, Y_i, t) - \Delta\phi_y(0, Y_{N+i}, t)] \qquad (5)$$

and compute the output signal $H_N(t)$ of the detector using Eq. (3). It contains the GW signal $h(t)$, as well as the detection noise $\epsilon(t)$ and the NN $a(X, t)$. To derive the detector strain sensitivity curve, e.g., the minimum detectable GW power spectral density (PSD) $S_h(\omega)$ [21,22], we compute the PSD of the detector output, $S_{H_N}(\omega)$, using Eqs. (2), (3), and (5):

$$S_{H_N}(\omega) = (2nkL)^2\omega^4 S_h(\omega)|\hat{s}_\alpha(\omega)|^2 + (2nk)^2 S_a(\omega)|\hat{s}_\alpha(\omega)|^2 + \frac{4S_\epsilon(\omega)}{N}. \qquad (6)$$

Here $\hat{s}_\alpha(\omega) = 4\sin^2(\omega T/2)/\omega^2$ is the Fourier transform of the AI sensitivity function to acceleration $s_\alpha(t)$, and $S_\epsilon(\omega)$ is the PSD of the detection noise. The reduction by the factor N reflects the uncorrelated detection noise in the different AIs. The ratio between the first term (the GW contribution) and the last two terms (the noise PSD) of Eq. (6) defines the SNR of our detection. If we consider a minimum sensitivity with a SNR of 1, we obtain the strain sensitivity function

$$S_h(\omega) = \frac{S_a(\omega)}{\omega^4 L^2} + \frac{4S_\epsilon(\omega)}{16NL^2(2nk)^2\sin^4(\omega T/2)}. \qquad (7)$$

The NN PSD $S_a(\omega)$ contains two contributions: one given by the gravity acceleration correlations between AIs at two positions $\{X_i, X_j\}$ in the same arm, and one given by the correlations between AIs at two positions $\{X_i, Y_j\}$ in orthogonal arms. The calculation of these contributions is detailed below.

Before looking into the details of the AI array rejection method, we review the sources of NN, which are related to the modification of the mass distribution around the detector. We focus on the two main sources previously identified for ground based detectors: (i) seismic noise related to elastic waves propagating within the ground [10,23,24] (seismically induced Newtonian noise—SNN), and (ii) air mass fluctuations in the near atmosphere [10,25]. We base our calculation on the Saulson model [10]: For each frequency $f = \omega/2\pi$, the ground is subdivided into cells of fluctuating density whose size corresponds to the half wavelength $\mathcal{L}_\rho(\omega) = v_u/2f$ of a propagating compression wave of velocity v_u. More specifically, we use an upgrade of the Saulson model that guarantees the mass conservation by assuming an anticorrelation between adjacent cells [23]. We plot in Fig. 2 the spatial behavior of the gravity acceleration correlation between two distant points. Mass conservation yields a negative minimum of the correlation function for a characteristic length, which has been reported for the seismic noise in Ref. [26]. The main other sources of low frequency NN are those related to air pressure fluctuations caused by wind induced air turbulence [10] (Infrasound Newtonian Noise, INN), and to the effect of turbulence induced frozen cells of random temperature dragged by the wind [25]. For a detector at depth H, the latter effect has a cutoff frequency $f_c = v_{\mathrm{wind}}/(4\pi H)$ [25] which is out of the detector band for $H > 100$ m ($v_{\mathrm{wind}} \simeq 10-20$ m/s is the wind velocity).

We now give some details on the calculation of the NN contribution $S_a(\omega)$ appearing in Eq. (7), which we express as

$$S_a(\omega) = \frac{1}{N^2}\sum_{i,j=1}^{2N} \mathcal{C}_\parallel(X_i, X_j, \omega) + \frac{1}{N^2}\sum_{i,j=1}^{2N} \mathcal{C}_\perp(X_i, Y_j, \omega), \qquad (8)$$

with the single arm component

$$\sum_{i,j}^{2N} \mathcal{C}_\parallel(X_i, X_j) \equiv 4\sum_{i,j}^{N} C_{xx}(X_i, X_j) - 4\sum_{i,j}^{N} C_{xx}(X_i, X_{j+N}) \qquad (9)$$

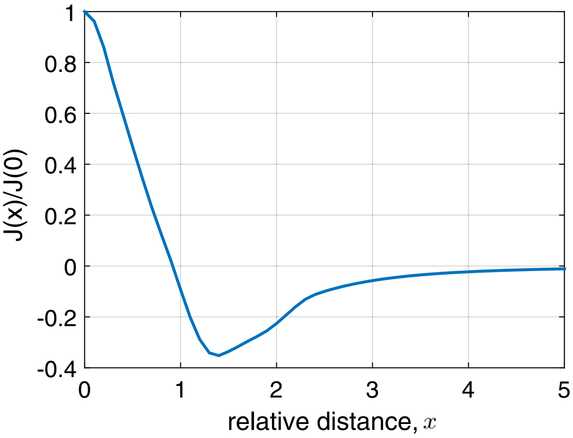

FIG. 2. Spatial behavior of the normalized NN correlations between two distant points separated by the relative distance $x = |X_j - X_i|/\mathcal{L}_\rho(\omega)$, where $\mathcal{L}_\rho(\omega)$ is the NN correlation length. The anticorrelation is a consequence of mass conservation between adjacent cells of fluctuating density.

and the crossed arms component

$$\sum_{i,j}^{2N} \mathcal{C}_{\perp}(X_i,X_j) \equiv -2\sum_{i,j}^{N} C_{xy}(X_i,Y_j) - 2\sum_{i,j}^{N} C_{xy}(X_{i+N},Y_{j+N}) + 4\sum_{i,j}^{N} C_{xy}(X_{i+N},Y_j). \tag{10}$$

In Eqs. (9) and (10), C_{xy} is the Fourier transform of the gravity acceleration correlation function between two AIs in arms (x, y), and we hid the ω dependency for clarity. We assumed isotropy of the NN and that the detector is surrounded by a homogeneous medium for both seismic and infrasound-air density fluctuations. We also consider the effects of the SNN and INN as independent, so that the incoherent sum of the two contributions provides an upper bound of our detector sensitivity. With this model, the correlation C_{xx} between two points in the same arm is given by

$$C_{xx}^{(u,a)}(X_i, X_j, \omega) \simeq G^2 \mathcal{L}_{\rho}^{(u,a)}(\omega)^2 \Delta\rho^2_{(u,a)}(\omega) J(x_{ij}^{(u,a)}(\omega)), \tag{11}$$

with $x_{ij}^{(u,a)}(\omega) = \frac{|X_i - X_j|}{\mathcal{L}_{\rho}^{(u,a)}(\omega)}$. Here G is the gravitational constant, (u, a) are indices denoting the seismic and infrasound NN contribution, and $\mathcal{L}_{\rho}^{(u,a)}(\omega) = \pi v_{u,a}/\omega$ is the corresponding correlation length, with v_u and v_a being, respectively, the speed of seismic waves in the underground and the speed of sound in the air. The function $J(x)$ is a 3D integral which represents the spatial behavior of NN correlations between two distant points X_i and X_j. It is represented in Fig. 2 against the relative distance x. A similar expression as in Eq. (11) holds for C_{xy}, the correlation between two points $\{X_i, Y_j\}$ in orthogonal arms.

Following Refs. [8,10], the density fluctuations for SNN and INN are respectively given by $\Delta\rho_u^2(\omega) = \frac{\rho_u^2 \Delta a_s^2(\omega)}{\pi\omega^2 v_u^2}$ and $\Delta\rho_a^2(\omega) = \frac{\rho_a^2}{\gamma^2 p_a^2}\Delta p^2(\omega)$. Here $\rho_u = 2300\ \mathrm{kg/m^3}$ is the mean underground density, $\Delta a_s(\omega)$ the seismic acceleration noise, $\rho_a = 1.3\ \mathrm{kg/m^3}$ the mean air density, $1/\gamma^2 \simeq 1/2$ the air coefficient of adiabatic compression, p_a the air pressure and $\Delta p^2(\omega)$ its PSD. We consider seismic waves with a typical speed for P waves of $v_u = 2$ km/s corresponding, for example, to porous rocks [27], yielding $\mathcal{L}_\rho = 1$ km at 1 Hz. The air pressure fluctuation spectrum used for the INN is $\Delta p^2(\omega) = 0.3 \times 10^{-5}/(f/1\,\mathrm{Hz})^2\,\mathrm{Pa^2/Hz}$ (as used by Saulson [10]). The seismic noise for the SNN is $1 \times 10^{-17}\ \mathrm{m^2\,s^{-4}/Hz}$ at 1 Hz as often reported in underground sites (see, e.g., Ref. [28,29]).

The gradiometer separation δ determines the NN rejection efficiency. For instance, if δ is much larger than the NN correlation length $\mathcal{L}_\rho(\omega)$ for all ω, then the successive measurement points are uncorrelated and Eq. (8) reduces to terms $i = j$, yielding

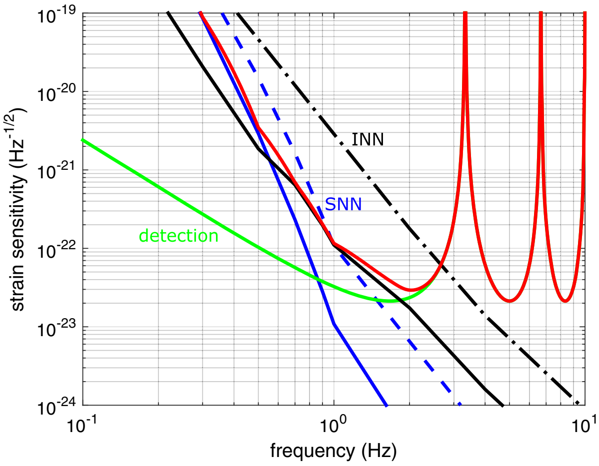

FIG. 3. Strain sensitivity curve for an AI array with $N = 80$, $\delta = 200$ m, $\delta_0 = \delta_N = 500$ m, $L = 16.3$ km and $L_a = 32.6$ km. The AI phase noise is $-140\ \mathrm{dB\,rad^2/Hz}$ with the interrogation time $T = 0.3$ s, and $n = 1000$ LMT beam splitters. Green: Detection noise. Dotted-dashed black (dashed blue): INN (SNN) for two test masses separated by the baseline L. Solid black line (blue): Residual INN (SNN) after NN rejection with the AI array. Red: Overall sensitivity curve.

$$S_a^{(u,a)}(\delta_\infty, \omega) \simeq \frac{4}{N} G^2 \mathcal{L}_{\rho}^{(u,a)}(\omega)^2 \Delta\rho^2_{(u,a)}(\omega) J(0). \tag{12}$$

This situation, which corresponds to the standard Monte Carlo method [see Eq. (4)], already determines a significant NN rejection of $\sqrt{N}$ (in noise amplitude). Choosing an optimal value for δ, it is then possible to benefit from the anticorrelation in the NN (corresponding to negative values in Fig. 2). In this case, the Monte Carlo variance reduction [20] increases the NN rejection of Eq. (12). The choice of the AI array sampling pattern (i.e., δ, δ_0 and δ_N) sets the correlation between the measurement points and thus the amount of additional NN rejection compared to $\sqrt{N}$. The INN and SNN rejection prefactors depend on the shape of $J(x)$, i.e., on the characteristics of the site [30].

We illustrate our discussion with a configuration of $N = 80$ gradiometers of baseline $L = 16.3$ km, separated by the distance $\delta = 200$ m. We plot the expected strain sensitivity function in Fig. 3, using Eqs. (7)–(10). We use a detection noise PSD $S_\epsilon = -140\ \mathrm{dB\,rad^2/Hz}$ which corresponds, for example, to $N_{at} = 10^{12}$ atoms per second and a 20 dB reduction (in variance) in the detection phase noise by using entangled atomic states. We assumed LMT beam splitters with $n = 1000$. Similar parameters have been considered in other AI proposals (see, e.g., Ref. [9]). The total AI interrogation time is chosen as $2T = 0.6$ s, which is compatible with the high sampling frequencies and the absence of dead times required for GW detection by using joint interrogation sequences [31].

The NN reduction offered by the AI array is maximal around 1 Hz where it exceeds 30 for the INN and 10 for the

SNN, yielding a shot noise limited strain sensitivity level of $3 \times 10^{-23}/\sqrt{\mathrm{Hz}}$ at 2 Hz. At low frequency ($\lesssim$0.3 Hz), the SNN correlation length becomes much greater than δ, which results in a high correlation between the different gradiometer measurements, thereby preventing the NN rejection. At high frequencies (>2 Hz), the detector is limited by detection noise.

IV. DISCUSSION

As shown in Fig. 4, such performances would allow observations in the frequency band $\sim 0.3-3$ Hz. This frequency band is covered neither by existing detectors nor by next generation detectors such as the Einstein Telescope [7] or ESA's L3 gravity observation mission eLISA [32], despite the presence of several astrophysical sources [33].

To conclude, we show that an array of AIs in an appropriate configuration can allow ground based GW detection in the $\sim 0.3-3$ Hz decade by overcoming the current limitation imposed by NN. The main idea consists in using a distribution of long baseline AI gradiometers to average the NN to zero. We show that a further NN reduction can be achieved by exploiting the NN correlation properties to configure the AI array. While the present concept can be tested on existing apparatuses, our method will take full advantage of the recent and future developments in atom interferometry. More advanced schemes might also lead to sensitivity improvements. For example, the measurement of higher order spatial derivatives of the gravity field [34], or the implementation of more complex spatial distributions of AIs, could achieve higher NN rejections, depending on the site-dependent NN correlations. Detectors based on AI arrays could then help fill the blind frequency band between ground-based and space-based detectors.

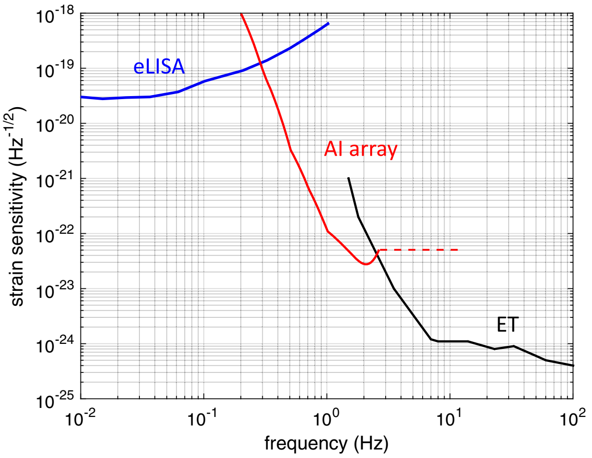

FIG. 4. The strain sensitivity of the proposed AI array covers the frequency region $\sim 0.3-3$ Hz, where future ground-based (Einstein Telescope, ET) and space-based (eLISA) detectors are blind. The dashed line represents an envelope of the proposed AI array sensitivity function at frequencies above 3 Hz and corresponds to an average detector response for different interrogation times T.

ACKNOWLEDGMENTS

We acknowledge P. Delva, P. Wolf, B. Chauvineau, J.-Y. Vinet, and T. Regimbau for discussions. We received financial support from the MIGA Equipex funded by the French National Research Agency (ANR-11-EQPX-0028).

APPENDIX A: REQUIREMENT ON SEISMIC ISOLATION OF BEAM SPLITTING OPTICS

In the proposed configuration consisting of two orthogonal arms [Fig. 1(b)], the beam splitting optical system that distributes the laser to the two arms introduces an asymmetry. Position noise (e.g., seismic noise) of the splitting optics results in laser frequency noise which will affect one arm and not the other: The phase φ_L of the laser beam propagating in the y direction picks up the position noise δy of the splitting optics, which results in a frequency noise contribution $\Delta\nu = \frac{1}{2\pi}\frac{d\varphi_L}{dt} = kf\delta y$ (with Fourier frequency f). According to Eq. (1), such frequency noise yields a

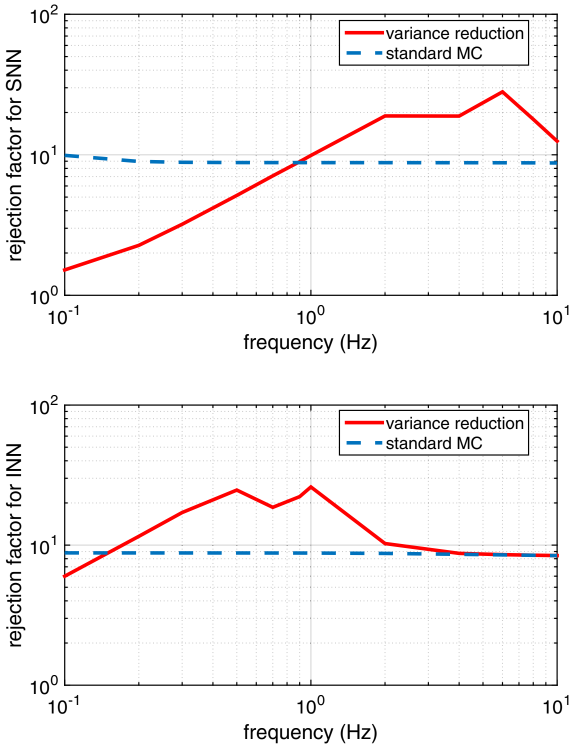

FIG. 5. Noise rejection factor of the SNN (top) and the INN (bottom) for the implementation of the AI array described in the main text.

contribution to the relative phase signal of the AI gradiometers in the y arm equal to $2nkL \times \Delta\nu(t)/\nu = 2nkL \times 2\pi f \delta y/c$, to be compared with the GW signal $2nk \times Lh$. Considering a minimum sensitivity with a SNR of 1 yields the requirement on the position noise δy_{min} of the splitting optics given by $\delta y_{\mathrm{min}} = hc/2\pi f$. To reach a detector peak sensitivity of $3 \times 10^{-23}/\sqrt{\mathrm{Hz}}$ at $f = 2$ Hz, the seismic noise must be below $\delta y_{\mathrm{min}}(2\ \mathrm{Hz}) \approx 7 \times 10^{-16}\ \mathrm{m}/\sqrt{\mathrm{Hz}}$. At $f = 0.3$ Hz, the AI array can feature a sensitivity of $1 \times 10^{-19}/\sqrt{\mathrm{Hz}}$ if the seismic noise is mitigated below $\delta y_{\mathrm{min}}(0.3\ \mathrm{Hz}) \approx 2 \times 10^{-11}\ \mathrm{m}/\sqrt{\mathrm{Hz}}$. Such seismic noise levels can be obtained with a dedicated low frequency suspension system (see, e.g., Ref. [35]). Finally, the contribution resulting from NN induced position fluctuations of the splitting optics is negligible at the targeted sensitivity level.

APPENDIX B: NEWTONIAN NOISE REJECTION EFFICIENCY

Figure 5 illustrates the NN rejection efficiency of the AI array. The dashed line shows the rejection in the case of a standard Monte Carlo average illustrating the $\sqrt{80}$ rejection factor. The plain line shows the rejection using the Monte Carlo variance reduction method exploiting the spatial behavior of the gravity acceleration correlation function. The maximum rejection is obtained when the NN correlation length $\mathcal{L}_{\rho}^{(u,a)} = v_{u,a}/2f$ approaches the distance corresponding to the anticorrelation of the gravity acceleration correlation function, which, from Fig. 2, is obtained for $x_{\mathrm{ac}} \approx 1.3$. This condition on the length translates in the frequency where the maximum rejection is observed, given by $f = v_{u,a}x_{\mathrm{ac}}/2\delta$, and equals 1.1 Hz for the INN and 6.5 Hz for the SNN.

[1] G. Cella and A. Giazotto, Rev. Sci. Instrum. **82**, 101101 (2011).

[2] K. Somiya, Classical Quantum Gravity **29**, 124007 (2012).

[3] F. Acernese *et al.*, Classical Quantum Gravity **32**, 024001 (2015).

[4] C. Affeldt *et al.*, Classical Quantum Gravity **31**, 224002 (2014).

[5] LIGO Scientific Collaboration, Classical Quantum Gravity **32**, 074001 (2015).

[6] J. Abadie *et al.*, Classical Quantum Gravity **27**, 173001 (2010).

[7] M. Punturo *et al.*, Classical Quantum Gravity **27**, 194002 (2010).

[8] J. Harms, B. Slagmolen, R. Adhikari, M. Miller, M. Evans, Y. Chen, H. Müller, and M. Ando, Phys. Rev. D **88**, 122003 (2013).

[9] S. Dimopoulos, P. W. Graham, J. M. Hogan, M. A. Kasevich, and S. Rajendran, Phys. Rev. D **78**, 122002 (2008).

[10] P. Saulson, Phys. Rev. D **30**, 732 (1984).

[11] F. Vetrano and A. Viceré, Eur. Phys. J. C **73**, 2590 (2013).

[12] P. Amaro-Seoane *et al.*, Classical Quantum Gravity **29**, 124016 (2012).

[13] J. C. Driggers, J. Harms, and R. X. Adhikari, Phys. Rev. D **86**, 102001 (2012).

[14] J. Harms and S. Hild, Classical Quantum Gravity **31**, 185011 (2014).

[15] J. Harms and H. J. Paik, Phys. Rev. D **92**, 022001 (2015).

[16] B. Canuel *et al.*, E3S Web Conf. **4**, 01004 (2014).

[17] C. Bordé, Gen. Relativ. Gravit. **36**, 475 (2004).

[18] H. Müller, S.-w. Chiow, Q. Long, S. Herrmann, and S. Chu, Phys. Rev. Lett. **100**, 180405 (2008).

[19] P. Cheinet, B. Canuel, F. Pereira Dos Santos, A. Gauguet, F. Leduc, and A. Landragin, IEEE Trans. Instrum. Meas. **57**, 1141 (2008).

[20] R. E. Caflisch, Acta Numer. **7**, 1 (1998).

[21] J. Creighton and W. Anderson, *Gravitational-Wave Physics and Astronomy*, Wiley Series in Cosmology (Wiley, Weinheim, Germany, 2012).

[22] C. J. Moore, R. H. Cole, and C. P. L. Berry, Classical Quantum Gravity **32**, 015014 (2015).

[23] M. Beccaria *et al.*, Classical Quantum Gravity **15**, 3339 (1998).

[24] S. Hughes and K. Thorne, Phys. Rev. D **58**, 122002 (1998).

[25] T. Creighton, Classical Quantum Gravity **25**, 125011 (2008).

[26] S. Mykkeltveit, K. Astebol, D. J. Doornbos, and E. S. Husebye, Bull. Seismol. Soc. Am. **73**, 173 (1983).

[27] G. Mavko, Conceptual Overview of Rock and Fluid Factors that Impact Seismic Velocity and Impedance (2015), https://pangea.stanford.edu/courses/gp262/Notes/8.SeismicVelocity.pdf.

[28] T. Farah, C. Guerlin, A. Landragin, P. Bouyer, S. Gaffet, F. Pereira Dos Santos, and S. Merlet, Gyroscopy Navigation **5**, 266 (2014).

[29] See Supplemental Material at http://link.aps.org/supplemental/10.1103/PhysRevD.93.021101 for the seismic and air pressure noise spectra used for the calculation of the NN.

[30] T. Braun and J. Schweitzer, Bull. Seismol. Soc. Am. **98**, 1876 (2008).

[31] M. Meunier, I. Dutta, R. Geiger, C. Guerlin, C. L. Garrido Alzar, and A. Landragin, Phys. Rev. A **90**, 063633 (2014).

[32] L3 Gravitational Observatory Advisory Team Intermediate Report at http://www.cosmos.esa.int/web/goat/home.

[33] R. X. Adhikari, Rev. Mod. Phys. **86**, 121 (2014).

[34] G. Rosi, L. Cacciapuoti, F. Sorrentino, M. Menchetti, M. Prevedelli, and G. M. Tino, Phys. Rev. Lett. **114**, 013001 (2015).

[35] J. Liu, L. Ju, and D. G. Blair, Phys. Lett. A **228**, 243 (1997).

Proposal for a Quantum Test of the Weak Equivalence Principle with Entangled Atomic Species

Remi Geiger[*]
LNE-SYRTE, Observatoire de Paris, Sorbonne Université,
PSL Université Paris, CNRS, 61 avenue de l'Observatoire, 75014 Paris, France

Michael Trupke[†]
Vienna Center for Quantum science and technology (VCQ), Faculty of Physics, Research Platform TURIS,
University of Vienna, A-1090 Vienna, Austria

(Received 16 June 2017; published 25 January 2018)

We propose an experiment to test the weak equivalence principle (WEP) with a test mass consisting of two entangled atoms of different species. In the proposed experiment, a coherent measurement of the differential gravity acceleration between the two atomic species is considered, by entangling two atom interferometers operating on the two species. The entanglement between the two atoms is heralded at the initial beam splitter of the interferometers through the detection of a single photon emitted by either of the atoms, together with the impossibility of distinguishing which atom emitted the photon. In contrast to current and proposed tests of the WEP, our proposal explores the validity of the WEP in a regime where the two particles involved in the differential gravity acceleration measurement are not classically independent, but entangled. We propose an experimental implementation using ^{85}Rb and ^{87}Rb atoms entangled by a vacuum stimulated rapid adiabatic passage protocol implemented in a high-finesse optical cavity. We show that an accuracy below 10^{-7} on the Eötvös parameter can be achieved.

DOI: 10.1103/PhysRevLett.120.043602

The current understanding of gravity is formulated by the theory of general relativity which has been proven to accurately describe many astronomical phenomena. The weak equivalence principle (WEP), also known as the universality of free fall, represents one of the three pillars of the Einstein equivalence principle, which was the basis of the elaboration of general relativity [1]. According to Damour [2], the equivalence "principle" is not satisfactory, as it sets an absolute structure for fundamental coupling constants (e.g., the fine-structure constant), in contrast to how physics (and relativity in particular) is constructed, i.e., avoiding the assumption of absolute structures. Unification theories, which aim at describing gravity and the three interactions of the standard model within a single mathematical framework, therefore commonly imply violations of the equivalence principle. WEP tests thus represent key probes in the search of new physical phenomena [2]. As the types of WEP violations, as well as the levels at which they could occur, are theoretically elusive, an experiment with improved accuracy or involving a different type of test mass might therefore point towards new physics [2].

WEP tests are quantified by the Eötvös parameter $\eta = 2(a_A - a_B)/(a_A + a_B)$, which deviates from zero if the accelerations a_A and a_B of the two bodies are different in a given gravitational field. WEP has been tested at the level of 10^{-13} uncertainty on the Eötvös parameter in continuously improved experiments involving torsion balances [3] or lunar laser ranging [4]. The first results of the MICROSCOPE experiment [5], which involves two free-falling macroscopic differential accelerometers, show the validity of WEP at the level of 2×10^{-14}. Apart from these high-precision experiments involving macroscopic masses, efforts are also being pursed to test the WEP with microscopic or exotic particles. These efforts started with experiments involving electrons [6] and neutron interferometers [7–9]. More recently, several results with cold atoms have been reported [10–16], together with proposals for improved tests [17–19]. Experiments using antimatter are also being developed [20,21].

The WEP and the role of inertial and gravitational masses in quantum mechanics have been studied theoretically in numerous works; see, e.g., Refs. [22,23]. It was shown recently in Ref. [24] that the validity of the equivalence principle for classical objects does not imply the validity of its quantum formulation, i.e., the equivalence between inertial and gravitational mass operators. Such considerations point towards new experimental approaches involving quantum test particles described by superposition states of internal degrees of freedom, e.g., as proposed in Ref. [25]. Very recently, an atom interferometry test of such a quantum formulation of the equivalence principle has been performed by measuring the free-fall acceleration of an atom in a superposition of different internal energy states [16].

In this Letter we propose a test of the WEP with a fundamentally different type of object than in previous or ongoing experiments, namely two entangled atoms of different species. The experiment considers the comparison of the free-fall acceleration of an atom $\mathcal{A}$ when it is entangled with a different atomic species $\mathcal{B}$ to the free-fall acceleration of the atoms without entanglement. We describe a particular implementation with ^{85}Rb and ^{87}Rb atoms and an entangling process based on a vacuum stimulated rapid adiabatic passage protocol implemented in a high-finesse optical cavity.

The concept of our proposal relies on a vertical atom interferometer in which atomic species $\mathcal{A}$ and $\mathcal{B}$ are entangled. The entanglement is heralded at the first beam splitter of the interferometer by the detection of a single photon. The scheme is related to the seminal work in Refs. [26,27], but operates here on freely propagating, distinguishable atoms instead of trapped, identical particles. In the event of the emission of a single photon from one of the two atoms in the direction of a photon detector, and assuming that it is not possible to distinguish which atom emitted the photon, a detection event will herald a superposition state: Atom $\mathcal{A}$ acquires the momentum $\hbar\vec{k}$ ($\mathcal{A}$ emitted the photon of wave vector $\vec{k}$) and atom $\mathcal{B}$ is left unperturbed, or vice versa. The corresponding entangled state can be written as

$$|\psi\rangle = \frac{1}{\sqrt{2}}(|\mathcal{A},\hbar\vec{k};\mathcal{B},\vec{0}\rangle + e^{i\phi}|\mathcal{A},\vec{0};\mathcal{B},\hbar\vec{k}\rangle). \qquad (1)$$

The beam splitter thus creates a superposition of the momenta of the two atomic species $\mathcal{A}$ and $\mathcal{B}$, with ϕ a fixed (nonrandom) phase in the case of a coherent superposition. To complete the interferometer, the two paths produced at the first beam splitter are subsequently manipulated with conventional atom optics (e.g., two-photon Raman transitions [28]) in order for the paths of each species to interfere. Single atom detectors are finally used to probe the atomic interference at the interferometer output.

We focus in this Letter on a particular implementation of this idea using ^{85}Rb and ^{87}Rb atoms, as sketched in Fig. 1. To entangle the two atoms, we propose to employ a vacuum stimulated Raman adiabatic passage (vSTIRAP) protocol [29], where the detection of a single photon exiting a high-finesse optical ring cavity heralds the entangled state of Eq. (1). The cavity is on resonance with a mode of frequency ω_c. The two atoms are initialized in one of their two hyperfine ground states, respectively, $|F=3\rangle$ for $\mathcal{A}=$ ^{85}Rb and $|F=2\rangle$ for $\mathcal{B}=$ ^{87}Rb; see Fig. 1(b). The vSTIRAP process is triggered at time $t=t_0$ by a pulse of two pump laser beams at frequencies $\omega_p^{\mathcal{A}}$ and $\omega_p^{\mathcal{B}}$ (red and blue vertical arrows), which fulfill the two-photon Raman resonance condition for each atom: $\omega_p^{\alpha}-\omega_c = G^{\alpha}+\omega_R^{\alpha}$, where G^{α} is the hyperfine splitting frequency, and ω_R^{α} is the two-photon recoil frequency, with $\alpha=\mathcal{A}$, $\mathcal{B}=$ ^{85}Rb, ^{87}Rb [30]. Assuming that the probability of the adiabatic passage for each atom is small [26,27], the vSTIRAP process will in all likelihood deposit at most a single photon into the cavity. The photon can then escape the cavity while one of the atoms is transferred from one hyperfine state to the other [29,31]. If the photon emission of both atomic species can be made to have the same envelope and frequency, then a detection event will herald the desired entangled state.

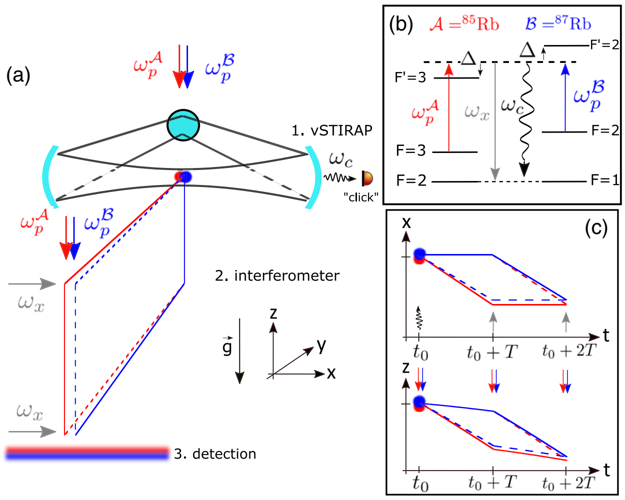

FIG. 1. Implementation with ^{85}Rb and ^{87}Rb atoms and a vSTIRAP protocol to realize the entangling beam splitter. (a) General sketch of the experiment: the atoms are laser cooled and then released in a high-finesse optical cavity made of three mirrors lying in the (xy) plane. During the vSTIRAP process, a photon is extracted from the pump beam (red and blue arrows for ^{85}Rb and ^{87}Rb, respectively), and a photon is emitted into the cavity mode. The emitted photon (frequency ω_c) is detected at one output of the cavity ("click"). (b) Energy levels of the atoms subject to two-photon Raman transitions. The high-finesse cavity is resonant for a mode of frequency ω_c. The vSTIRAP process is initiated at time $t=t_0$ by a pulse of the pump beams of frequency $\omega_p^{\mathcal{A},\mathcal{B}}$. The gray arrow represents a laser beam (frequency $\omega_x=\omega_c$) used to perform the Raman transitions in the mirror pulse and final beam splitter pulse of the interferometer. (c) Space-time diagrams of the atom interferometer in the x and z directions. In (a) and (c), the difference in recoil velocities between ^{85}Rb and ^{87}Rb has been exaggerated to 10% (instead of 2.3%). In the bottom of (c), gravity has been reduced to $g=0.01$ m s^{-2} in order to highlight the recoil effect.

In view of the WEP test, we aim to measure the gravitational acceleration with the atom interferometer, requiring a vertical accelerometer [28]. Therefore, at least one of the light beams realizing the Raman transition must have a projection on the gravity direction (z). We choose a configuration where the cavity is horizontal (xy plane in Fig. 1) and where the pump beams are aligned with gravity. As a consequence, the beam splitter operates in two dimensions, with a transfer of momentum $\hbar\vec{k}_{\text{tot}}\equiv\hbar(k_x\hat{x}-k_z\hat{z})$ along the $\hat{x}$ and $\hat{z}$ direction, with $k_x=\omega_c/c$ (k_z) the wave vector of the cavity (pump) photon. The remaining part of the interferometer is a typical Mach-Zehnder configuration [28], apart from the fact that the mirror and final beam splitter pulses are two-dimensional in the momentum transfer; see Fig. 1(c).

After the last beam splitter pulse occurring at time $t = t_0 + 2T$, the detection of each single-atom state can be performed by fluorescence detection with a photodiode [32], or by imaging using a light sheet detector [33].

We compute the atom interferometer phase shift following the path integral approach [34]. In atom interferometers using two-photon Raman transitions, the phase of the interferometer originates from the relative phase between the Raman lasers $\phi(t)$, which is imprinted on the diffracted atomic wave by the different Raman pulses [35,36]. More precisely, the phase shift imprinted on atom $\alpha = \mathcal{A}, \mathcal{B}$ by a light pulse is $\phi_\alpha(t) = \vec{k}^\alpha_{\mathrm{tot}} \cdot \vec{r}^\alpha(t) + \varphi^\alpha_0(t)$, with $\vec{r}^\alpha(t)$ the position of the atom in the laboratory frame holding the lasers and the cavity, and $\varphi^\alpha_0(t)$ a phase offset associated with the change of the internal energy state. Assuming that all Raman lasers are phase locked [i.e., red (gray) and blue (gray) lasers in Fig. 1], we can leave aside the φ_0 term and neglect the finite duration of the Raman pulse ($\sim 10\ \mu$s typically). The laser phase can then be written more explicitly as $\phi^\alpha(t) = -k_x x_\alpha(t) - k^\alpha_z z_\alpha(t)$. Note that k_x is the same for both atoms (gray arrow); the relative difference in k_z is $\sim 10^{-5}$ (difference in hyperfine splitting between ^{85}Rb and ^{87}Rb) and will be omitted from now on [37].

After the vSTIRAP process, the two-particle state reads

$$|\psi(t_0)\rangle = \frac{1}{\sqrt{2}}(|\mathcal{A}, \hbar\vec{k}_{\mathrm{tot}}; \mathcal{B}, \vec{0}\rangle e^{i\phi^{\mathcal{A}}_0} + |\mathcal{A}, \vec{0}; \mathcal{B}, \hbar\vec{k}_{\mathrm{tot}}\rangle e^{i\phi^{\mathcal{B}}_0}), \tag{2}$$

with $\phi^\alpha_0 \equiv \phi^\alpha(t_0)$. Note that we have treated the phase shift imprinted on the atom during the vSTIRAP process as for a conventional Raman transition, although the emission of the photon occurs in the vacuum of the cavity mode [38]. In the Raman process, the change of momentum $\vec{0} \leftrightarrow \vec{k}_{\mathrm{tot}}$ is accompanied by a change of the hyperfine state of the atom [39], which we omit in Eq. (2) to simplify the notations.

After the mirror pulse at time $t_0 + T$, the state reads

$$\begin{aligned}|\psi(t_0 + T)\rangle = \frac{1}{\sqrt{2}}[&|\mathcal{A}, \vec{0}; \mathcal{B}, \hbar\vec{k}_{\mathrm{tot}}\rangle e^{i\phi^{\mathcal{A}}_0} e^{i(\phi^{\mathcal{B}}_T - \phi^{\mathcal{A}}_T)} \\ &+ |\mathcal{A}, \hbar\vec{k}_{\mathrm{tot}}; \mathcal{B}, \vec{0}\rangle e^{i\phi^{\mathcal{B}}_0} e^{i(\phi^{\mathcal{A}}_T - \phi^{\mathcal{B}}_T)}],\end{aligned} \tag{3}$$

with $\phi^\alpha_T \equiv \phi^\alpha(t_0 + T)$ the relative Raman laser phase at time $t_0 + T$. The last beam splitter occurring at $t_0 + 2T$ acts globally on both atoms [27], which results in the output state

$$\begin{aligned}|\psi(t_0+2T)\rangle = \frac{1}{2\sqrt{2}}[&|\mathcal{A},\vec{0};\mathcal{B},\vec{0}\rangle(ie^{i(\varphi-\phi^{\mathcal{A}}_{2T})} + ie^{i(\Psi-\phi^{\mathcal{B}}_{2T})}) \\ &+ |\mathcal{A},\hbar\vec{k}_{\mathrm{tot}};\mathcal{B},\hbar\vec{k}_{\mathrm{tot}}\rangle(ie^{i(\varphi+\phi^{\mathcal{B}}_{2T})} + ie^{i(\Psi+\phi^{\mathcal{A}}_{2T})}) \\ &+ |\mathcal{A},\vec{0};\mathcal{B},\hbar\vec{k}_{\mathrm{tot}}\rangle(i^2 e^{i(\varphi-\phi^{\mathcal{A}}_{2T}+\phi^{\mathcal{B}}_{2T})} + e^{i\Psi}) \\ &+ |\mathcal{A},\hbar\vec{k}_{\mathrm{tot}};\mathcal{B},\vec{0}\rangle(e^{i\varphi} + i^2 e^{i(\Psi+\phi^{\mathcal{A}}_{2T}-\phi^{\mathcal{B}}_{2T})})],\end{aligned} \tag{4}$$

where $\varphi = \phi^{\mathcal{B}}_0 + \phi^{\mathcal{A}}_T - \phi^{\mathcal{B}}_T$ and $\Psi = \phi^{\mathcal{A}}_0 + \phi^{\mathcal{B}}_T - \phi^{\mathcal{A}}_T$.

The detection of the four possible states at the interferometer output can be performed by fluorescence detection (light sheets in Fig. 1), which resolves the two hyperfine states of each atom [39]. For example, the probability of detecting atom $\mathcal{A}$ and atom $\mathcal{B}$ in the output port corresponding to the null momentum (projector on state $|\mathcal{A}, \vec{0}; \mathcal{B}, \vec{0}\rangle$) is given by

$$P_{00} = |\langle\mathcal{A},\vec{0};\mathcal{B},\vec{0}|\psi(t_0+2T)\rangle|^2 = \frac{1}{8}|1+e^{i(\Phi_{\mathcal{A}}-\Phi_{\mathcal{B}})}|^2, \tag{5}$$

with $\Phi_\alpha = \phi^\alpha_0 - 2\phi^\alpha_T + \phi^\alpha_{2T}$.

The expression of the phase shift Φ_α is the same as in a traditional three light pulse interferometer [34]. However, in contrast to two classically independent interferometers that would operate in parallel on atom $\mathcal{A}$ and atom $\mathcal{B}$, the phase of the entangled interferometer, $\Delta\Phi \equiv \Phi_{\mathcal{A}} - \Phi_{\mathcal{B}}$, is determined by the phase shifts experienced by both atoms, as a result of two-particle interferometry [40,41]. The entanglement between the two interferometers can thus be verified experimentally by applying controlled phase shifts on the relative phase of the (phase-locked) Raman lasers: while a phase shift applied to only one pair of lasers (say, for $\mathcal{A}$) affects the mutual signal P_{00}, the same phase shift applied on both pairs of lasers should not affect P_{00}.

Finally, $\Delta\Phi$ results from the terms in Eq. (4), and writing the trajectories of the atoms as $x^\alpha(t) = x^\alpha_0 + v^\alpha_{x0}(t - t_0) + a^\alpha_x(t - t_0)^2/2$ and $z^\alpha(t) = z^\alpha_0 + v^\alpha_{z0}(t - t_0) - g^\alpha_z(t - t_0)^2/2$, we obtain

$$\Delta\Phi = k_z(g^{\mathcal{A}}_z - g^{\mathcal{B}}_z)T^2 + k_x(a^{\mathcal{A}}_x - a^{\mathcal{B}}_x)T^2, \tag{6}$$

which reflects the bidirectional acceleration sensitivity of the interferometer. Provided that the experiment is not constantly accelerated in the horizontal direction with respect to the freely falling atoms ($a^\alpha_x = 0$), the second term vanishes on average. The main phase shift of the interferometer, $\Delta\Phi_{\mathrm{WEP}} \equiv k_z(g^{\mathcal{A}}_z - g^{\mathcal{B}}_z)T^2$, represents a coherent measurement of the difference in the gravitational acceleration between the two atoms.

Details of implementation and expected sensitivity.— The design of the experiment is driven by the need for indistinguishability of the emitted photon during the vSTIRAP process, and of the two atoms in the interferometer up to the last beam splitter. On the technical aspects, the design must take into account (i) the preparation of two cold atoms of ^{85}Rb and ^{87}Rb with high probability, (ii) the design of the high-finesse ring cavity, (iii) the optical access for the laser beams realizing the mirror and final beam splitter pulses, and (iv) the detection of the two atoms. We consider atoms loaded in the cavity mode and exiting the cavity for the second and third interferometer pulses. This requires a sufficient interrogation time, set to $T = 50$ ms in the following.

The first step consists of preparing two cold ($\sim$ few μK) ^{85}Rb and ^{87}Rb atoms, which can be achieved in microscopic dipole traps operating in the collisional blockade regime [32,42,43]. The ^{85}Rb and ^{87}Rb atoms are prepared in the states $|F=3, m_F=3\rangle$ and $|F=2, m_F=2\rangle$, respectively, and driven with individual, π-polarized pump beams. We envisage a ring cavity with coupling strength, field amplitude decay, and atomic decay rates $\{g, \kappa, \gamma\}/2\pi = \{2.24, 0.5, 2.9\}$ MHz for the $|F=2, m_F=2\rangle \leftrightarrow |F'=3, m'_F=3\rangle$ transition of the D_1 line of ^{85}Rb [31]. The cavity is also coupled to the $|F=1, m_F=1\rangle \leftrightarrow |F'=2, m'_F=2\rangle$ transition of the D_1 line of ^{87}Rb. The coupling strength g is reduced to $2\pi \times 2.12$ MHz for ^{87}Rb because of its slightly smaller transition matrix element. The cavity is detuned by $\Delta/2\pi = 1.367$ GHz from the ^{85}Rb transition and by $-\Delta$ from the ^{87}Rb line, leading to identical emission frequencies. This setting is chosen as neighboring transitions are either far detuned or forbidden.

Using a three-level master equation approach, we calculate the dynamics of the vSTIRAP process, and confirm that the power envelopes of the photons emitted by the two atomic species can be made almost perfectly indistinguishable by tuning the Rabi frequencies of the two processes [37,44,45]. We further find that the efficiency of the processes and the probability of spontaneous emission can be tuned to achieve a workable success probability $P_S = 2 \times P_{\mathrm{stim}} \times (1 - P_{\mathrm{stim}}) \times P_{\mathrm{coll}} \times (1 - P_{\mathrm{spon}})^2$, where P_{stim}, P_{coll}, and P_{spon} indicate the probabilities for stimulated emission, photon collection, and spontaneous emission, respectively. We also extract the probability for false-positive detection (both atoms emit a photon, but only one is detected), $P_F = P_{\mathrm{stim}}^2 \times P_{\mathrm{coll}} \times (1 - P_{\mathrm{coll}})$, where we assume number-resolving photon detectors [31,46]. From the numerical calculations we find the best ratio $P_{\mathrm{stim}}/P_{\mathrm{spon}} \simeq 3.2$ for $P_{\mathrm{stim}} < 0.2$. In this regime there is therefore a simple trade-off between success probability and false-positive detection. For example, if we assume $P_{\mathrm{coll}} = 0.4$ and $P_{\mathrm{stim}} = 0.1$ (Ref. [47]), then $P_S = 7.0\%$ and $P_F = 0.26\%$ [37]. Spontaneous emission is not problematic as such, since it will in all likelihood lead to a loss of the affected atom from the spatial or temporal detection windows.

Ensuring that the two atoms couple in the same way to the cavity mode requires their separation to be less than the mode waist (~40 μm) in the radial direction and less than the cavity mode Rayleigh length in the longitudinal direction (~ few mm). This is not a concern for atoms at few μK temperatures and a free evolution time $t_0 \sim 1$ ms between the atom preparation and the vSTIRAP pulse.

Because of the different masses of the two atoms, the recoil is different by 2.3% for the two species, which results in different paths followed by the particles (this effect is exaggerated in Fig. 1). For $T = 50$ ms, the maximum displacement between the two species within one interferometer path is $\simeq 5$ μm [48].

We conclude by estimating the sensitivity that could be achieved in a WEP test. The interferometer fringes can be reconstructed shot after shot by varying the Raman laser relative phase for one species (e.g., before the last beam splitter), allowing one to extract $\Delta\Phi_{\mathrm{WEP}}$. Assuming a single-atom quantum projection noise limited sensitivity [32], the acceleration sensitivity is given by $\sigma_{\mathrm{WEP}} \simeq 1/(k_z T^2 \sqrt{N})$, where N is the number of measurements. With $N = 10^4$ successful measurements (10 mrad phase sensitivity) and $T = 50$ ms, a differential acceleration sensitivity $\sim 5 \times 10^{-7}$ m s^{-2} can be reached, corresponding to a potential sensitivity $\sim 5 \times 10^{-8}$ on the Eötvös parameter. Note that vibration noise is expected to have a negligible effect as it is common to both interferometers [see Eq. (6)]. Further measurements can then be performed independently with one species at a time to extract the values of the gravitational acceleration separately for each species, and to investigate systematic effects [49].

The effect of entanglement on the free fall can thus be directly assessed by comparing the differential gravity obtained with the entangled atoms ($g^{\mathcal{A}} - g^{\mathcal{B}}$ in $\Delta\Phi_{\mathrm{WEP}}$) to that obtained with the classically independent atoms ($g^{\mathcal{A}}$ and $g^{\mathcal{B}}$ measured independently).

WEP tests have so far relied on a differential measurement between two classically independent proof masses. This includes experiments with cold atom interferometers [11–16], which explore the validity of the WEP in a different regime than experiments involving macroscopic objects, because the measurement principle involves matter-wave interference, and therefore rely on superpositions of quantum degrees of freedom. For example, the recent result reported in Ref. [16] uses an atom in an incoherent superposition of two internal energy states separated by ~30 μeV, allowing one to probe new possible WEP violations [24]. Our proposal makes a conceptual stride beyond previous works, by enforcing entanglement between two atomic species of different mass (~2 GeV energy difference), allowing one to probe directly the effect of entanglement on the free fall. More specifically, our scheme could, for example, be used to assess the quantum formulation of the WEP presented in Ref. [24] at the scale of 2 GeV [50].

To the best of our knowledge, there is currently no theoretical model which addresses the question of whether or not the presence of entanglement in a system could lead to a violation of the WEP at a given level of accuracy. In general, WEP tests involving new types of physical objects, such as matter waves or antimatter, are motivated by the qualitatively different nature of the involved proof masses, rather than by a consensual theoretical argument predicting a violation in such systems. Our proposal follows this approach by aiming for a test of a foundational principle of physics with a qualitatively new system not considered before [51].

Beyond a conceptually new type of WEP test, our proposal can be used for a test of Bell's inequalities with free-falling massive particles of different species.

Following Ref. [52], a correlation coefficient E can be formed from the measurement of the four joint probabilities associated to the four modes appearing in Eq. (4). It reads $E = V\cos(\Delta\Phi) \simeq V\cos[k_z T^2(g_z^{\mathcal{A}} - g_z^{\mathcal{B}})]$ and can be interpreted as a measure for a Bell test in the presence of gravity.

We thank P. Wolf, C. Garrido Alzar, Y. Sortais, A. Landragin, A. Browaeys, F. Pereira Dos Santos, J.-P. Uzan, and Č. Brukner for fruitful discussions.

---

[*] remi.geiger@obspm.fr

[†] michael.trupke@univie.ac.at

[1] C. M. Will, Living Rev. Relativity **9**, 3 (2006).
[2] T. Damour, Classical Quantum Gravity **29**, 184001 (2012).
[3] T. A. Wagner, S. Schlamminger, J. H. Gundlach, and E. G. Adelberger, Classical Quantum Gravity **29**, 184002 (2012).
[4] J. G. Williams, S. G. Turyshev, and D. H. Boggs, Phys. Rev. Lett. **93**, 261101 (2004).
[5] P. Touboul *et al.*, Phys. Rev. Lett. **119**, 231101 (2017).
[6] F. C. Witteborn and W. M. Fairbank, Phys. Rev. Lett. **19**, 1049 (1967).
[7] R. Colella, A. W. Overhauser, and S. A. Werner, Phys. Rev. Lett. **34**, 1472 (1975).
[8] U. Bonse and T. Wroblewski, Phys. Rev. Lett. **51**, 1401 (1983).
[9] H. Abele and H. Leeb, New J. Phys. **14**, 055010 (2012).
[10] S. Fray, C. A. Diez, T. W. Hänsch, and M. Weitz, Phys. Rev. Lett. **93**, 240404 (2004).
[11] M. G. Tarallo, T. Mazzoni, N. Poli, D. V. Sutyrin, X. Zhang, and G. M. Tino, Phys. Rev. Lett. **113**, 023005 (2014).
[12] D. Schlippert, J. Hartwig, H. Albers, L. L. Richardson, C. Schubert, A. Roura, W. P. Schleich, W. Ertmer, and E. M. Rasel, Phys. Rev. Lett. **112**, 203002 (2014).
[13] L. Zhou, S. Long, B. Tang, X. Chen, F. Gao, W. Peng, W. Duan, J. Zhong, Z. Xiong, J. Wang, Y. Zhang, and M. Zhan, Phys. Rev. Lett. **115**, 013004 (2015).
[14] A. Bonnin, N. Zahzam, Y. Bidel, and A. Bresson, Phys. Rev. A **92**, 023626 (2015).
[15] X.-C. Duan, X.-B. Deng, M.-K. Zhou, K. Zhang, W.-J. Xu, F. Xiong, Y.-Y. Xu, C.-G. Shao, J. Luo, and Z.-K. Hu, Phys. Rev. Lett. **117**, 023001 (2016).
[16] G. Rosi, G. D'Amico, L. Cacciapuoti, F. Sorrentino, M. Prevedelli, M. Zych, C. Brukner, and G. M. Tino, Nat. Commun. **8**, 15529 (2017).
[17] S. Dimopoulos, P. W. Graham, J. M. Hogan, and M. A. Kasevich, Phys. Rev. Lett. **98**, 111102 (2007).
[18] G. Varoquaux, R. A. Nyman, R. Geiger, P. Cheinet, A. Landragin, and P. Bouyer, New J. Phys. **11**, 113010 (2009).
[19] B. Altschul *et al.*, Adv. Space Res. **55**, 501 (2015).
[20] P. Debu, Hyperfine Interact. **212**, 51 (2012).
[21] A. Kellerbauer *et al.*, Nucl. Instrum. Methods Phys. Res., Sect. B **266**, 351 (2008).
[22] L. Viola and R. Onofrio, Phys. Rev. D **55**, 455 (1997).
[23] E. Kajari, N. L. Harshman, E. M. Rasel, S. Stenholm, G. Süßmann, and W. P. Schleich, Appl. Phys. B **100**, 43 (2010).
[24] M. Zych and C. Brukner, arXiv:1502.00971.
[25] P. J. Orlando, R. B. Mann, K. Modi, and F. A. Pollock, Classical Quantum Gravity **33**, 19LT01 (2016).
[26] C. Cabrillo, J. I. Cirac, P. García-Fernández, and P. Zoller, Phys. Rev. A **59**, 1025 (1999).
[27] L. Slodicka, G. Hétet, N. Röck, P. Schindler, M. Hennrich, and R. Blatt, Phys. Rev. Lett. **110**, 083603 (2013).
[28] M. Kasevich and S. Chu, Phys. Rev. Lett. **67**, 181 (1991).
[29] M. Hennrich, T. Legero, A. Kuhn, and G. Rempe, Phys. Rev. Lett. **85**, 4872 (2000).
[30] We neglect here the Doppler effect originating from the velocity of the atom in the direction of the beams.
[31] T. Wilk, S. C. Webster, H. P. Specht, G. Rempe, and A. Kuhn, Phys. Rev. Lett. **98**, 063601 (2007).
[32] L. P. Parazzoli, A. M. Hankin, and G. W. Biedermann, Phys. Rev. Lett. **109**, 230401 (2012).
[33] R. Bücker, A. Perrin, S. Manz, T. Betz, C. Koller, T. Plisson, J. Rottmann, T. Schumm, and J. Schmiedmayer, New J. Phys. **11**, 103039 (2009).
[34] P. Storey and C. Cohen-Tannoudji, J. Phys. II (France) **4**, 1999 (1994).
[35] C. J. Bordé, Gen. Relativ. Gravit. **36**, 475 (2004).
[36] P. Wolf, L. Blanchet, C. J. Bordé, S. Reynaud, C. Salomon, and C. Cohen-Tannoudji, Classical Quantum Gravity **28**, 145017 (2011).
[37] See Supplemental Material at http://link.aps.org/supplemental/10.1103/PhysRevLett.120.043602 for details on the vSTIRAP dynamics, and for a discussion of the peculiar effects associated to the center of mass of the two-entangled-species state.
[38] M. S. Chapman, T. D. Hammond, A. Lenef, J. Schmiedmayer, R. A. Rubenstein, E. Smith, and D. E. Pritchard, Phys. Rev. Lett. **75**, 3783 (1995).
[39] C. Bordé, Phys. Lett. A **140**, 10 (1989).
[40] M. A. Horne, A. Shimony, and A. Zeilinger, Phys. Rev. Lett. **62**, 2209 (1989).
[41] J. G. Rarity and P. R. Tapster, Phys. Rev. Lett. **64**, 2495 (1990).
[42] N. Schlosser, G. Reymond, and P. Grangier, Phys. Rev. Lett. **89**, 023005 (2002).
[43] P. Xu, J. Yang, M. Liu, X. He, Y. Zeng, K. Wang, J. Wang, D. J. Papoular, G. V. Shlyapnikov, and M. Zhan, Nat. Commun. **6**, 7803 (2015).
[44] G. S. Vasilev, D. Ljunggren, and A. Kuhn, New J. Phys. **12**, 063024 (2010).
[45] N. V. Vitanov, A. A. Rangelov, B. W. Shore, and K. Bergmann, Rev. Mod. Phys. **89**, 015006 (2017).
[46] See, for example, the single photon counting modules from Excelitas, http://www.excelitas.com/Pages/Product/Single-Photon-Counting-Modules-SPCM.aspx.
[47] M. Mücke, J. Bochmann, C. Hahn, A. Neuzner, C. Nölleke, A. Reiserer, G. Rempe, and S. Ritter, Phys. Rev. A **87**, 063805 (2013).
[48] We note further that the paths of the two isotopes can be made near identical by operating on the D2 line for ^{87}Rb and, e.g., rendering the emitted photons indistinguishable by wavelength conversion.
[49] Isotope-dependent phase shifts must be carefully controlled. For example, the difference in magnetic field response of the two isotopes corresponds to a systematic effect of the order of 500 mrad for a magnetic field gradient of 1 $\mathrm{mG\,cm^{-1}}$ and $T = 50$ ms, which must be controlled at the 2% level to achieve an accuracy of 5×10^{-8} on the Eötvös parameter.

[50] More precisely, our scheme could be used to constrain the nondiagonal elements of the dimensionless operator $\hat{\eta} = \hat{I}_{\mathrm{int}} - \hat{M}_g \hat{M}_i^{-1}$ defined in Ref. [24], and constrained at the level of 5×10^{-8} for a $\sim 30\ \mu\mathrm{eV}$ energy difference in Ref. [16].

[51] M. Aspelmeyer, C. Brukner, D. Giulini, and G. Milburn, New J. Phys. **19**, 050401 (2017).

[52] P. Dussarrat, M. Perrier, A. Imanaliev, R. Lopes, A. Aspect, M. Cheneau, D. Boiron, and C. I. Westbrook, Phys. Rev. Lett. **119**, 173202 (2017).